Simulation of penetration in normal strength concrete for a projectile with L/D=9

Håkan Hansson

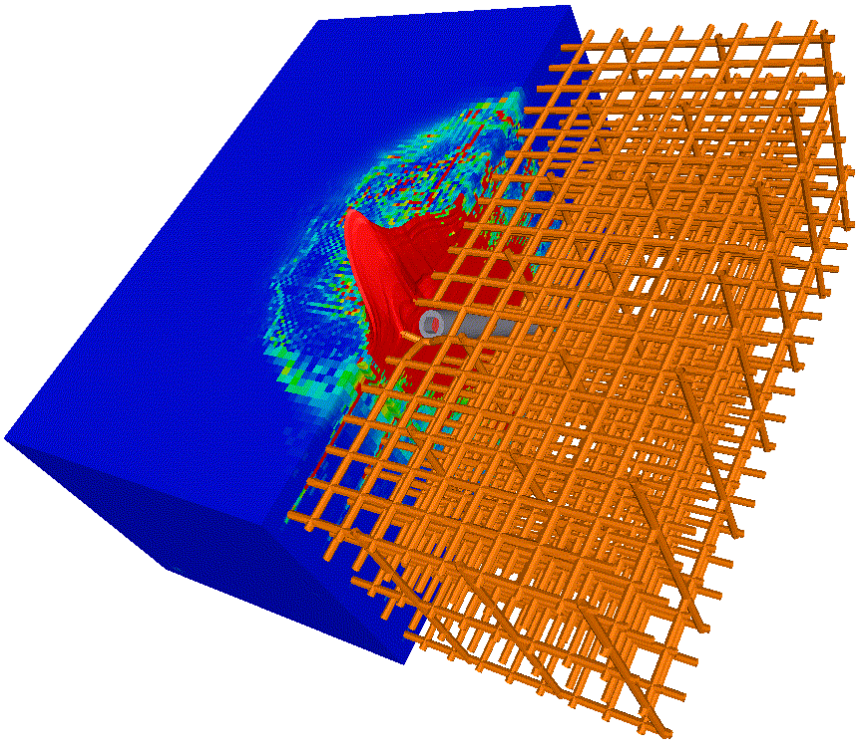

FOI-R-- 1759 --SE
ISSN 1650-1942

Weapons and Protection
Technical report

December 2005

FOI is an assignment-based authority under the Ministry of Defence. The core activities are research, method and technology development, as well as studies for the use of defence and security. The organization employs around 1350 people of whom around 950 are researchers. This makes FOI the largest research institute in Sweden. FOI provides its customers with leading expertise in a large number of fields such as security-policy studies and analyses in defence and security, assessment of different types of threats, systems for control and management of crises, protection against and management of hazardous substances, IT-security and the potential of new sensors.

FOI
Defence Research Agency
Weapons and Protection
SE-147 25 Tumba

Phone: +46 8 555 030 00
Fax: +46 8 555 031 00

www.foi.se

Simulation of penetration in normal strength concrete for a projectile with L/D=9

FOI-R--1759--SE
ISSN 1650-1942

Weapons and Protection
Technical report

December 2005

Issuing organization FOI – Swedish Defence Research Agency Weapons and Protection SE-147 25 Tumba	**Report number, ISRN** FOI-R--1759--SE	**Report type** Technical report
	Research area code 5. Strike and protection	
	Month year December 2005	**Project no.** E2358
	Sub area code 53 Protection and Fortification	
	Sub area code 2	
Author/s (editor/s) Håkan Hansson	**Project manager** Håkan Hansson	
	Approved by	
	Sponsoring agency Swedish Armed Forces	
	Scientifically and technically responsible	

Report title

Simulation of penetration in normal strength concrete for a projectile with L/D=9

Abstract

The performance of penetrating warheads has increased the last few years by introducing penetrators with a length to diameter ratio of almost 10. This requires new designs to prevent penetration of future protective structures. Penetration of concrete targets is studied by the use of numerical simulation. The diameter of the used model penetrators is 50 mm, and the length to diameter ratio is 9 for the projectiles. Comparisons are also made with reinforced and unreinforced concrete targets constructed of normal strength concrete. The nominal impact velocities for these reference tests are 420 and 460 m/s.

Keywords

Concrete, penetration, simulation, reinforcement

Further bibliographic information	**Language** English
ISSN 1650-1942	**Pages** 160 p.
	Price acc. to pricelist

Utgivare	Rapportnummer, ISRN	Klassificering
FOI - Totalförsvarets forskningsinstitut Vapen och skydd 147 25 Tumba	FOI-R--1759--SE	Teknisk rapport
	Forskningsområde 5. Bekämpning och skydd	
	Månad, år December 2005	**Projektnummer** E2358
	Delområde 53 Skydd och anläggningsteknik	
	Delområde 2	

Författare/redaktör	Projektledare
Håkan Hansson	Håkan Hansson
	Godkänd av
	Uppdragsgivare/kundbeteckning Försvarsmakten
	Tekniskt och/eller vetenskapligt ansvarig

Rapportens titel

Simulering av penetration i standardbetong av en projektil med L/D=9

Sammanfattning

Penetrerande stridsdelar har förbättrats avseende penetrationsförmåga de senaste åren. Dessa nya stridsdelar har ett förhållande mellan längd och diameter (L/D) på nästan 10. Verkan från denna typ av stridsdelar behöver kunna bedömas för att utveckla nya skyddskonstruktioner, samt även bedöma verkan i befintliga konstruktioner. Penetration i betong har studerats med hjälp av numeriska modeller. Diametern för den undersökta modellpenetratorn är 50 mm och L/D är 9. Jämförelser mellan simuleringar och modellförsök presenteras både för oarmerade och armerade standardbetongmål. Den nominella anslagshastigheten för försöken är 420 och 460 m/s.

Nyckelord

Betong, penetration, simulering, armering

Övriga bibliografiska uppgifter	Språk Engelska
ISSN 1650-1942	**Antal sidor:** 160 s.
Distribution enligt missiv	**Pris: Enligt prislista**

This page intentionally blank.

Contents

This page intentionally blank.

Utökad sammanfattning

Introduktion: Prestandan för penetrerande stridsdelar har ökat de senaste åren med introduktionen av penetratorer med ett förhållande mellan längd och diameter (L/D) på nästan 10. Denna vapentyp är främst avsedd att användas mot fortifikatoriska skydd och därmed krävs förbättrade typer av skyddskonstruktioner för att förhindra penetration. Denna del av studien är huvudsakligen inriktad på att ta fram en metodik för att bedöma verkan från denna typ av stridsdelar i betongkonstruktioner. Resultat av studien kan även användas för att bedöma verkan av andra typer av stridsdelar mot byggnadskonstruktioner, t ex vid strid i bebyggelse och för att bedöma behov av förstärkningsåtgärder vid internationella operationer.

Numerisk simulering: Inom projektet sker utvärdering av numerisk simulering för bedömning av penetrationsförlopp och av förbättrade skyddskonstruktioner. Ett antal försök har studerats med numeriska modeller och simuleringar har t ex genomförts av oarmerade och armerade betongmål, med vinkelrätt och snett anslag, samt med olika hastigheter och tjocklek för målen. Resultaten redovisas i kapitel 3, dock riktar sig detta kapitel främst till den som är intresserade och relativt väl insatt i simuleringsmetodik och kan förbigås av övriga läsare.

Jämförelse mellan simuleringar och försök: Simuleringarna ger generellt en bra överensstämmelse med försöksresultaten. En sammanställning och jämförelse mellan simuleringar och försöksresultat återfinns i kapitel 4.

Diskussion och rekommendationer för simuleringar: Fördelen med numerisk simulering är att flera parametrar kan studeras, exempel på detta är snedställning av mål och projektil, inverkan av armering, samt projektilens deformation. Även kombinationer av olika verkanssätt kan studeras, t ex RSV och penetrerande stridsdelar. Detta ökar möjligheten att bedöma verkan från nuvarande och framtida stridsdelar mot skyddskonstruktioner.

Även om simuleringar ger bra överensstämmelse i flera fall, måste ett antal parametrar väljas med omsorg för att detta resultat ska erhållas. Rekommendationer för att erhålla acceptabla resultat vid simuleringar avseende penetrationsdjup och genomslag i konstruktioner av standardbetong redovisas i kapitel 5. Genom förbättringar av beräkningsmetodiken och de använda materialmodellerna kan sannolikt resultaten ytterligare förbättras, samt andra typer av fall studeras med godtagbart resultat.

Framtida forskning och utveckling: Det rekommenderas att en beräkningsmetodik avseende vapenverkan mot skyddskonstruktioner och byggnader etableras. Denna metodik kan sedan lätt kompletteras för att även användas för att studera verkan från andra typer av vapen, t ex spränggranater och RSV. Även verkan från detonationer mot strukturer är av intresse.

Simuleringar av tidigare genomförda försök i högpresterande betong (HPC) bör genomföras med användande av materialdata framtagna vid EMI på uppdrag av FOI.

För att studera verkan från RSV och kontaktdetonationer, samt även olika typer av tandemladdningar, mot betongmål bör förbättrade materialmodeller avseende brottutveckling i materialen användas. En inledande studie av en laddning som kombinerar stråL- och projektilbildande RSV har genomförts vid FOI. Denna visar på de framtida möjligheter som finns avseende s k ”wall breaching”-stridsdelar. För utförligare diskussion angående fortsatt forskning och utveckling hänvisas till kapitel 6.

Appendix 1 innehåller några definitioner av generella samband för materialparametrar. Materialmodellerna finns sedan beskrivna i appendix 2. De använda materialmodellerna för stål är olika varianter baserade på modellen utvecklad av Johnson och Cook (1983) och för betongen används RHT-modellen utvecklad vid EMI (Riedel, 2000).

De använda försöksresultaten är sammanställda i appendix 3. För ytterligare information hänvisas till Hansson (2005).

1. Introduction

The penetration performance of penetrating warheads has increased the last few years by introducing penetrators with a length to diameter ratio of almost 10. This requires new designs to prevent penetration of future protective structures. The main objective of the study is to investigate the protective performance of concrete structures by using numerical simulations. Reference tests of penetration in concrete are used for comparison with the simulation.

The investigations of highly dynamic events like projectile penetration, or loading by blast waves, are supported by numerical simulations. These calculations are usually performed with explicit codes. In addition, models that describe the mechanical response of the materials are needed. Constitutive equations for concrete exposed to weapons effects have been a major area of interest for a long time, and several material models for concrete behaviour are developed. However, it is not until recent years that it seems possible to simulate the behaviour of concrete targets during projectile penetration with acceptable results. The aim for the study is to evaluate the possibilities to use numerical simulations to predict penetration in concrete structures. The numerical simulations were performed in parallel with ongoing experimental research at FOI (Hansson, 2005).

The RHT concrete model is used in this study for the simulations of steel projectiles, with a length to diameter ratio of nine, penetrating concrete targets. This advanced material model was developed at EMI (Riedel, 2000), and is shortly described in appendix 2. The used version of the material model is implemented as a standard material model in Autodyn version 4.2, or higher. An earlier study of numerical simulation of concrete penetration with the use of the RHT model was performed by Hansson (2003a). This study showed that with the latest development in material and numerical modelling it is possible to use advanced material models together with alternative meshless formulations, e.g. SPH formulations. Another approach to avoid heavily distorted elements is to use an Eulerian formulation, i.e. with a fixed mesh for the target. However, these methods are more time consuming than the normally used Lagrange formulation, and also they have their limitations. Therefore, this study is performed with the use of the Lagrange element formulation for the target.

The simulations are based on a reference penetration tests in normal strength concrete reported earlier (Hansson, 2003b), and also reprinted in appendix 3. This reference test of concrete penetration was performed in a normal strength concrete with an uniaxial compressive strength of 48 MPa. A projectile design developed at FOI with a length to diameter (L/D) ratio of nine, projectile diameter of 50 mm and a calibre to ogive head radius (CRH) of 8.0, was used for the test. Further, the simulations are also compared with tests performed in 2004 (Hansson, 2005), the data from these tests are compiled in appendix 3. Measurements of impact velocity by both high speed film and short circuit screens, estimations of yaw and pitch of the projectile at impact and measurement of penetrations depth were performed. The penetration depth for a 3.64 kg projectile was 49 cm at an impact velocity of 420 m/s. The simulations were performed during 2004 and 2005, with the early simulations used to support the experimental work performed in 2004.

Readers not directly involved in numerical simulations are recommended to go directly to chapters 4 to 6, and use chapter 3 and the appendices for reference.

This page intentionally blank.

2. Material modelling

The RHT material model is used for concrete (Riedel, 2000), and variations of the material model by Johnson & Cook (1983) are used for the different types of steel in this study. These material models and the required parameters for the simulations are described in appendix 2. Material parameters, and variations of the material models, that are used for specific simulations are given and described in connection to the description of the numerical simulations in chapter 3.

The filling material for the projectiles is simulated with a linear equation of state and an elastic-plastic yield surface. The material parameters are given in table 2.1.

Table 2.1. Parameters for the filling material of the projectiles.

Parameter	**Value**
Density	2.40 g/cm^3
Bulk modulus	20.0 GPa
Reference temperature	300 K
Specific heat	640 J/kgK
Shear modulus	12.0 GPa
Yield stress	100 MPa

The RHT model is used for the normal strength concrete, with parameters according to Riedel (2000). However, the uni-axial strength for the concrete is increased from original value of 35.0 MPa to 48.0 MPa to represent the used concrete for the targets. According to this the initial compaction pressure for the EOS is also recommended to be increased, in this case from 23.3 MPa to 35.0 MPa. The data sets used for the RHT model were subjected to minor changes during the progress of the simulations, and these are compiled in table 2.2.

Table 2.2. Used data sets for the RHT strength model for normal strength concrete, including initial density and pore compaction pressure. See also appendix 2. Values in the table that are printed in normal type refer to original values according to Riedel (2000) for a concrete with a compressive strength of 35 MPa.

Parameter	**Data set 1**	**Data set 2**	**Data set 3**
ρ_0	***2.330 g/cm^3***	2.140 g/cm^3	2.140 g/cm^3
p_{crush}	23.3 GPa	***35.0 MPa***	***35.0 MPa***
G	16.7 GPa	16.7 GPa	16.7 GPa
f_c	***48.0 MPa*** [a]	***48.0 MPa*** [a]	***48.0 MPa*** [a]
f_t/f_c	0.10 [b]	0.10 [b]	***0.0833*** [b]
f_s/f_c	0.18 [b]	0.18 [b]	0.18 [b]
A	1.60	1.60	1.60
N	0.61	0.61	0.61
Q_2	0.6805	0.6805	0.6805
BQ	0.0105	0.0105	0.0105
$\frac{G_{elastic}}{G_{elastic-plastic}}$	2	2	2
$f_{t,\,elastic}/f_t$	0.70	0.70	0.70
$f_{c,\,elastic}/f_c$	0.53	0.53	0.53
Cap option	Yes	Yes	Yes
B	1.6	1.6	1.6
M	0.61	0.61	0.61
α	0.032	0.032	0.032
δ	0.036	0.036	0.036
D_1	0.04	0.04	0.04
D_2	1	1	1
$\varepsilon_{fail,\,min}$	0.01	0.01	0.01
$G_{residual}/G_{elastic}$	0.13	0.13	0.13
Tensile failure model	Hydro tensile limit [c]	Hydro tensile limit [c]	Hydro tensile limit [c]
$\sigma_{tensile\ failure}$	Not used [d]	Not used [d]	Not used [d]
$\tau_{maximum}$	Not used	Not used	Not used
Gf	Not used [d]	Not used [d]	Not used [d]

Note: [a] Value modified according to uni-axial cylinder test of the used concrete. The data set is originally developed for a concrete with 35 MPa compressive strength.
[b] Value modified for use with crack softening tensile failure models.
[c] The use of "Hydro tensile limit" results in the use of the original damage evolution description for the RHT material model.
[d] Modified for use with tensile failure conditions, i.e. crack softening models.

3. Numerical simulations

The numerical simulations are performed with Autodyn 3D versions 4.3.02m to 5.0.02k, and are mainly run in parallel on four computer systems consisting of 2.8 and 3.4 GHz Intel P4 computers with 1 GB memory/node running Windows 2000/XP and WMPI. Simulations of concrete penetration with projectiles with a ratio of length to diameter of 3.6 were reported earlier (Hansson, 2003a), and the simulations performed in this study are an attempt to use numerical simulations to study the modern type of penetrators with an increased length to diameter ratio. This type of models can also be used to study penetration of deformable projectiles into concrete and other protective materials.

The Lagrangian element formulation is used for the projectile and target for all simulations in this study, and the geometry for the simulations is based on tests performed in 2002 (Hansson, 2003b) and 2004 (Hansson, 2005) at FOI, Weapons and Protection Division. One penetration test was conducted with a normal strength concrete in 2002, with a penetration depth of approximately 0.49 m for a 3.64 kg penetrator. This test is used as a reference case for the simulations (case no. 0). Further tests with normal strength concrete were performed in 2004 with a modified projectile design. The tests that are used for comparison with the simulation results are compiled in appendix 3, and comparison between simulation and test results are shown in chapter 4 later.

50 mm projectiles of two design types with 5.0 mm and 10.0 mm case thickness are used for the simulations, representing the two designs used for the tests. The projectile design with the 5.0 mm case thickness was used for the test series in 2002, this projectile design used a projectile nose with a CRH (calibre to radius head) value of 8 and is shown in figure 3.1. Projectiles with 10.0 mm case thickness, and CRH values of 3, 8 and 12, were used for further penetration tests during 2004. These penetrators are shown in figure 3.2. However, only the projectile design with a CRH value of 8 is used for the simulations in this study. The mass for the projectile used in 2002 was approximately 3.64 kg, and for the tests in 2004 the projectile mass was increased to approximately 4.50 kg.

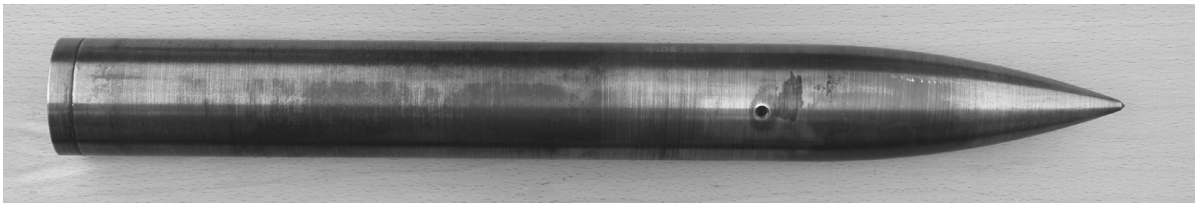

Figure 3.1. 50 mm projectile with 5.0 mm case thickness, mass of approximately 3.64 kg and a CRH value of 8 used for tests in 2002.

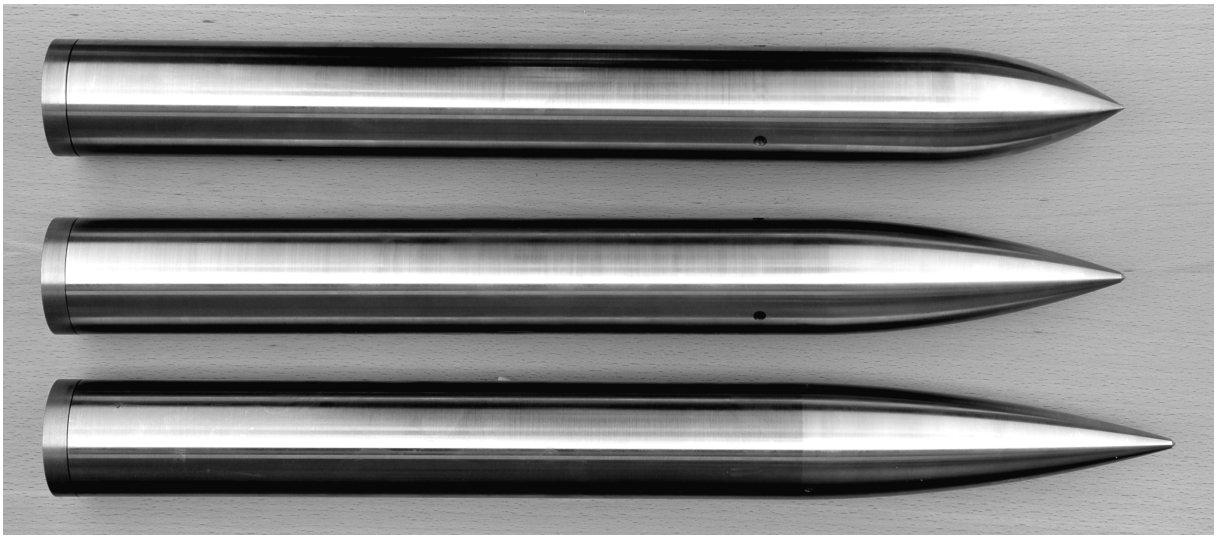

Figure 3.2. 50 mm projectiles with 10.0 mm case thickness, a mass of approximately 4.50 kg, and CRH values of 3, 8 and 12. These projectile types were used for the tests performed during 2004.

The ½ symmetry model shown in figure 3.3 of the projectile with 5.0 mm case thickness consists of approximately 900 elements. Material parameters for steel S-7 is used for the projectile, see appendix 2. Due to the unfavourable geometry of the projectile nose and the relative large elements in the projectile, resulting in an initial contact between target and projectile at one node, there is a high risk of large local deformations of the projectile nose and a progressive failure of the projectile. To avoid this, the yield strength of the first two element rows is increased to 2.5 GPa after the first simulations were run. The lower yield strength (f_y=1.539 GPa) of the projectile nose is specified for the models for which it is used. All other models use the increased value of the yield strength for the nose of the projectile. The reference density of the steel was increased by approximately 1% to obtain the correct mass for the projectiles with the used simplified geometry. The model of the penetrator with increased mass uses the same mesh with only the location of the projectile material changed. The material location for this projectile type is shown in figure 3.4.

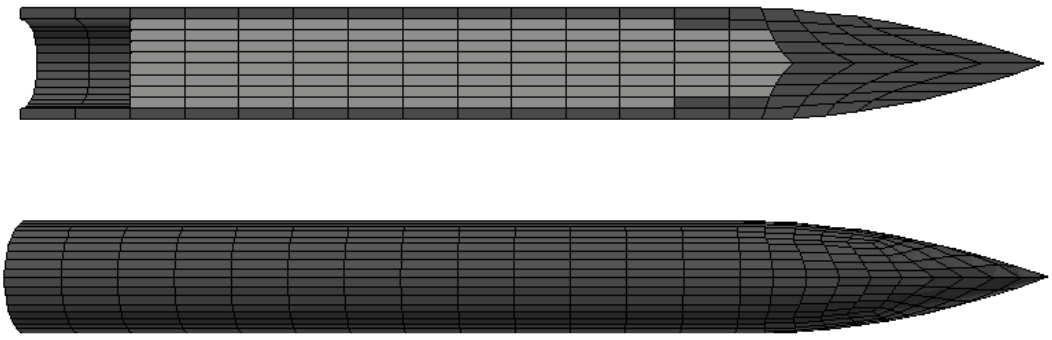

Figure 3.3. Mesh and material location for projectile with 5.0 mm case thickness and a mass of 3.64 kg.

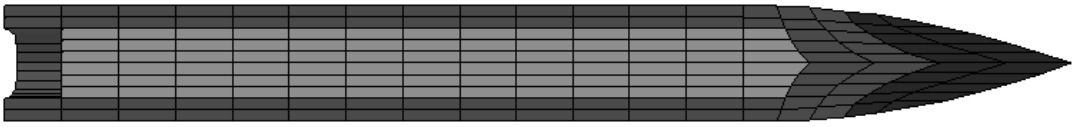

Figure 3.4. Mesh and material location for projectile with increased case thickness to 10.0 mm with a mass of 4.53 kg.

The default value of 2 for the erosion strain is used for the models, if not a different value is specified. Part of the simulations is run both with and without the use of friction between projectile and target material. All simulations are compiled in tables for easy comparison of the obtained results, and the used version of Autodyn 3D is also given in the tables.

3.1. Simulations of unreinforced targets

The base geometry for the simulations is a Lagrange model with half symmetry, 10 mm elements and normal impact conditions. The unreinforced concrete target is in the reference case enclosed in a thin walled steel cylinder with 5.0 mm thickness, see table 3.1 and figure 3.5. Figure 3.5 also show the scale for the damage plots later in the report. This model is then modified for different boundaries and impact conditions, and also element sizes and target lengths. These conditions are given for the different models where they apply. Yaw/pitch is 0° for the simulations, if not another value is specified for the actual simulation. The required time for a simulation of this type, i.e. for model identity PEN034, is approximately 70 h when the model run in parallel on four 2.8 GHz Intel P4 computers.

Table 3.1. Target geometry for models.

		Long target		**Short target**	
Model symmetry		½ symmetry	¼ symmetry	½ symmetry	
Target length		1200 mm		600 mm	
Concrete cylinder	Diameter	1200 mm		1200 mm	
	Element size	10 mm	5 mm [a]	10 mm	5 mm [a]
	No. of elements	486 000	810 000	324 000	1080 000
Steel cylinder	Thickness	5 mm		5 mm	
	No. of elements	10 800	10 800	7 200	14400
Time step		≈3.5×10^{-5} ms		≈3.5×10^{-5} ms	
Run time on four P4 2.8 GHz processors [b]		≈70 h	≈120 h	---	---

Note: [a] Graded element size in radial direction for radius greater than 300 mm.
[b] Time requirement is valid for an impact velocity of 420 m/s and a projectile mass of 3.64 kg. The simulation time is increased for models with higher impact velocity and with increased mass of the projectile.

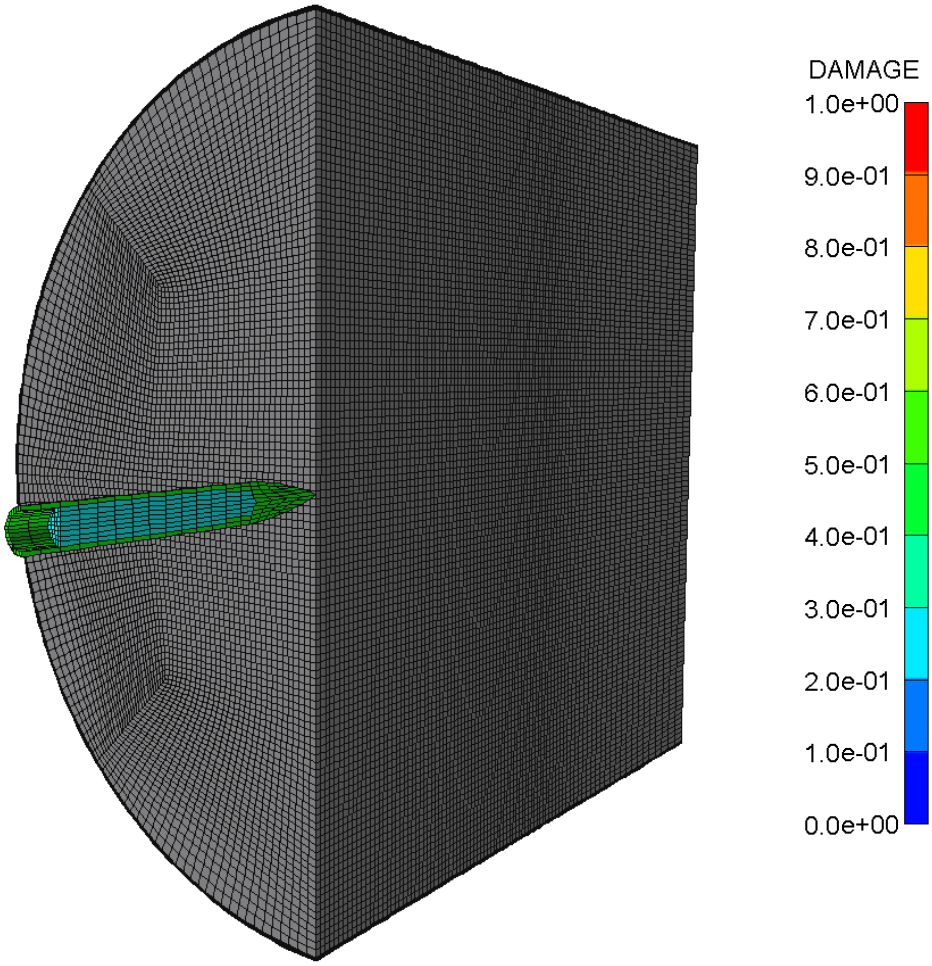

Figure 3.5. Reference mesh geometry including 5 mm thin walled steel cylinder and projectile, with material location shown. The scale for damage plots for concrete is also shown to the right.

3.1.1. Simulations of targets with 1.20 m length

The number of simulations for this target with 1.20 m length, or thickness, is greater than for the other target configurations. The reason for this is that a greater number of parameters are studied for this case, and these results are used to determine the parameters for later models in the report.

Influence from boundary conditions

Simulations of the reference case based on test 2002-10 are run with varying boundary conditions for the cylindrical surface. The confining steel pipe was 8 mm thick for this test performed in 2002. However, there is likely to be a small gap between steel and concrete for the target caused by the shrinkage of the concrete during curing. Therefore, a thickness of the steel pipe equal to 5 mm, and with the concrete and steel parts joined together seems to be an acceptable estimation of the real boundary. The first set of simulations studied the influence of the boundary condition and is compiled in table 3.2. The different types of boundary conditions for the concrete cylinder resulted only in minor changes of the penetration depths. As expected, the model with free surfaces (PEN018) results in the greatest penetration depth and the models with fixed boundaries in the shortest penetrations (PEN019 and PEN031), with the model with steel mantle in between. The calculated penetration depths are 0.52±0.03 m, which is close to the experimental result of 0.49 m. However, the angle of attack (yaw/pitch) for the projectile for this test was approximately 1.25°, and this is likely to decrease the penetration depth. The effect of this phenomenon was also studied by increasing the yaw for the projectile for a few simulations, see models PEN038 and PEN039 later in the report. Further, it is likely that the simulation without confinement underestimates the penetration depth due to the limited capability of the material model to describe tensile failure due to radial cracking of the concrete target.

Table 3.2. Simulations of targets using varying boundary conditions.

	PEN016	**PEN018**	**PEN019**	**PEN031**
Model symmetry	½	½	½	½
Target length	1200 mm	1200 mm	1200 mm	1200 mm
Element size	10 mm	10 mm	10 mm	10 mm
Boundary condition [a]	5 mm steel pipe	Free surface	Fixed boundary	Radial fixed boundary [b]
Projectile mass	3.64 kg	3.64 kg	3.64 kg	3.64 kg
Impact velocity	420 m/s	420 m/s	420 m/s	420 m/s
Impact angle	90°	90°	90°	90°
ρ_0	2.330 g/cm^3	2.330 g/cm^3	2.330 g/cm^3	2.330 g/cm^3
P_{crush}	35.0 MPa	35.0 MPa	35.0 MPa	35.0 MPa
Tensile failure for the concrete	Original RHT with f_t= 4.8 MPa			
Friction coefficient	μ=0	μ=0	μ=0	μ=0
Comment	Yield stress for the nose of the projectile is 1.539 GPa AD v. 4.3.02			
Penetration depth	514 mm	547 mm	491 mm	488 mm
Energy error	-1.7%	-1.8%	-1.7%	-1.6%

Note: [a] Displacement of target in axial direction is free for all cases.
[b] The nodes on the boundary are free in tangential direction of the surface, as well as in axial direction.

Friction between projectile and target is normally not considered for penetration simulations. One reason to neglect friction is the increased shear deformation for Lagrangian elements, which even may increase penetration depths for a simulation when friction is introduced. However, even if it is suitable to neglect the friction for many penetration cases this might not be adequate for low velocity penetration in concrete. Simulations with and without friction are run to show the influence of this parameter for a Lagrangian target, see tables 3.3 and 3.4. The introducing of friction with a friction coefficient of 0.05 results in approximately 16% decrease of the penetration depth for the simulation. This indicates that the interaction between target and projectile is an important factor to study in the future. Models PEN030 and PEN032 are also shown in figure 3.6. Based on these simulations it was decided to increase the yield strength of penetrators nose to 2.50 GPa for the remaining simulations. This is to avoid extensive deformation of the nose elements due to the relative coarse element mesh in the penetrator. This has only a minor influence on the penetration depth, compare models PEN030 and PEN033 in table 3.4. Further, the influence of the initial compaction pressure is also studied and can be neglected. The results are also given in table 3.3. However, the initial compaction pressure is used to define the elastic surface via the cap function so some care needs to be taken when this parameter is determined. Retaining the inertia from eroded nodes and increasing the confinement from 5 mm to 8 mm of steel show minor influence on the penetration depth, see table 3.4 and figure 3.7.

Table 3.3. Simulations of targets using varying friction coefficient, and initial compaction pressure.

	PEN030	**PEN032**	**PEN016**	**PEN017**
Model symmetry	½	½	½	½
Target length	1200 mm	1200 mm	1200 mm	1200 mm
Element size	10 mm	10 mm	10 mm	10 mm
Boundary condition [a]	5 mm steel pipe			
Projectile mass	3.64 kg	3.64 kg	3.64 kg	3.64 kg
Impact velocity	420 m/s	420 m/s	420 m/s	420 m/s
Impact angle	90°	90°	90°	90°
ρ_0	2.330 g/cm^3	2.330 g/cm^3	2.330 g/cm^3	2.330 g/cm^3
P_{crush}	23.3 MPa	23.3 MPa	35.0 MPa	35.0 MPa
Friction coefficient	μ=0	μ=0.05	μ=0	μ=0.05
Comment	Yield stress for the nose of the projectile is 1.539 GPa AD 4.3.02			
Penetration depth	513 mm	429 mm	514 mm	430 mm
Energy error	-1.7%	-17.6%	-1.7%	-17.6%

Note: [a] Displacement of target in axial direction is free for all cases.

Table 3.4. Simulations using different yield strength for the nose of the projectile, compaction pressure, friction coefficient, retained inertia of eroded elements and increased thickness for the confinement.

	PEN030	**PEN033**	**PEN033B**	**PEN034**	**PEN060**
Model symmetry	½	½	½	½	½
Target length	1200 mm	1200 mm	1200 mm	1200 mm	1200 mm
Element size	10 mm	10 mm	10 mm	10 mm	10 mm
Boundary condition [a]	5 mm steel pipe	5 mm steel pipe	5 mm steel pipe	5 mm steel pipe	8 mm steel pipe
Projectile mass	3.64 kg	3.64 kg	3.64 kg	3.64 kg	3.64 kg
Impact velocity	420 m/s	420 m/s	420 m/s	420 m/s	420 m/s
Impact angle	90°	90°	90°	90°	90°
ρ_0	2.330 g/cm^3	2.330 g/cm^3	2.330 g/cm^3	2.330 g/cm^3	2.330 g/cm^3
P_{crush}	23.3 MPa	23.3 MPa	23.3 MPa	23.3 MPa	23.3 MPa
Friction coefficient	μ=0	μ=0	μ=0.05	μ=0	μ=0
Comment	Yield stress for the nose of the projectile is 1.539 GPa AD 4.3.02	AD 4.3.02	AD 5.0.02c	Retain inertia from eroded nodes AD v. 4.3.02	AD 4.3.02
Penetration depth	513 mm	528 mm	448 mm	533 mm	518 mm
Energy error	-1.7%	-1.5%	-17.6%	-2.1%	-1.5%

Note: [a] Displacement of target in axial direction is free for all cases.

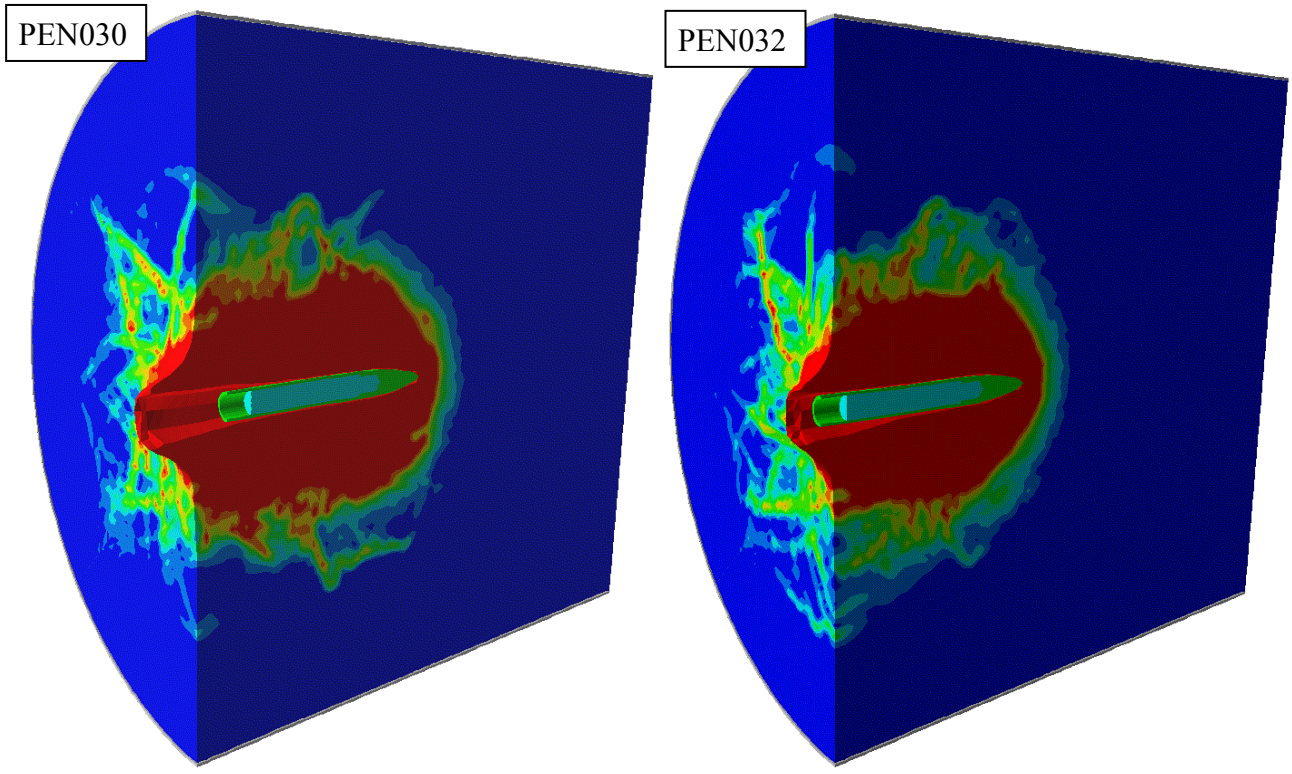

Figure 3.6. Damage and deformations for models PEN030 without friction and PEN032 with the use of friction (μ=0.05) between target and projectile.

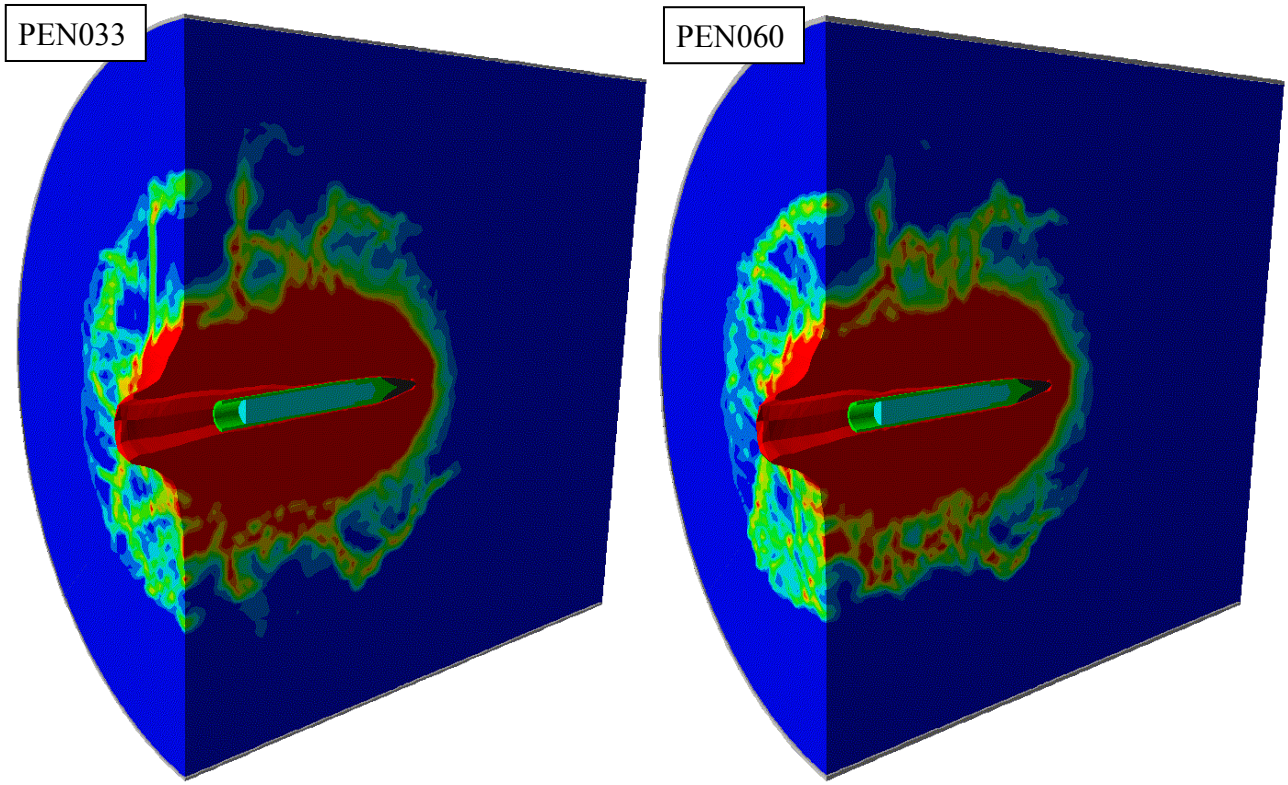

Figure 3.7. Damage and deformations for models PEN033 and PEN060 with increased yield strength for the projectile nose, using 5 mm and 8 mm steel confinement respectively.

The model PEN060 is rerun with Autodyn version 5.0.01c as model PEN560. The reason for this is to determine if the different versions of the code produced the same result, at least regarding the projectile deceleration. The projectile velocities for these simulations are shown in figure 3.8 below.

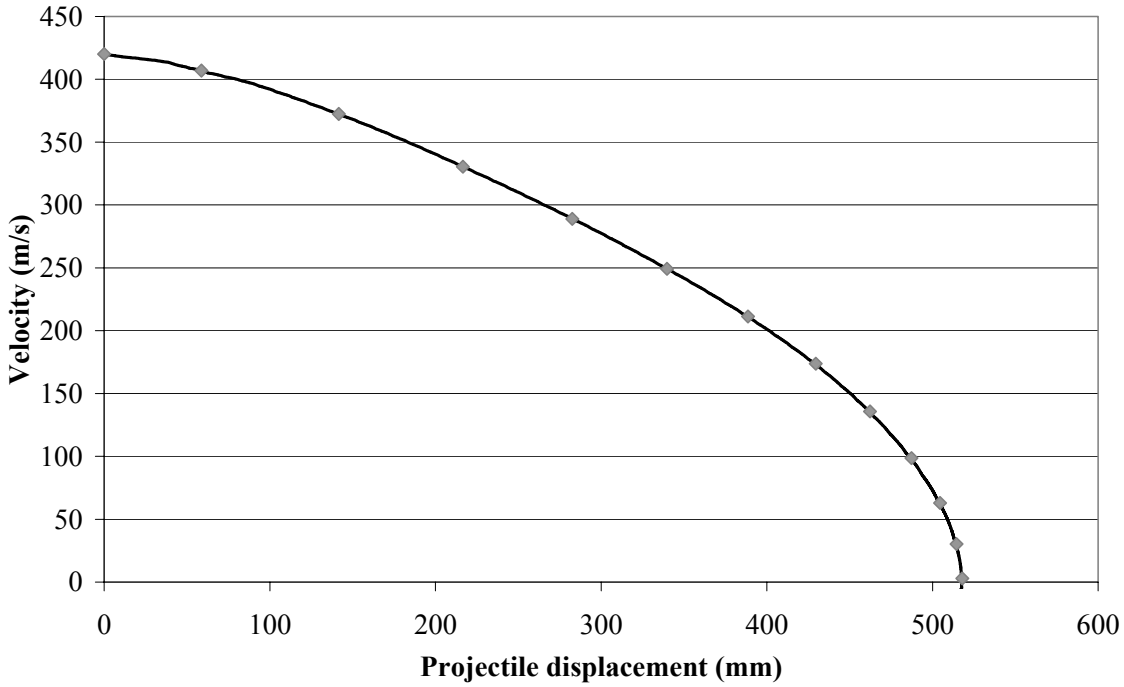

Figure 3.8. Simulation results of projectile velocity vs. penetration with Autodyn versions 4.3.02 (black line, model id. PEN060) and 5.0.01c (grey markers, model id. PEN560).

Influence of increased mass and impact velocity for the penetrator

Simulations with increased impact velocity and projectile mass are run with and without the use of friction between the projectile and the target, see tables 3.5 and 3.6. The models with increased projectile mass to 4.53 kg, e.g. PEN036, use the same projectile mesh as e.g. model PEN030, with only the location of the projectile material changed. See figure 3.4. This 24.4% increase of the projectile mass results in a 24.7% increase in penetration depth for the impact velocity 420 m/s, and an increase of penetration by 18.9% for the impact velocity 460 m/s. This indicates that the calculated penetration depth is roughly proportional to the projectile mass, at least for the studied ranges of mass and impact velocity. The decrease of the penetration depths are approximately 16 to 17% when the friction is introduced, which is consequent with earlier shown results for the 3.65 kg projectile and an impact velocity of 420 m/s. See also figure 3.9 showing velocity vs. displacement for models PEN036 and PEN046. The models without friction considered are shown in figures 3.10 to 3.12.

Table 3.5. Simulations with increased projectile mass and velocity, with friction neglected.

	PEN035	**PEN061**	**PEN036**	**PEN037**	**PEN062**
Model symmetry	½	½	½	½	½
Target length	1200 mm	1200 mm	1200 mm	1200 mm	1200 mm
Element size	10 mm	10 mm	10 mm	10 mm	10 mm
Projectile mass	3.64 kg	3.64 kg	4.53 kg	4.53 kg	4.53 kg
Impact velocity	460 m/s	500 m/s	420 m/s	460 m/s	500 m/s
Impact angle	90°	90°	90°	90°	90°
ρ_0	2.330 g/cm^3	2.330 g/cm^3	2.330 g/cm^3	2.330 g/cm^3	2.330 g/cm^3
P_{crush}	23.3 MPa	23.3 MPa	23.3 MPa	23.3 MPa	23.3 MPa
Friction coefficient	μ=0	μ=0	μ=0	μ=0	μ=0
Comment	AD v. 4.3.02	AD v. 4.3.02	AD v. 4.3.02	AD v. 4.3.02	AD v. 4.3.02
Penetration depth	581 mm	640 mm	620 mm	691 mm	756 mm
Energy error	-1.6%	-1.7%	-1.4%	-1.5%	-1.6%

Table 3.6. Simulations with increased projectile mass and velocity, with friction considered.

	PEN035B	**PEN061B**	**PEN046**	**PEN047**	**PEN048**
Model symmetry	½	½	½	½	½
Target length	1200 mm	1200 mm	1200 mm	1200 mm	1200 mm
Element size	10 mm	10 mm	10 mm	10 mm	10 mm
Projectile mass	3.64 kg	3.64 kg	4.53 kg	4.53 kg	4.53 kg
Impact velocity	460 m/s	500 m/s	420 m/s	460 m/s	500 m/s
Impact angle	90°	90°	90°	90°	90°
ρ_0	2.330 g/cm^3	2.330 g/cm^3	2.330 g/cm^3	2.330 g/cm^3	2.330 g/cm^3
P_{crush}	23.3 MPa	23.3 MPa	23.3 MPa	23.3 MPa	23.3 MPa
Friction coefficient	μ=0.05	μ=0.05	μ=0.05	μ=0.05	μ=0.05
Comment	AD 5.0.02c	AD 5.0.02c	AD 5.0.02c	AD 5.0.02c	AD 5.0.02c
Penetration depth	487 mm	535 mm	520 mm	570 mm	625 mm
Energy error	-18.1%	-18.7%	-18.6%	-19.2%	-19.7%

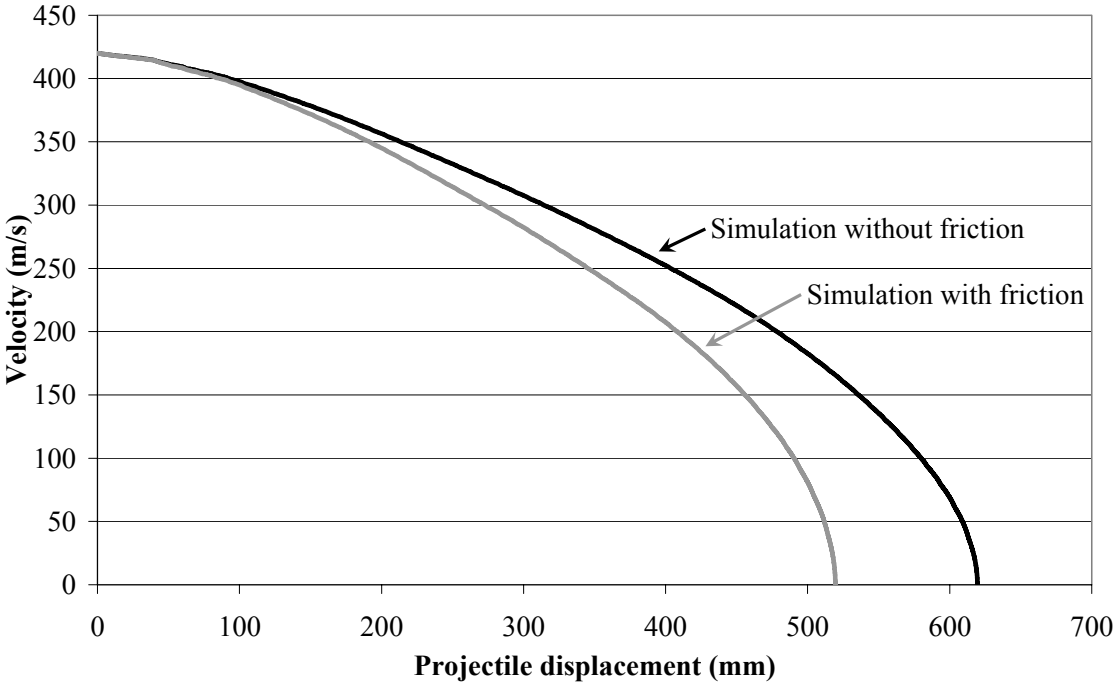

Figure 3.9. Projectile velocity vs. penetration for models PEN036 without friction and PEN046 with friction.

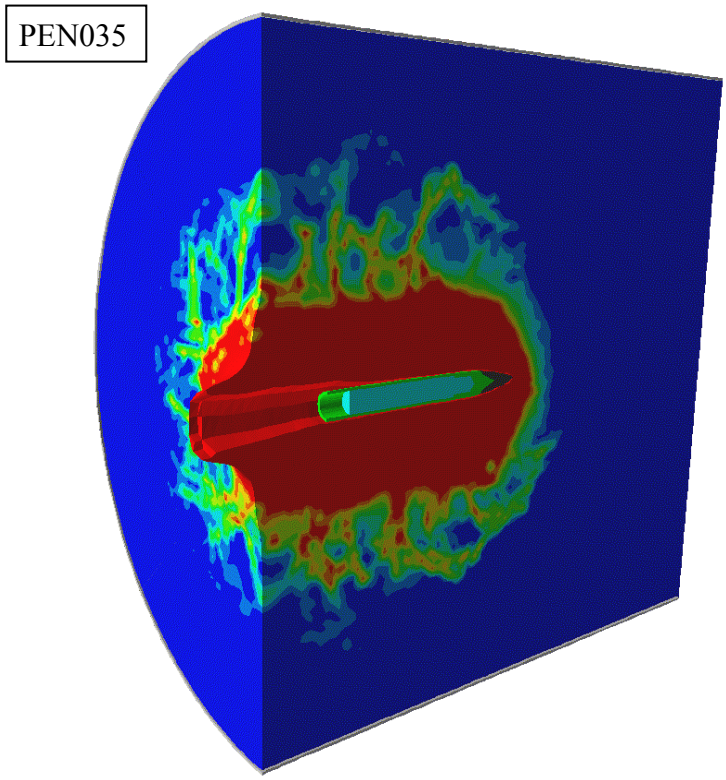

Figure 3.10. Damage and deformations for model PEN035 with impact velocity 460 m/s and mass 3.64 kg for the penetartor.

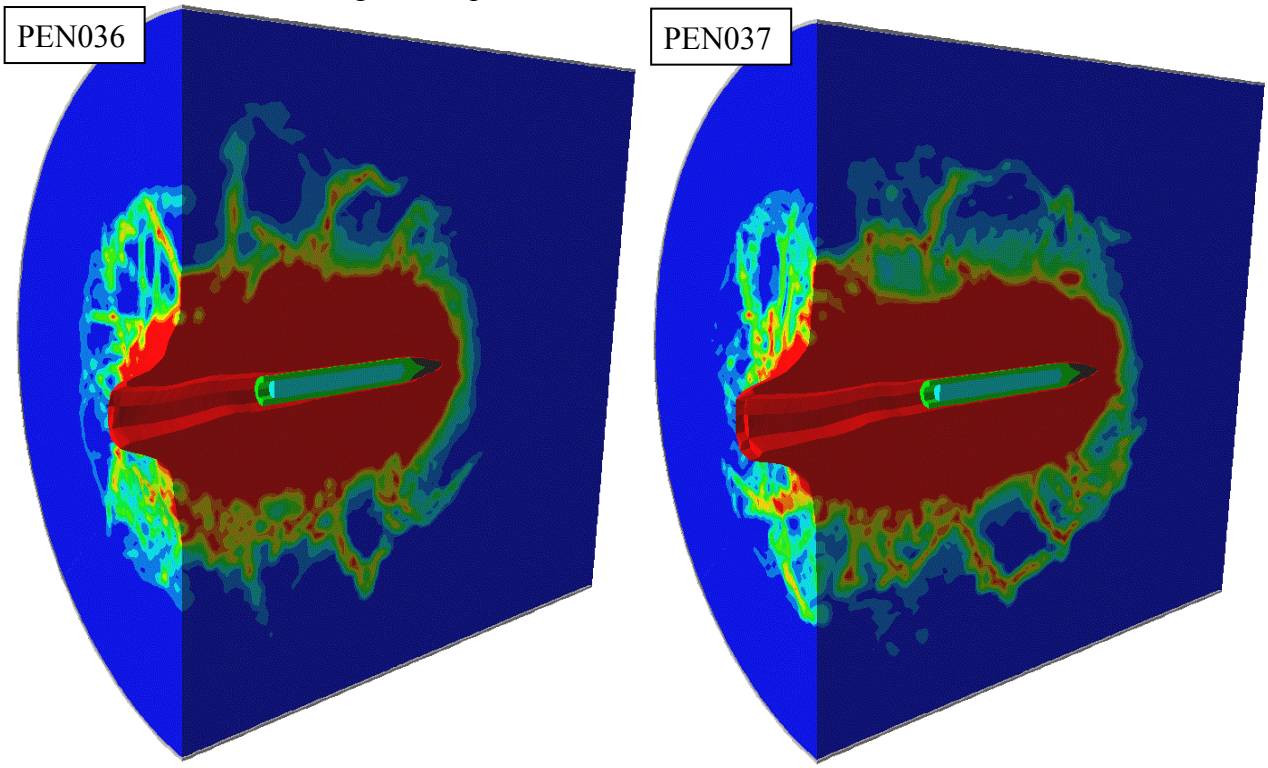

Figure 3.11. Damage and deformations for models PEN036 with impact velocity 420 m/s and PEN037 with impact velocity 460 m/s, both models with an increased mass to 4.53 kg.

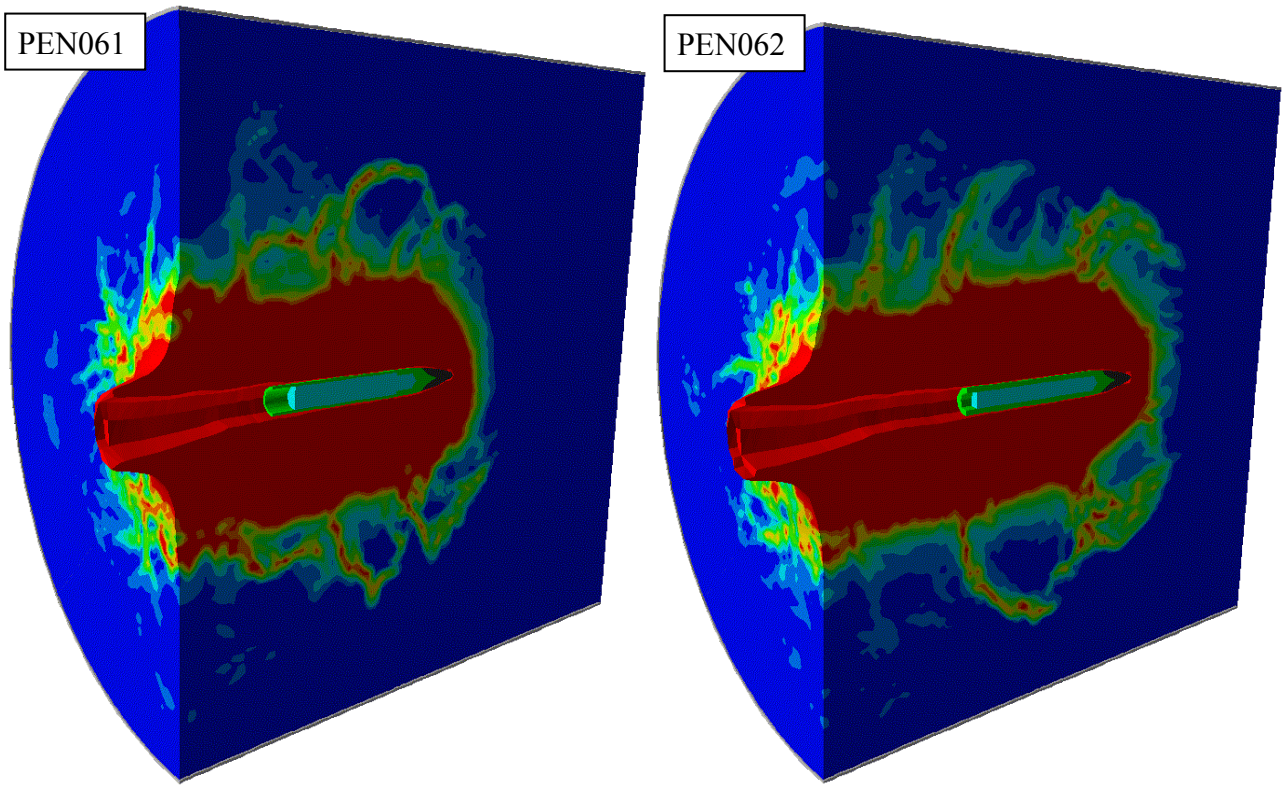

Figure 3.12. Damage and deformations for models PEN061 with 3.64 kg projectile and PEN062 with 4.53 kg projectile, both models with an impact velocity of 500 m/s.

Influence of initial density and initial compaction pressure
Simulations with different initial density for the concrete only show minor influence from this parameter on the penetration depth. The models are compared in table 3.7. Simulation with different initial compaction pressure are also compared, see table 3.8. This parameter resulted in ±2 mm variation of the penetration depth for values between 23.3 and 64 MPa.

Table 3.7. Simulations with varying initial density for the concrete.

	PEN036	**PEN063**
Model symmetry	½	½
Target length	1200 mm	1200 mm
Element size	10 mm	10 mm
Projectile mass	4.53 kg	4.53 kg
Impact velocity	420 m/s	420 m/s
Impact angle	90°	90°
ρ_0	2.330 g/cm^3	2.314 g/cm^3
P_{crush}	23.3 MPa	23.3 MPa
Friction coefficient	μ=0	μ=0
Comment	AD v. 4.3.02	AD v. 5.0.01c
Penetration depth	620 mm	637 mm
Energy error	-1.4%	-1.3%

Table 3.8. Simulations with varying initial compaction pressure.

	PEN046	**PEN046P2**	**PEN046P3**	**PEN046P4**
Model symmetry	½	½	½	½
Target length	1200 mm	1200 mm	1200 mm	1200 mm
Element size	10 mm	10 mm	10 mm	10 mm
Projectile mass	4.53 kg	4.53 kg	4.53 kg	4.53 kg
Impact velocity	420 m/s	420 m/s	420 m/s	420 m/s
Impact angle	90°	90°	90°	90°
ρ_0	2.330 g/cm^3	2.330 g/cm^3	2.330 g/cm^3	2.330 g/cm^3
P_{crush}	23.3 MPa	35 MPa	48 MPa	64 MPa
Friction coefficient	μ=0.05	μ=0.05	μ=0.05	μ=0.05
Comment	AD 5.0.02c	AD 5.0.02c	AD 5.0.02c	AD 5.0.02c
Penetration depth	520 mm	519 mm	522 mm	521 mm
Energy error	-18.6%	-18.6%	-18.6%	-18.7%

Influence of erosion strain
Simulations with a reduced value of the erosion strain for the concrete are run, and the values 1.0, 1.5 and 2.0 results in the same penetration depth for the model with the 4.53 kg penetrator. The results are given in table 3.9.

Table 3.9. Simulations with varied erosion strain for the concrete.

	PEN036	**PEN064**	**PEN065**
Model symmetry	½	½	½
Target length	1200 mm	1200 mm	1200 mm
Element size	10 mm	10 mm	10 mm
Projectile mass	4.53 kg	4.53 kg	4.53 kg
Impact velocity	420 m/s	420 m/s	420 m/s
Impact angle	90°	90°	90°
ρ_0	2.330 g/cm^3	2.330 g/cm^3	2.330 g/cm^3
P_{crush}	23.3 MPa	23.3 MPa	23.3 MPa
Friction coefficient	μ=0	μ=0	μ=0
Erosion strain for concrete	2.0	1.5	1.0
Comment	AD v. 4.3.02	AD v. 5.0.01c	AD v. 5.0.01c
Penetration depth	620 mm	622 mm	621 mm
Energy error	-1.4%	-1.4%	-1.4%

Influence of symmetry conditions and element size
Simulations are also run to check the influence of symmetry conditions and element size, see table 3.10 and figure 3.13. The quarter symmetry models are introduced to reduce the number of elements and required time for the simulations. The use of quarter symmetry models, in comparison with the earlier shown half symmetry models, seems to have a minor influence on the penetration depth for this case with normal impact of a semi-infinite target normal strength concrete target, see figure 3.14. The influence of element size on the penetration depth for the same case is less than 10 %, compare e.g. models PEN203 and PEN204. This influence will be discussed later in the report.

Table 3.10. Simulations with different element sizes, friction coefficient and symmetry conditions.

	PEN036	**PEN204**	**PEN206**	**PEN203**	**PEN205**
Model symmetry	½	¼	¼	¼	¼
Target length	1200 mm	1200 mm	1200 mm	1200 mm	1200 mm
Element size	10 mm	10 mm	10 mm	5 mm	5 mm
Projectile mass	4.53 kg	4.53 kg	4.53 kg	4.53 kg	4.53 kg
Impact velocity	420 m/s	420 m/s	420 m/s	420 m/s	420 m/s
Impact angle	90°	90°	90°	90°	90°
ρ_0	2.330 g/cm^3	2.330 g/cm^3	2.330 g/cm^3	2.330 g/cm^3	2.330 g/cm^3
P_{crush}	23.3 GPa	23.3 GPa	23.3 GPa	23.3 GPa	23.3 GPa
Friction coefficient	μ=0	μ=0	μ=0.05	μ=0	μ=0.05
Comment	AD 4.3.02	AD 4.3.02	AD 5.0.02c	AD 4.3.02	AD 5.0.02c
Penetration depth	620 mm	624 mm	529 mm	583 mm	512 mm
Energy error	-1.4%	-1.3%	-18.7%	-1.2%	-16.0%

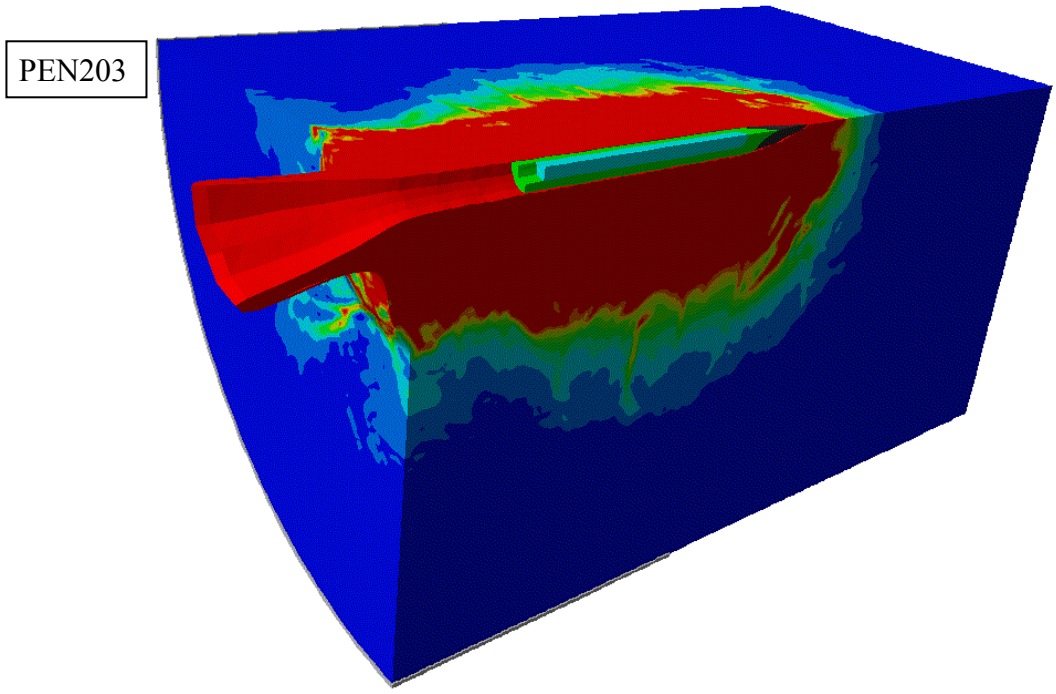

Figure 3.13. Damage and deformations for model PEN203 with quarter symmetry and 5 mm elent size for the target.

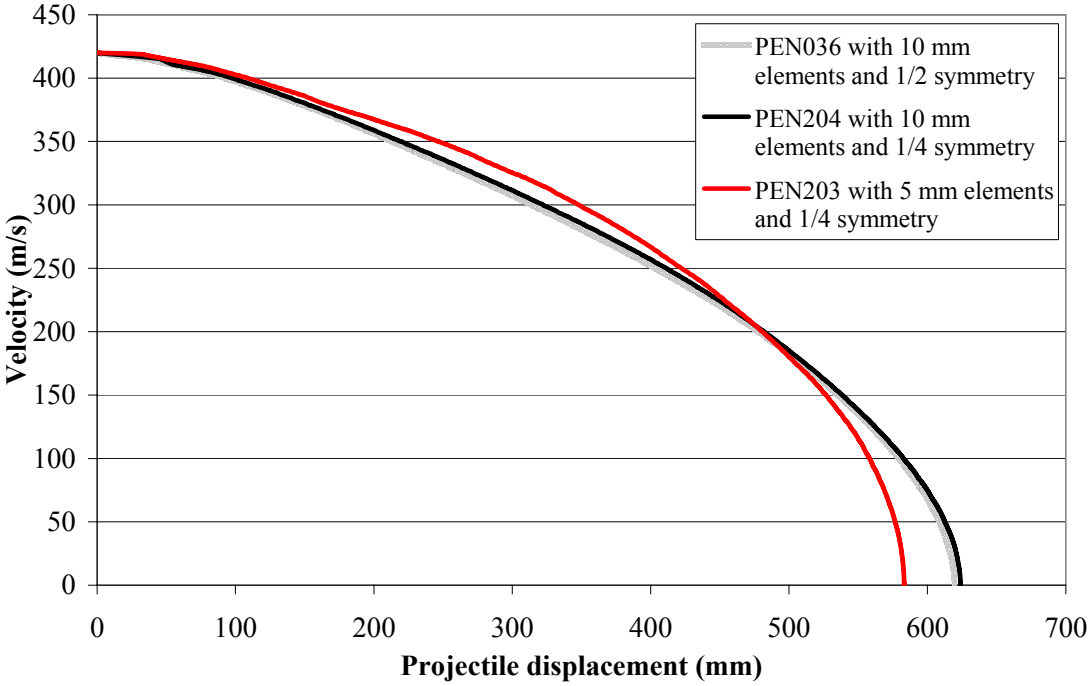

Figure 3.14. Projectile velocity vs. penetration for models PEN036, PEN203 and PEN204 with different elements size and symmetry conditions.

Non-normal impact conditions, i.e. yaw and pitch

The influence of yaw and non-normal impact angle are also studied. Results from simulations with 0°, 1.25° and 2.5° yaw are given in table 3.11. It seems that there is only a minor influence on the penetration depth for yaw/pitch less than approximately1.2°. The models with introduced yaw for the penetrator are shown in figure 3.15. Compare also model PEN033 shown earlier in figure 3.7.

Table 3.11. Simulations of concrete penetration with induced yaw/pitch for projectiles.

	PEN033	**PEN038**	**PEN039**
Model symmetry	½	½	½
Target length	1200 mm	1200 mm	1200 mm
Element size	10 mm	10 mm	10 mm
Projectile mass	3.64 kg	3.64 kg	3.64 kg
Impact velocity	420 m/s	420 m/s	420 m/s
Yaw/Pitch	0°	1.25°	2.5°
Impact angle	90°	90°	90°
ρ_0	2.330 g/cm^3	2.330 g/cm^3	2.330 g/cm^3
P_{crush}	23.3 MPa	23.3 MPa	23.3 MPq
Friction coefficient	μ=0	μ=0	μ=0
Comment	AD v. 4.3.02	AD v. 4.3.02	AD v. 4.3.02
Penetration depth	528 mm	519 mm	472 mm
Penetration length	---	---	---
Energy error	-1.5%	-1.5%	-1.2%

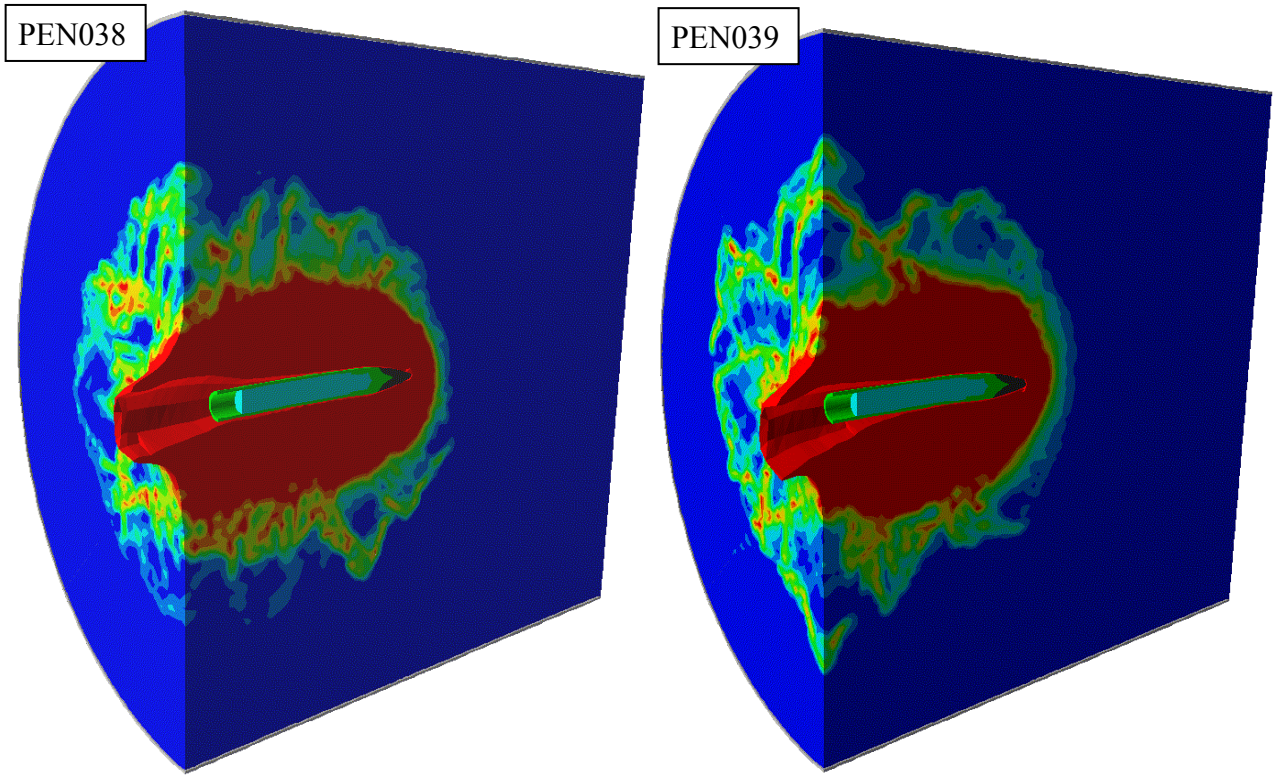

Figure 3.15. Damage and deformations for model PEN038 with 1.25° yaw, and model PEN039 with 2.5° yaw.

The introduction of inclined targets with an impact angle for the projectile equal to 60° reduces the penetration length for the projectile with approximately 13 to 15 %, and the penetration depth calculated from the front face with 44 to 46 %. The models with 60° impact angle are shown in figure 3.16.

Table 3.12. Simulations of concrete penetration with varied impact angle for the projectiles.

	PEN033	**PEN035**	**PEN040**	**PEN041**
Model symmetry	½	½	½	½
Target length	1200 mm	1200 mm	1200 mm	1200 mm
Element size	10 mm	10 mm	10 mm	10 mm
Projectile mass	3.64 kg	3.64 kg	3.64 kg	3.64 kg
Impact velocity	420 m/s	460 m/s	420 m/s	460 m/s
Impact angle	90°	90°	60°	60°
ρ_0	2.330 g/cm^3	2.330 g/cm^3	2.330 g/cm^3	2.330 g/cm^3
P_{crush}	23.3 MPa	23.3 MPa	23.3 MPa	23.3 MPa
Friction coefficient	μ=0	μ=0	μ=0	μ=0
Comment	AD v. 4.3.02	AD v. 4.3.02	AD v. 4.3.02	AD v. 4.3.02
Penetration depth	528 mm	581 mm	297 mm	313 mm
Penetration length [b]	528 mm	581 mm	448 mm	503 mm
Energy error	-1.5%	-1.6%	-1.8%	-1.9%

Note: [b] Distance between point of impact and final position for the projectile nose.

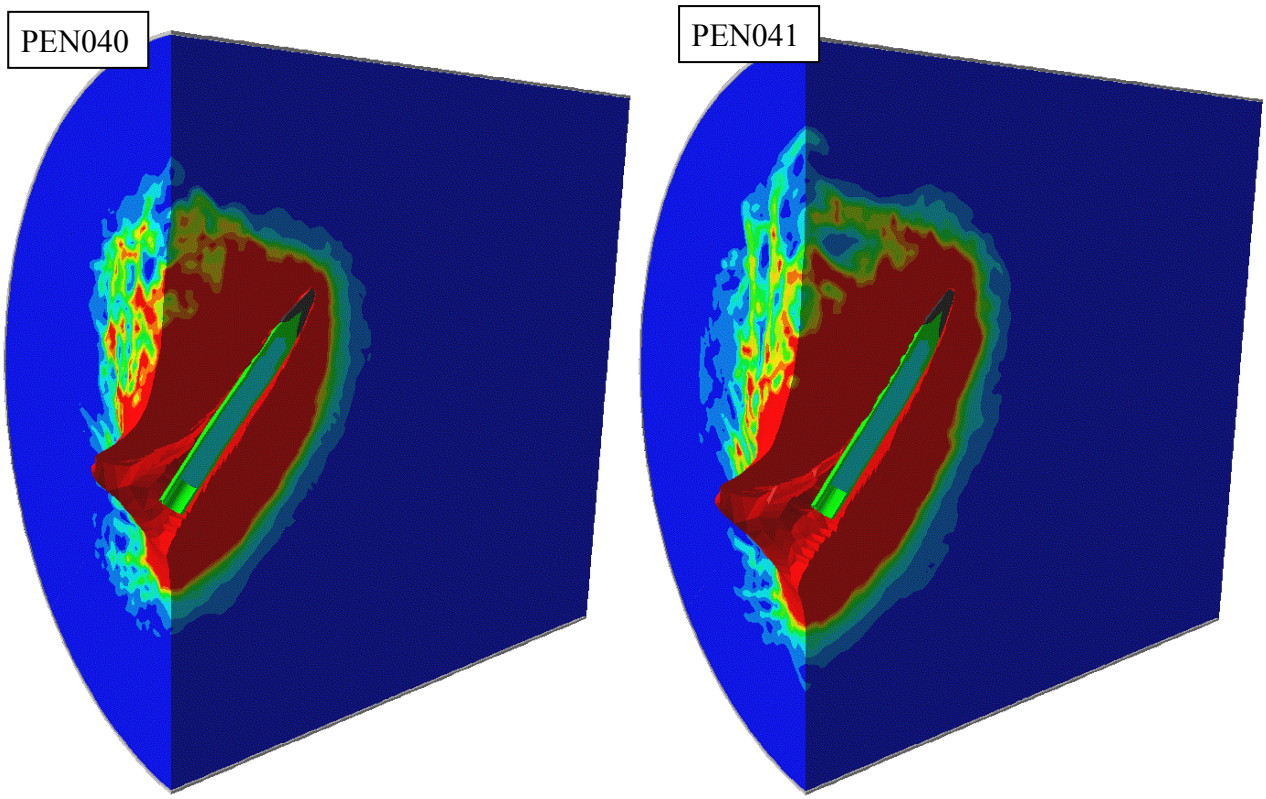

Figure 3.16. Damage and deformations for models with 60° impact angle, model PEN040 with 420 m/s impact velocity and model PEN041 with 460 m/s impact velocity.

Influence of tensile failure conditions for the concrete

Simulations are performed to compare different tensile failure for the concrete, i.e. the original damage evaluation according to the RHT model and the crack softening failure condition. The chosen tensile strength of the concrete, i.e. 4 MPa, corresponds roughly to the "static" value of the tensile strength. One simulation uses associative flow both in π-plane and meridional plane, i.e. bulking, for the crack softening option of the concrete during tensile failure. The bulking option increases the penetration resistance of the concrete target, and this is not a phenomenon that is likely to represent the physical behaviour of the concrete subjected to compaction at the pressures created during deep penetration. However, at low pressures without any substantial compaction of the concrete it is likely that bulking occur for the material, e.g. close to free surfaces and at low penetration velocities. It is likely that the coupling between bulking due to tensile cracking of the material and crushing of the concrete due to hydrostatic pressure needs to be further analysed to take advantage of crack softening tensile failure models. The tensile strength is increased to 8 MPa, for the option without bulking of the concrete. This corresponds to a dynamic tensile strength at a strain rate of approximately 5 s^{-1}. The crack softening models needs to be modified to describe the penetration behaviour if they are to be used for this type of simulations. The models are compiled in tables 3.13 and 3.14. Damage plots of models PEN066 to PEN069 are shown in figures 3.17 and 3.18. Comparisons of velocity vs. time and displacement for simulations using the original RHT damage evolution model and the tensile crack softening model are shown in figures 3.19 and 3.20.

The original RHT damage evolution model seems to be better suitable for these models with relative long/thick targets where the influence from surface effects caused by the back face are negligible, and where the radial cracking is partly prohibited by a steel confinement. Further simulations with varying tensile strength for the concrete targets with 0.60 m length are shown later in the report. Tensile failure models are also discussed in chapter 5.

Table 3.13. Penetration simulations with varying failure conditions for the concrete.

	PEN036	**PEN066**	**PEN067**
Model symmetry	½	½	½
Target length	1200 mm	1200 mm	1200 mm
Element size	10 mm	10 mm	10 mm
Projectile mass	4.53 kg	4.53 kg	4.53 kg
Impact velocity	420 m/s	420 m/s	420 m/s
Impact angle	90°	90°	90°
ρ_0	2.330 g/cm^3	2.330 g/cm^3	2.330 g/cm^3
P_{crush}	23.3 MPa	23.3 MPa	23.3 MPa
Tensile failure for the concrete	Original RHT f_t= 4.8 MPa	Crack softening with f_t= 4 MPa and Gf=180 J/m^2 No bulking [b]	Crack softening with f_t= 4 MPa and Gf=180 J/m^2 Bulking [c]
Friction coefficient	μ=0	μ=0	μ=0
Comment	AD v. 4.3.02	AD v. 5.0.01c	AD v. 5.0.01c
Penetration depth	620 mm	>750 mm	542 mm
Energy error	-1.4%	-1.7%	-1.3%

Note: [b] No bulking - Associative flow in π-plane combined with non-associative flow in meridional plane for the crack softening option.

[c] Bulking - Associative flow in π-plane and meridional plane for the crack softening option.

Table 3.14. Penetration simulations with varying friction and failure conditions for the concrete.

	PEN046	**PEN068**	**PEN069**
Model symmetry	½	½	½
Target length	1200 mm	1200 mm	1200 mm
Element size	10 mm	10 mm	10 mm
Projectile mass	4.53 kg	4.53 kg	4.53 kg
Impact velocity	420 m/s	420 m/s	420 m/s
Impact angle	90°	90°	90°
ρ_0	2.330 g/cm^3	2.330 g/cm^3	2.330 g/cm^3
P_{crush}	23.3 MPa	23.3 MPa	23.3 MPa
Tensile failure for the concrete	Original RHT f_t= 4.8 MPa	Crack softening [d] with f_t= 8 MPa and Gf=180 J/m^2 No bulking [b]	Crack softening [d] with f_t= 8 MPa and Gf=180 J/m^2 No bulking [b]
Friction coefficient	μ=0.05	μ=0	μ=0.05
Comment	AD v. 5.0.01c	AD v. 5.0.01c	AD v. 5.0.01t
Penetration depth	520 mm	>690 mm	>700 mm
Energy error	-18.6%	-1.7%	-7.4%

Note: [b] No bulking - Associative flow in π-plane combined with non-associative flow in meridional plane for the crack softening option.

[d] Increased values for tensile and shear strength used for the RHT model to avoid influence on crack softening failure, f_t/f_c= 0.3 and f_s/f_c= 0.5.

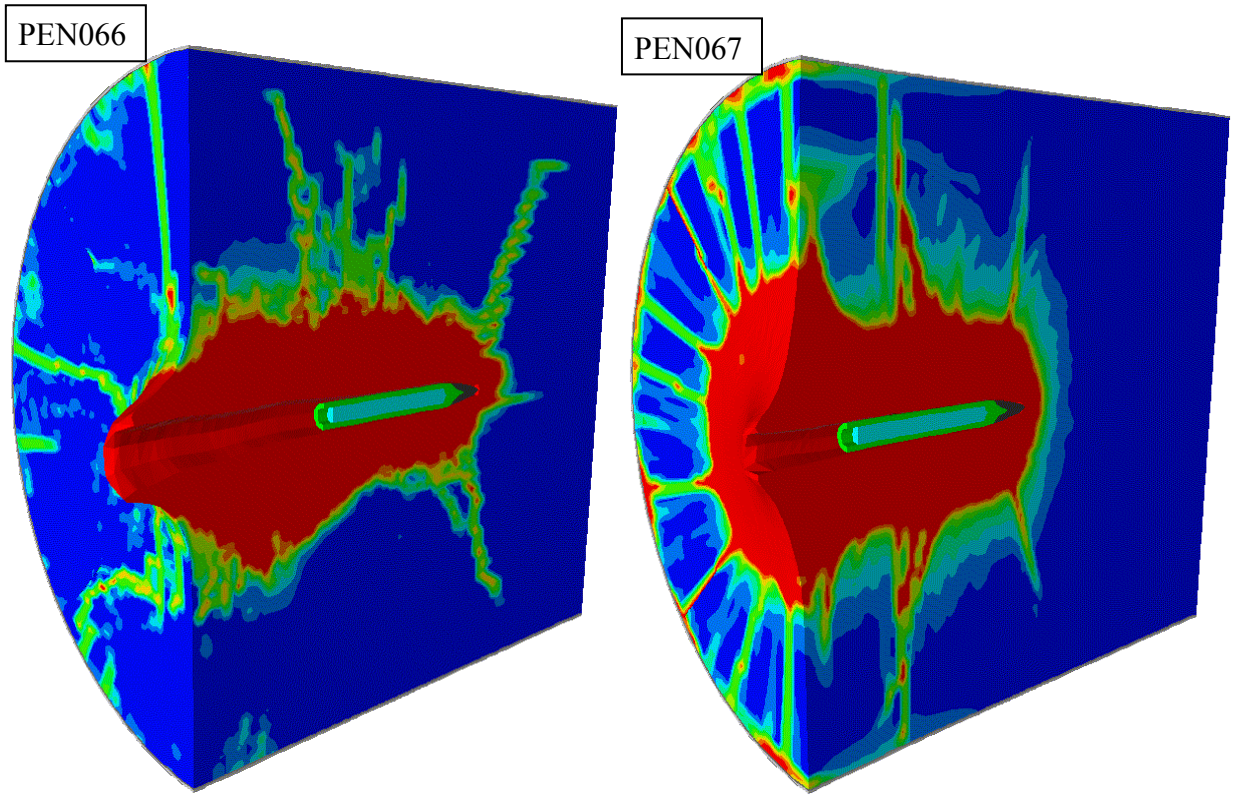

Figure 3.17. Damage and deformations for models PEN066 (left) and PEN067 (right) with different flow rules for the crack softening behaviour. Both models uses crack softening with f_t=4 MPa and no friction between target and projectile.

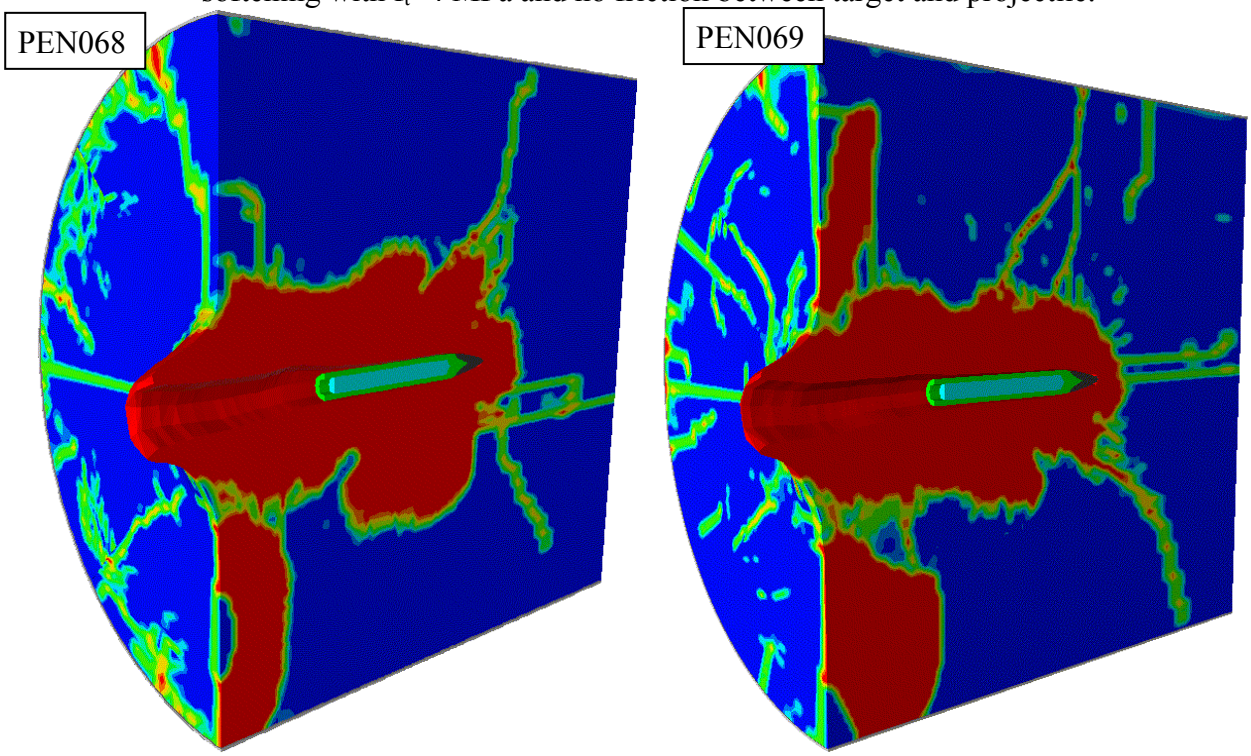

Figure 3.18. Damage and deformations for models PEN068 (left) and PEN069 (right), with and without friction between target and projectile. Both models uses crack softening with f_t=8 MPa and without bulking of the concrete.

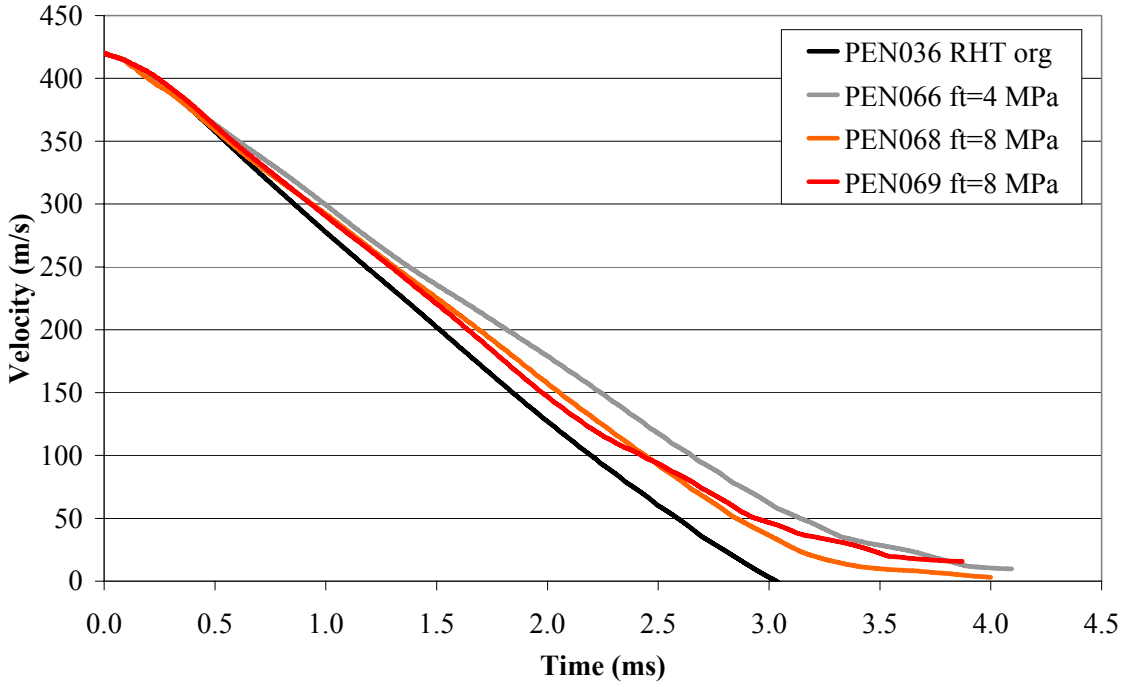

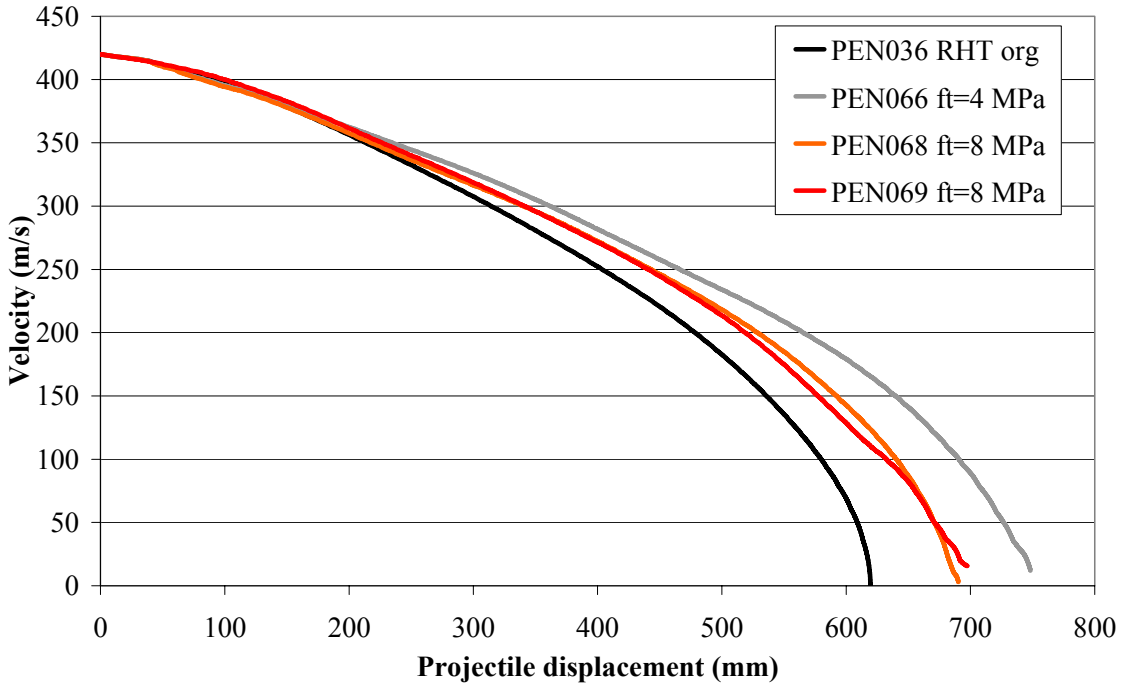

Figure 3.19. Projectile velocity vs. time and penetration for reference model PEN036, compared with models PEN066, PEN068 and PEN069. These models uses an additional crack softening tensile failure condition combined with the “No bulking” option for the concrete. Model PEN069 also have friction specified between target and projectile. Tables 3.13 and 3.14 gives the input data for the models.

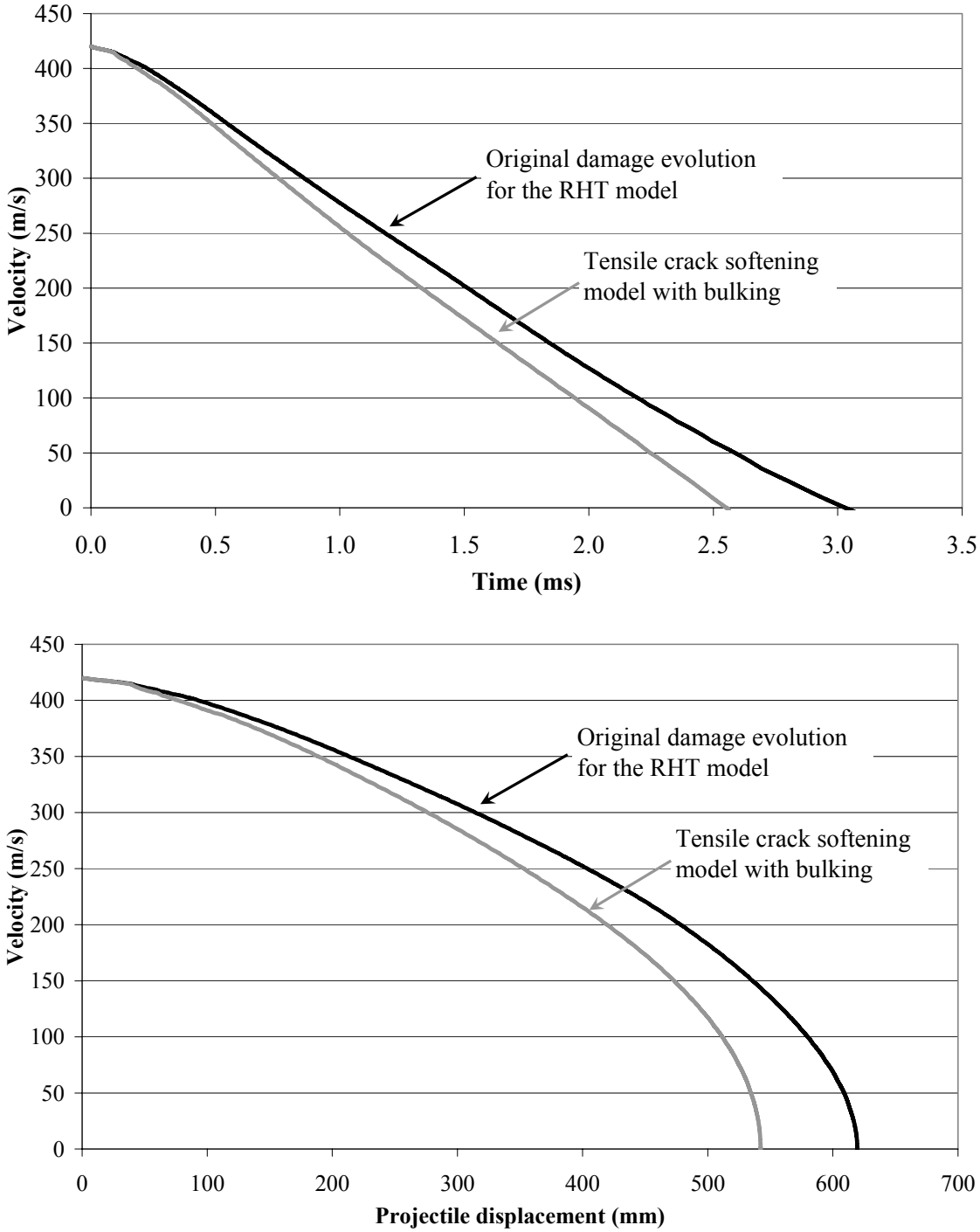

Figure 3.20. Projectile velocity vs. time and penetration for reference model PEN036, compared to model PEN067 with crack softening failure condition for the concrete. The "Bulking option" is used for the later model. Tables 3.13 and 3.14 gives the input data for the models.

A more suitable value for the static tensile strength of a normal strength concrete with compressive strength 48 MPa should be 4 MPa, as discussed earlier. Further simulations with f_t/f_c=0.0833 are therefore run for the mesh with 5 mm elements, i.e. models PEN205B and PEN208B. These models only show a minor increase of the penetration depth compared with earlier model with f_t/f_c=0.10, i.e. a tensile strength of 4.8 MPa. These final models of 1.2 m concrete targets are also used with the projectile mass 3.64 kg for comparison with the test performed in 2002. The results from these simulations are compiled in tables 3.15 and 3.16. A plot of the damage and deformations for the model PEN209B with 3.64 kg penetrator is shown in figure 3.21, and the influence on the projectile deceleration of projectile mass and impact velocity are shown in figure 3.22.

Table 3.15. Penetration simulations with 5 mm elements and different tensile strength of the concrete.

	PEN206	**PEN205**	**PEN205B**	**PEN208B**
Model symmetry	¼	¼	¼	¼
Target length	1200 mm	1200 mm	1200 mm	1200 mm
Element size	10 mm	5 mm	5 mm	5 mm
Projectile mass	4.53 kg	4.53 kg	4.53 kg	4.53 kg
Impact velocity	420 m/s	420 m/s	420 m/s	460 m/s
Impact angle	90°	90°	90°	90°
ρ_0	2.330 g/cm^3	2.330 g/cm^3	2.314 g/cm^3	2.314 g/cm^3
P_{crush}	23.3 GPa	23.3 GPa	35.0 GPa	35.0 GPa
Tensile failure for the concrete	Original RHT f_t= 4.8 MPa	Original RHT f_t= 4.8 MPa	Original RHT f_t= 4.0 MPa	Original RHT f_t= 4.0 MPa
Friction coefficient	μ=0.05	μ=0.05	μ=0.05	μ=0.05
Comment	AD 5.0.02c	AD 5.0.02c	ρ_0=2.314 g/cm^3 AD 5.0.02k	ρ_0=2.314 g/cm^3 AD 5.0.02k
Penetration depth	529 mm	512 mm	527 mm	587 mm
Energy error	-18.7%	-16.0%	-15.8%	-16.7%

Table 3.16. Penetration simulations with 5 mm elements and different tensile strength of the concrete.

	PEN209	**PEN209B**
Model symmetry	¼	¼
Target length	1200 mm	1200 mm
Element size	5 mm	5 mm
Projectile mass	3.64 kg	3.64 kg
Impact velocity	420 m/s	420 m/s
Impact angle	90°	90°
ρ_0	2.314 g/cm^3	2.314 g/cm^3
P_{crush}	35.0 GPa	35.0 GPa
Tensile failure for the concrete	Original RHT with f_t= 4.8 MPa	Original RHT with f_t= 4.0 MPa
Friction coefficient	μ=0.05	μ=0.05
Comment	AD 5.0.02k	AD 5.0.02k
Penetration depth	432 mm	450 mm
Energy error	-15.4%	-15.3%

PEN209B

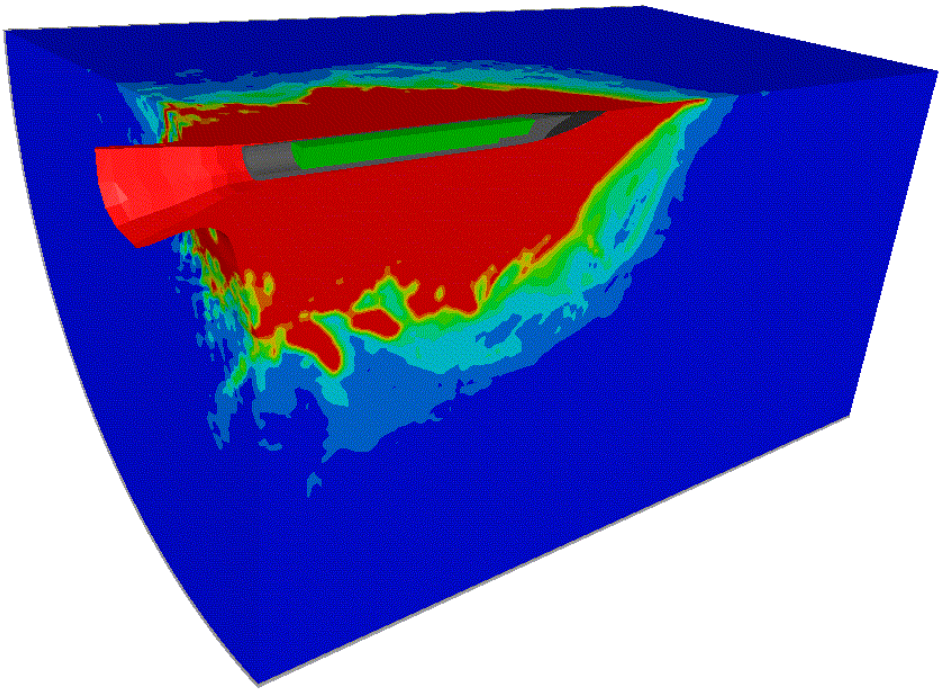

Figure 3.21. Damage and deformations for model PEN209B with 3.64 kg penetrator.

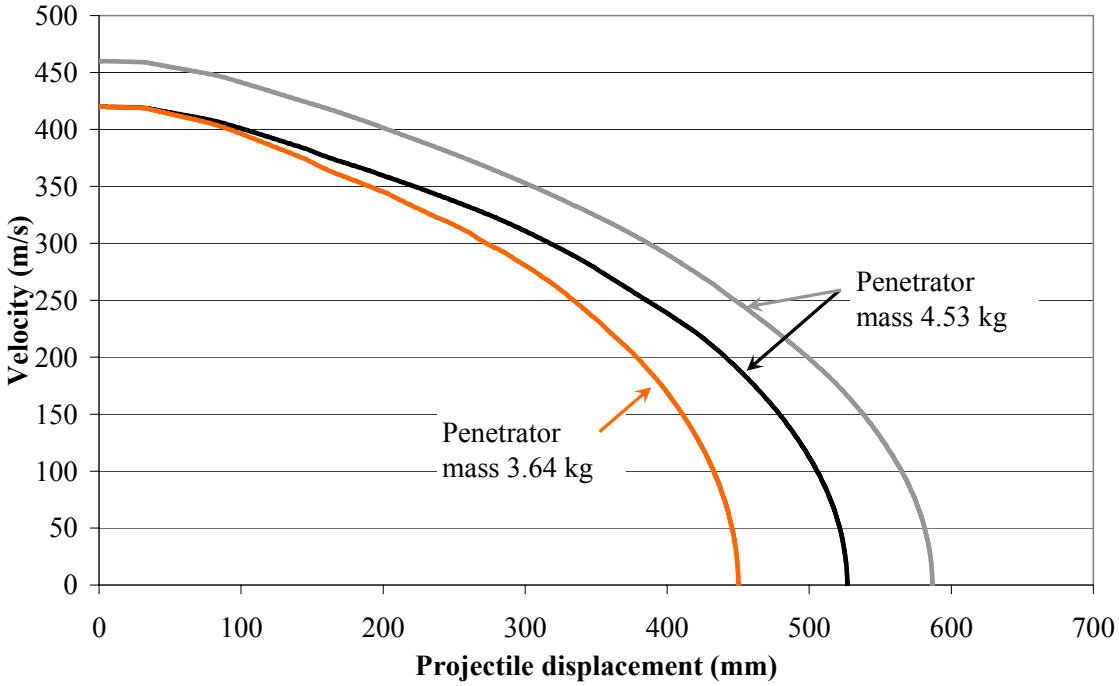

Figure 3.22. Influence of projectile mass and impact velocity on penetration depth for semi-infinite targets.

3.1.2. Simulations of targets with 0.60 m length

Simulations are also performed of short 0.60 m concrete targets to study perforation of targets. These simulations of perforation of unreinforced concrete targets focus on the modelling of the tensile failure of the concrete, e.g. crater formation. The reason for this is that only a small part in the central area of the target is fully confined, and a large part of the target is lost due to cratering at the front and back side. For this perforation case, i.e. test no. 2004-6 in appendix 3, approximately 25% of the target thickness is lost due to the cratering. The energy consumption to obtain a tensile failure due to cratering is only a small part of the energy needed to crush the material during projectile penetration. The chosen material and model parameters are based on the simulations of the 1.20 m targets, with the major part of the simulations performed using the projectile with a mass of 4.53 kg. All these simulations use the increased yield strength, i.e. 2.50 GPa, for the nose of the penetrator. This is to avoid extensive deformation of the nose elements.

Influence of mass and impact velocity for the penetrator

The results from initial simulations with different mass and impact velocity for the penetrator, and using 10 mm element size, are given in table 3.17. The models doesn't consider friction between penetrator and concrete material. Damage and deformation plots are shown in figures 3.23 and 3.24 for these models.

Table 3.17. Simulations of concrete perforation, with different impact velocity and projectile mass.

	PEN022	**PEN023**	**PEN024**
Model symmetry	½	½	½
Target length	600 mm	600 mm	600 mm
Element size	10 mm	10 mm	10 mm
Projectile mass	3.64 kg	4.53 kg	4.53 kg
Impact velocity	420 m/s	420 m/s	460 m/s
Impact angle	90°	90°	90°
ρ_0	2.330 g/cm^3	2.330 g/cm^3	2.330 g/cm^3
P_{crush}	35.0 MPa	35.0 MPa	35.0 MPa
Tensile failure for the concrete	Original RHT f_t= 4.8 MPa	Original RHT f_t= 4.8 MPa	Original RHT f_t= 4.8 MPa
Friction coefficient	μ=0	μ=0	μ=0
Comment	AD v. 4.3.02	AD v. 4.3.02	AD v. 4.3.02
Exit velocity	66 m/s	156 m/s	213 m/s
Decrease of kinetic energy for projectile	97.5%	86.2%	74.3%
Energy error	-1.5%	-1.4%	-1.1%

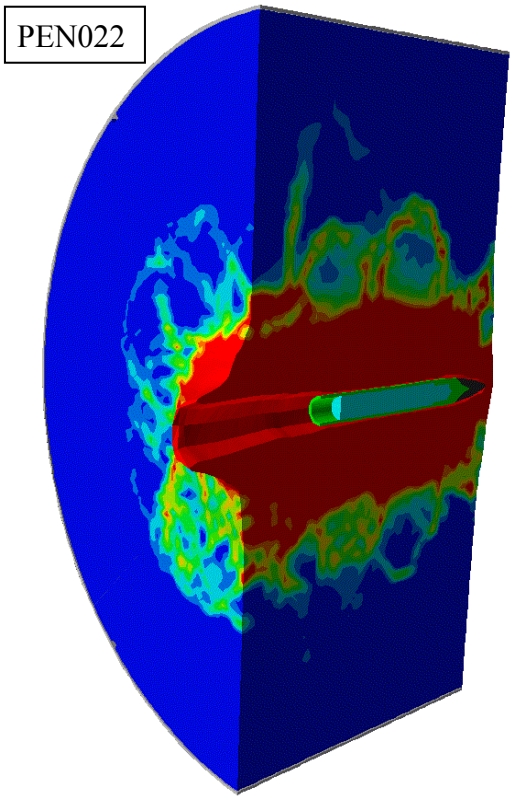

Figure 3.23. Damage and deformations for model PEN022 with a 3.64 kg projectile and an impact velocity of 420 m/s.

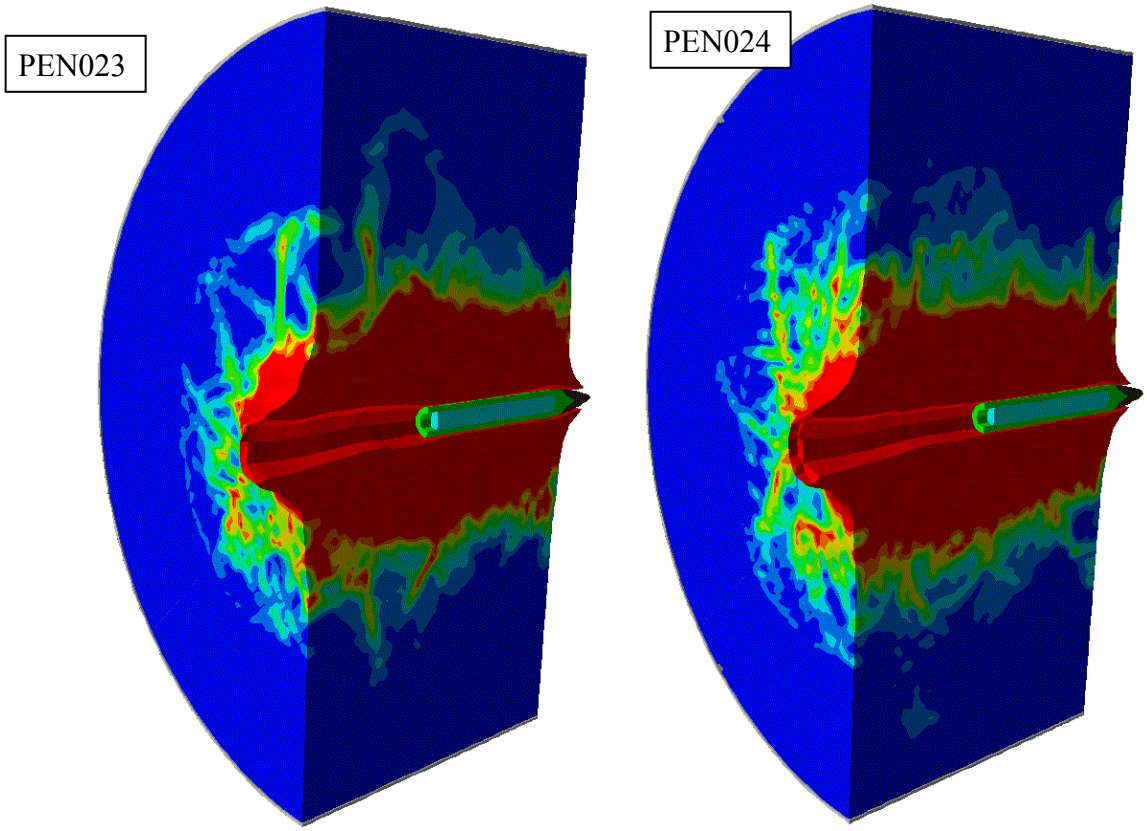

Figure 3.24. Damage and deformations for models PEN023 (left) and PEN024 (right) with 4.53 kg projectile mass. The impact velocities are 420 m/s and 460 m/s, respectively for the models.

Further simulations are performed based on the model with 4.53 kg penetrator and an impact velocity of 420 m/s to study the influence of inertia from eroded nodes, friction and pore collapse pressure. These simulations are compiled in table 3.18. It is shown that an increase of the pore collapse pressure from 23.3 to 35 MPa doesn't influence the exit velocity of the penetrator, and neither does the retained inertia from the eroded nodes. These results agree with the earlier results for penetration into the semi-infinite concrete target, i.e. with 1.2 m length. A damage and deformation plot for the model with retained inertia is shown in figure 3.25. However, as for the earlier models with the semi-infinite target the results are strongly influenced by the introduction of friction between the penetrator and target material. For model PEN080, with friction between the penetrator and the target, the energy error includes the energy loss due to friction is increased by roughly the same amount of energy as the kinetic energy of the penetrator decreases compared to the model without friction introduced. The increased energy lost due to friction reduces the exit velocity of the projectile from 156 m/s to approximately 58 m/s, see also figure 3.26.

Table 3.18. Simulations of concrete perforation using different friction coefficient and pore collapse pressure, and also include inertia from eroded nodes.

	PEN023	**PEN023B**	**PEN025**	**PEN080**
Model symmetry	½	½	½	½
Target length	600 mm	600 mm	600 mm	600 mm
Element size	10 mm	10 mm	10 mm	10 mm
Projectile mass	4.53 kg	4.53 kg	4.53 kg	4.53 kg
Impact velocity	420 m/s	420 m/s	420 m/s	420 m/s
Impact angle	90°	90°	90°	90°
ρ_0	2.330 g/cm^3	2.330 g/cm^3	2.330 g/cm^3	2.330 g/cm^3
P_{crush}	35.0 MPa	23.3 MPa	35.0 MPa	35.0 MPa
Tensile failure for the concrete	Original RHT f_t= 4.8 MPa	Original RHT f_t= 4.8 MPa	Original RHT f_t= 4.8 MPa	Original RHT f_t= 4.8 MPa
Friction coefficient	μ=0	μ=0	μ=0	μ=0.05
Comment	AD v. 4.3.02	AD v.5.0.02c	Retain inertia from eroded nodes AD v. 4.3.02	AD v. 5.0.01c
Exit velocity	156 m/s	156 m/s	156 m/s	≈58 m/s
Decrease of kinetic energy for projectile	86.2%	86.2%	86.2%	98.1%
Energy error	-1.4%	-1.4%	-1.9%	-18.4%

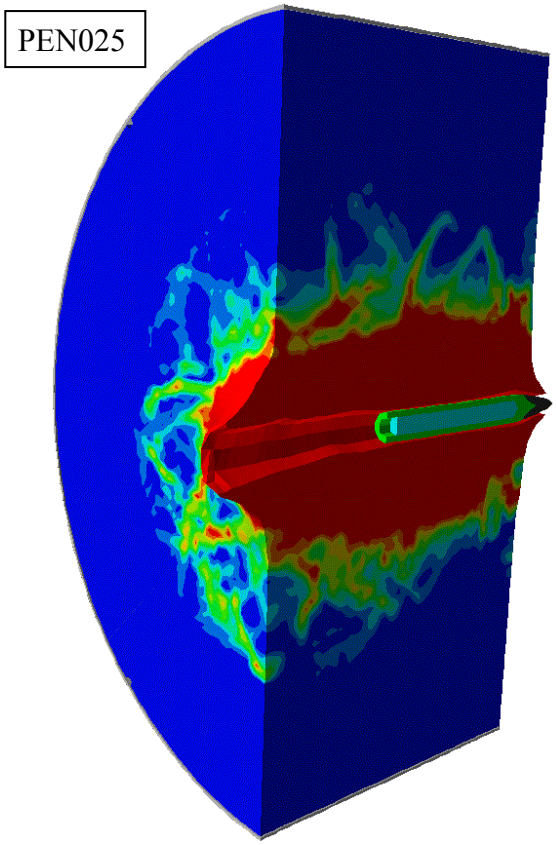

Figure 3.25. Damage and deformations for model PEN025 with 4.53 kg projectile mass and impact velocity 420 m/s. The inertia from eroded nodes is retained for this model.

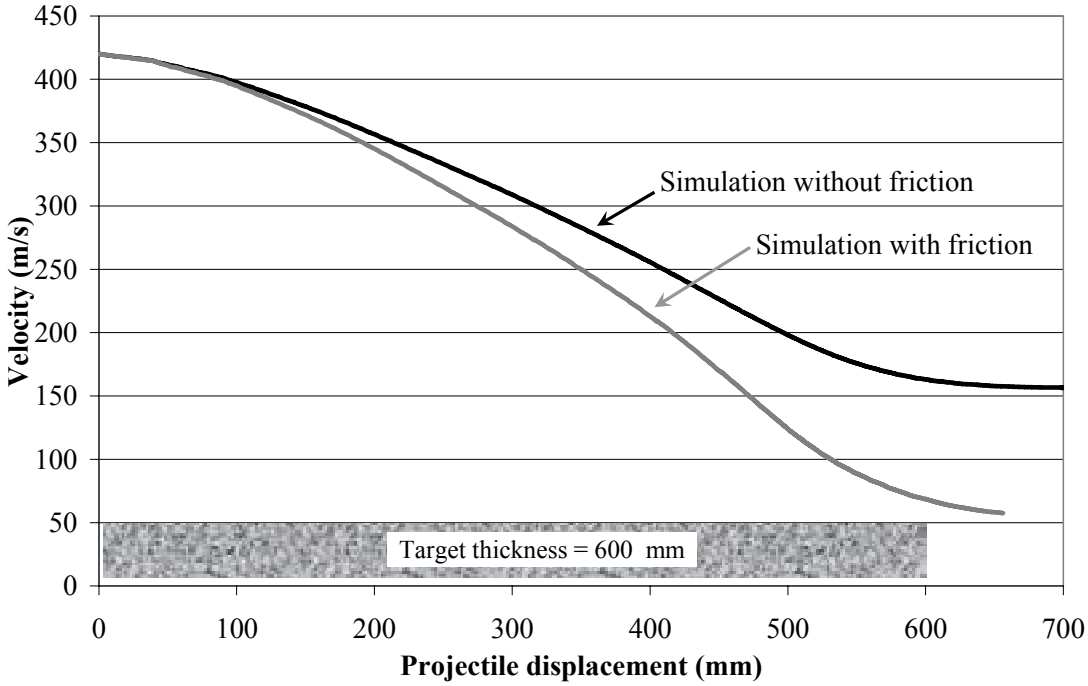

Figure 3.26. Velocity vs. projectile displacement for models PEN023 and PEN080, i.e. with and without friction between penetrator and target.

Influence of tensile failure conditions for the concrete

Simulations are also run with additional tensile failure conditions for the concrete, i.e. using the crack softening failure conditions with different parameters. The use of additional tensile failure models was discussed earlier in chapter 3.1.1. The chosen tensile strengths of the concrete, i.e. 4, 8 and 16 MPa, roughly corresponds to dynamic increased tensile strengths at strain rates 1×10^{-5} s^{-1} ("static"), 5 $s^{-1}$and 50 s^{-1}, respectively. When the crack softening parameter is used with increased failure strength it is necessary to also increase the values for f_t/f_c and f_s/f_c in the RHT model, otherwise these values might limit the failure envelope. The results for the models without friction are given in table 3.19, and for models with friction in table 3.20. The increase of tensile failure strength from 4 MPa to 16 MPa reduces the exit velocity from 230 m/s to 163 m/s for the models without friction considered. For the models with friction considered the decrease of exit velocity is from 198 m/s to 93 m/s for the same material parameters. The increase of the total energy loss, including friction energy, roughly corresponds to the decrease of kinetic energy for the penetrator when friction is introduced.

Simulations with the use of associative flow in both π-plane and meridional plane, i.e. bulking, for the crack softening option of the concrete during tensile failure, are also performed as for the 1.2 m target. The bulking option increases the penetration resistance of the concrete target, and is not a phenomenon that is likely to represent the physical behaviour of the concrete during these loading conditions. The results from models using the bulking option are given in table 3.21. However, at low pressures without any substantial compaction of the concrete it is likely that bulking occur for the material. Simulations with different bulking options, and without the use of friction, are compared in figures 3.27 and 3.28. Figure 3.29 shows the models with increased tensile failure strength for the crack softening model. The fracture energy is independent of strain rate for these models, and actually valid only for low strain rates. The deformation of an element before total fracturing (damage) of the element is decreased for an increase of the tensile strength of the concrete, if the same fracture energy is used in both cases. A concrete with increased tensile strength also has a decreased deformation capacity before damage reaches the value of unity, i.e. ε_{fail} decreases. This seems to make the material more "brittle". Figure 3.30 shows the velocity vs. penetration depth for the crack softening model without bulking and friction considered.

Table 3.19. Simulations of perforation with varying tensile failure conditions and with friction neglected.

	PEN023	**PEN026**	**PEN028**	**PEN029**
Model symmetry	½	½	½	½
Target length	600 mm	600 mm	600 mm	600 mm
Element size	10 mm	10 mm	10 mm	10 mm
Projectile mass	4.53 kg	4.53 kg	4.53 kg	4.53 kg
Impact velocity	420 m/s	420 m/s	420 m/s	420 m/s
Impact angle	90°	90°	90°	90°
ρ_0	2.330 g/cm^3	2.330 g/cm^3	2.330 g/cm^3	2.330 g/cm^3
P_{crush}	35.0 MPa	35.0 MPa	35.0 MPa	35.0 MPa
Tensile failure for concrete	Original RHT f_t= 4.8 MPa	Crack softening with f_t= 4 MPa and Gf=180 J/m^2 No bulking [b]	Crack softening [d] with f_t= 8 MPa and Gf=180 J/m^2 No bulking [b]	Crack softening [d] with f_t= 16 MPa and Gf=180 J/m^2 No bulking [b]
Friction coefficient	μ=0	μ=0	μ=0	μ=0
Comment	AD v. 4.3.02	AD v. 5.0.01c	AD v. 5.0.01c	AD v. 5.0.01c
Exit velocity	156 m/s	230 m/s	204 m/s	163 m/s
Decrease of kinetic energy for projectile	86.2%	70.0%	76.4%	84.9%
Penetration depth	---	---	---	---
Energy error	-1.4%	-1.4%	-1.5%	-1.4%

Note: [b] No bulking - Associative flow in π-plane combined with non-associative flow in meridional plane for the crack softening option.

[d] Increased values for tensile and shear strength used for the RHT model to avoid influence on crack softening failure, f_t/f_c= 0.3 and f_s/f_c= 0.5.

Table 3.20. Simulations of perforation with different tensile failure conditions and with friction between target and projectile.

	PEN080	**PEN081**	**PEN082**	**PEN083**
Model symmetry	½	½	½	½
Target length	600 mm	600 mm	600 mm	600 mm
Element size	10 mm	10 mm	10 mm	10 mm
Projectile mass	4.53 kg	4.53 kg	4.53 kg	4.53 kg
Impact velocity	420 m/s	420 m/s	420 m/s	420 m/s
Impact angle	90°	90°	90°	90°
f_y for steel nose	2.50 GPa	2.50 GPa	2.50 GPa	2.50 GPa
ρ_0	2.330 g/cm^3	2.330 g/cm^3	2.330 g/cm^3	2.330 g/cm^3
P_{crush}	35.0 MPa	35.0 MPa	35.0 MPa	35.0 MPa
Tensile failure for concrete	Original RHT f_t= 4.8 MPa	Crack softening with f_t= 4 MPa and Gf=180 J/m^2 No bulking [b]	Crack softening [d] with f_t= 8 MPa and Gf=180 J/m^2 No bulking [b]	Crack softening [d] with f_t= 16 MPa and Gf=180 J/m^2 No bulking [b]
Friction coefficient	μ=0.05	μ=0.05	μ=0.05	μ=0.05
Comment	AD v. 5.0.01c	AD v. 5.0.01c	AD v. 5.0.01c	AD v. 5.0.01c
Exit velocity	≈58 m/s	198 m/s	164 m/s	93 m/s
Decrease of kinetic energy for projectile	98.1%	77.8%	84.8%	95.1%
Energy error	-18.4%	-10.0%	-12.5%	-14.6%

Note: [b] No bulking - Associative flow in π-plane combined with non-associative flow in meridional plane for the crack softening option.

[d] Increased values for tensile and shear strength used for the RHT model to avoid influence on crack softening failure, f_t/f_c= 0.3 and f_s/f_c= 0.5.

Table 3.21. Simulations of perforation using bulking of the concrete for the tensile cracking option, compared with reference simulation PEN023.

	PEN023	**PEN027**	**PEN090**
Model symmetry	½	½	½
Target length	600 mm	600 mm	600 mm
Element size	10 mm	10 mm	10 mm
Projectile mass	4.53 kg	4.53 kg	4.53 kg
Impact velocity	420 m/s	420 m/s	420 m/s
Impact angle	90°	90°	90°
ρ_0	2.330 g/cm^3	2.330 g/cm^3	2.330 g/cm^3
P_{crush}	35.0 MPa	35.0 MPa	35.0 MPa
Tensile failure for concrete	Original RHT f_t= 4.8 MPa	Crack softening with f_t= 4 MPa and Gf=180 J/m^2 Bulking [c]	Crack softening with f_t= 4 MPa and Gf=180 J/m^2 Bulking [c]
Friction coefficient	μ=0	μ=0	μ=0.05
Comment	AD v. 4.3.02	AD v. 5.0.01c	AD v. 5.0.02c
Exit velocity	156 m/s	---	---
Decrease of kinetic energy for projectile	86.2%	100%	100%
Penetration depth	---	589 mm	471 mm
Energy error	-1.4%	-1.3%	-20.5%

Note: [c] Bulking - Associative flow in π-plane and meridional plane for the crack softening option.

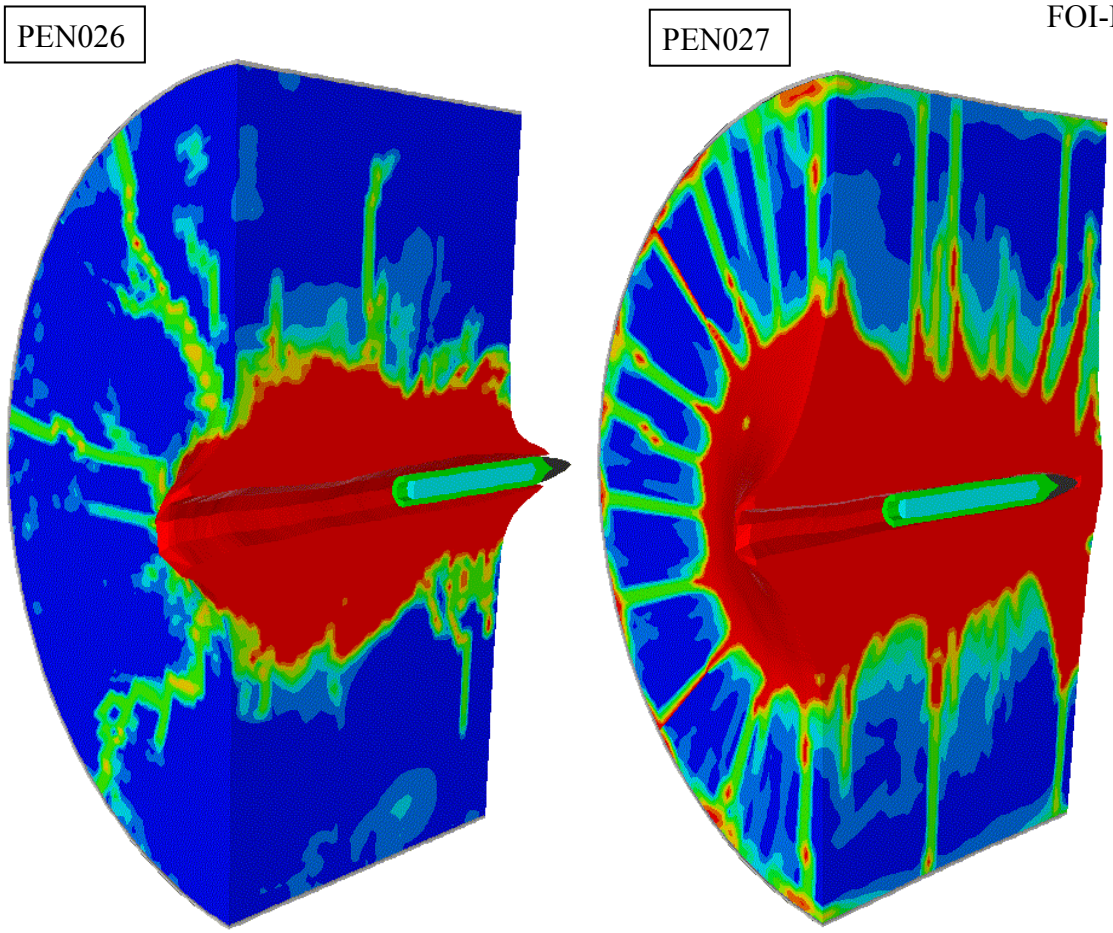

Figure 3.27. Damage and deformations for models without bulking of the concrete PEN026 (left), and with bulking of the concrete PEN027 (right). The impact velocity is 420 m/s and the projectile mass is 4.53 kg for both models.

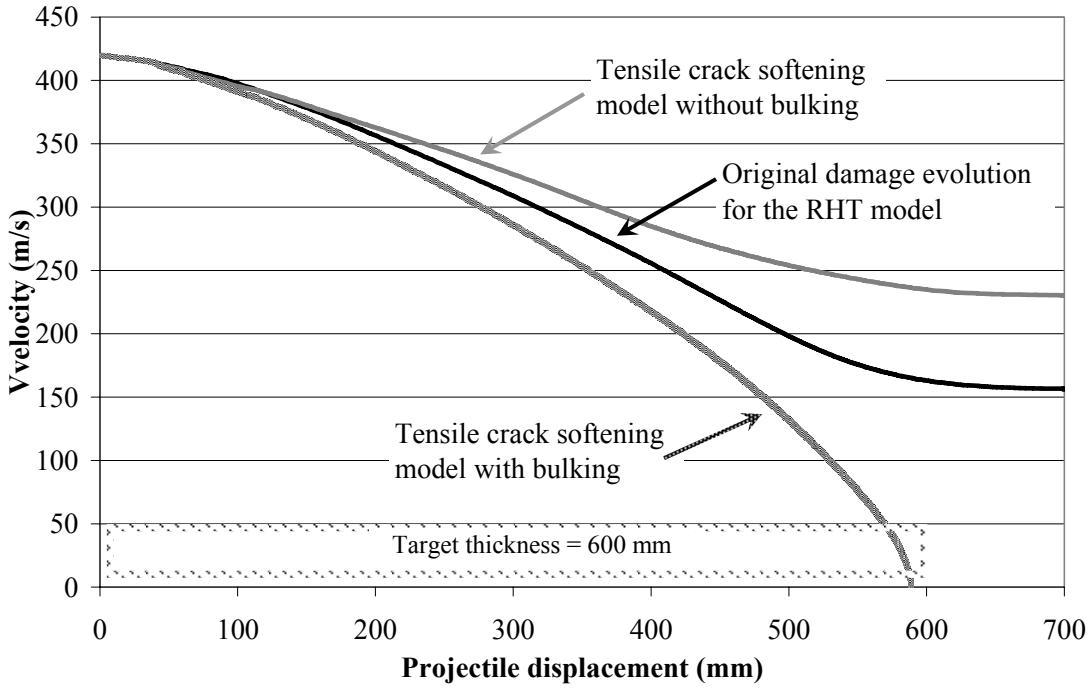

Figure 3.28. Velocity vs. projectile displacement for models PEN023, PEN026 and PEN027 with different tensile failure conditions. All models with 10 mm elements and without friction considered. Model PEN023 uses the original damage evolution with f_t=4.8 MPa, and the models with crack softening tensile failure use f_t=4.0 MPa.

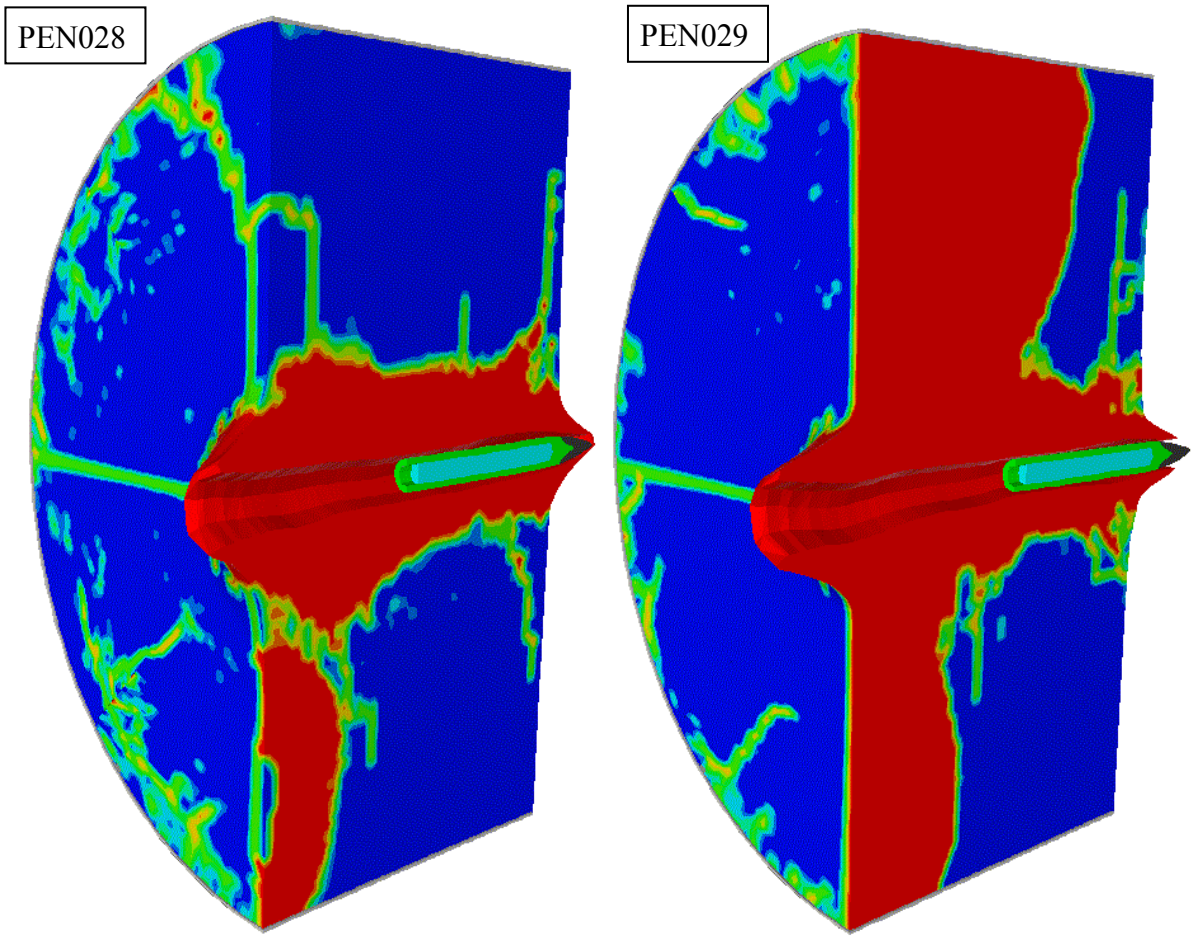

Figure 3.29. Damage and deformations for models PEN028 (left) and PEN029 (right) with 4.53 kg projectile mass. The impact velocity is 420 m/s for both models.

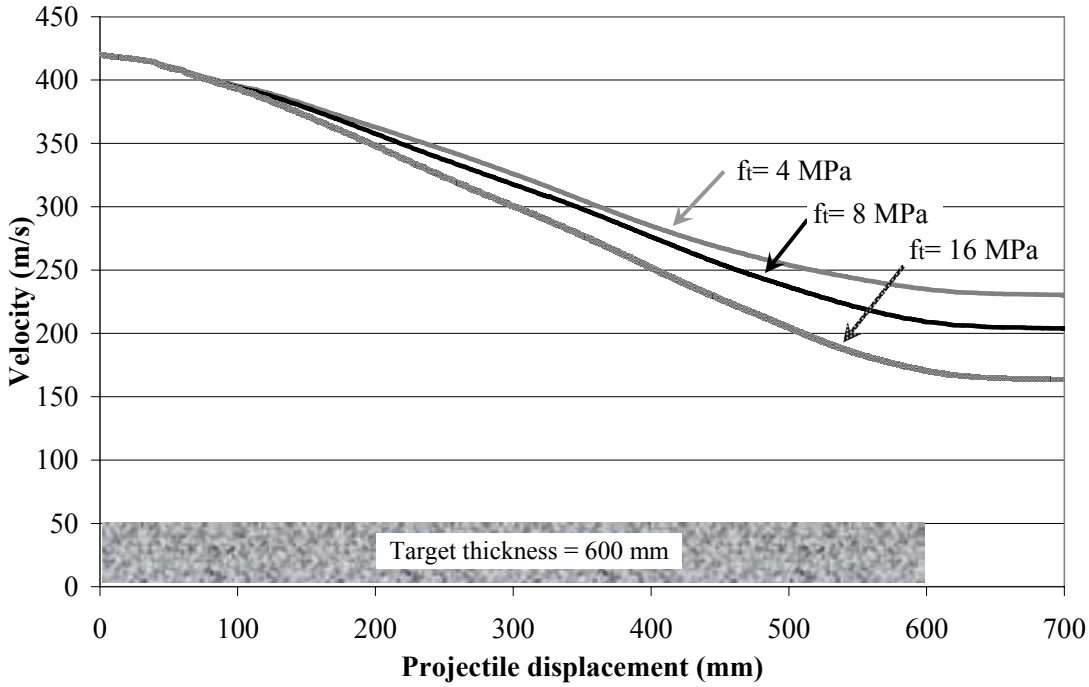

Figure 3.30. Velocity vs. projectile displacement for models PEN026, PEN028 and PEN029 with crack softening tensile failure and varying tensile failure stress between 4 and 16 MPa. All models with 10 mm elements and without friction considered.

Figures 3.31 and 3.32 show damage and deformations for the models that consider friction between the target and penetrator. The simulations with crack softening models are compared with a model using the original RHT damage formulation, i.e. model PEN080. The velocity vs. penetration depth for these models are shown in figure 3.33.

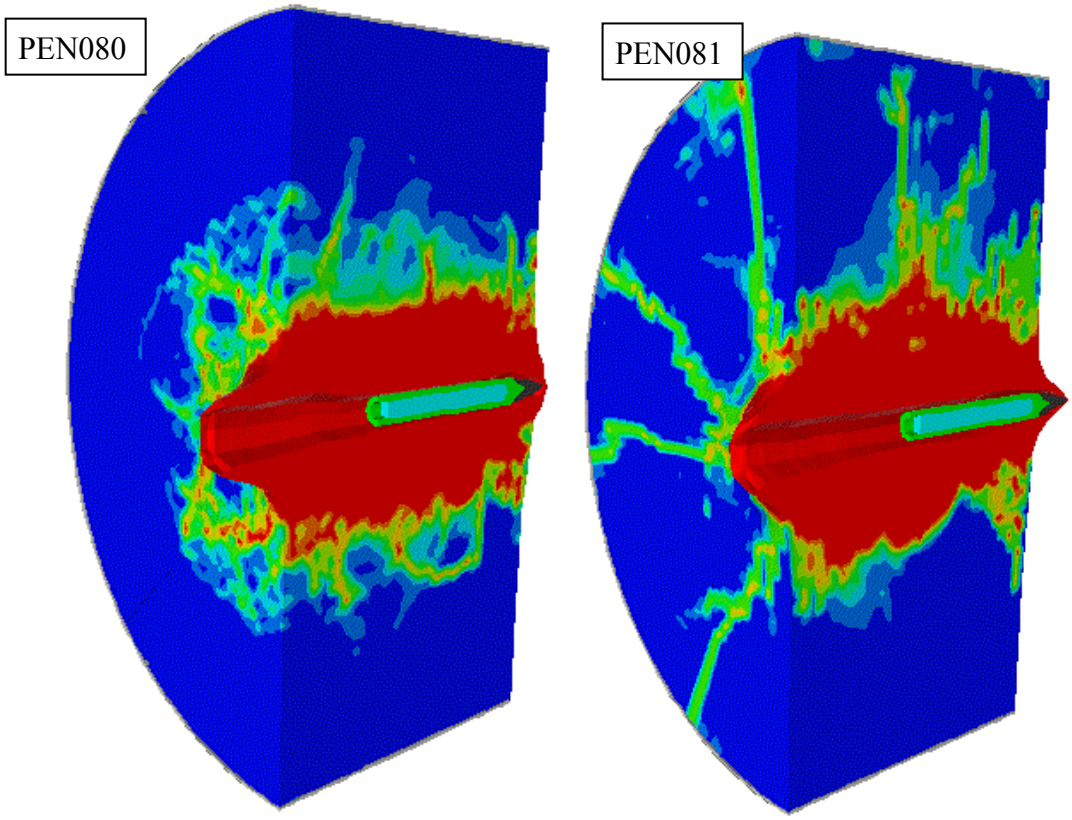

Figure 3.31. Damage and deformations for models PEN080 (left) and PEN081 (right) with 4.53 kg projectile mass. The impact velocity is 420 m/s for both models.

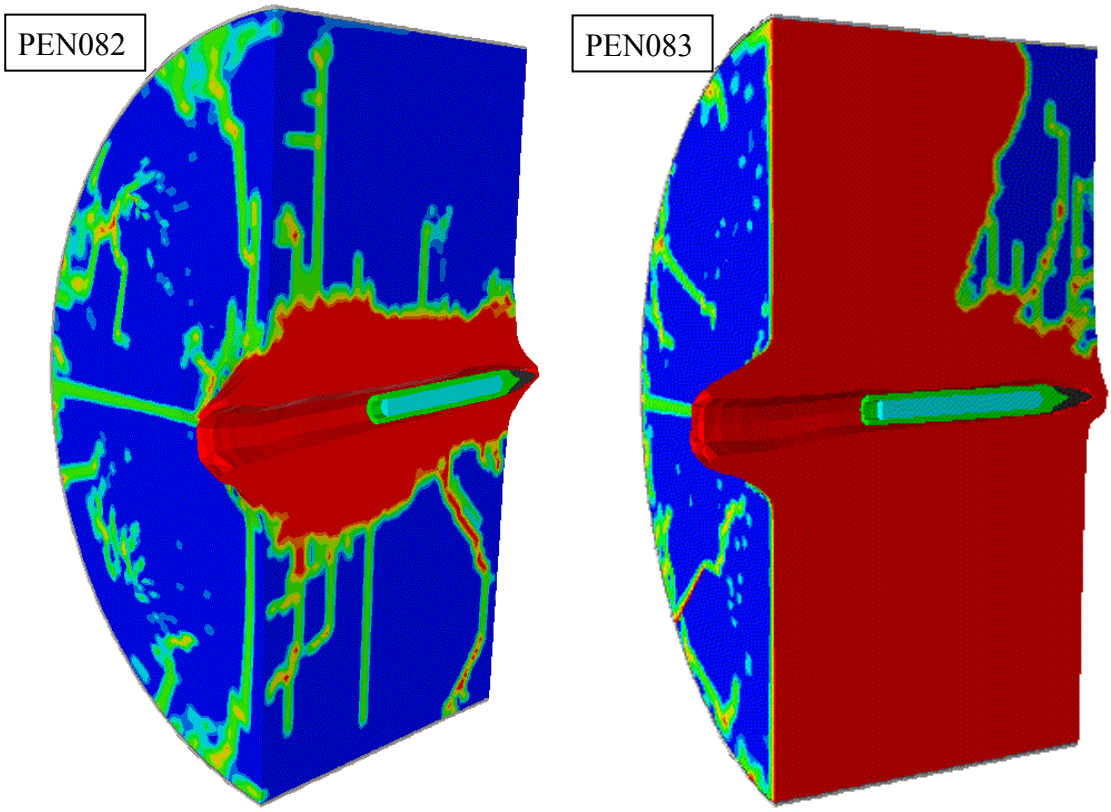

Figure 3.32. Damage and deformations for models PEN082 (left) and PEN083 (right) with 4.53 kg projectile mass. The impact velocity is 420 m/s for both models.

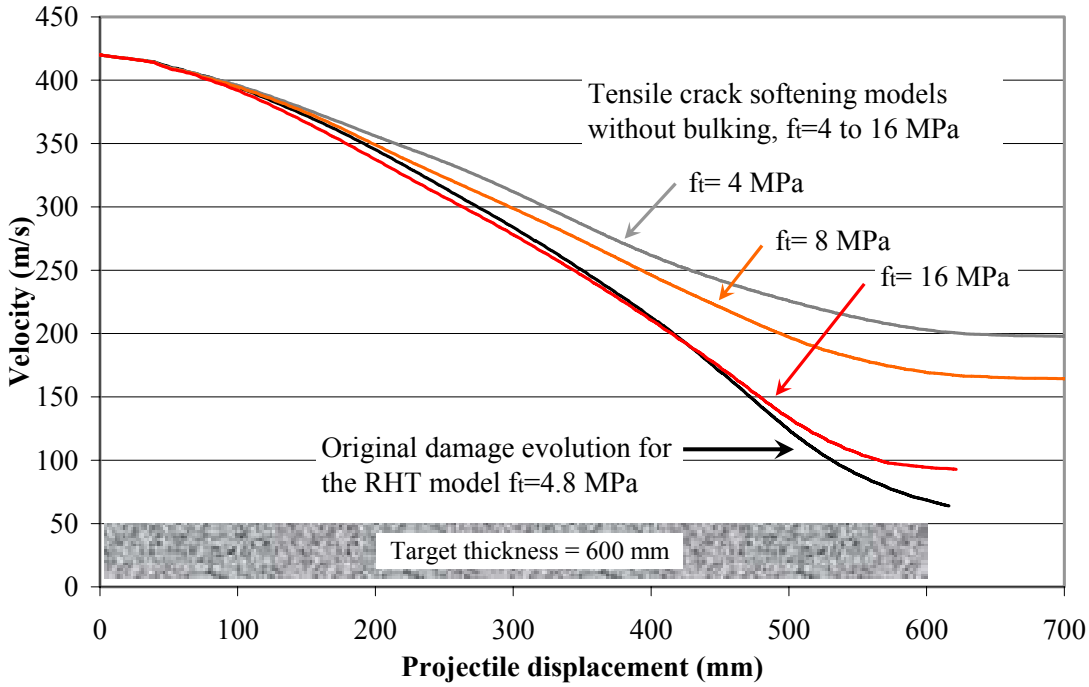

Figure 3.33. Velocity vs. projectile displacement for models PEN080 to PEN083. All models use friction between target and penetrator, and 10 mm element size for the target.

Influence of symmetry conditions

The influence of using half symmetry models is studied for the 0.60 m unreinforced targets, using the crack softening model with tensile strength 16 MPa for the concrete. The simulations with and without half symmetry, and also with and without the use of friction, are compiled in table 3.22. Only a small change of the exit velocity is noticed when introducing the models without symmetry. Further, the results are not conclusive for the models with and without the use of friction. Damage and deformation plots for the models without symmetry are shown in figure 3.34, and projectile velocity vs. penetration depth is shown for models with and without symmetry conditions in figure 3.35.

Table 3.22. Simulations of perforation with and without the use of symmetry and using crack softening tensile failure for the concrete.

	PEN084	**PEN029**	**PEN085**	**PEN083**
Model symmetry	None	½	None	½
Target length	600 mm	600 mm	600 mm	600 mm
Element size	10 mm	10 mm	10 mm	10 mm
Projectile mass	4.53 kg	4.53 kg	4.53 kg	4.53 kg
Impact velocity	420 m/s	420 m/s	420 m/s	420 m/s
Impact angle	90°	90°	90°	90°
ρ_0	2.330 g/cm^3	2.330 g/cm^3	2.330 g/cm^3	2.330 g/cm^3
P_{crush}	35.0 MPa	35.0 MPa	35.0 MPa	35.0 MPa
Tensile failure for concrete	Crack softening [d] with f_t= 16 MPa and Gf=180 J/m^2 No bulking [b]	Crack softening [d] with f_t= 16 MPa and Gf=180 J/m^2 No bulking [b]	Crack softening [d] with f_t= 16 MPa and Gf=180 J/m^2 No bulking [b]	Crack softening [d] with f_t= 16 MPa and Gf=180 J/m^2 No bulking [b]
Friction coefficient	μ=0	μ=0	μ=0.05	μ=0.05
Comment	AD v. 5.0.01t	AD v. 5.0.01c	AD v. 5.0.02c	AD v. 5.0.01c
Exit velocity	145 m/s	163 m/s	104 m/s	93 m/s
Decrease of kinetic energy for projectile	88.1%	84.9%	93.9%	95.1%
Energy error	-1.4%	-1.4%	-14.9%	-14.6%

Note: [b] No bulking - Associative flow in π-plane combined with non-associative flow in meridional plane for the crack softening option.

[d] Increased values for tensile and shear strength used for the RHT model to avoid influence on crack softening failure, f_t/f_c= 0.3 and f_s/f_c= 0.5.

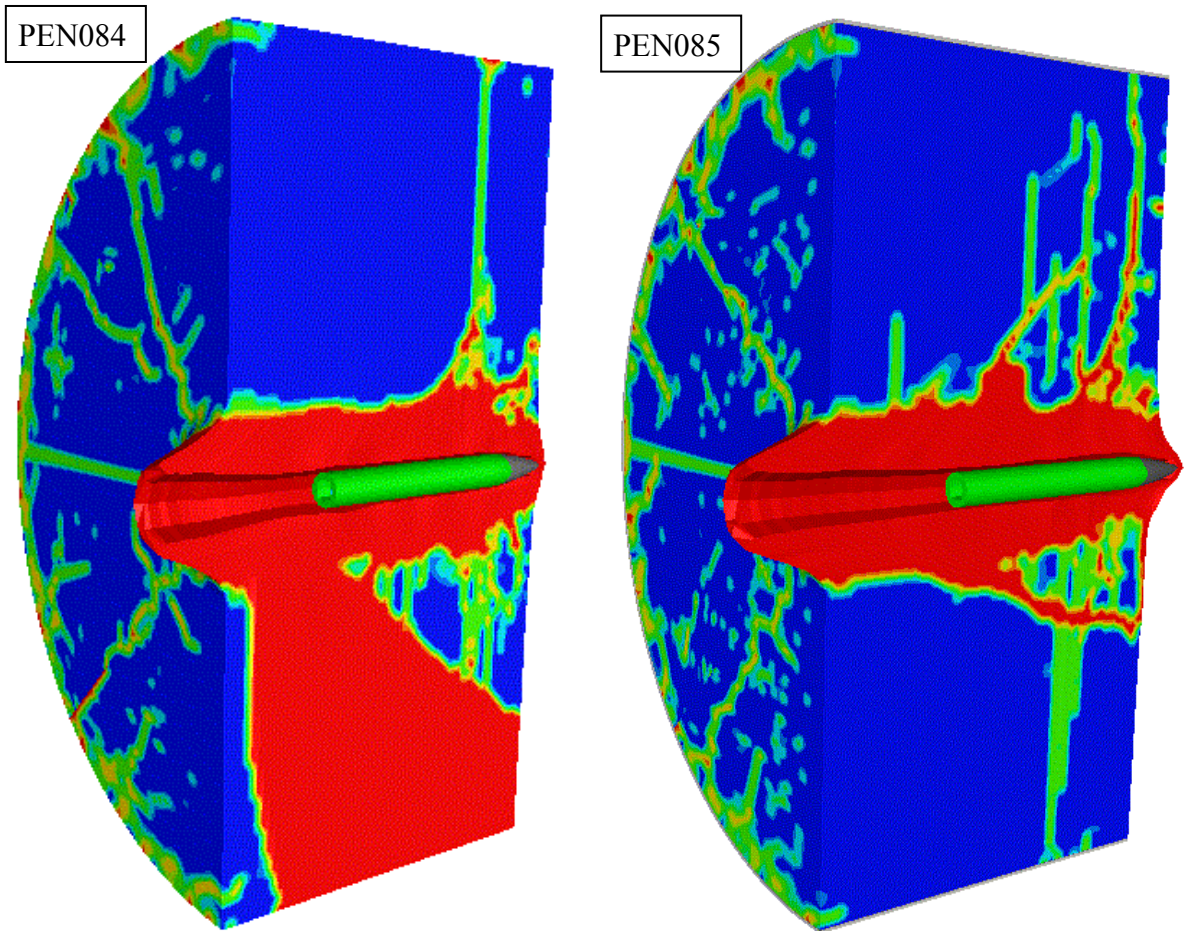

Figure 3.34. Damage and deformations for models PEN084 (left) and PEN085 (right) with 4.53 kg projectile mass. The impact velocity is 420 m/s for both models.

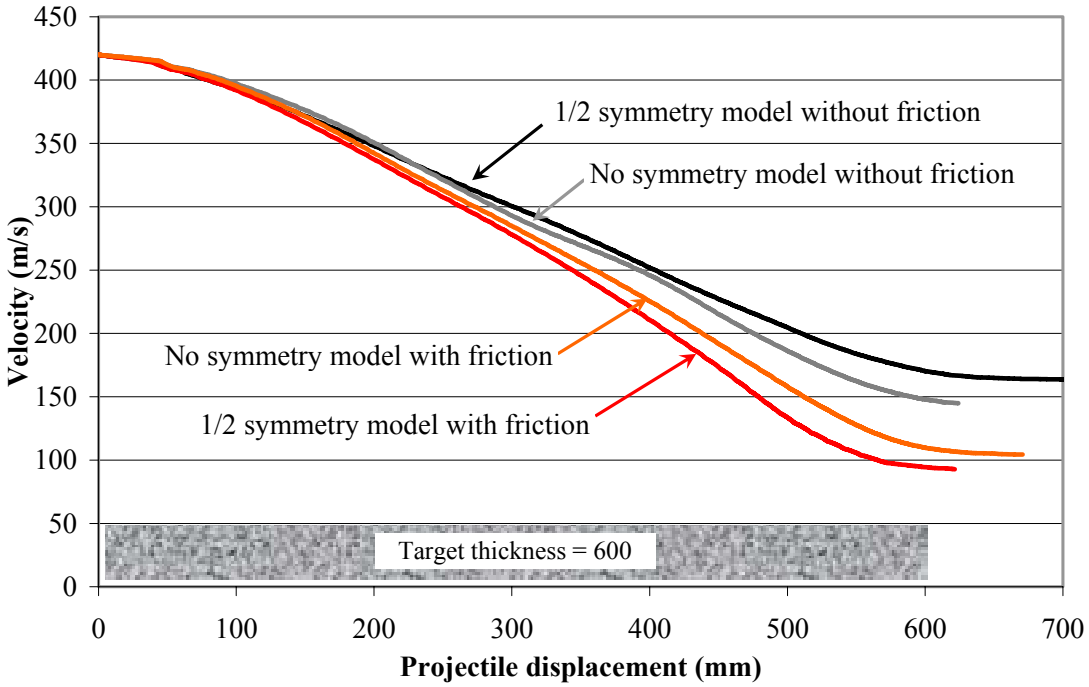

Figure 3.35. Velocity vs. projectile displacements for models PEN029 and PEN083 to PEN085, with varying symmetry conditions and friction coefficient. All models use crack softening tensile failure with 16 MPa tensile strength and 10 mm elements.

Influence of element size and concrete strength

The model with 4.53 kg penetrator and with an impact velocity of 420 m/s is used to study the influence of element size for different tensile failure conditions, i.e. with the original RHT damage model (f_t= 4.0 and 4.8 MPa) and the crack softening tensile failure (f_t = 8 and 16 MPa). The side of the elements are decreased from 10 mm to 5 mm in the central part of the target, giving 10 elements in the target across the projectile diameter. The models are compiled in tables 3.23 to 3.25. There is a major influence of the element size for this case with perforation of the concrete target. For the models with the use of the original RHT damage model and a tensile strength of 4.8 MPa the exit velocity is increased from 58 m/s to 98 m/s when the element size is decreased. Using the crack softening tensile failure with a tensile strength of 8 MPa the exit velocity is increased from 164 m/s to 216 m/s when the element size is decreased. The tensile strength crack softening models seems more sensitive to the element size for this type of loading of the concrete, even though the fracture energy are normalised against the used element length. These types of models needs to be further investigated, and may also need to be improved to be useful for future penetration research. For the models using the original RHT damage model and the tensile strength 4 MPa of the concrete the increase of the exit velocity is from 64 m/s to 143 m/s. The exit velocities for 4.0 MPa and 4.8 MPa tensile strengths, for the models that use 10 mm elements and the original damage evolution for the RHT model, are almost identical. This is probably due to lock up of the elements caused by too large element size. See figure 3.38. The influence of a change of the initial density of the concrete from 2.314 to 2.330 g/cm^3 is also studied, with a small influence on the exit velocity. The difference in exit velocity between models PEN080-2B and PEN080-2E is approximately 11 m/s.

Table 3.23. Simulations of perforation with friction between target and projectile using varying element size and tensile failure condition.

	PEN080	**PEN080-2**	**PEN082**	**PEN082-2**
Model symmetry	½	½	½	½
Target length	600 mm	600 mm	600 mm	600 mm
Element size	10 mm	5 mm	10 mm	5 mm
Projectile mass	4.53 kg	4.53 kg	4.53 kg	4.53 kg
Impact velocity	420 m/s	420 m/s	420 m/s	420 m/s
Impact angle	90°	90°	90°	90°
ρ_0	2.330 g/cm^3	2.330 g/cm^3	2.330 g/cm^3	2.330 g/cm^3
P_{crush}	35.0 MPa	35.0 MPa	35.0 MPa	35.0 MPa
Tensile failure for concrete	Original RHT f_t= 4.8 MPa		Crack softening [d] with f_t= 8 MPa and Gf=180 J/m^2, No bulking [b]	
Friction coefficient	μ=0.05	μ=0.05	μ=0.05	μ=0.05
Comment	AD v. 5.0.01c	AD v. 5.0.02k	AD v. 5.0.01c	AD v. 5.0.02k
Exit velocity	≈58 m/s	98 m/s	164 m/s	216 m/s
Decrease of kinetic energy for projectile	98.1%	94.6%	84.8%	73.6%
Energy error	-18.4%	-15.1%	-12.5%	-9.7%

Note: [b] No bulking - Associative flow in π-plane combined with non-associative flow in meridional plane for the crack softening option.

[d] Increased values for tensile and shear strength used for the RHT model to avoid influence on crack softening failure, f_t/f_c= 0.3 and f_s/f_c= 0.5.

Table 3.24. Simulations of perforation with friction between target and projectile using varying element size and crack softening tensile failure condition with f_t = 8 and 16 MPa.

	PEN082	**PEN082-2**	**PEN083**
Model symmetry	½	½	½
Target length	600 mm	600 mm	600 mm
Element size	10 mm	5 mm	10 mm
Projectile mass	4.53 kg	4.53 kg	4.53 kg
Impact velocity	420 m/s	420 m/s	420 m/s
Impact angle	90°	90°	90°
ρ_0	2.330 g/cm^3	2.330 g/cm^3	2.330 g/cm^3
P_{crush}	35.0 MPa	35.0 MPa	35.0 MPa
Tensile failure for concrete	Crack softening [d] with f_t= 8 MPa and Gf=180 J/m^2 No bulking [b]	Crack softening [d] with f_t= 8 MPa and Gf=180 J/m^2 No bulking [b]	Crack softening [d] with f_t= 16 MPa and Gf=180 J/m^2 No bulking [b]
Friction coefficient	μ=0.05	μ=0.05	μ=0.05
Comment	AD v. 5.0.01c	AD v. 5.0.02k	AD v. 5.0.01c
Exit velocity	164 m/s	216 m/s	93 m/s
Decrease of kinetic energy for projectile	84.8%	73.6%	95.1%
Energy error	-12.5%	-9.7%	-14.6%

Note: [b] No bulking - Associative flow in π-plane combined with non-associative flow in meridional plane for the crack softening option.

[d] Increased values for tensile and shear strength used for the RHT model to avoid influence on crack softening failure, f_t/f_c= 0.3 and f_s/f_c= 0.5.

Table 3.25. Simulations of perforation with friction between target and projectile using varying element size and tensile strength of the concrete. The initial density of the concrete is also varied for one model.

	PEN080A	**PEN080B**	**PEN080-2E**	**PEN080-2B**
Model symmetry	½	½	½	½
Target length	600 mm	600 mm	600 mm	600 mm
Element size	10 mm	10 mm	5 mm	5 mm
Projectile mass	4.53 kg	4.53 kg	4.53 kg	4.53 kg
Impact velocity	420 m/s	420 m/s	420 m/s	420 m/s
Impact angle	90°	90°	90°	90°
ρ_0	2.314 g/cm^3	2.314 g/cm^3	2.314 g/cm^3	2.330 g/cm^3
P_{crush}	35.0 MPa	35.0 MPa	35.0 MPa	35.0 MPa
Tensile failure for concrete	Original RHT f_t= 4.8 MPa	Original RHT f_t= 4.0 MPa	Original RHT f_t= 4.0 MPa	Original RHT f_t= 4.0 MPa
Friction coefficient	μ=0.05	μ=0.05	μ=0.05	μ=0.05
Comment	AD v. 5.0.02kc	AD v. 5.0.02k	AD v. 5.0.02k	AD v. 5.0.02k
Exit velocity	≈60 m/s	≈64 m/s	143 m/s	155 m/s
Decrease of kinetic energy for projectile	98.0%	97.7%	88.4%	86.5%
Energy error	-18.5%	-18.5%	-14.1%	-13.6%

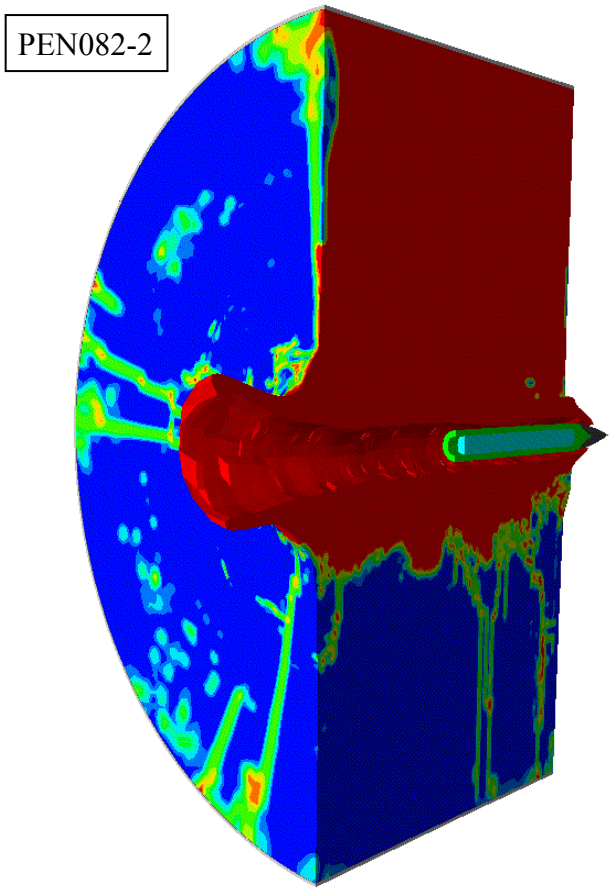

Figure 3.36. Damage and deformations for model PEN082-2 with 8.0 MPa strength of the concrete. The model use crack softening with Gf=180 J/m^2 and 5 mm element size for the target. The impact velocity is 420 m/s and the projectile mass is 4.53 kg for the model.

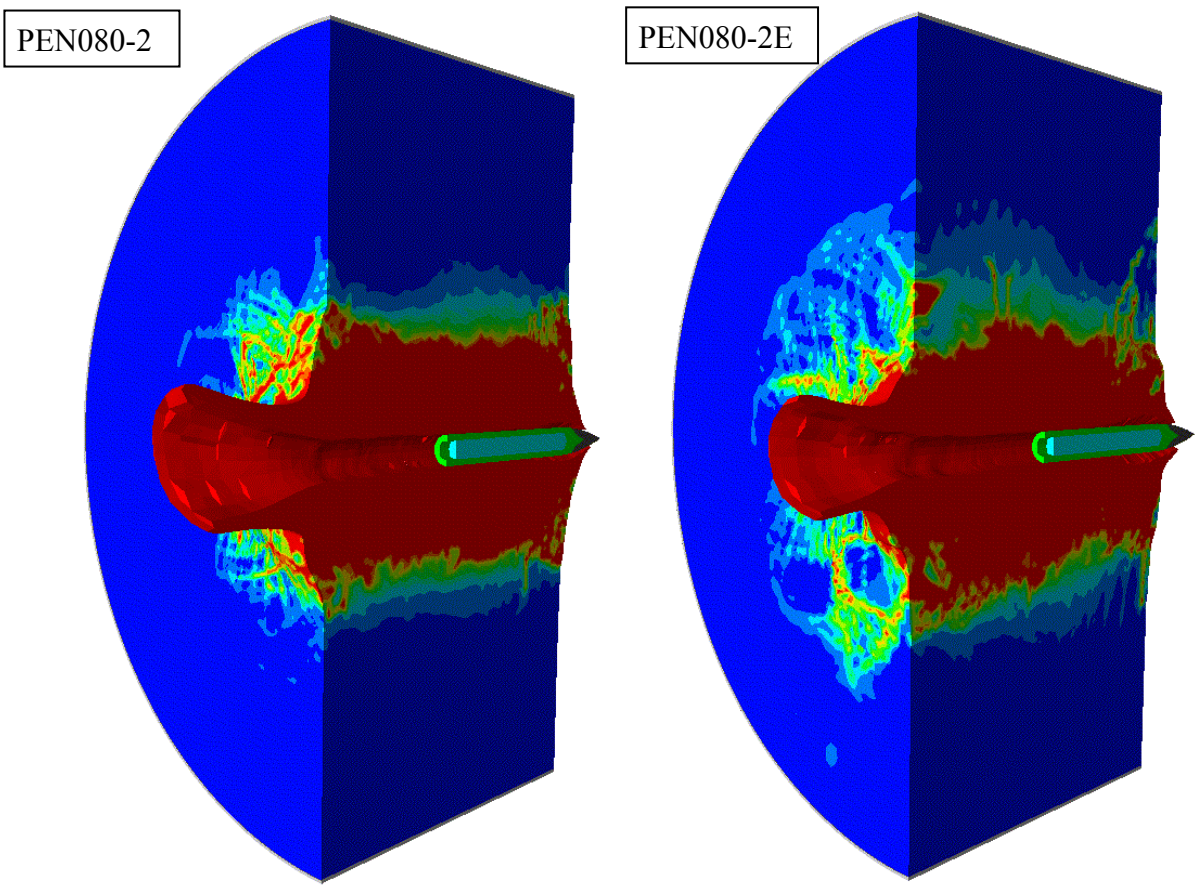

Figure 3.37. Damage and deformations for models PEN080-2 with 4.8 MPa tensile strength and PEN080-2E with 4.0 MPa tensile strength. The impact velocity and projectile mass are 420 m/s and 4.53 kg, respectively. Both models use 5 mm elements.

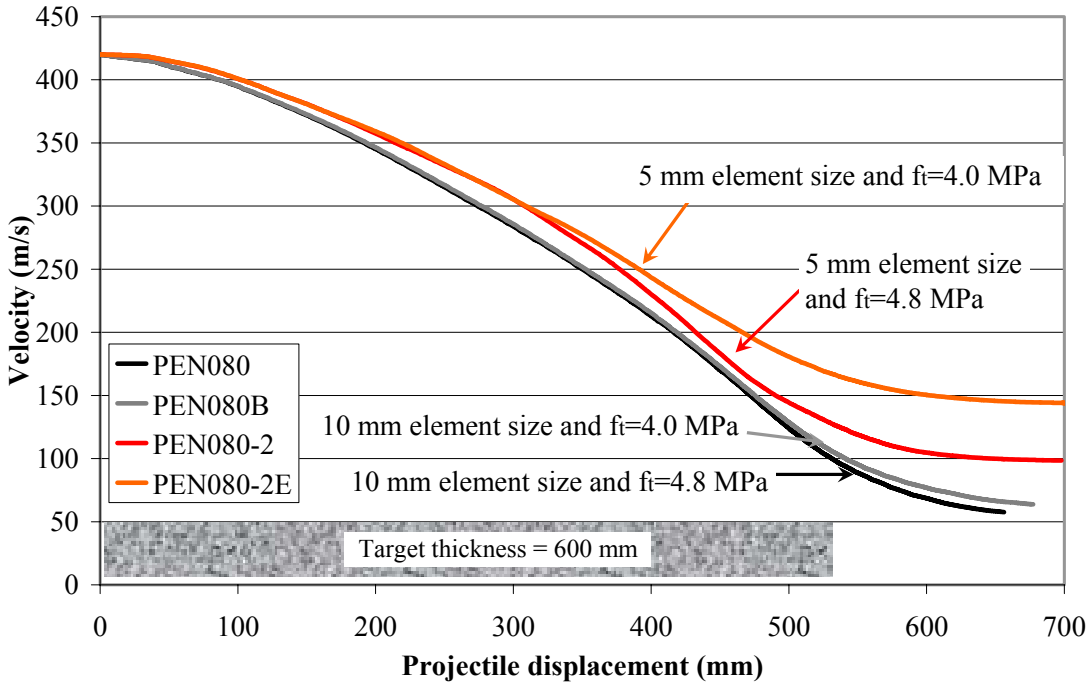

Figure 3.38. Velocity vs. penetration depth for simulations with different element sizes and tensile strengths of the concrete using the original RHT damage model. The projectile mass is 4.53 kg for both models. For details of the models see tables 3.23 and 3.25.

The influence of the compressive strength for the concrete is also studied by reducing the strength to 45 MPa, with a negligible influence on the exit velocity for the projectile. The influence of concrete strength for the models with 5 mm elements is shown in table 3.26.

Table 3.26. Simulations with different tensile and compressive strength of the concrete, and the use of the original RHT damage model and 5 mm element size.

	PEN080-2	**PEN080-2B**	**PEN080-2C**
Model symmetry	½	½	½
Target length	600 mm	600 mm	600 mm
Element size	5 mm	5 mm	5 mm
Projectile mass	4.53 kg	4.53 kg	4.53 kg
Impact velocity	420 m/s	420 m/s	420 m/s
Impact angle	90°	90°	90°
ρ_0	2.330 g/cm^3	2.330 g/cm^3	2.330 g/cm^3
P_{crush}	35.0 MPa	35.0 MPa	35.0 MPa
Tensile failure for concrete	Original RHT f_t= 4.8 MPa	Original RHT f_t= 4.0 MPa	Original RHT f_t= 4.0 MPa
Friction coefficient	μ=0.05	μ=0.05	μ=0.05
Comment	f_c= 48 MPa AD v. 5.0.02k	f_c= 48 MPa AD v. 5.0.02k	f_c= 45 MPa AD v. 5.0.02k
Exit velocity	98 m/s	155 m/s	154 m/s
Decrease of kinetic energy for projectile	94.6%	86.5%	86.6%
Energy error	-15.1%	-13.6%	-13.7%

Influence of stochastic tensile failure conditions for the concrete
Simulations are performed to study the behaviour of a stochastic variation on the tensile failure strength for the elements in the target. The probability of failure shown vs. the normalised tensile strength is shown in figure 3.39 for three values of the stochastic variance (γ).

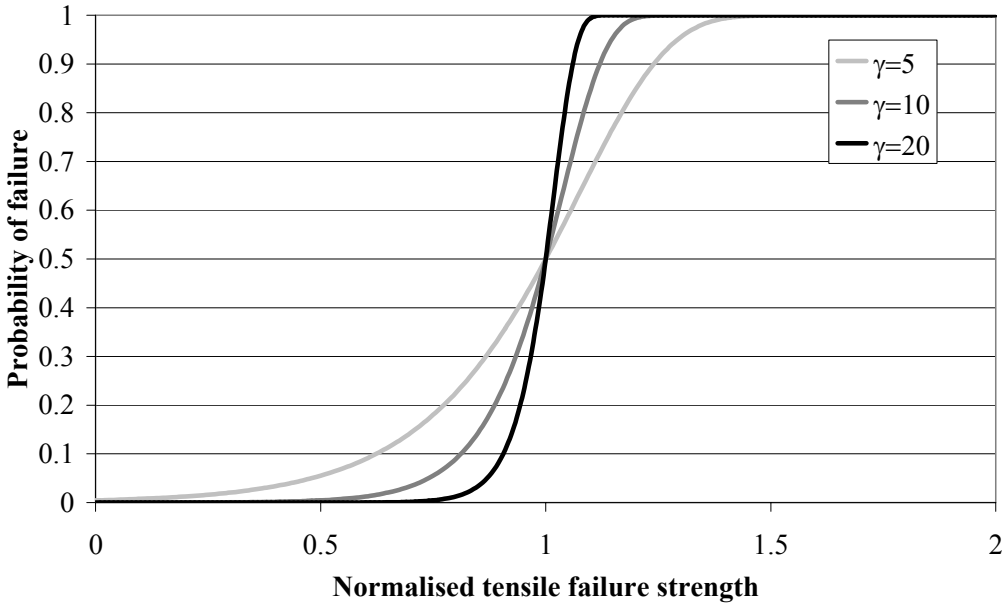

Figure 3.39. Probability of failure for varying γ vs. normalised tensile strength, i.e. $f_t/f_{t,\ average}$.

The simulations with the use of stochastic tensile failure, i.e. models PEN092 and PEN093, produced almost an identical exit velocity for the projectile when compared to a model that uses the same tensile failure strength for all elements in the model, i.e. PEN082. The models are compiled in table 3.27. However, there is a minor change in the location of damage zones/areas between the two models, see figures 3.40 and 3.41.

Table 3.27. Simulations of perforation using stochastic failure strength and with friction between target and projectile. The stochastic variation is given by the parameter γ.

	PEN082	**PEN092**	**PEN093**
Model symmetry	½	½	½
Target length	600 mm	600 mm	600 mm
Element size	10 mm	10 mm	10 mm
Projectile mass	4.53 kg	4.53 kg	4.53 kg
Impact velocity	420 m/s	420 m/s	420 m/s
Impact angle	90°	90°	90°
ρ_0	2.330 g/cm^3	2.330 g/cm^3	2.330 g/cm^3
P_{crush}	35.0 MPa	35.0 MPa	35.0 MPa
Tensile failure for concrete	Crack softening [d] with f_t= 8 MPa and Gf=180 J/m^2 No bulking [b]	Crack softening [d] with f_t= 8 MPa and Gf=180 J/m^2 No bulking [b]	Crack softening [d] with f_t= 8 MPa and Gf=180 J/m^2 No bulking [b]
Friction coefficient	μ=0.05	μ=0.05	μ=0.05
Comment	AD v. 5.0.01c	Stochastic failure with γ=10 AD v. 5.0.01c	Stochastic failure with γ=20 AD v. 5.0.01c
Exit velocity	164 m/s	164 m/s	162 m/s
Decrease of kinetic energy for projectile	84.8%	84.8%	85.1%
Energy error	-12.5%	-12.2%	-12.9%

Note: [b] No bulking - Associative flow in π-plane combined with non-associative flow in meridional plane for the crack softening option.

[d] Increased values for tensile and shear strength used for the RHT model to avoid influence on crack softening failure, f_t/f_c= 0.3 and f_s/f_c= 0.5.

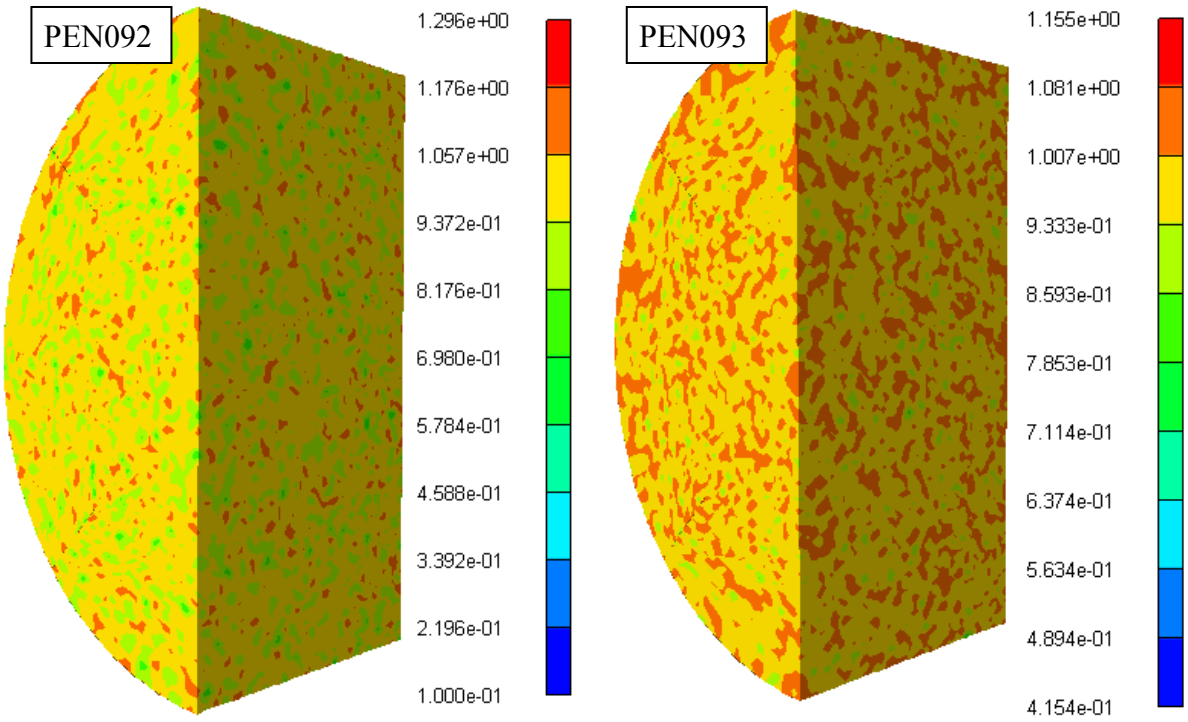

Figure 3.40. Normalised failure strength for models with γ=10 (left) and γ=20.

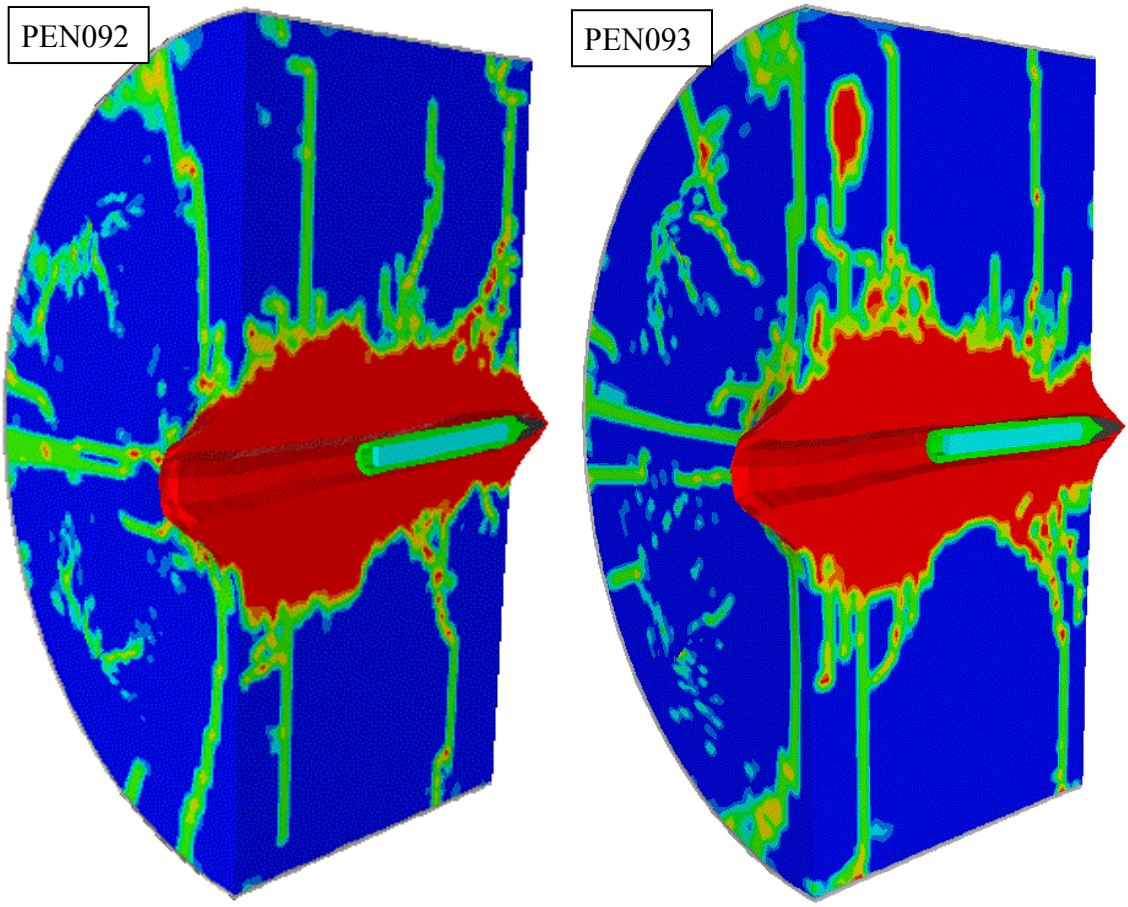

Figure 3.41. Damage and deformations for models PEN092 (left) and PEN093 (right) with varying stochastic variance. The projectile mass is 4.53 kg and the impact velocity is 420 m/s for both models.

3.1.3. Simulations of inclined targets with 0.54 to 0.60 m thickness

Simulations are performed with inclined unreinforced targets, as earlier shown simulations with 3.64 kg projectile and the 1.20 m target. The angle between the front face of the target and the projectile is 60°. The test in appendix 3 showed that in principle the 4.50 kg projectile with a nominal velocity of 420 m/s is close to the ballistic limit for this target, with one penetrator stopped in the target and one barely penetrating the target. Therefore, an attempt to calculate the required thickness for an inclined target to stop this penetrator at an impact velocity of 420 m/s is performed.

These simulations are performed with an element size of 5 mm in the central part of the target to reduce the number of elements. The models also use half symmetry to reduce the number of elements and the required simulation time. The diameters of the targets are 1.50 m. Figure 3.42 shows the geometry for the simulations. All these simulations use the increased yield strength, i.e. 2.50 GPa, for the nose of the penetrator. This is to avoid extensive deformation of the nose elements in the projectile.

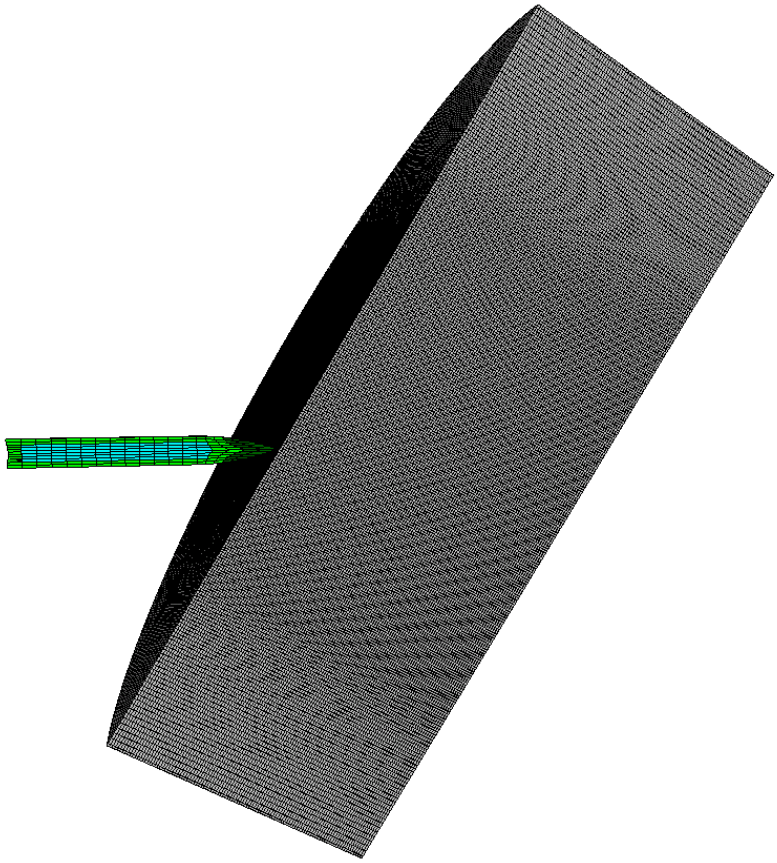

Figure 3.42. Geometry for simulations of inclined unreinforced concrete targets, with the model with 0.54 m thick target shown.

The simulations of unreinforced inclined concrete targets are compiled in table 3.28. The target thicknesses varies from 0.54 m to 0.60 m. The target with 0.54 m thickness is of the same thickness used for the tests of inclined targets, and the thickness is then increased. The damage and deformations for the models with 0.54 and 0.60 m thickness are shown at a few times after impact in figures 3.43 and 3.44. The velocity vs. the projectile displacement for varying target thicknesses are shown in figure 3.45.

Table 3.28. Simulations of inclined concrete targets with thickness between 0.54 and 0.60 m.

	PEN600-B	**PEN602-B**	**PEN603-B**	**PEN601-B**
Model symmetry	½	½	½	½
Target length	540 mm	567 mm	589 mm	600 mm
Element size	5 mm	5 mm	5 mm	5 mm
Projectile mass	4.53 kg	4.53 kg	4.53 kg	4.53 kg
Impact velocity	420 m/s	420 m/s	420 m/s	420 m/s
Impact angle	60°	60°	60°	60°
ρ_0	2.314 g/cm^3	2.314 g/cm^3	2.314 g/cm^3	2.314 g/cm^3
P_{crush}	35.0 MPa	35.0 MPa	35.0 MPa	35.0 MPa
Tensile failure for the concrete	Original RHT f_t= 4.0 MPa	Original RHT f_t= 4.0 MPa	Original RHT f_t= 4.0 MPa	Original RHT f_t= 4.0 MPa
Friction coefficient	μ=0.05	μ=0.05	μ=0.05	μ=0.05
Comment	AD v. 5.0.02k	AD v. 5.0.02k	AD v. 5.0.02k	AD v. 5.0.02k
Penetration depth [b]	---	---	>479 mm [c]	445 mm
Exit velocity	117 m/s	≈57 m/s	<8.0 m/s [c]	---
Decrease of kinetic energy for projectile	92.4%	98.2%	>99.9% [c]	100%
Energy error	-10.4%	-11.2%	-11.4%	-11.6%

Note: [b] Measured from the front face of the target.
[c] Simulation terminated after 5.6 ms

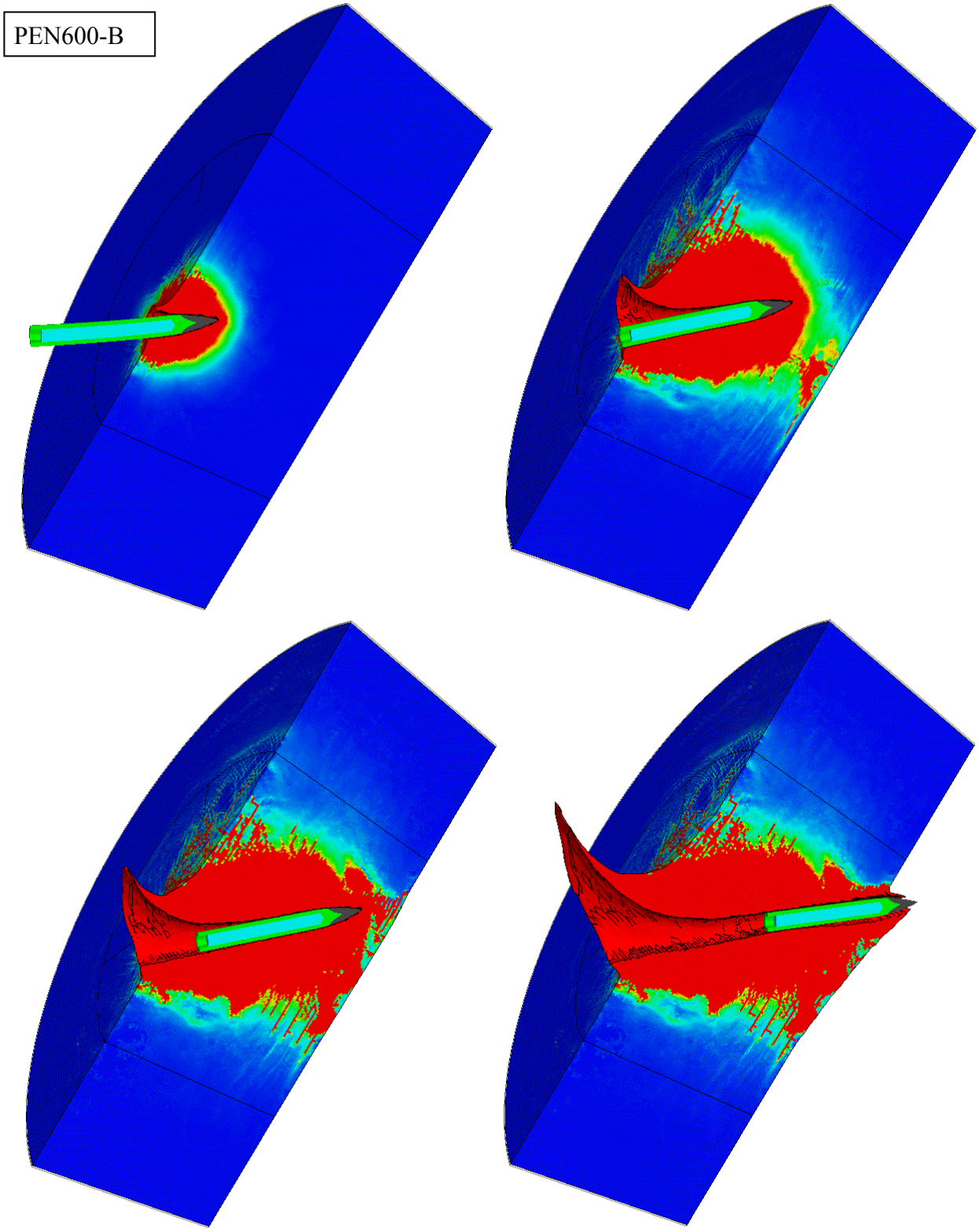

Figure 3.43. Damage and deformations for model PEN600-B at 0.4, 1.2, 2.0 and 4.0 ms after impact.

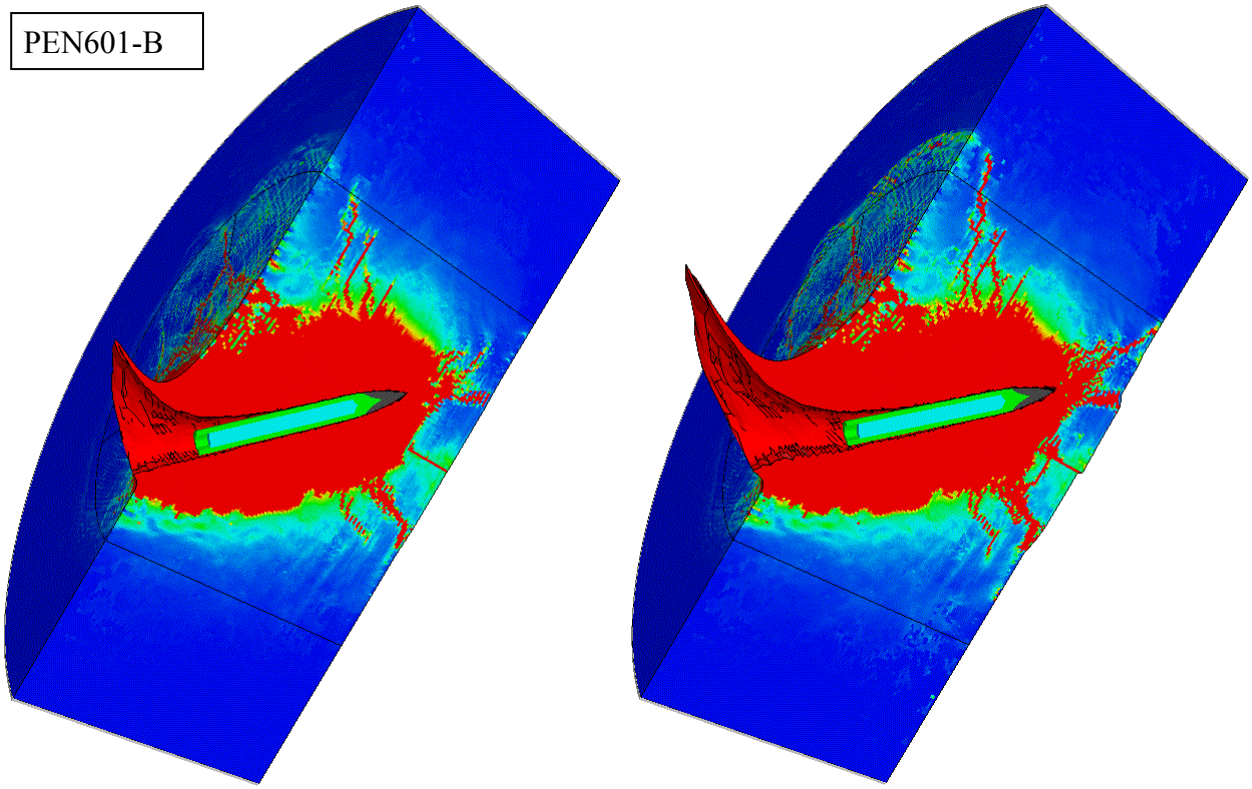

Figure 3.44. Damage and deformations for model PEN601-B at 2.0 and approximately 3.9 ms after impact.

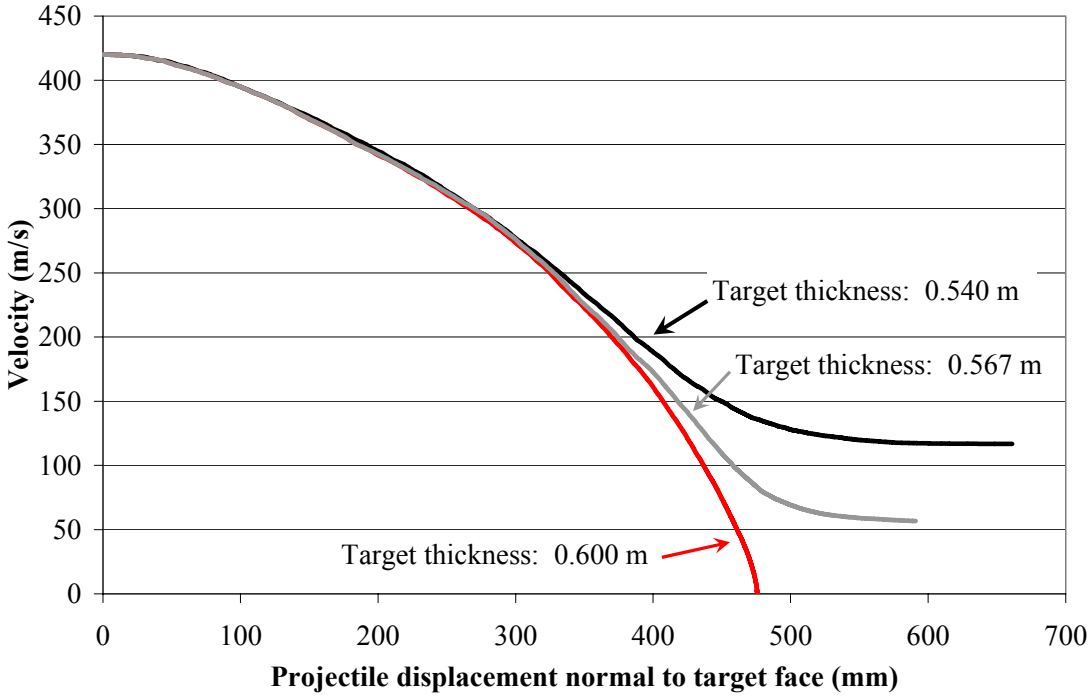

Figure 3.45. Calculated velocity for projectile penetration into an inclined concrete targets vs. projectile displacement.

3.2. Simulations of penetration in reinforced concrete targets

The reinforced concrete targets are simulated with the use of beam elements representing the reinforcement and solid Lagrange elements representing the concrete. The beam elements are joined to the coinciding solid elements in the concrete target. The main contribution to increased performance due to the reinforcement in a concrete target is the prevention of tensile failure in the concrete, and the direct contact between the projectile and reinforcement may be of secondary interest. Relatively short element lengths are used for the beam elements, this is caused by the necessity to have identical locations of nodes in the concrete and reinforcement to be able to join these in the model. See previous chapter 3.1 regarding un-reinforced targets for details regarding concrete modelling.

Depending on the used element size/length it is necessary to adjust the stress-strain relationship after necking of the test sample or reinforcement bar. This is due to the non-uniform strain field caused by the localised deformations during large deformations of the reinforcement, i.e. a decrease of the gauge length results in an increase of the measured strain. Therefore, a failure strain that corresponds to an elongation of 0.6 to 0.8 might be more suitable for the used element length. However, only a few reinforcement bars in the model close to the path of the projectile will be subjected to large strains. Therefore, a failure strain that corresponds to the elongation at the ultimate strain is chosen for the initial model with beam elements for the steel bars. The stress-strain relationships that are used for the reinforcement are shown in figure 3.46. Initially the strain rate dependence is not considered, see also appendix 2.2 for further discussion regarding the properties of reinforcement bars.

The simulations with reinforced targets use the default initial density of 2314 kg/m^3, and an initial compaction pressure of 23.3 or 35.0 MPa. Simulations are performed both with normal impact of the projectiles, and with inclined targets. All these simulations use the increased yield strength, i.e. 2.50 GPa, for the nose of the penetrator. This is to avoid extensive deformation of the nose elements in the projectile. Yaw/pitch is 0° for all the simulations of reinforced targets.

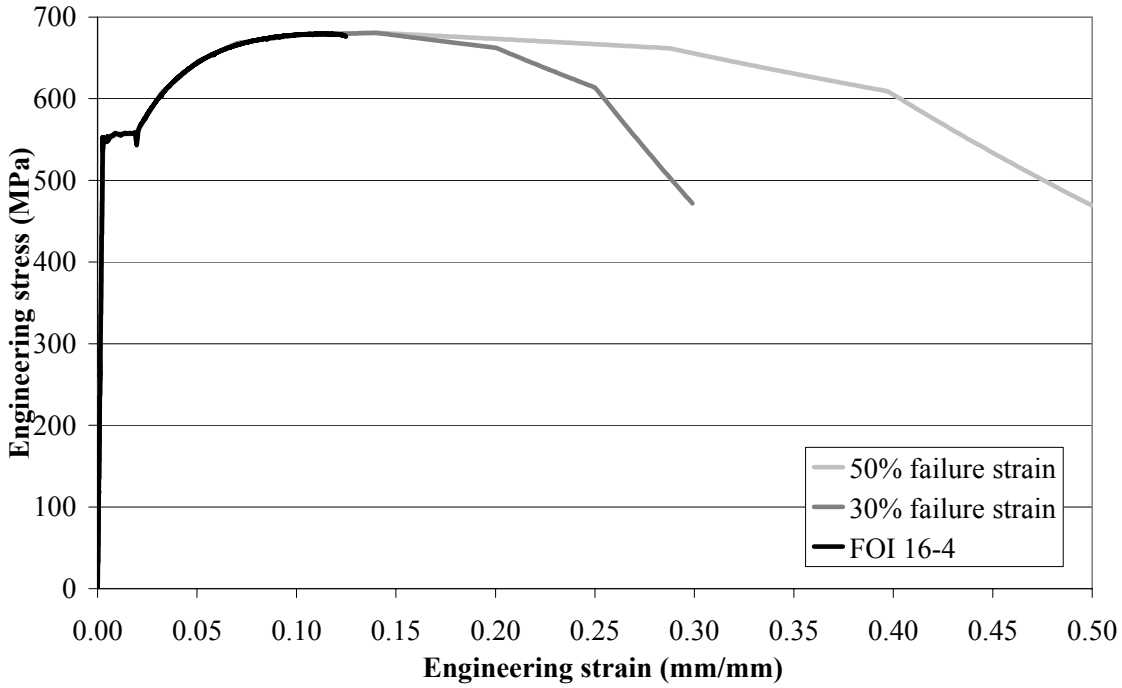

Figure 3.46. Stress-strain relationship used for reinforcement bars in the models.

3.2.1. Normal impact of reinforced concrete targets.

A short descriptions of the models of reinforced concrete targets are given in table 3.29 below. Two different element sizes is used for the central part of the target.

Table 3.29. Target geometry for Lagrange models with reinforcement bars.

Target type		**Cylindrical target**	**Reinforced targets**	
Reinforcement		No	Yes	
Model symmetry		½ symmetry	None	
Target length	(mm)	600	600	
Concrete	Diameter/Side (mm)	1200	1200	
	Element size (mm)	10	15×15×7.5	7.5×7.5×3.75
	No. of elements	324 000	512 000	1 792 000
Steel cylinder	Thickness	5 mm	---	
	No. of elements	7 200	---	
Reinforcement	No. of rebars	---	239	
	No. of elements	---	17 968	
	Type of elements	---	Beams with bending solution	
	Length of beam elements [a] (mm)	---	7.5 and 15	
Time step		$\approx 3.5\times10^{-5}$ ms	$\approx 3.5\times10^{-5}$ ms	
Model id.		e.g. PEN023B	e.g. PEN224	e.g. PEN242

Note: [a] The rebars are divided into elements with equal length along each beam, with the short 7.5 mm elements used for the reinforcement parallel to the projectile path.

Introducing reinforcement into models

A reinforcement cage for a concrete target is shown in figure 3.47, with a drawing of the same reinforcement cage shown in figure 3.48. The reinforcement is of B500BT type 1 grade, and nominal diameter is 14 mm. The reinforcement layers consist of 19 bars in each direction with a centre to centre distance of 60 mm. The cover of concrete for the first and last reinforcement layers are approximately 30 mm, and layer two to four are then distributed equally along the length of the target. The individual reinforcement layers are welded to longitudinal reinforcement with a centre to centre distance of 180 mm. As can be seen in figure 3.48, layer no. 2 and 4 of the reinforcement are shifted 28 mm sideways. This applies to the bars in both directions for these layers. This is to avoid a clear path for a projectile through the target at impact angles close to normal impact.

The simplified mesh that is used for the reinforcement in the simulations is shown in figure 3.49.

Figure 3.47. Example of a welded reinforcement cage for a 1.2×1.2×0.6 m target used in tests performed during 2004.

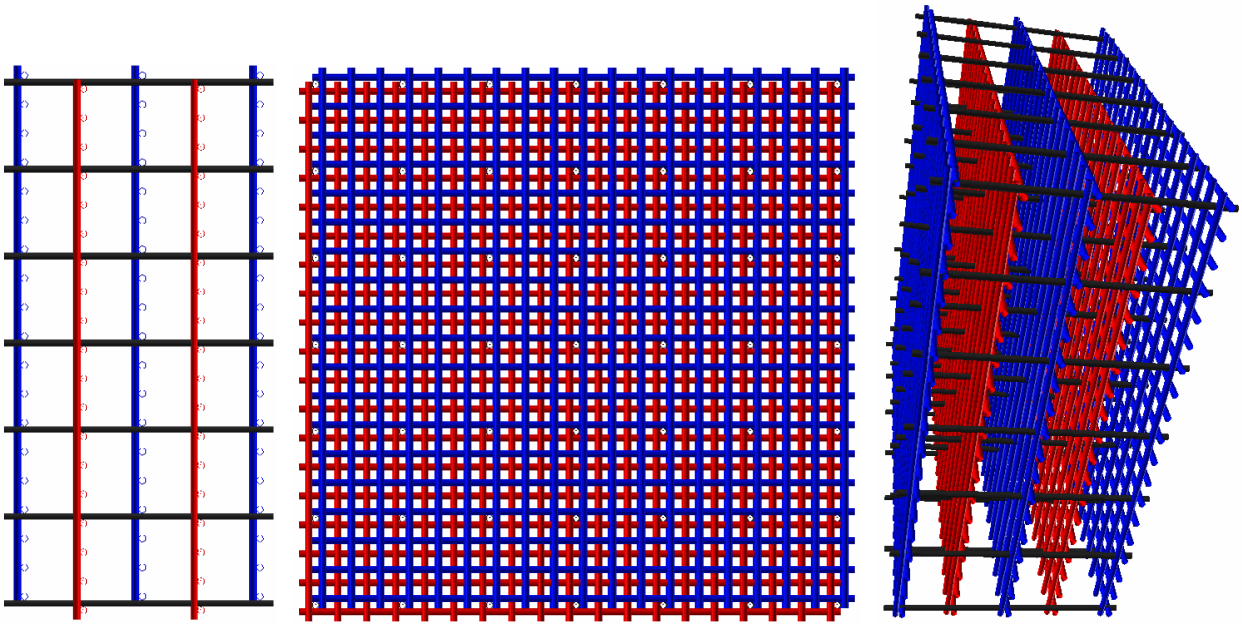

Figure 3.48. Location of reinforcement for a 1.2×1.2×0.6 m target, from left is side view, front view and a perspective view shown.

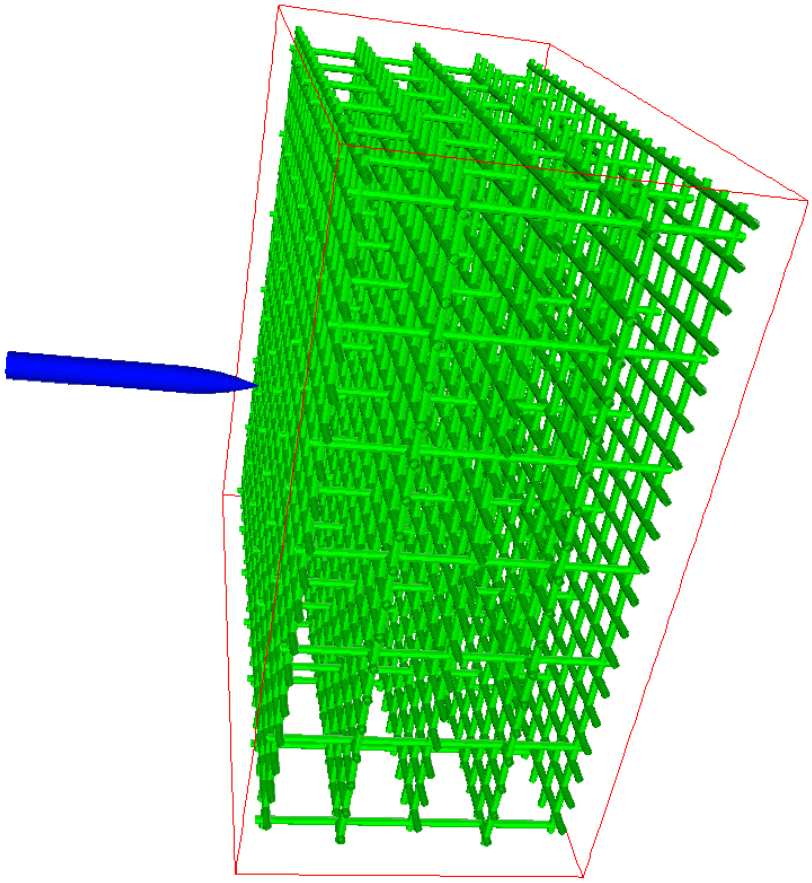

Figure 3.49. Simplified reinforcement mesh for model of a 1.2×1.2×0.6 m target.

The result from the initial simulation with beam elements for the reinforcement (PEN224) is shown in table 3.30 below. Results from an earlier simulation with a cylindrical target, and a concrete target where the beam elements are removed, are also given in this table. Damage and deformations for the model PEN223 without reinforcement are shown in figure 3.50, with scale for damage plots of concrete shown to the right. This scale is used for all damage plots in the report. Damage and deformations for the model PEN224 with reinforcement are shown in figure 3.51, with a close up shown in figure 3.52. The velocity of the projectiles vs. penetration depths for the models are shown in figure 3.53. The kinetic energy for the penetrator is reduced by approximately 24% with the introducing of reinforcement for the target. However, the exit velocities for these two cases are too high when compared to the test results in appendix 3. Further simulations are therefore performed to study the influence of reinforcement strength, friction concrete strength and element size.

Table 3.30. Lagrange simulations with and without reinforcement, and without friction between projectile and target.

	PEN023B	**PEN223**	**PEN224**
Model symmetry	½	None	None
Target cross section	Cylindrical	Square	Square
Target length	600 mm	600 mm	600 mm
Element size	10 mm	15×15×7.5 mm	15×15×7.5 mm
Boundary condition [a]	5 mm steel pipe	Free surface	Free surface
Projectile mass	4.53 kg	4.53 kg	4.53 kg
Impact velocity	420 m/s	420 m/s	420 m/s
Impact angle	90°	90°	90°
P_{crush}	23.3 MPa	23.3 MPa	23.3 MPa
Tensile failure for concrete	Original RHT f_t= 4.8 MPa	Original RHT f_t= 4.8 MPa	Original RHT f_t= 4.8 MPa
Friction coefficient	μ=0	μ=0	μ=0
Comment	No reinforcement AD v. 5.0.02c	No reinforcement AD v. 4.3.02	Reinforcement as beam elements with 50% failure strain AD v. 5.0.02c
Exit velocity	156 m/s	213 m/s	≈58 m/s
Penetration depth	---	---	---
Decrease of kinetic energy for projectile	86.2%	74.3%	98.1%
Energy error	-1.4%	-1.9%	-1.9%

Note: [a] Displacement of target in axial direction is free for all cases.

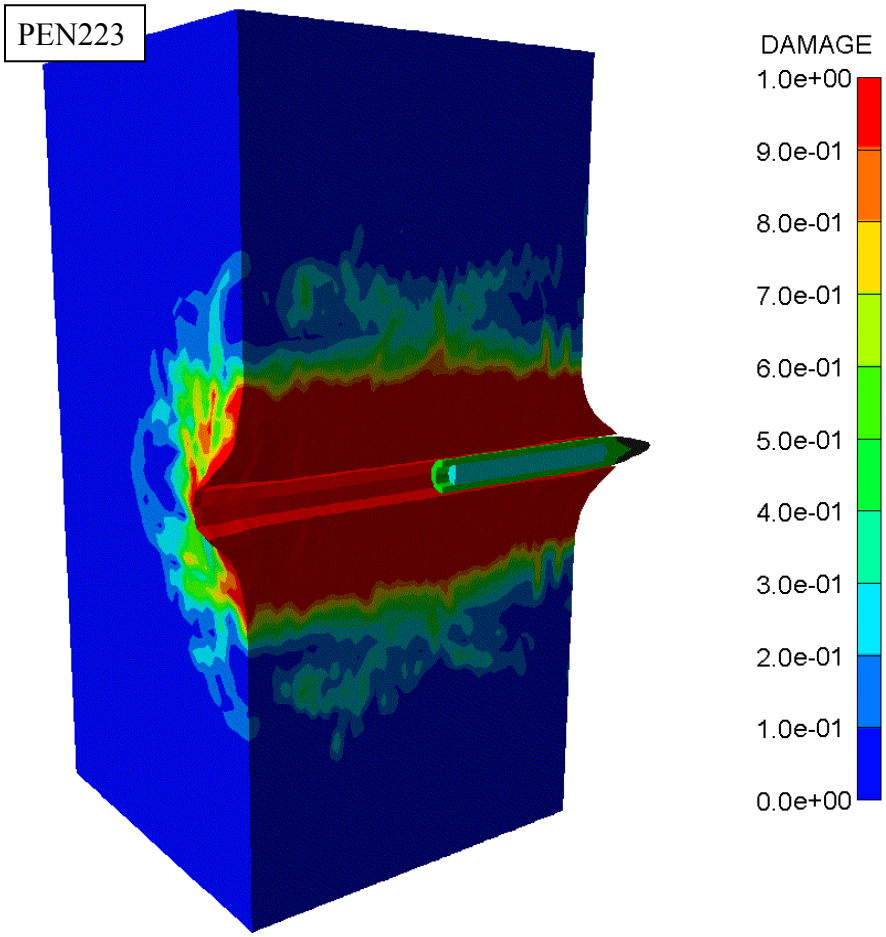

Figure 3.50. Model PEN223 without reinforcement shown 2.8 ms after impact.

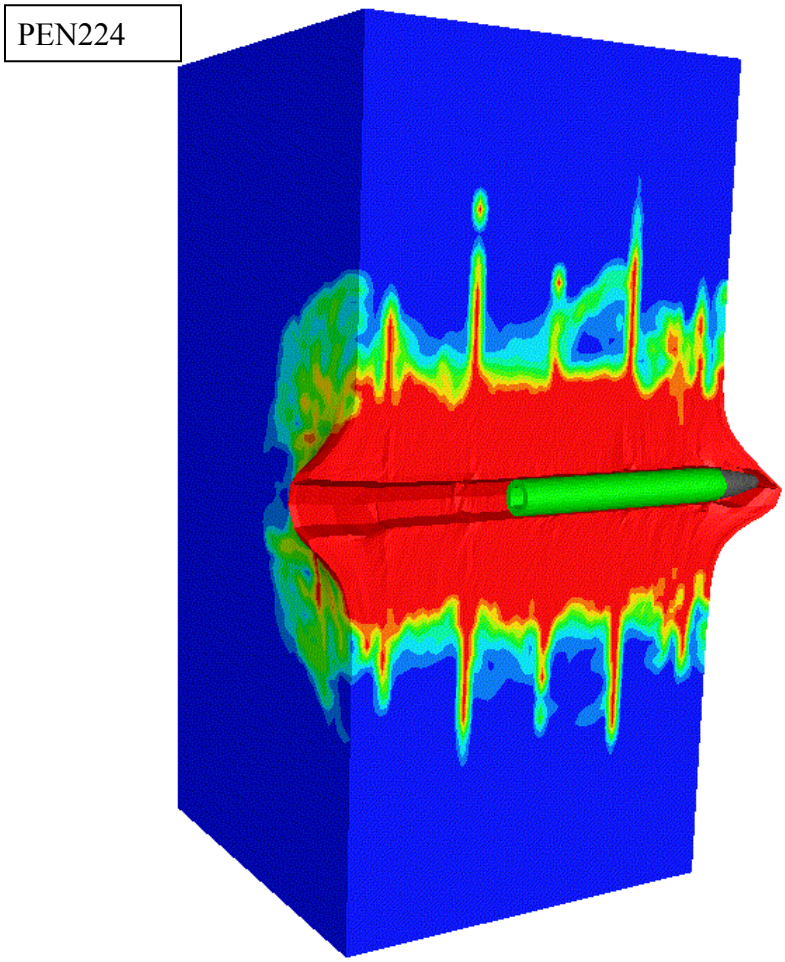

Figure 3.51. Model PEN224 with reinforcement shown 4.0 ms after impact.

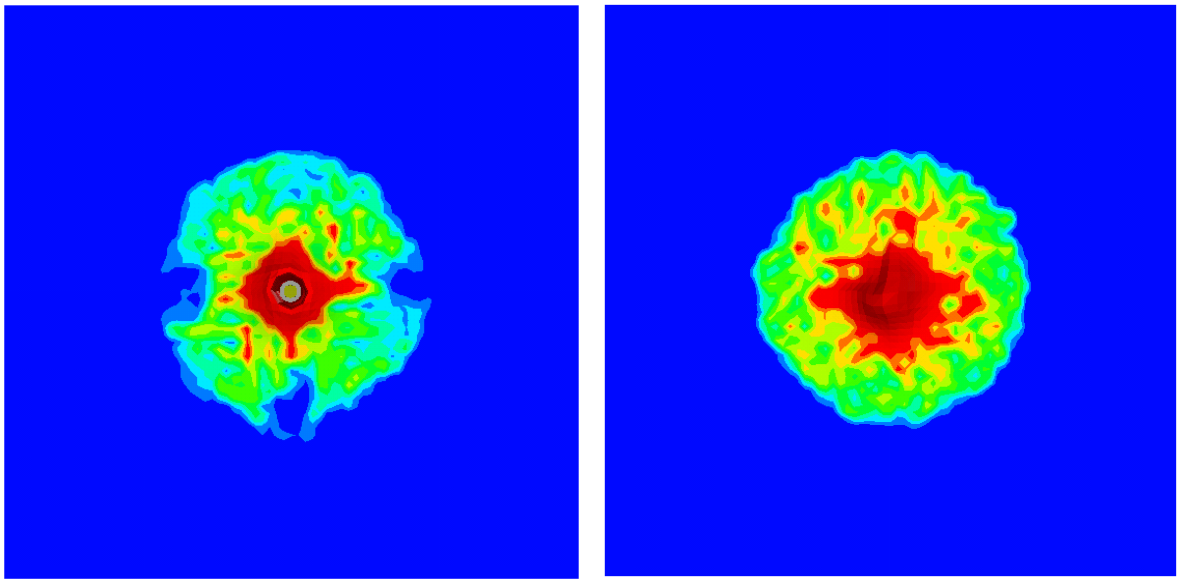

Figure 3.52. Front and back side of model PEN224 with reinforcement shown 4.0 ms after impact.

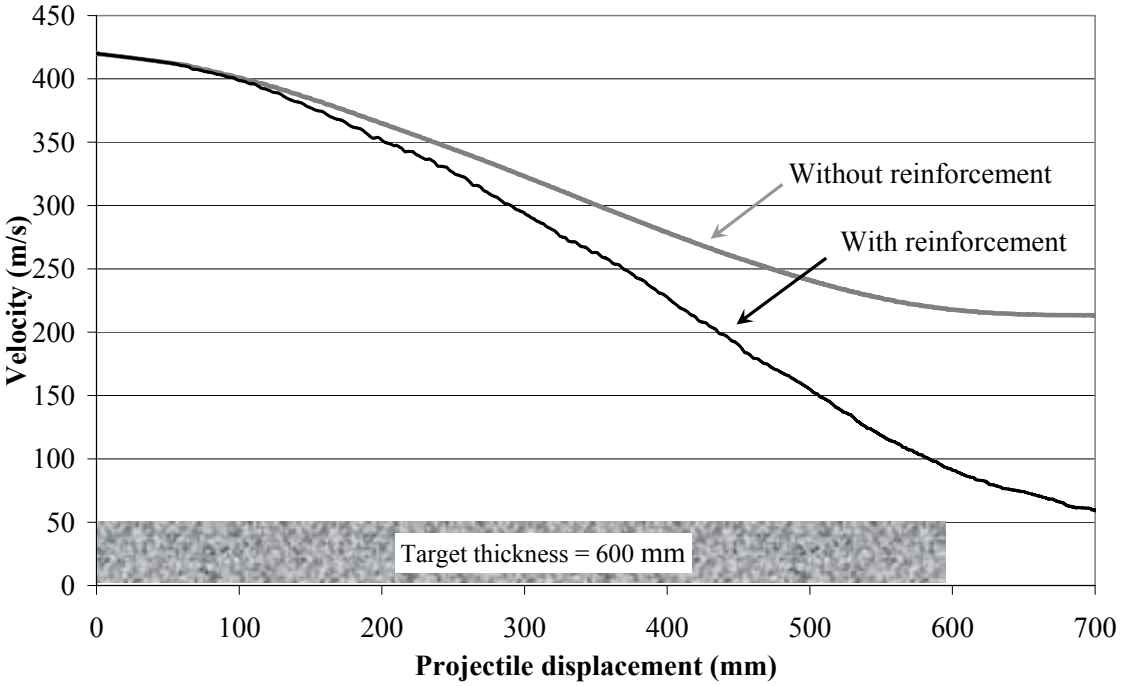

Figure 3.53. Projectile velocity vs. penetration for models PEN223 and PEN224, with and without reinforcement. Both model use 15×15×7.5 mm elements and the original damage evolution for the RHT model with f_t=4.8 MPa.

Influence of reinforcement properties and friction

The influence of strain rate enhancement for the reinforcement is investigated by introducing a strain rate factor into the material model, see appendix 2.2. A value of 0.014 is used for the strain rate constant C in model PEN226. This value is assumed based on the behaviour of 4340 steel with the yield strength 792 MPa (Johnson and Cook, 1983). The influence of this strain rate parameter on the deceleration of the projectile is negligible, and the reason for this is that only parts of the reinforcement close to the projectile is subjected to deformations at a strain rate higher than 1 s^{-1}. The maximal strain rate for these beam elements close to the projectile path are approximately in the order of 2×10^3 s^{-1}.

A modified stress-strain relationship for the reinforcement for strain rate 1 s^{-1} is also used, this material model are based on the quasi-static test data for the B500BT steel and dynamic behaviour for reinforcement reported by Malvar and Crawford (1998). Increases of 25% and 5% are assumed for the yield strength and ultimate strength, respectively. The modified stress-strain relationship is shown in figure 3.54 below, and is used for simulation identity PEN228 and later also PEN229 with the use of friction between penetrator and target.

These simulations are compiled in table 3.31. A damage and deformation plot for the model with increased yield strength of the reinforcement is shown in figure 3.55, with a comparison of projectile velocity vs. penetration for different yield strength of the concrete shown in figure 3.56.

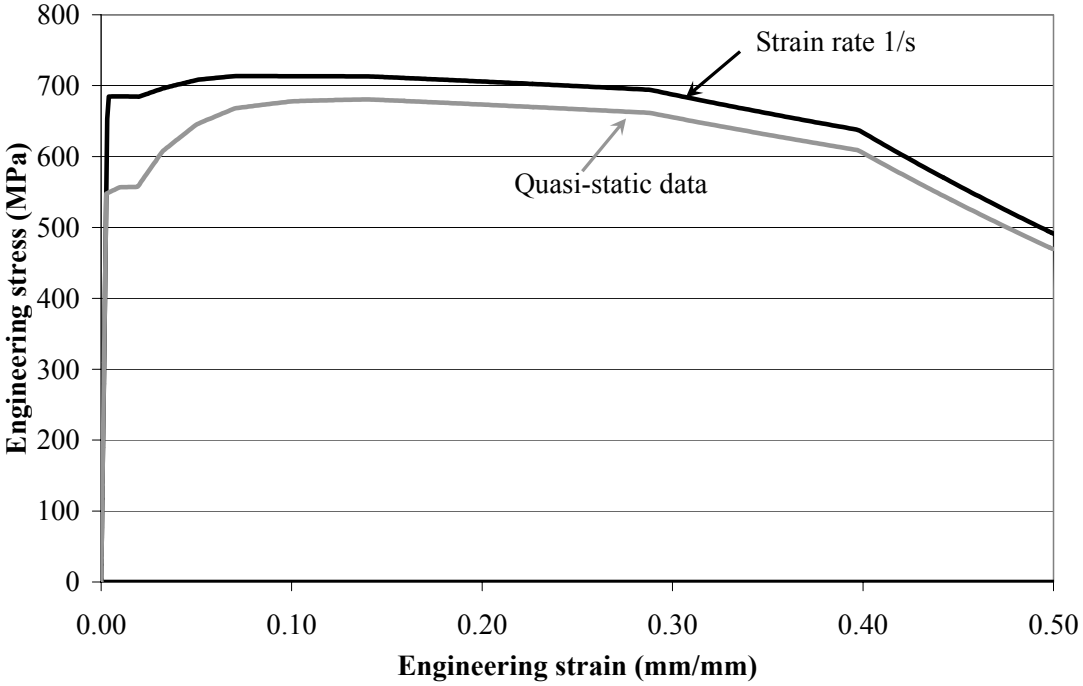

Figure 3.54. Assumed stress-strain relationship for the reinforcement at strain rate 1 s^{-1}, compared with quasi-static data for strain rate 0.0003 s^{-1}.

Table 3.31. Simulations with reinforced concrete target with varying strain rate enhancement for the rebars. No friction used between projectile and target.

	PEN224	**PEN226**	**PEN228**
Model symmetry	None	None	None
Target cross section	Square	Square	Square
Target length	600 mm	600 mm	600 mm
Element size	15×15×7.5 mm	15×15×7.5 mm	15×15×7.5 mm
Boundary condition [a]	Free surface	Free surface	Free surface
Projectile mass	4.53 kg	4.53 kg	4.53 kg
Impact velocity	420 m/s	420 m/s	420 m/s
Impact angle	90°	90°	90°
P_{crush}	23.3 MPa	23.3 MPa	23.3 MPa
Tensile failure for concrete	Original RHT f_t= 4.8 MPa	Original RHT f_t= 4.8 MPa	Original RHT f_t= 4.8 MPa
Friction coefficient	μ=0	μ=0	μ=0
Comment	Reinforcement with 50% failure strain AD v. 5.0.02c	Reinforcement, with strain rate enhancement C=0.014 AD v. 5.0.02c	Reinforcement with increased yield strength AD v. 5.0.02c
Exit velocity	≈58 m/s	≈57 m/s	≈44 m/s
Penetration depth	---	---	---
Energy error	-1.9%	-1.9%	-1.9%

Note: [a] Displacement of target in axial direction is free for all cases.

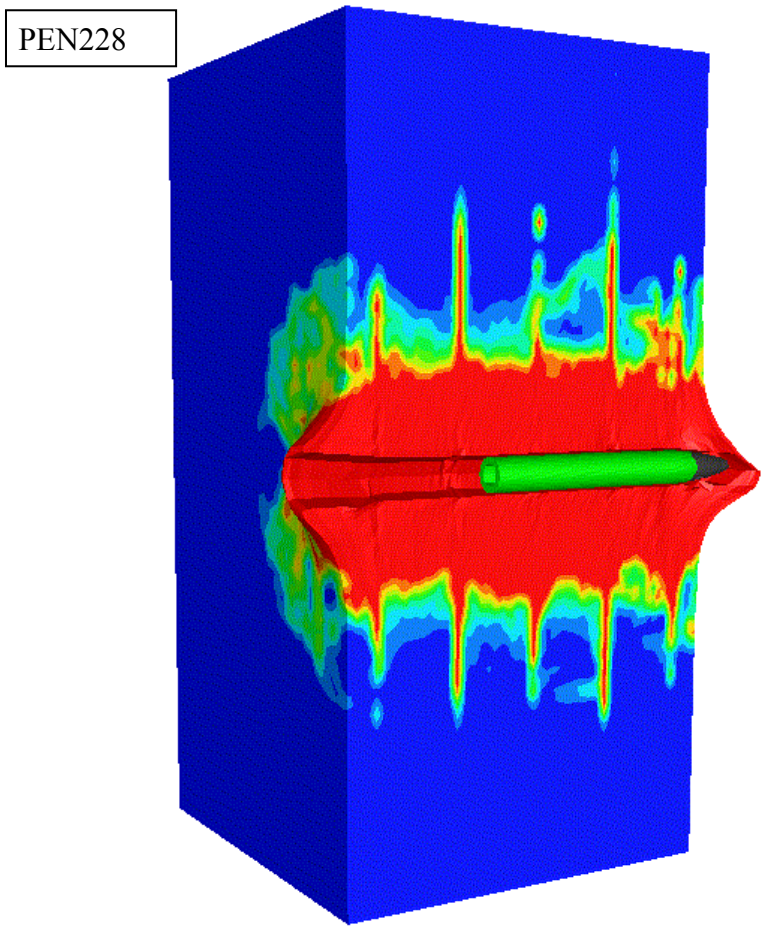

Figure 3.55. Model PEN228 with reinforcement shown 4.0 ms after impact.

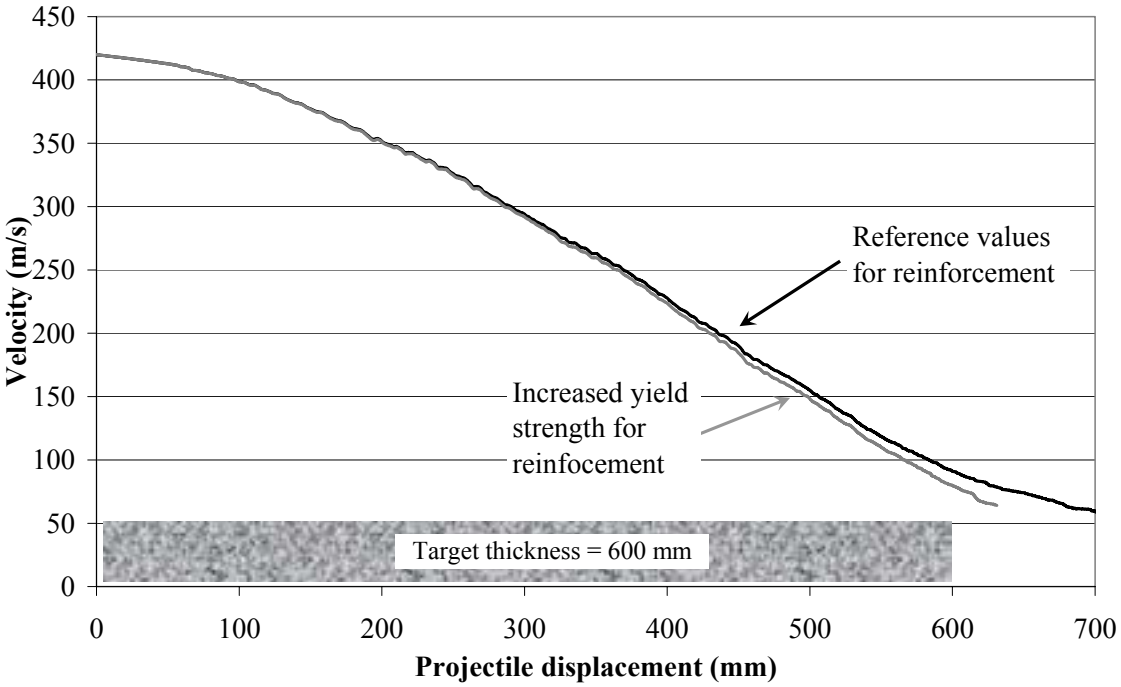

Figure 3.56. Influence of increased yield strength for reinforcement on the projectile velocity vs. penetration for models without friction, i.e. PEN224 and PEN228 is compared. Both models use 15×15×7.5 mm element size.

The influence of friction is studied by introducing a friction coefficient in the same way as for the unreinforced targets earlier. The result of this is that the penetrator is stopped in the target, and the penetration is further decreased by increasing the friction coefficient. These simulations are compiled in table 3.32, with damage and deformation plots shown in figures 3.57 to 3.59. The projectile velocity vs. penetration depth is shown for these models in figure 3.60.

Table 3.32. Simulations of reinforced concrete targets with varying reinforcement properties and friction coefficient.

	PEN231	**PEN232**	**PEN229**
Model symmetry	None	None	None
Target cross section	Square	Square	Square
Target length	600 mm	600 mm	600 mm
Element size	15×15×7.5 mm	15×15×7.5 mm	15×15×7.5 mm
Boundary condition [a]	Free surface	Free surface	Free surface
Projectile mass	4.53 kg	4.53 kg	4.53 kg
Impact velocity	420 m/s	420 m/s	420 m/s
Impact angle	90°	90°	90°
P_{crush}	23.3 MPa	23.3 MPa	23.3 MPa
Tensile failure for concrete	Original RHT f_t= 4.8 MPa	Original RHT f_t= 4.8 MPa	Original RHT f_t= 4.8 MPa
Friction coefficient	μ=0.05	μ=0.10	μ=0.05
Comment	Reinforcement with 50% failure strain AD v. 5.0.02c	Reinforcement with 50% failure strain AD v. 5.0.02c	Reinforcement with increased yield strength AD v. 5.0.02c
Exit velocity	---	---	---
Penetration depth	537 mm	465 mm	524 mm
Energy error	-15.3%	-24.1 %	-15.0%

Note: [a] Displacement of target in axial direction is free for all cases.

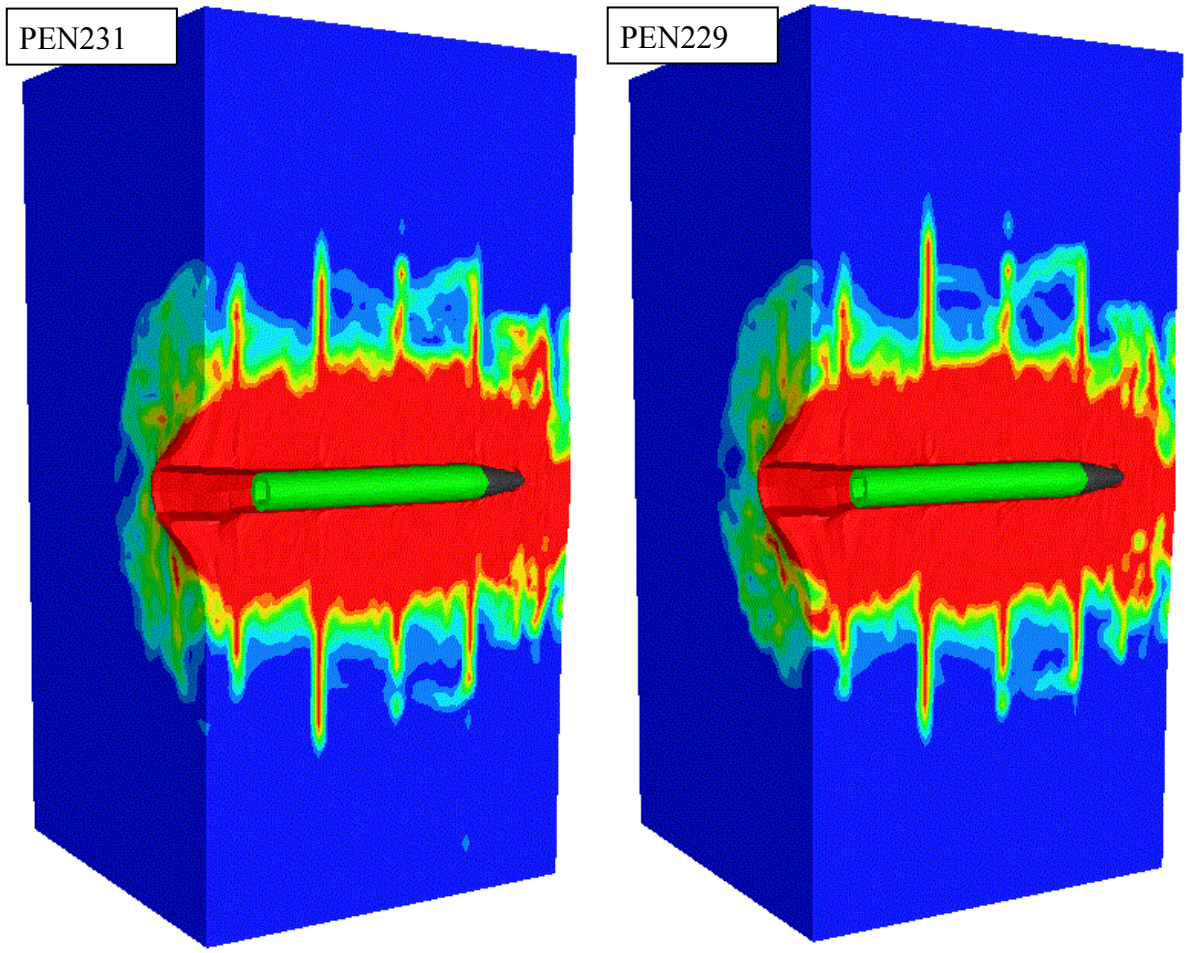

Figure 3.57. Models PEN231 and PEN229 with reinforcement shown 3.2 ms after impact.

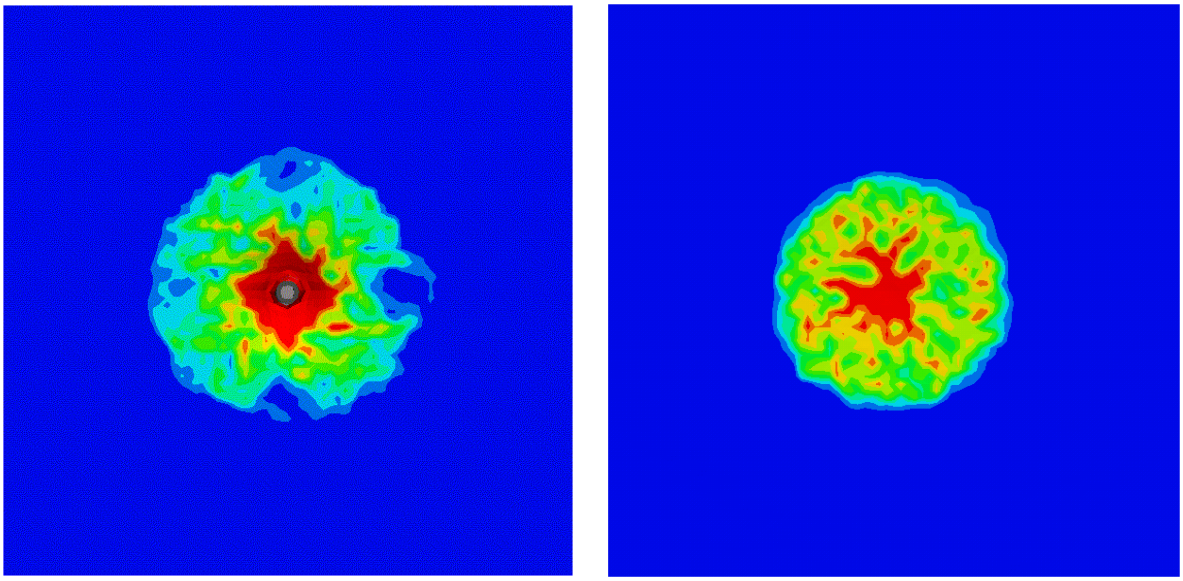

Figure 3.58. Front and back side of model PEN231 with reinforcement shown 3.2 ms after impact.

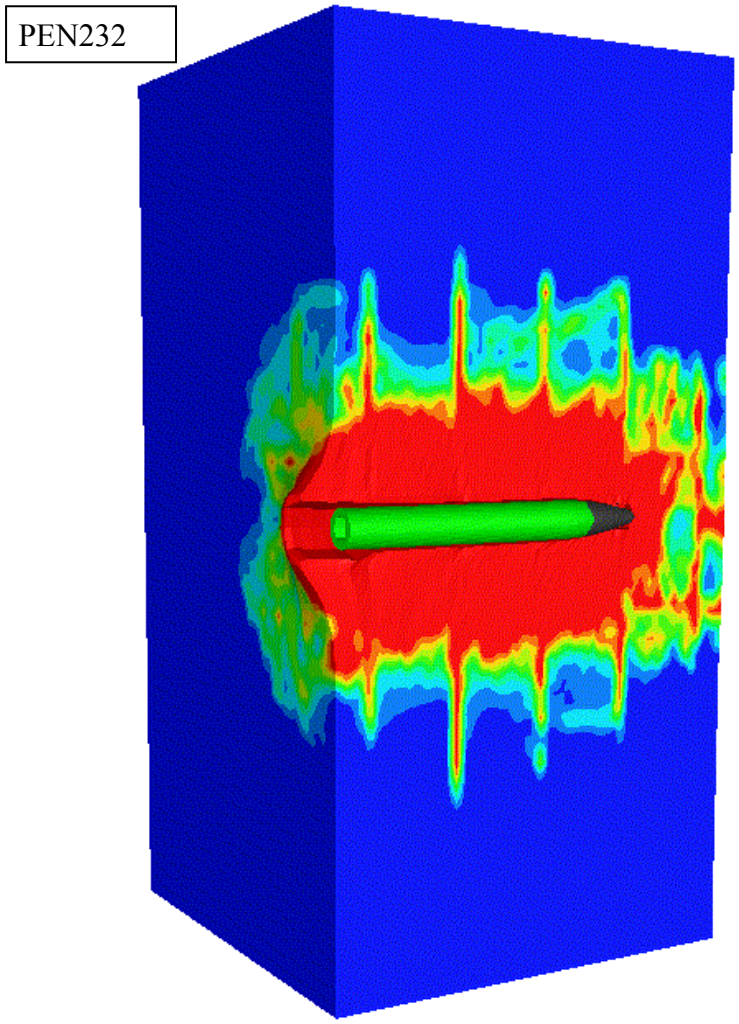

Figure 3.59. Model PEN232 with reinforcement shown 3.2 ms after impact.

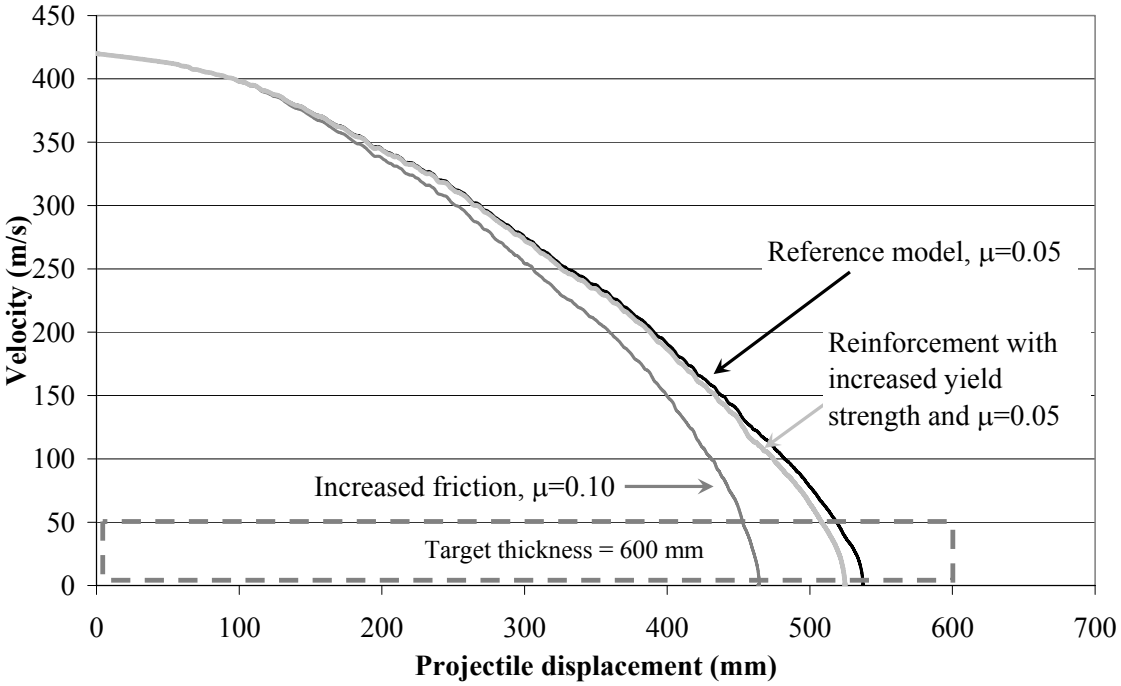

Figure 3.60. Projectile velocity vs. penetration for models with varying friction coefficient and yield strength of the reinforcement, i.e. PEN229, PEN231 and PEN232. All models with 15×15×7.5 mm elements.

Further, Malvar and Crawford (1998) also suggest the following simple equation to estimate the dynamic increase factors (DIF) for yield and ultimate strength for reinforcement bars;

$$DIF = \left(\frac{\dot{\varepsilon}}{1 \times 10^{-4}} \right)^{\alpha} \tag{1}$$

where for the yield stress;

$$\alpha_{fy} = 0.074 - 0.04 \frac{f_y}{414} \tag{2}$$

and for the ultimate yield stress;

$$\alpha_{fu} = 0.019 - 0.009 \frac{f_y}{414} \tag{3}$$

with strain rate given in s^{-1} and the stresses in MPa. The reference strain rate for this model is 1×10^{-4} s^{-1}, and the formulation are valid for strain rates between 1×10^{-4} and 225 s^{-1} and for rebars with static yield strengths (f_y), determined at the reference strain, between 290 and 710 MPa. The equations 1 and 2 above are used to estimate the strain rate enhancement constant C for the J&C piece-wise model for the reinforcement with a yield strength of 685 MPa at the strain rate 1 s^{-1}, this equals a yield strength of 581 MPa at the strain rate 0.0001 s^{-1} according to the equations above. The yield strength vs. strain rate for these models are shown in figure 3.61, and the J&C data for 4340 steel with similar yield strength is also shown for comparison (Johnson and Cook, 1983). An improved model for the strain rate dependency of the yield strength for reinforcement is currently implemented at FOI. This material model is used for simulations of reinforced concrete structures (Magnusson and Hansson, 2005).

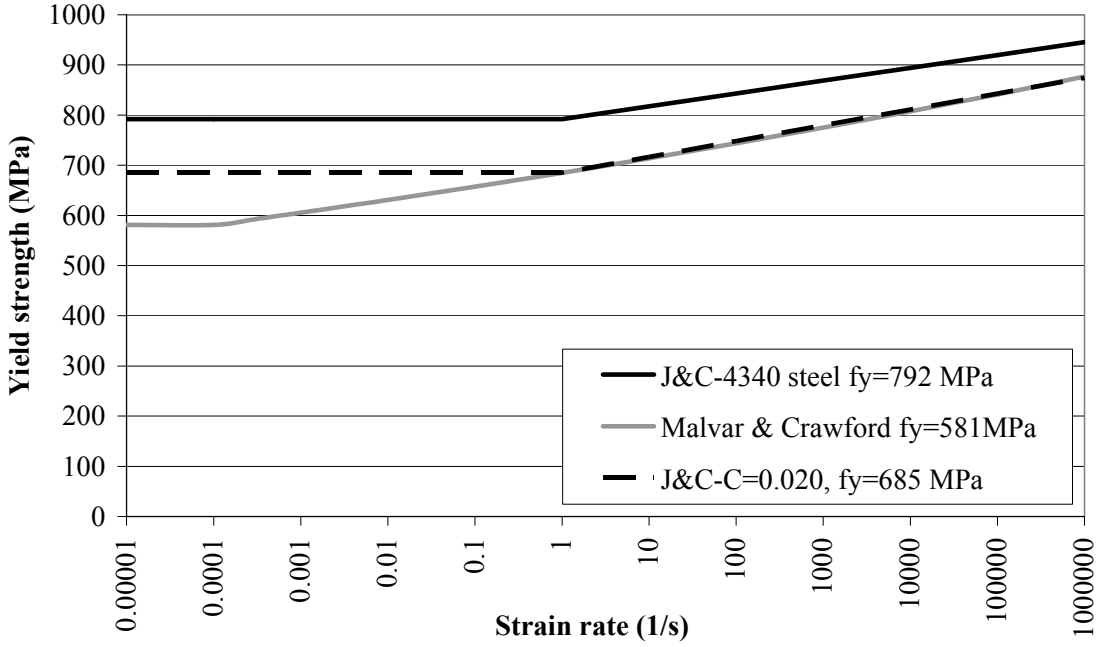

Figure 3.61. Strain rate vs. yield strength for 4340 steel and reinforcement (Johnson and Cook, 1983, and Malvar and Crawford, 1998). Parameters for the J&C model are also adapted to the reinforcement data giving C=0.020 and yield strength 685 MPa at the strain rate s^{-1}.

Influence of element size

A simulation with decreased element size from 15×15×7.5 mm to 7.5×7.5×3.75 mm showed a decrease of the penetration depth from 537 mm to 473 mm. The models are compiled in table 3.33 for comparison. For the unreinforced models with 1.2 m long targets there were only a minor change of the penetration depth when the element size was decreased from 10 to 5 m, and for the 0.54 m thick targets the exit velocity was increased from 58 to 98 m/s for the same decrease in element size. Further, for the model PEN242 there is an instant energy error occurring 0.8 ms after impact that may influence the results. This energy error needs to be further investigated in the future, and it is likely that it is due to the used contact algorithms.

The damage and deformations for the model with decreased element size are shown in figures 3.62 and 3.63. Figure 3.64 show the projectile velocity vs. penetration depth for the models with different element size.

Table 3.33. Simulations of reinforced concrete targets with varying element size, and with reinforcement and the use of friction between projectile and target.

	PEN231	**PEN242**
Model symmetry	None	None
Target cross section	Square	Square
Target length	600 mm	600 mm
Element size	15×15×7.5 mm	7.5×7.5×3.75 mm
Boundary condition [a]	Free surface	Free surface
Projectile mass	4.53 kg	4.53 kg
Impact velocity	420 m/s	420 m/s
Impact angle	90°	90°
P_{crush}	23.3 MPa	23.3 MPa
Tensile failure for concrete	Original RHT f_t= 4.8 MPa	Original RHT f_t= 4.8 MPa
Friction coefficient	μ=0.05	μ=0.05
Comment	Reinforcement with 50% failure strain AD v. 5.0.02c	Reinforcement with 50% failure strain AD v. 5.0.02c
Exit velocity	---	---
Penetration depth	537 mm	473 mm
Energy error	-15.3%	-4.5% [e]

Note: [a] Displacement of target in axial direction is free for all cases.

[e] There is an instant increase of the energy for the central part of the model at 0.8 ms after the projectile impact, this energy increase corresponds approximately to 12% of the initial energy for the model. This might influence the results, and also reduces the value of energy error. This value also includes the energy lost due to friction, and should be greater for models with friction. This needs to be further investigated.

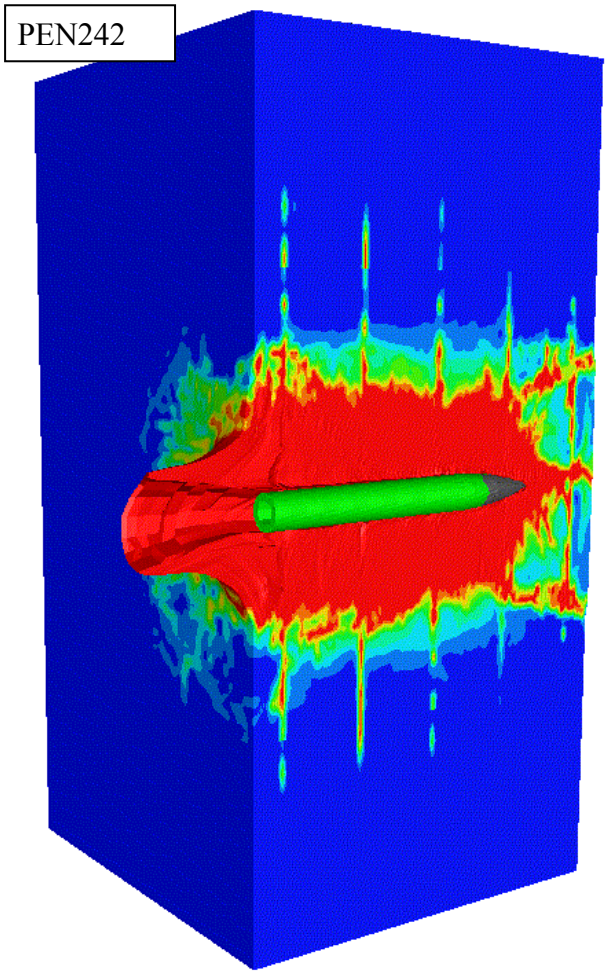

Figure 3.62. Model PEN242, with reinforcement and decreased element size, shown 3.2 ms after impact. Material location is shown for the projectile.

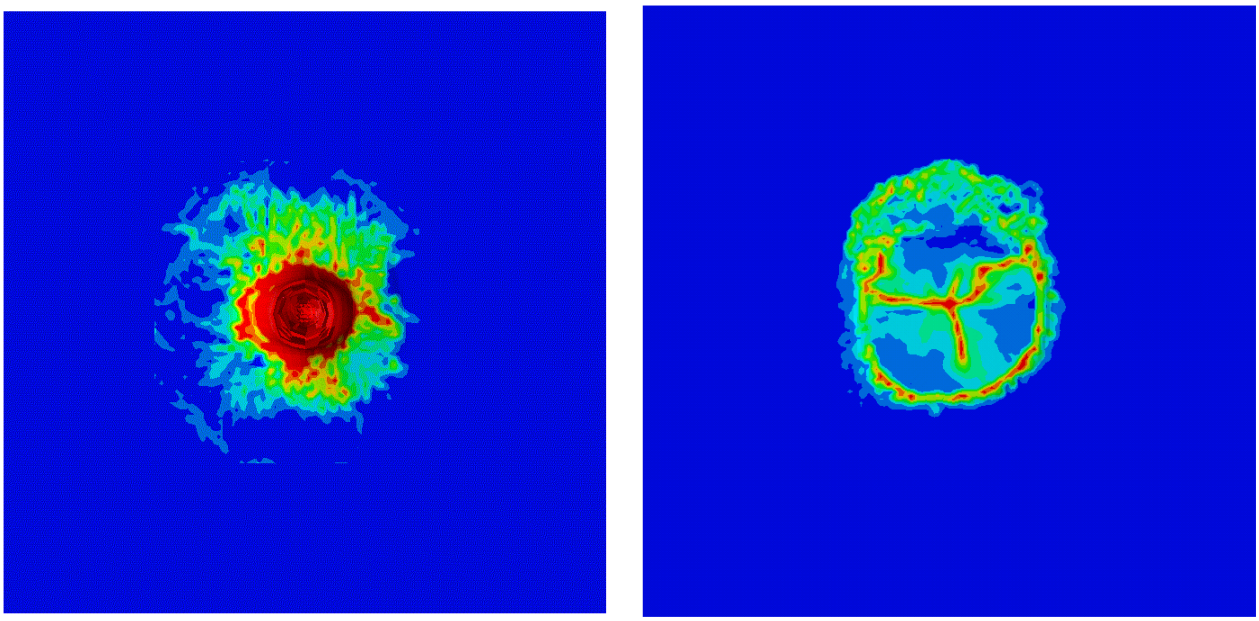

Figure 3.63. Front and back side of model PEN242 with reinforcement and decreased element size, shown 3.2 ms after impact. Front view without projectile shown.

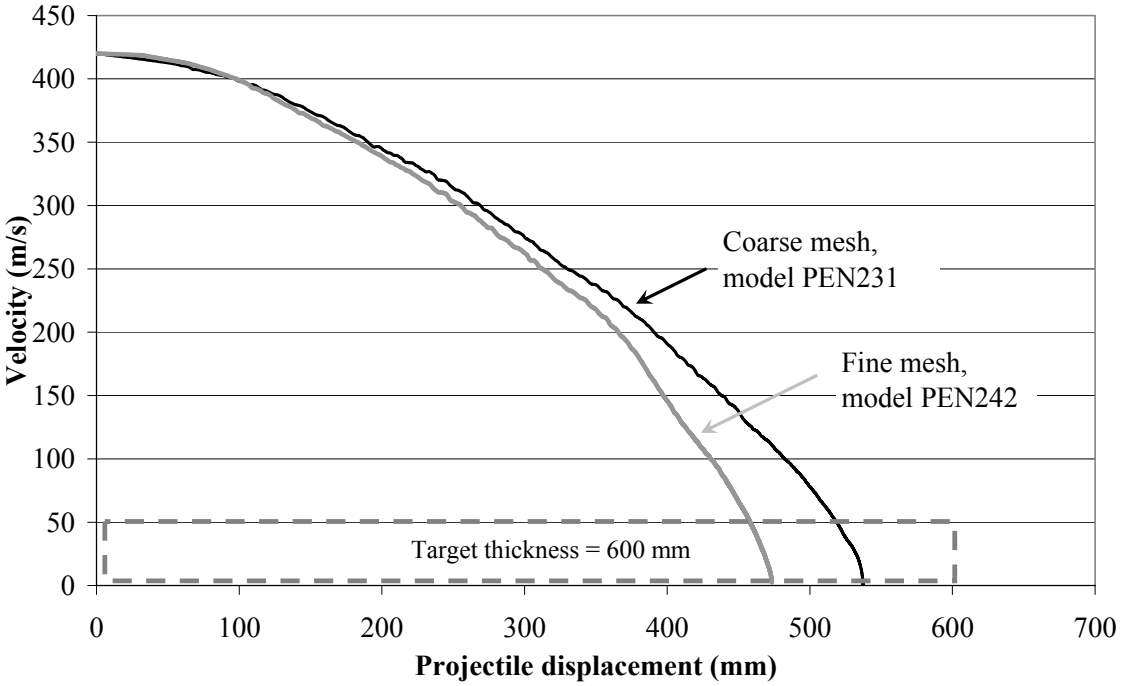

Figure 3.64. Projectile velocity vs. penetration for models with friction and with the use of different elements size, i.e. PEN231 and PEN242. The element sizes are 7.5×7.5×3.75 mm and 15×15×7.5 mm, respectively.

Influence of concrete tensile strength and the amount of reinforcement

The model with decreased element size is also used together with the more appropriate tensile strength of 4.0 MPa. The earlier used tensile strength for the concrete was based on the f_t/f_c relationship for a 35 MPa concrete (Riedel, 2000). The value of the ratio f_t/f_c is considered to decrease with increasing compressive strength of the concrete. This increases the penetration depth from 473 mm for f_t=4.8 MPa to 510 mm for f_t=4 MPa. Further, this later model doesn't show the type of energy errors that occurred earlier for model PEN242. The results for the models are compared in table 3.34, and figures 3.65 and 3.66 show the damage and deformations for the model with 4.0 MPa tensile strength. The velocity of the projectile vs. penetration depth for both models are shown in figure 3.67.

Table 3.34. Simulations with reinforcement, use of friction, and with varying tensile strength for the concrete.

	PEN242	**PEN243**
Model symmetry	None	None
Target cross section	Square	Square
Target length	600 mm	600 mm
Element size	7.5×7.5×3.75 mm	7.5×7.5×3.75 mm
Boundary condition [a]	Free surface	Free surface
Projectile mass	4.53 kg	4.53 kg
Impact velocity	420 m/s	420 m/s
Impact angle	90°	90°
P_{crush}	23.3 MPa	35.0 MPa
Tensile failure for concrete	Original RHT f_t= 4.8 MPa	Original RHT f_t= 4.0 MPa
Friction coefficient	μ=0.05	μ=0.05
Comment	Reinforcement with 50% failure strain AD v. 5.0.02c	Reinforcement with 50% failure strain AD v. 5.0.02k
Exit velocity	---	---
Penetration depth	473 mm	510 mm
Energy error	-4.5% [e]	-10.3%

Note: [a] Displacement of target in axial direction is free for all cases.

[e] There is an instant increase of the energy for the central part of the model at 0.8 ms after the projectile impact, this energy increase corresponds approximately to 12% of the initial energy for the model. This might influence the results, and also reduces the value of energy error. This value also includes the energy lost due to friction, and should be greater for models with friction. This needs to be further investigated.

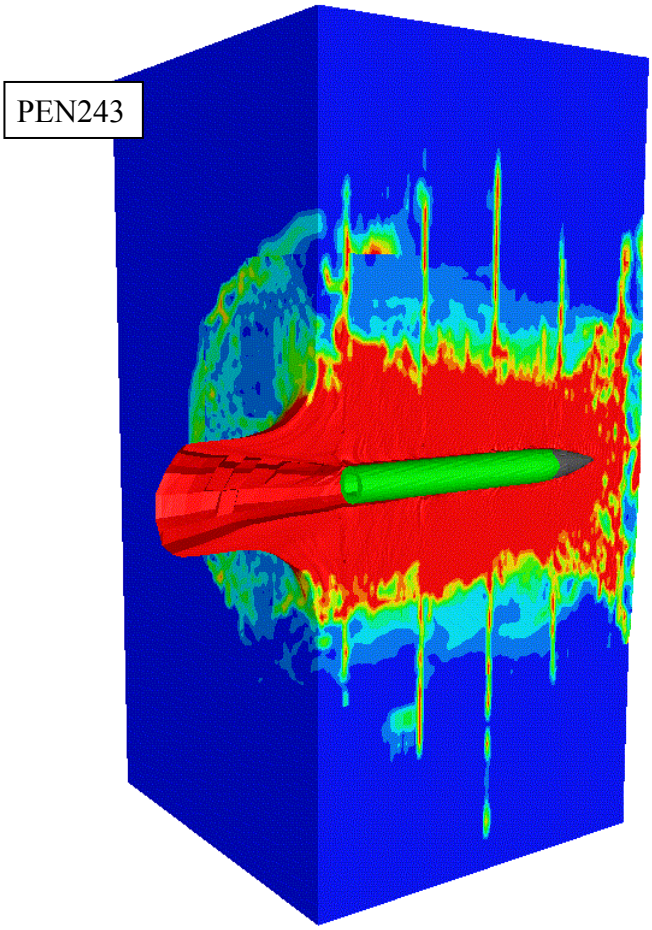

Figure 3.65. Damage and deformations for model PEN243 with decreased tensile strength of the concrete to 4.0 MPa shown approximately 3.9 ms after impact.

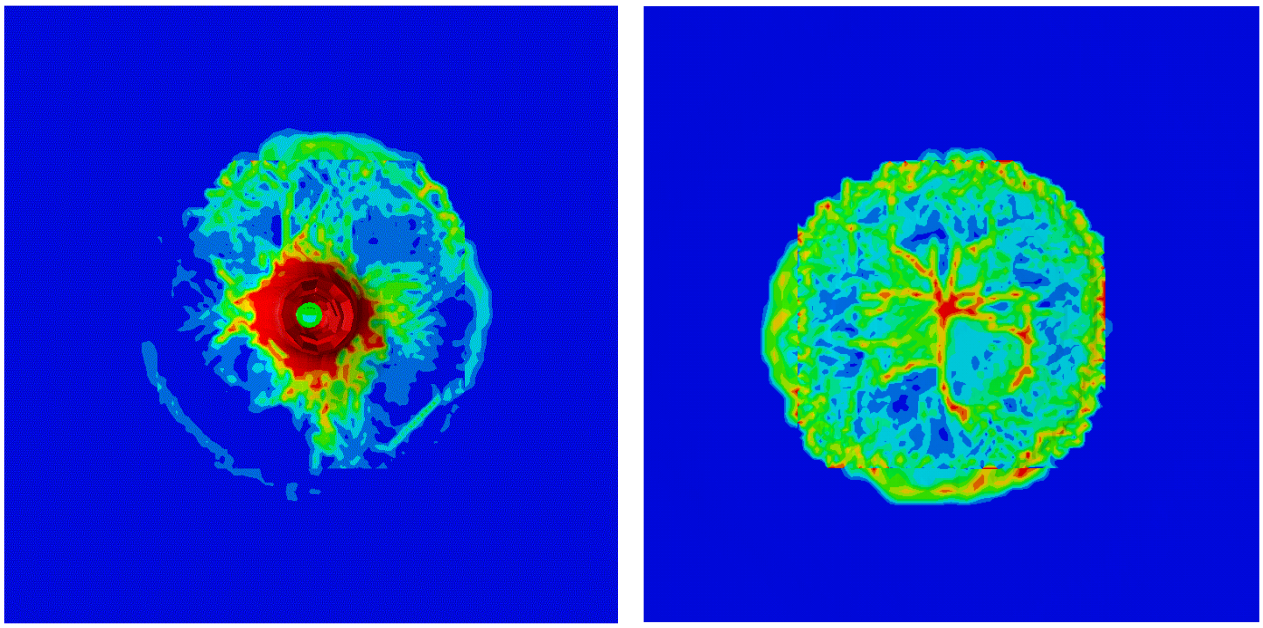

Figure 3.66. Damage and deformations for model PEN243 with decreased tensile strength of the concrete to 4.0 MPa shown approximately 3.9 ms after impact. Front (left) and back side of the target shown. Front view with projectile shown.

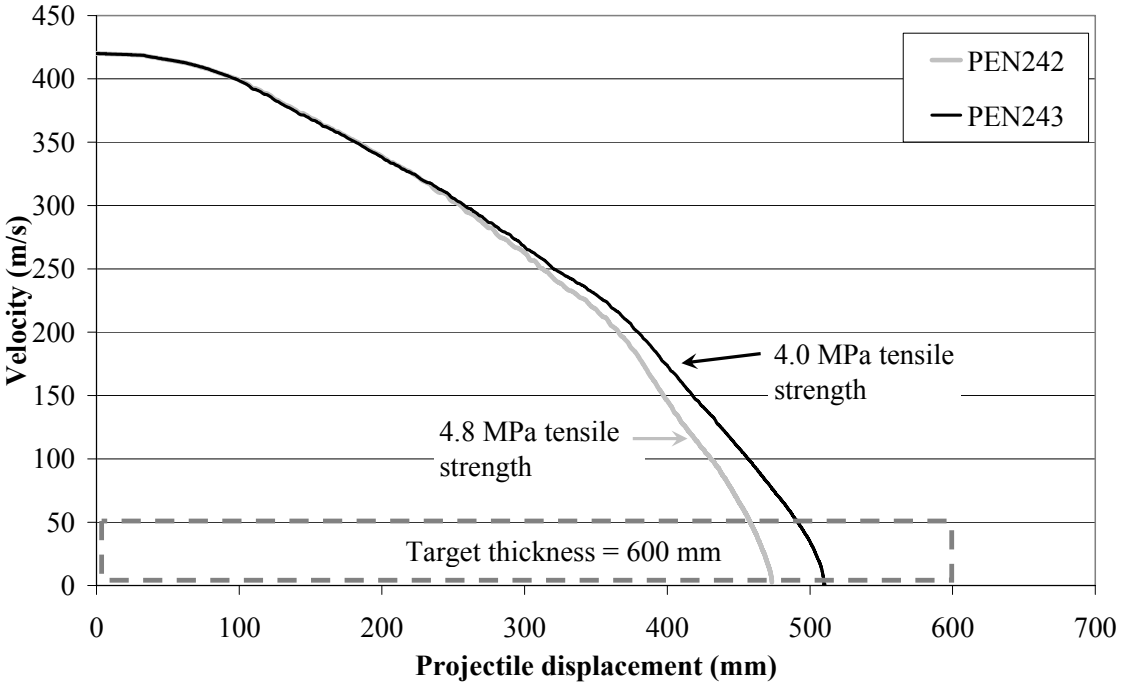

Figure 3.67. Projectile velocity vs. penetration for models with different tensile strength of the concrete, i.e. PEN242 to PEN244. See table 3.34 for details.

Further, one simulation is performed based on the simulation with a tensile strength of 4.0 MPa to study the influence of reinforcement parallel to the projectile path. This reinforcement bars are removed for simulation PEN245, leaving only the five reinforcement net with c/c 60 mm. The earlier discussed type of energy errors occurs again for this model, and this time to a much greater degree. This type of instantaneous energy errors needs to be further investigated, and also increases the uncertainties regarding the calculation results for this mode. Further, it's likely that the confinement effect due to the rebars connecting the reinforcement net is underestimated for this type of models due to the limited capability to describe tensile failure in the concrete. The models are compiled in table 3.35, and damage and deformation plots are shown in figure 3.68. Comparison of the projectile velocity vs. the penetration depth for the models with different amount of reinforcement are shown in figure 3.69.

Table 3.35. Simulations with reduced amount of reinforcement and also without reinforcement. Friction is considered for the models. Compare also model PEN243 in table 3.34.

	PEN244	**PEN245**
Model symmetry	None	None
Target cross section	Square	Square
Target length	600 mm	600 mm
Element size	7.5×7.5×3.75 mm	7.5×7.5×3.75 mm
Boundary condition [a]	Free surface	Free surface
Projectile mass	4.53 kg	4.53 kg
Impact velocity	420 m/s	420 m/s
Impact angle	90°	90°
P_{crush}	35.0 MPa	35.0 MPa
Tensile failure for concrete	Original RHT f_t= 4.0 MPa	Original RHT f_t= 4.0 MPa
Friction coefficient	μ=0.05	μ=0.05
Comment	Reinforcement with 50% failure strain No axial reinforcement AD v. 5.0.02k	No reinforcement AD v. 5.0.02k
Exit velocity	---	174 m/s
Penetration depth	535 mm	---
Energy error	-5.1% [f]	-12.5%

Note: [a] Displacement of target in axial direction is free for all cases.

[f] Several instant energy increases occur during the calculation that reduces the energy error. The total amount of instantaneous energy increases is approximately 13.6%, and a corrected value for the energy error is approximately -12.5%. This might influence the results. This value also includes the energy lost due to friction, and should be greater for models with friction. This needs to be further investigated.

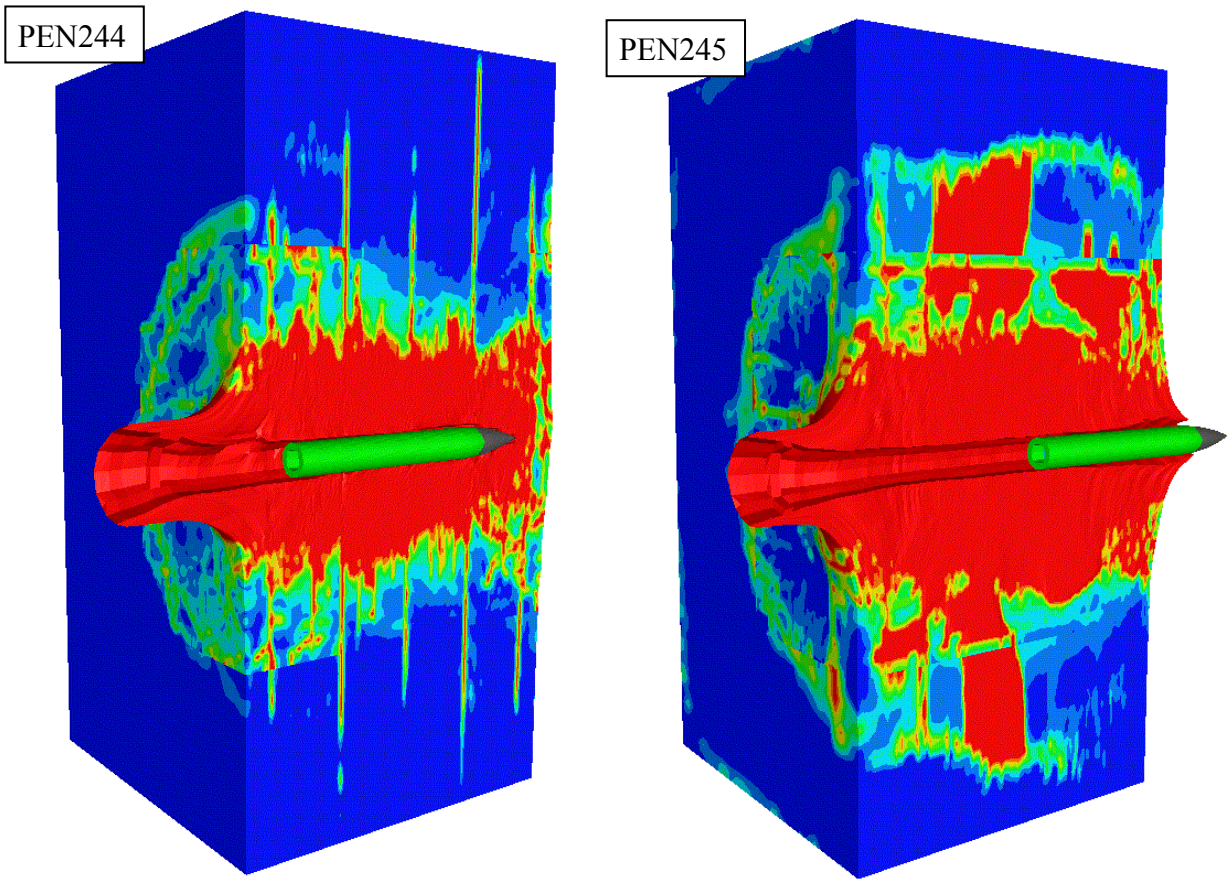

Figure 3.68. Damage and deformation plots for models PEN244 with reduced reinforcement (only nets) and PEN245 without reinforcement. The models are shown approximately 3.6 and 3.2 ms after impact, respectively.

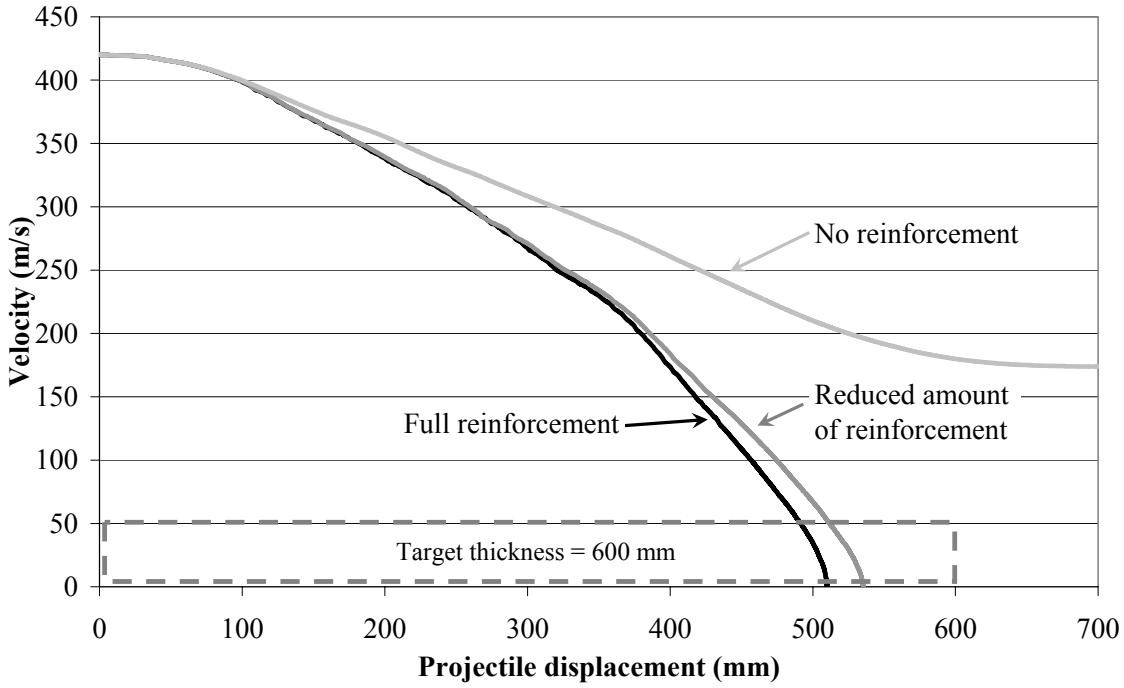

Figure 3.69. Projectile velocity vs. penetration for models with different amount of reinforcement, i.e. PEN243 to PEN245. See tables 3.34 and 3.35 for details.

3.2.2. Impact of inclined reinforced concrete targets.

Simulations of inclined reinforced targets are also performed, for details regarding concrete and reinforcement modelling see the previous chapters 3.1 regarding un-reinforced concrete targets and 3.2.1 regarding normal impact of reinforced concrete targets.

Influence of element size and friction

Simulations of inclined reinforced targets are performed with the same two element sizes as for the earlier simulations of normal impact of reinforced concrete targets, see table 3.36 for models without friction between penetrator and target. In this case there is a large influence on the behaviour of the model and it is clearly noticed that the coarse mesh is not suitable at all. The penetration depth measured from the front face of the target is more than doubled for the simulation with decreased element size, compared to the coarse mesh. The models are also shown in figure 3.70 and 3.71 for comparison, with a detail of the model with the fine mesh shown in figure 3.72. The velocity of the projectile nose vs. its displacement in the target is shown in figure 3.73 for the models with different element size.

Table 3.36. Simulations of inclined reinforced concrete targets with different element size for the central part of the model, and without friction between projectile and target.

	PEN258	**PEN256**
Model symmetry	None	None
Target cross section	Square	Square
Target length	540 mm	540 mm
Element size	15×15×7.5 mm	7.5×7.5×3.75 mm
Boundary condition [a]	Free surface	Free surface
Projectile mass	4.53 kg	4.53 kg
Impact velocity	420 m/s	420 m/s
Impact angle	60°	60°
P_{crush}	23.3 MPa	23.3 MPa
Tensile failure for concrete	Original RHT with f_t= 4.8 MPa	Original RHT with f_t= 4.8 MPa
Friction coefficient	μ=0	μ=0
Comment	Reinforcement with 50% failure strain AD v. 5.0.02c	Reinforcement with 50% failure strain AD v. 5.0.02c
Exit velocity	---	---
Penetration depth [b]	198 mm	440 mm
Energy error	-2.0%	+2.2%

Note: [a] Displacement of target in axial direction is free for all cases.
[b] The lengths of the projectile paths are longer than the penetration depths calculated from the front face of the target.

PEN258

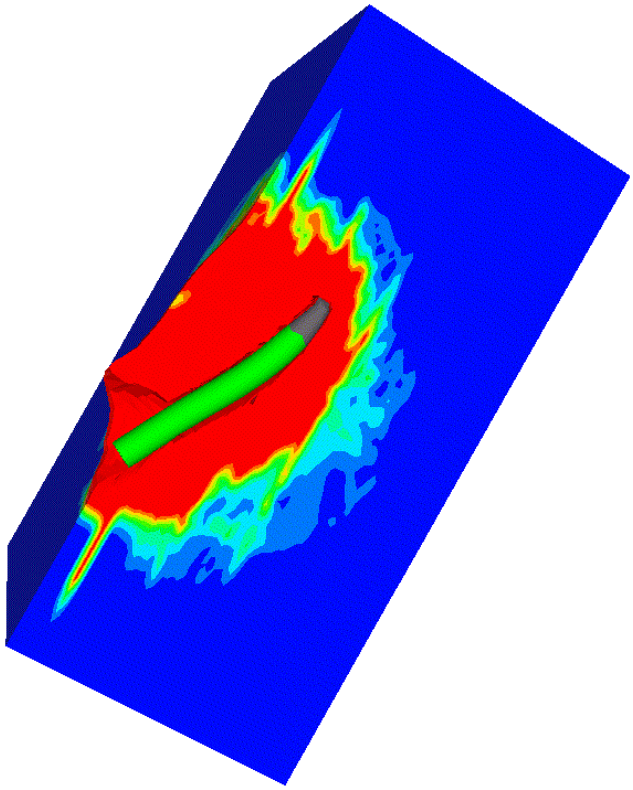

Figure 3.70. Model PEN258 with reinforcement shown 2.8 ms after impact.

PEN256

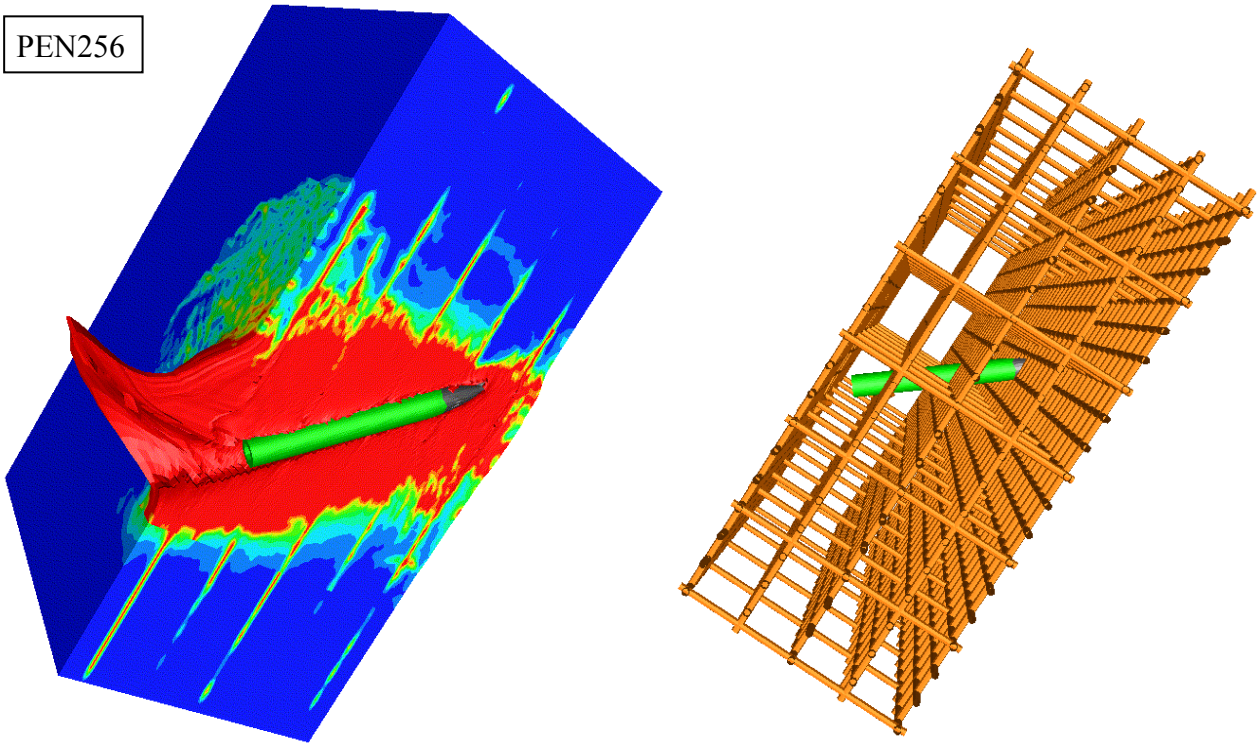

Figure 3.71. Model PEN256 with reinforcement and decreased element size to 7.5×7.5×3.75 mm shown 4.0 ms after impact.

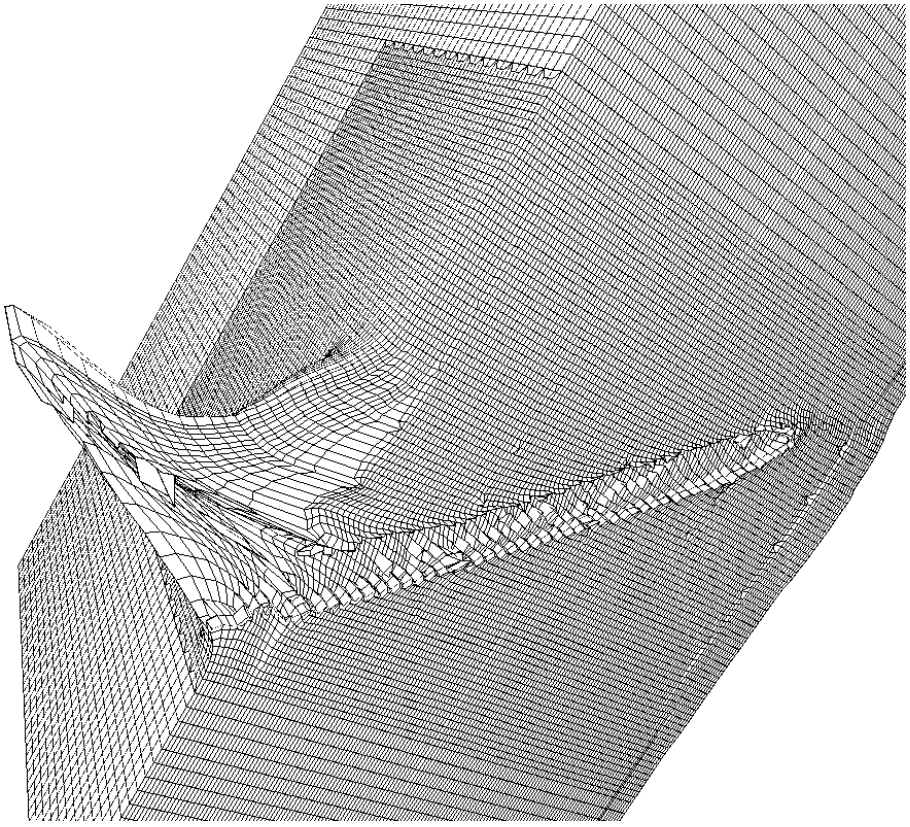

Figure 3.72. Details of the distorted mesh for the target of model PEN256 with reinforcement, and with decreased element size to 7.5×7.5×3.75 mm in the centre of the target, shown 4.0 ms after impact.

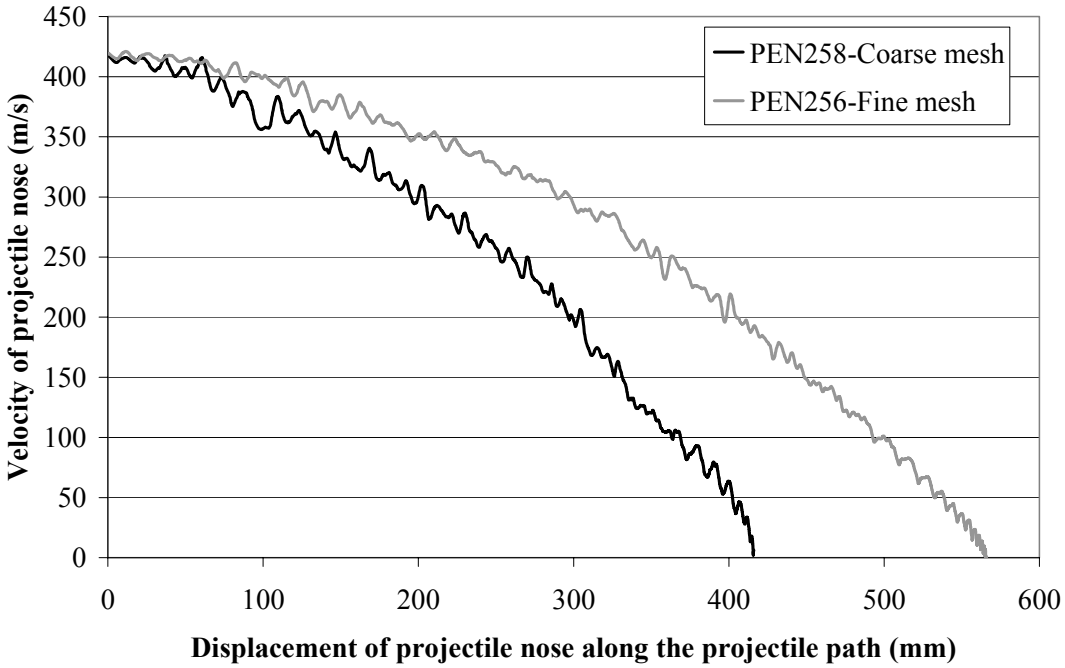

Figure 3.73. The velocity of the projectile nose along the projectile path for the two models PEN258 and PEN256. These models are without friction between projectile and target, and use different element size.

The models of inclined reinforced concrete targets are also run using friction between penetrator and target, in this case a simulation of a second impact in a target also is performed. These simulations are compiled in table 3.37. A second impact of the model with the coarse mesh shows only a minor change of the penetration depth. The localisation of the reinforcement bars is also likely to influence the penetration path of a projectile depending on the localisation of the impact point on the front face of the target. The models with the coarse mesh are shown in figures 3.74 and 3.75. The influence of element size on the penetration depth for the models with friction between penetrator and target is also large, with almost twice the penetration depth measured from the front face of the target for the model with the fine mesh in comparison with the model with coarse mesh. The damage and deformations for the model with fine mesh is shown in figure 3.76. The velocity of the projectile nose vs. its displacement in the target is shown in figure 3.77 for the models with different element size.

Table 3.37. Influence of element size for the central part of the model and of damaged target for simulations of inclined reinforced concrete targets. The models use friction between projectile and target.

	PEN252	**PEN252B**	**PEN257**
Model symmetry	None	None	None
Target cross section	Square	Square	Square
Target length	540 mm	540 mm	540 mm
Element size	15×15×7.5 mm	15×15×7.5 mm	7.5×7.5×3.75 mm
Boundary condition [a]	Free surface	Free surface	Free surface
Projectile mass	4.53 kg	4.53 kg	4.53 kg
Impact velocity	420 m/s	420 m/s	420 m/s
Impact angle	60°	60°	60°
P_{crush}	23.3 MPa	23.3 MPa	23.3 MPa
Tensile failure for concrete	Original RHT f_t= 4.8 MPa	Original RHT f_t= 4.8 MPa	Original RHT f_t= 4.8 MPa
Friction coefficient	μ=0.05	μ=0.05	μ=0.05
Comment	Reinforcement with 50% failure strain AD v. 5.0.02c	Reinforcement with 50% failure strain Second impact on target [c] AD v. 5.0.02c	Reinforcement with 50% failure strain AD v. 5.0.02c
Penetration depth [b]	215 mm	200 mm	382 mm
Energy error	-6.7%	+2.9%	-9.8%

Note: [a] Displacement of target in axial direction is free for all cases.
[b] The lengths of the projectile paths are longer than the penetration depths calculated from the front face of the target.
[c] The second impact is 280 mm to the left and 20 mm higher than impact from the first projectile. See figure 3.75 for the orientation of the target.

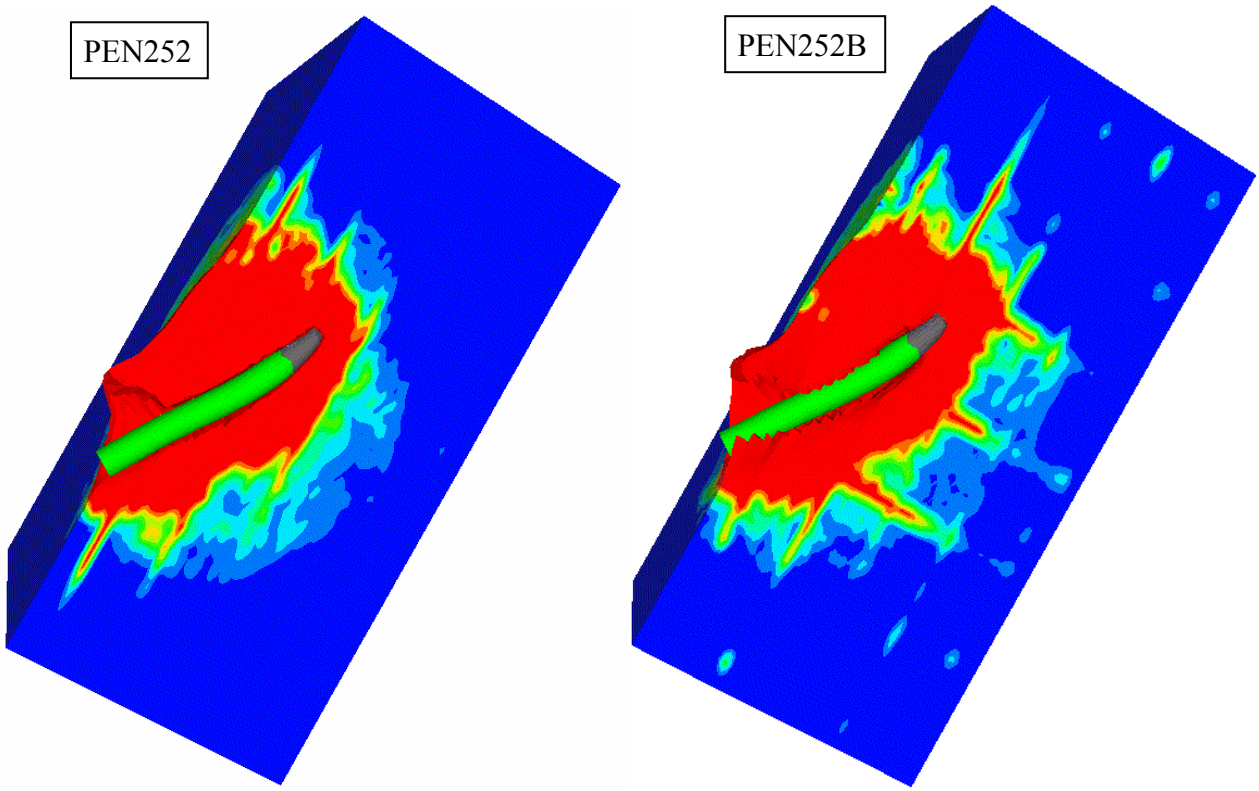

Figure 3.74. Model PEN252 with reinforcement shown 2.63 ms after impact, and model PEN252B shown 2.57 ms after impact of second projectile.

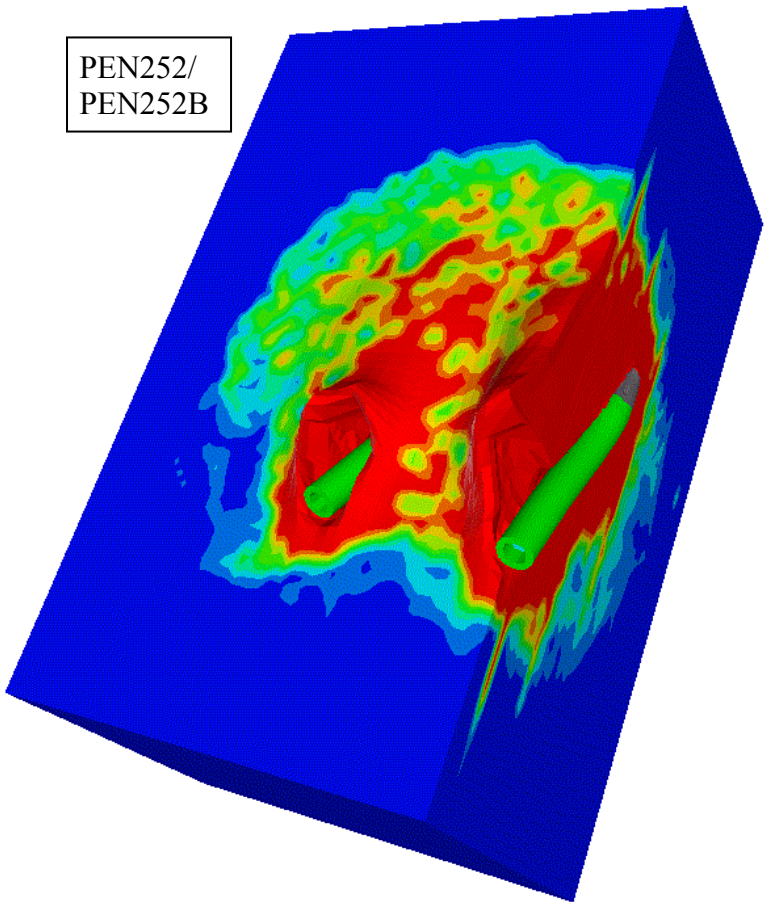

Figure 3.75 Model PEN252/PEN252B shown 2.57 ms after impact of second projectile.

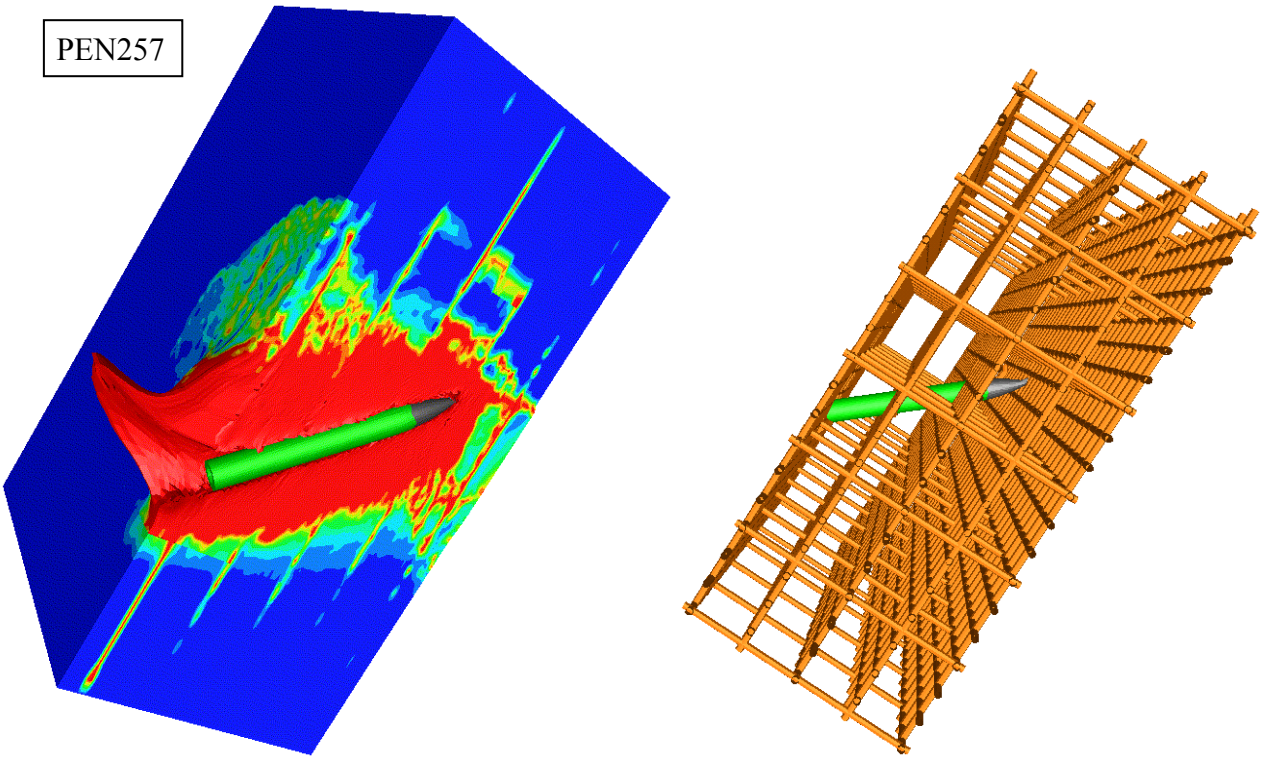

Figure 3.76. Model PEN257 with reinforcement and decreased element size to 7.5×7.5×3.75 mm shown 3.4 ms after impact.

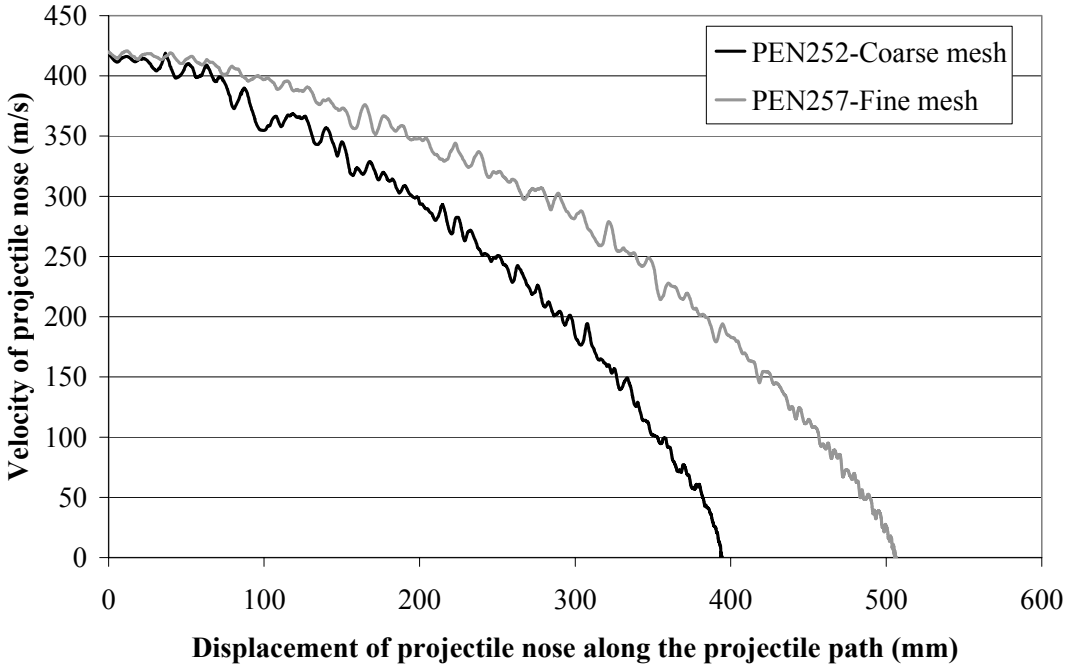

Figure 3.77. The velocity of the projectile nose along the projectile path for models PEN252 with coarse mesh and PEN257 with fine mesh. These models are with friction between projectile and target.

The velocity of the projectile nose vs. its displacement in the target is shown in figure 3.78 for the models with fine mesh, and with and without friction, i.e. PEN256 and PEN257.

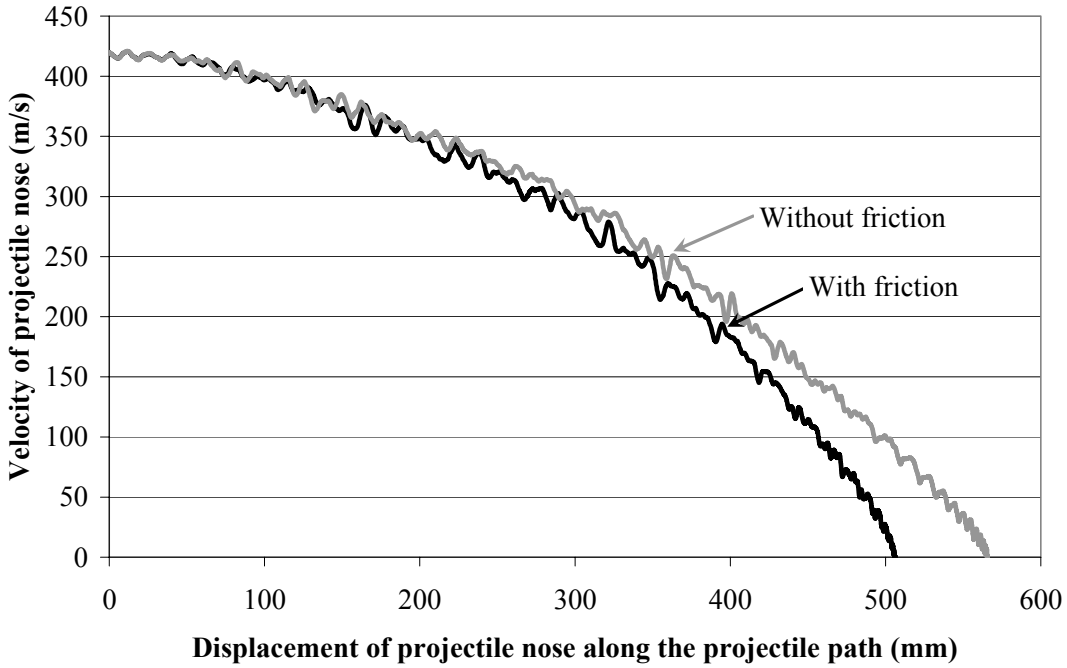

Figure 3.78. The velocity of the projectile nose along the projectile path for models PEN256 and PEN257, without and with friction, respectively. Both models use the element size 7.5×7.5×3.75 mm.

Influence of concrete tensile strength and of removed reinforcement

The model with fine mesh is also used to study the influence of tensile strength of the concrete and the reinforcement for concrete. These models are compiled in table 3.38, which show that there is only a minor influence on the penetration depth of the concrete strength for this case. The model PEN 260 is shown in figure 3.79 The reinforcement is removed for model PEN259, this results in a perforation of the target with an exit velocity of approximately 100 m/s.

Since the projectile is subjected to increased forces during penetration of a reinforced concrete target, it is likely that the used material properties for the steel material, i.e. steel reinforcement and projectile material, will have a strong influence on the simulation results. According to this it is necessary to determine the properties, i.e. yield strength and failure initiation, of these materials. It is important to be able to model the interaction between the two materials during penetration of a projectile. Further, simulations using the SPH formulation for the central part of the target may improve this type of models.

Table 3.38. Influence of tensile concrete strength and reinforcement for simulations of inclined reinforced concrete targets. The models use friction between projectile and target.

	PEN257	**PEN260**	**PEN259**
Model symmetry	None	None	None
Target cross section	Square	Square	Square
Target length	540 mm	540 mm	540 mm
Element size	7.5×7.5×3.75 mm	7.5×7.5×3.75 mm	7.5×7.5×3.75 mm
Boundary condition [a]	Free surface	Free surface	Free surface
Projectile mass	4.53 kg	4.53 kg	4.53 kg
Impact velocity	420 m/s	420 m/s	420 m/s
Impact angle	60°	60°	60°
P_{crush}	23.3 MPa	35.0 MPa	23.3 MPa
Tensile failure for concrete	Original RHT f_t= 4.8 MPa	Original RHT f_t= 4.0 MPa	Original RHT f_t= 4.8 MPa
Friction coefficient	μ=0.05	μ=0.05	μ=0.05
Comment	Reinforcement with 50% failure strain AD v. 5.0.02c	Reinforcement with 50% failure strain AD v. 5.0.02k	No reinforcement AD v. 5.0.02c
Exit velocity	---	---	101 m/s
Penetration depth [2]	382 mm	391 mm	---
Energy error	-9.8%	-9.7%	-10.9%

Note: [a] Displacement of target in axial direction is free for all cases.

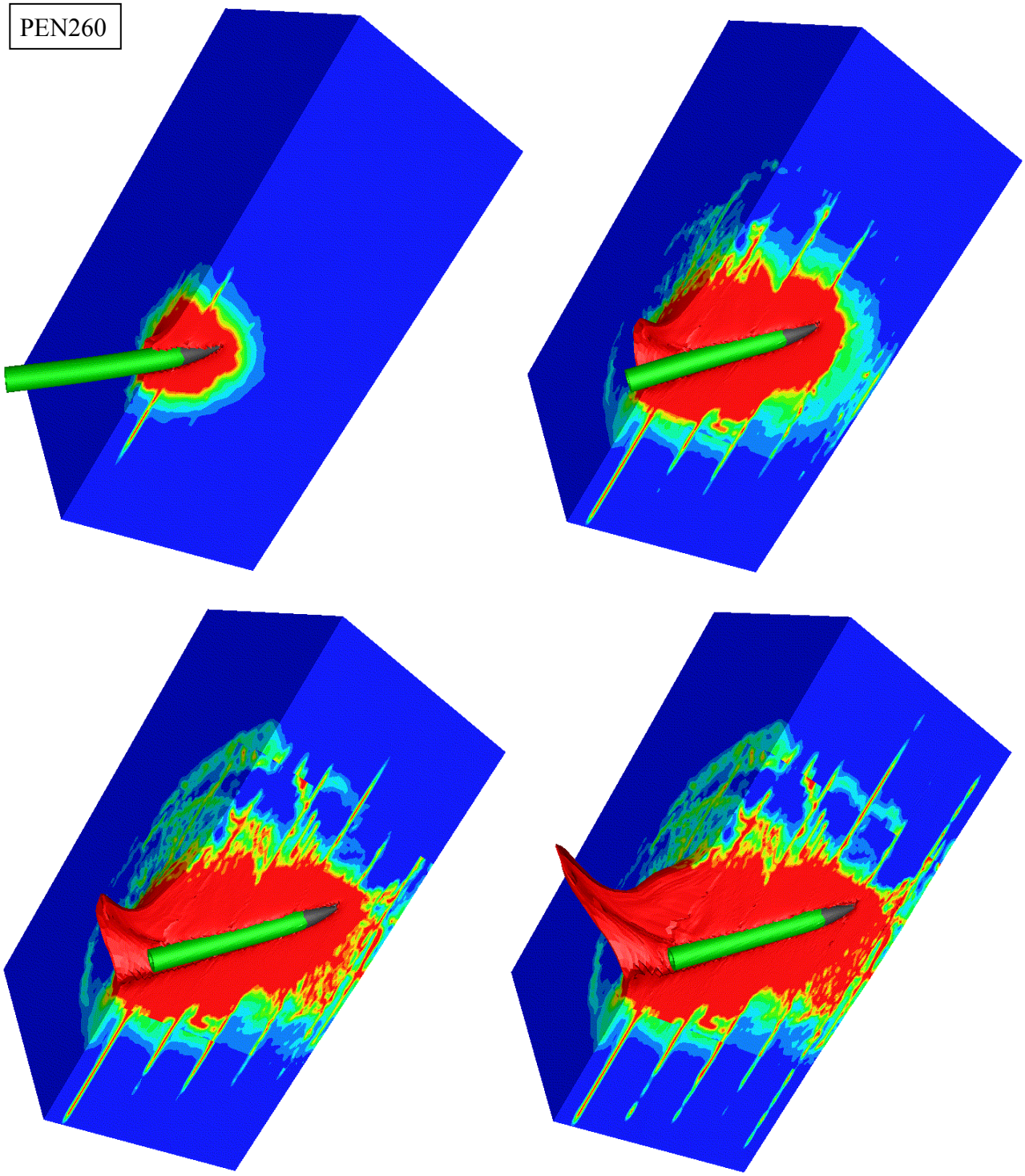

Figure 3.79. Model PEN260 with reduced tensile strength of the concrete, and an element size of 7.5×7.5×3.75 mm, shown 0.4, 1.2, 2.0 and 4.4 ms after impact.

This page intentionally blank.

4. Comparison between simulations and test results

Comparisons between test results and simulation results are given in this chapter. The test results are compiled in appendix 3, and for further details refer to the test report (Hansson, 2005). The used data set for the concrete for these final simulations are given in tables 4.1 and 4.2. The experimental results are compiled in tables 4.3 and 4.4 for easy comparison with the simulation results.

Table 4.1. Parameters for the RHT model used for the concrete.

Parameter	**Value**	**Parameter**	**Value**	**Parameter**	**Value**
G	16.7 GPa	BQ	0.0105	B	1.60
f_c	48 MPa	D_1	0.04	M	0.61
f_t/f_c	0.083	D_2	1	α	0.032
f_s/f_c	0.18	EFMIN	0.01	δ	0.036
A_{fail}	1.60	PREFACT	2	SHRATD	0.13
N_{fail}	0.61	TENSRAT	0.70		
Q_2	0.6805	COMPRAT	0.53		

Table 4.2. Parameters for the P-α equation of state used for the concrete.

Parameter	**Value**	**Parameter**	**Value**
ρ_{porous}, ρ_0	2.314 g/cm^3	A_2	39.58 GPa
C_{porous}	3000 m/s	A_3	9.04 GPa
p_{crush}	35 MPa	B_0	1.22
p_{lock}	6000 MPa	B_1	1.22
n	3	T_1	35.27 GPa
Solid EOS	Polynomial	T_2	0 GPa
ρ_{solid}	2.75 g/cm^3	T_{ref}	300 K
A_1	35.27 GPa	C_v	654 J/kgK

Table 4.3. Compiled experimental results.

Case no.	**Case no. 0**	**Case no. 1**	**Case no. 2**	**Case no. 2**
Test no.	2002-10	2004-6	2004-25	2004-26
Target diameter	1.25 m	1.20 m	1.50 m	1.50 m
Target length	1.50 m	0.60 m	0.54 m	0.54 m
Impact angle	90°	90°	59.5°	59.5°
Impact velocity	420 m/s	425 m/s	424 m/s	422 m/s
Pitch	≈0.8°	1.1°	1.1°	1.2°
Yaw	≈1.0°	0.2°	0.0°	0.2°
Penetration depth	0.49	---	---	0.50 m
Exit velocity	---	139 m/s	16 m/s	---
Energy loss for projectile	100%	89.3%	99.9%	100%
Comment	3.64 kg penetrator			

Table 4.4. Compiled experimental results.

	Case no. 3	**Case no. 4**	**Case no. 5**	**Case no. 6**
Test no.	2004-3	2004-4	2004-20	2004-24-1
Target diameter [a]	1.20 m	1.20 m	1.20 m	1.50 m
Target length	0.90 m	1.20 m	0.60 m	0.54 m
Impact angle	90°	90°	90°	59.5°
Impact velocity	409 m/s	463 m/s	424 m/s	421 m/s
Pitch	0.7°	0.2°	0.55°	1.59°
Yaw	0.8°	0.4°	0.69°	0.38°
Penetration depth	0.64 m	0.69 m	0.53 m	0.39 m
Exit velocity	---	---	---	---
Energy loss for projectile	100%	100%	100%	100%
Comment			Reinforced target	Reinforced target

Note: [a] Height of target given for the reinforced targets.

All simulations used the nominal impact velocities, i.e. 420 and 460 m/s, and without yaw or pitch of the projectile. A friction coefficient of 0.05 is also considered for the interaction between penetrator and target. The energy error given for the models in the tables includes the energy losses due to friction between target and projectile. Simulations of normal impact without friction normally results in an energy error between one and two percent, and to obtain an estimate of the energy lost due to frictional work it is necessary to adjust for the amount of the energy error not referring to friction work.

The results for the simulations of cases no. 0 to 4, with the use of 5 mm element size and 4.0 MPa tensile strength for the target, are given in tables 4.5 and 4.6, with velocity histories for case no. 1 to 3 shown in figure 4.1. Damage plots of the targets for cases no.1 and 2 are shown in figures 4.2 and 4.3, respectively. A minor study of the effects of different element size in the target and tensile strength of the concrete was performed for case no. 1, see figure 4.4. An increase of the tensile strength of the concrete from 4.0 MPa to 4.8 MPa resulted in a decrease of the exit velocity from 143 m/s to 92 m/s for the model with 5 mm elements. Further, an increased element size to 10 mm for the model with 4.8 MPa tensile strength results in a decrease of the exit velocity from 92 m/s to 60 m/s, and an increased energy error from -15.6% to -18.6%. The energy error includes the energy lost due to friction between the projectile and the target. Based on experiences from earlier simulations it is necessary to use roughly 10 elements across the diameter of the projectile to obtain useful results, i.e. 5 mm elements for this projectile geometry. The use of the larger element size probably causes lock up of the elements, and thereby increases the penetration resistance.

For case no. 1, the simulation shows good agreement with the experimental results from test no. 2004-6, with kinetic energy losses of the projectile given as 89% for the test and 88% for the simulation. However, for case no. 2 with an inclined target there is only at the most a fair agreement. The reason for this is probably due to the use of numerical erosion to remove heavily distorted elements. For case no. 1, with normal impact of the target, the distorted elements are located equally around the nose of the projectile. However, the calculated thickness for an inclined target to stop the penetrator is probably determined within 10% of the experimental results. This is based on the simulations with increased target thicknesses for the inclined target. For an inclined target, e.g. case no. 2, the heavily distorted elements are located mainly on one side of the projectile, and the rotating moment acting on the projectile is reduced due to the removal of these elements. The energy error, including the frictional work, is lower for case no. 2 than the other

models. This indicates that the frictional force probably also is lower. This may also be a result of the erosion of distorted elements. The use of a meshless technique, e.g. SPH, is likely to improve the simulation results for this type of impact conditions.

The simulation results for penetration cases no. 0, 3 and 4 are considered to have a fair agreement with the test results, with an average underestimate for the calculated penetration depth by 13%.

Table 4.5. Results for simulations with 4.0 MPa tensile strength for the concrete and 5 mm elements for the unreinforced concrete targets.

	Case no. 1	**Case no. 2**
Model identity	PEN080-2E	PEN600-B
Target diameter	1.20 m	1.50 m
Target length	0.60 m	0.54 m
Impact angle	90°	60°
Impact velocity	420 m/s	420 m/s
Model symmetry	½	½
Penetration depth	---	---
Exit velocity	143 m/s	117 m/s
Energy loss for projectile	88.4%	92.4%
Energy error for the simulation	-14.1%	-10.4%
Tests: Impact velocity	425 m/s	425 m/s, 422 m/s
Exit velocity/penetration	139 m/s	16 m/s, 0.50 m [a]

Note: [a] Penetration measured from front face of the target to the nose of the projectile.

Table 4.6. Results for simulations with 4.0 MPa tensile strength for the concrete and 5 mm elements for the unreinforced concrete targets.

	Case no. 0 [a]	**Case no. 3**	**Case no.4**
Model identity	PEN209B [a]	PEN205B	PEN208B
Target diameter	1.20 m	1.20 m	1.20 m
Target length	1.20 m	1.20 m	1.20 m
Impact angle	90°	90°	90°
Impact velocity	420 m/s	420 m/s	460 m/s
Model symmetry	¼	¼	¼
Penetration depth	0.45 m	0.53 m	0.59 m
Exit velocity	---	---	---
Energy loss for projectile	100%	100%	100%
Energy error for the simulation	-15.3	-15.8%	-16.7%
Tests: Impact velocity	420 m/s	409 m/s	463 m/s
Penetration	0.49 m	0.64 m	0.69 m

Note: [a] The mass of the penetrator used in 2002 was 3.64 kg.

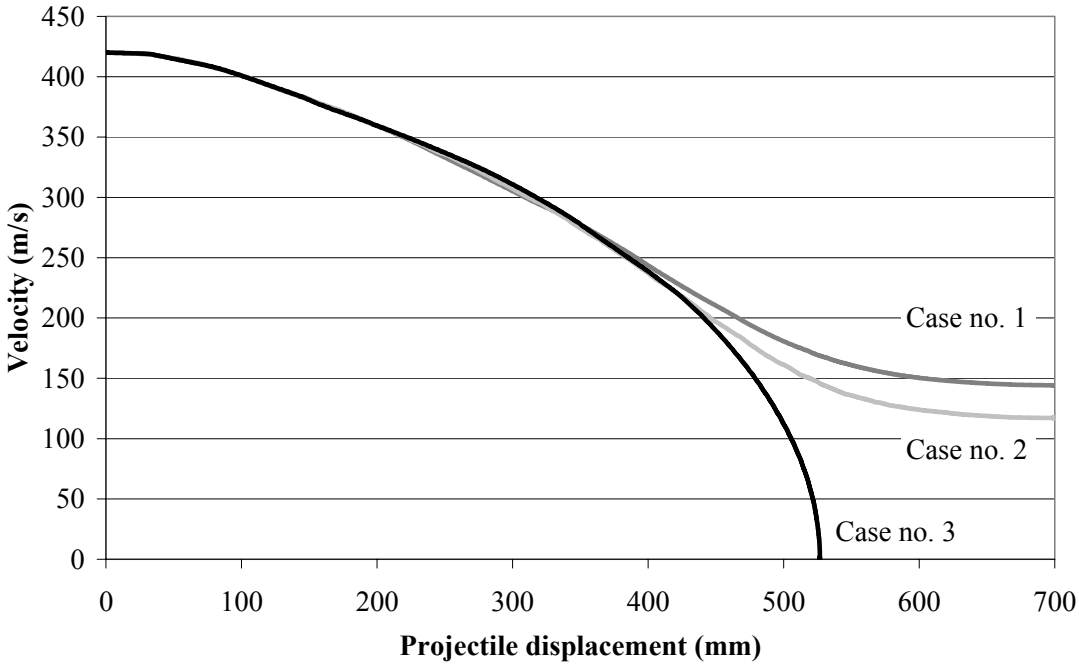

Figure 4.1. Projectile velocity vs. displacement for the projectile in the direction of the initial velocity vector. All simulations are with f_t=4.0 MPa and 5 mm element size.

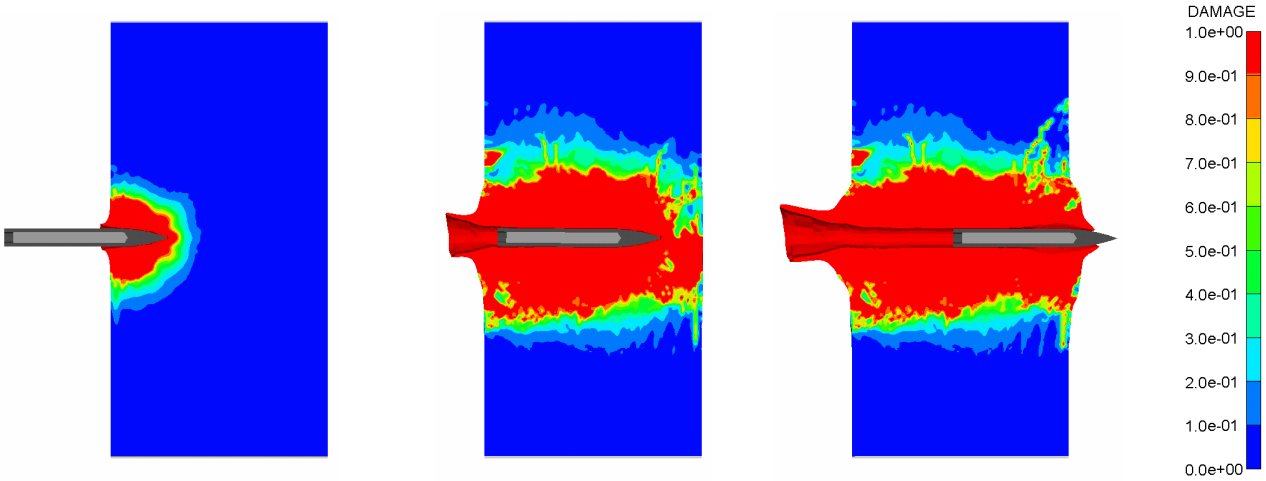

Figure 4.2. Calculated damage and deformations for case no. 1. Plots are shown 0.4, 1.6 and 3.2 ms after impact. Scale for the damage plots is shown to the right.

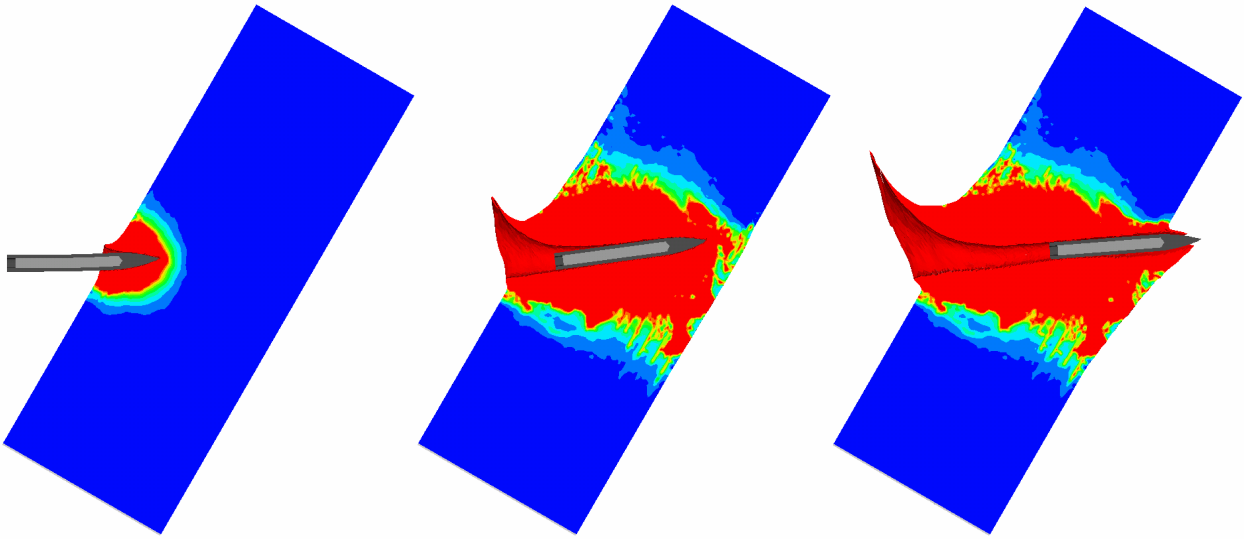

Figure 4.3. Calculated damage and deformations for case no. 2. Plots are shown 0.4, 2.0 and 4.0 ms after impact. Scale for the damage plots is shown to the right in figure 4.2.

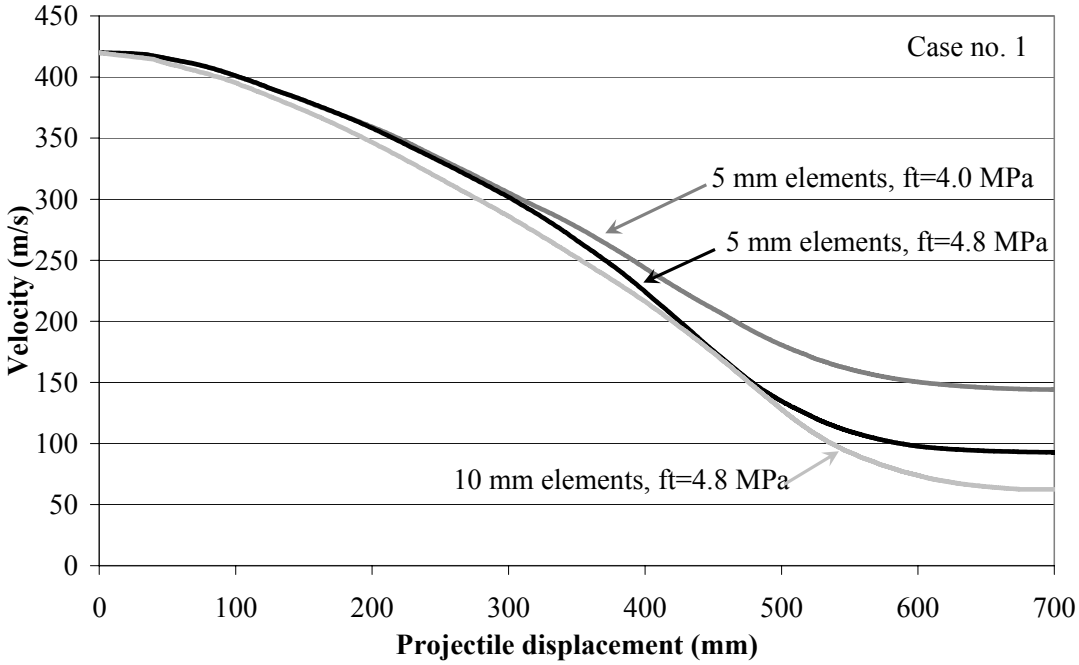

Figure 4.4. Influence of the tensile strength and element size for the concrete on velocity vs. penetration history for case no. 1.

The simulations of reinforced targets, i.e. cases no. 5 and 6, shows good agreement with the test results with only penetration depths estimated within 5% of the test results. The results from the simulations are compared with the test results in table 4.6. The tensile strength of the concrete is 4.0 MPa, and the element size in the central part of the target is 7.5×7.5×3.75 mm.

Table 4.6. Results for simulations with 4.0 MPa tensile strength for the concrete and 7.5×7.5×3.75 mm elements for the reinforced concrete targets.

	Case no. 5	**Case no. 6**
Model identity	PEN243	PEN260
Target height	1.20 m	1.50 m
Target length	0.60 m	0.54 m
Impact angle	90°	60°
Impact velocity	420 m/s	420 m/s
Model symmetry	None	None
Penetration depth	0.51 m	0.39 m [a]
Exit velocity	---	---
Energy loss for projectile	100%	100%
Energy error for the simulation	-10.3%	-9.7%
Tests: Impact velocity	424 m/s	421 m/s
Penetration	0.53 m	0.39 m [a]

Note: [a] Penetration measured from front face of the target to the nose of the projectile.

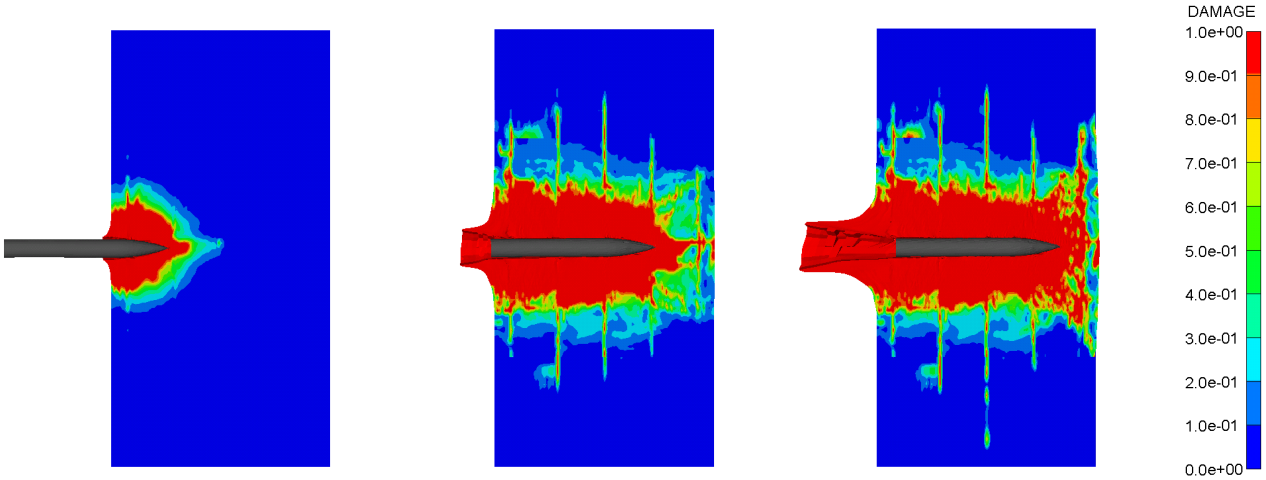

Figure 4.5. Calculated damage and deformations for case no. 5 with a reinforced concrete target. Plots are shown 0.4, 1.6 and approximately 3.9 ms after impact. Scale for the damage plots is shown to the right.

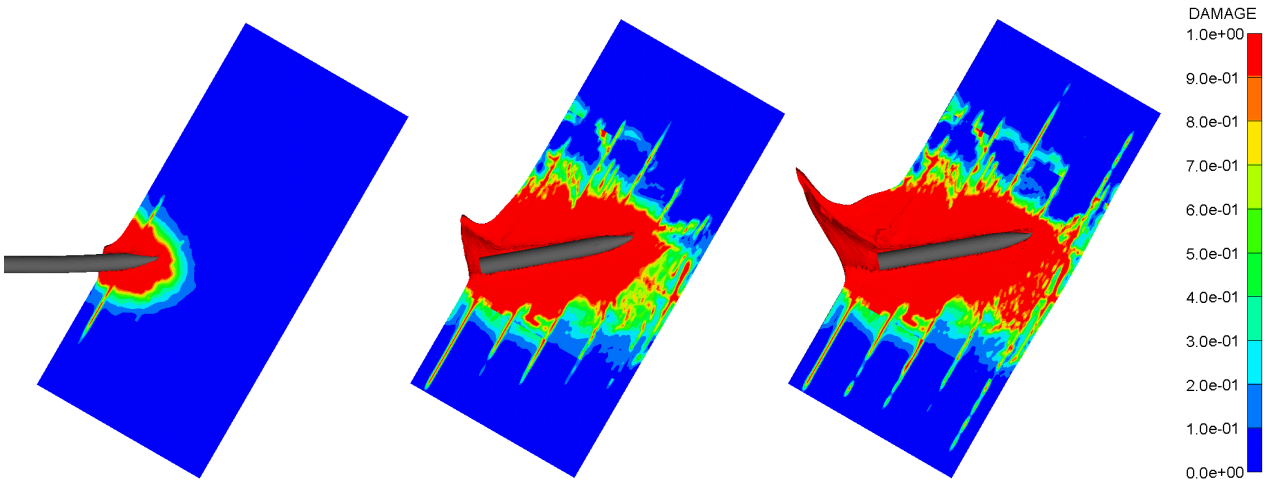

Figure 4.6. Calculated damage and deformations for case no. 6 with a reinforced concrete target. Plots are shown 0.4, 1.6 and 4.4 ms after impact. Scale for the damage plots is shown to the right.

This page intentionally blank.

5. Discussion and simulation recommendations

The use of numerical simulations as a tool to estimate penetration performance for warheads require a thorough understanding of the behaviour of the material subjected to high pressures, high strain rates and large deformations. Further, a thorough understanding of the numerical formulations and their limitations are also necessary to be able to perform useful simulations. The use of 3D models seems necessary in order to study the penetration in concrete, e.g. reinforced concrete structures. The limitations of 2D models make them suitable only to obtain quick estimations of penetration into concrete, e.g. during ongoing test series. However, to be able to use 3D simulations to its full potential it is necessary to have access to parallel computer systems with suitable simulation capacity. A minimum simulation capacity to study this type of problems seems to be systems with a total of 16 processors. A more suitable capacity to perform 3D simulations would be a Linux parallel system with at least 32 processors. For future 3D simulations of penetration, or other weapon effects, it will be necessary to use 64 bit processors, due to the memory limitations for 32 bit systems, which limits the number of elements that can be used for a model. In some cases, e.g. simulation of air blast propagation, it is possible to use adaptive meshes to enhance the effectiveness of a simulation. However, this does not seem to be suitable for this type of penetration simulations.

5.1. Discussion

In general the simulations gave reasonable results for the different simulation cases, with the best results for normal impact conditions. The reason for this is probably the use of numerical erosion which removes the target material, and thereby reduces the rotational force on the projectile for non-normal impacts, i.e. with impact of an inclined target. However, to be able to predict warhead performance against hardened structures of different types it is necessary to verify the use of these types of models for other target configurations and materials.

It is clear that the 3D simulations can give additional and valuable information considering projectile penetration. The use of 3D models allows oblique impact, as well as simulations with varying yaw and pitch, and needs to be considered for accurate predictions of the interaction between target and projectile. Both experiments and simulations show that non-normal impacts of the projectile results in increased stresses in the projectile during the penetration phase due to lateral forces.

Considering the concrete material description, the RHT model seems promising. However, to be able to predict penetration depths in concrete it is important that correct material properties are determined for the material used. This requires extensive laboratory testing at high pressures and deformation rates of the concrete type used. Further, enhanced descriptions of the damage evolution and residual strength of concrete using the RHT model have been developed by Schuler (2004). These types of modifications to the material model will enhance the possibilities to accurately predict effects from penetrating warheads with large length to diameter ratios, shaped charges, dual charge warheads and multiple impact attacks on hardened concrete structures.

Parameters for yield and damage models describing the used steel casing material for the projectile need to be determined for future studies of penetration in reinforced concrete and high performance concrete (HPC).

For penetration simulations it is necessary to use numerical erosion for Lagrangian or ALE elements. For Lagrangian models it seems that an erosion strain of 1 to 2 give acceptable estimations of penetration depths in normal strength concretes, when compared with available

experimental penetration performance. However, for simulations performed using a Lagrangian element formulation it is difficult to distinguish between errors caused by numerical problems, such as distorted elements and erosion, and errors caused by the material models. To avoid this unphysical behaviour it is necessary to use Eulerian or meshfree methods, e.g. SPH. Both Euler and SPH formulations make it possible to retain both the material of the target and confinement around the projectile during the simulation. However, Eulerian element formulation, or ALE formulations with the use of remeshing, cannot be used for reinforced targets. The reason for this is that the mesh, or nodes, with concrete material needs to interact with the reinforcement mesh during the deformation of the target. Therefore, a combination of SPH nodes and beam elements is more suitable for simulations of reinforced concrete targets in the future. The use of the SPH formulation is likely to also improve the behaviour of models of unreinforced concrete targets, especially for cases with non-normal impacts.

The energy error for the simulation includes energy lost due to the friction between parts in the model, this energy should be stored as a separate variable to distinguish it from the energy errors for the simulation.

Simulations of penetration in concrete with the use of the RHT material model seems to give acceptable results if the dominating mode of failure for the concrete is crushing, e.g. deep penetration into confined concrete. If the concrete fails due to tensile cracking, e.g. caused by radial expansion of an unreinforced target, the accuracy of the predictions of the penetration depth is considerably reduced. Further, calculated exit velocities after perforation, and also ballistic limits of concrete targets, is likely to be strongly influenced by the tensile failure description. However, the RHT material model might work well for cases were crater formation and radial cracking are prohibited, i.e. for heavily reinforced concrete structures. Further, the used parameters for the pressure dependent yield strength of the concrete is determined for a concrete with a compressive strength of only 35 MPa, and thereby it is likely that the strength of the material during the penetration is slightly overestimated. The simulation results are likely to improve with the use of a pressure dependent yield surface determined by tri-axial testing for the specific concrete, or for a similar type of concrete. This also applies to the parameters describing tensile and shear strength of the used concrete.

The underestimation of the penetration depth obtained by numerical simulation using the RHT material model is likely to be caused by the tensile failure description for the RHT model, and its limited ability to model the tensile cracking and crater formation at the front face of the target. It is likely that the penetration resistance is relatively low during this first part of the projectile penetration, when compared to the penetration resistance of the deeper parts of the concrete targets. However, the numerical models can be enhanced with additional tensile failure conditions to better describe the crater formation and radial cracking of concrete targets. A model for the strain rate dependent tensile strength for concrete subjected to strain rates in the range 1×10^{-6} to 160 s^{-1} is reported by Malvar and Ross (1998). These equations are given below. Figure 5.1 shows the dynamic increase factor for a concrete with 48 MPa compressive strength.

$$DIF = \frac{f_t}{f_{ts}} = \left(\frac{\dot{\varepsilon}}{\dot{\varepsilon}_s}\right)^{\delta} \qquad \text{for } \dot{\varepsilon} \le 1\,s^{-1} \tag{4}$$

$$DIF = \frac{f_t}{f_{ts}} = \beta\left(\frac{\dot{\varepsilon}}{\dot{\varepsilon}_s}\right)^{1/3} \qquad \text{for } 1\,s^{-1} < \dot{\varepsilon} \le 160\,s^{-1} \tag{5}$$

where

f_t = dynamic tensile strength at $\dot{\varepsilon}$
f_{ts} = static tensile strength at $\dot{\varepsilon}_s$
f_t/f_{ts} = DIF (dynamic increase factor)
$\dot{\varepsilon}$ = strain rate, with a valid range of 1×10^{-6} to 160 s^{-1}
$\dot{\varepsilon}_s$ = 1×10^{-6} s^{-1} (static strain rate)
$\log \beta = 6\delta-2$

$$\delta = \frac{1}{1+\frac{8f'_c}{f'_{co}}}$$

f'_{co} = 10 MPa
f'_c = uni-axial compressive strength (MPa)

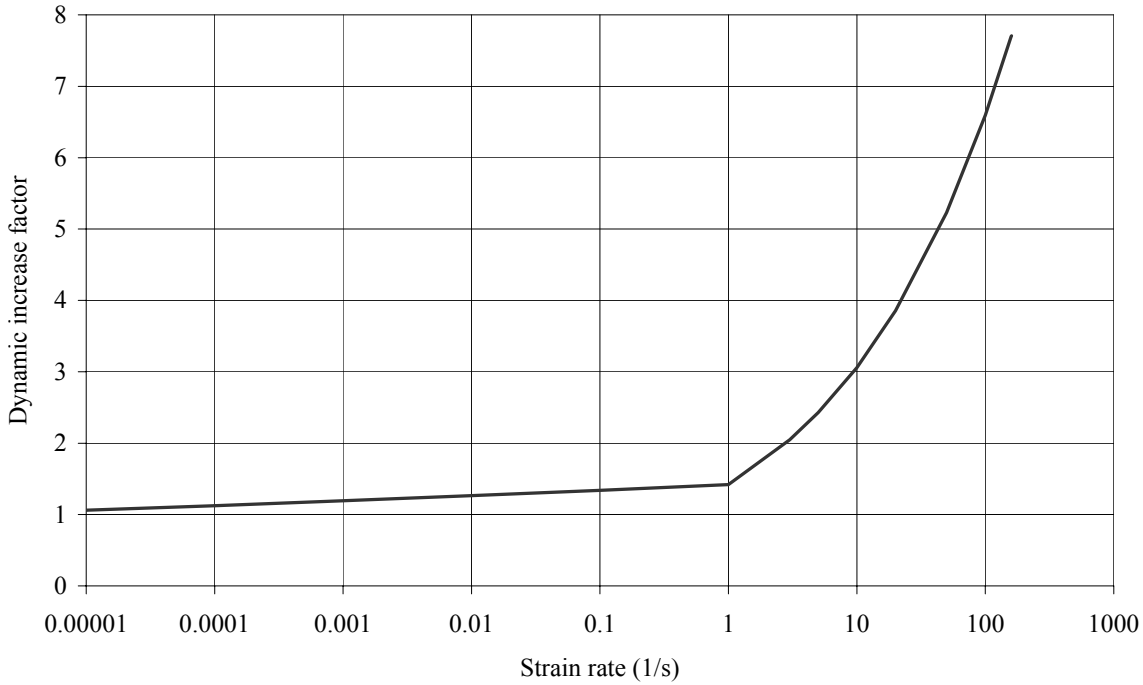

Figure 5.1. Dynamic increase factor for the tensile strength of a concrete with 48 MPa compressive strength vs. strain rate (Malvar and Ross, 1998).

This type of material description enhances the possibility to predict concrete penetration, and may also be suitable for determinations of the ballistic limit for concrete targets. Further, it seems that it is probably necessary to use a fracture energy that corresponds to a dynamic tensile failure at high strain rates, i.e. spalling, for this type of simulations. Therefore, it is necessary to determine the dynamic tensile strength and fracture energy for the used concrete material. A material model that includes strain rate dependent tensile strength and fracture energy, e.g. Schuler (2004), is therefore likely to improve the prediction performance of the penetration into concrete targets.

A tensile failure model with a bi-linear crack softening relationship for concrete is implemented as an user defined model in Autodyn by Leppänen (2004). The failure model also uses the strain rate dependency for the tensile strength described above. However, this crack softening tensile failure model uses a fracture energy that is independent of strain rate. This assumption is based on Weerheijm (1992). However, an increase of the fracture energy for a normal strength concrete by a factor of 2.5 from quasi-static tests (1×10^{-3} s^{-1}) to dynamic tests with a strain rate of 50 s^{-1} is

reported by Schuler et al. (2003) and Schuler (2004). A crack softening failure model that considers the dependence of the crack opening velocity might be necessary to use for penetration simulations. Improvements to the tensile failure model implemented by Leppänen (2004) are currently performed within another project at FOI to further enhance the tensile failure description of concrete (Magnusson and Hansson, 2005). However, main focus of this work is the behaviour of air blast loaded reinforced concrete structures.

The use of symmetry planes to reduce the number of elements, and thereby the required memory and CPU time, sets constraints to the nodes along these planes. This may influence the local results along these planes, e.g. damage evolution. However, the influence on the global response for the models seems to be small. This assumption is only valid for normal strength concrete, and the influence of the constraints along the symmetry planes may increase for more brittle material, e.g. High Performance Concrete (HPC). The use of tensile crack softening material models may also be more sensitive to constraints along symmetry planes.

The solid elements for concrete in the central part of the target and the beam elements for the reinforcement should have the same length, in order to avoid hourglass deformations of the solid elements. Hourglass deformations, or other zero energy modes, will induce damage propagation in the solid elements, and thereby the strength of the target is likely to be reduced. This is even more important if structural response is considered, e.g. failure of air blast loaded reinforced concrete beams.

Empirical equations for penetration in concrete can be used in a limited number of penetration cases, e.g. normal impact of semi-infinite unreinforced concrete targets. These equations normally neglect yaw and pitch of projectiles, and projectile deformations are not considered. For further discussion regarding empirical equations see Hansson (2005), where a semi-empirical model is suggested and compared with the experimental data.

5.2. Simulation recommendations

An estimation of the importance of different parameters for the simulations, together with other recommendations regarding penetration simulations are compiled below.

Parameters that are likely to have a major influence on the results of penetration and perforation simulations of concrete targets are the following:

- The element size in the target.
- The friction coefficient for the interaction between target and projectile.
- Parameters for the pressure dependent strength of the concrete
- The tensile failure criteria.
- The flow rule for the return to the yield surface in crack softening fracture models.
- The parameters for the damage evolution, including the chosen damage model for the concrete.

These parameters need to be chosen with care to obtain useful results from the simulations, and further work may be needed to obtain reliable simulation results.

The following parameters are likely to have a minor influence on the results of penetration and perforation simulation:

The initial compaction pressure (p_{crush}) within reasonable ranges.
Initial density of the concrete for values between 2.314 g/cm^3 and 2.330 g/cm^3.
Erosion strain of the concrete for values between 1 and 2.

The influence of the following parameters needs to be further investigated to determine their importance on the results of penetration simulations results:

The fracture energy of the concrete, and its variation due to different strain rates.
The volumetric compaction of the concrete during penetration.
The chosen numerical method, e.g. Lagrange elements or the meshless SPH method.

Recommendations for simulations of concrete penetration using Autodyn 3D, Lagrange elements and the RHT material model are given in tables 5.4 to 5.6. These material parameters and simulation rules show reasonable simulation results of penetration into concrete targets, and also perforation of concrete targets, when compared to test data.

The data set in table 5.6 is for the use of the RHT model without any additional failure conditions, this model may be used for both unreinforced and heavily reinforced concrete as discussed earlier. The use of an additional tensile failure condition might enhance the prediction of exit velocity of a thin target. However, further work is needed to use this type of material model with crack softening failure models and the recommendation for the moment is to use the original damage model also for tensile failure of the concrete. Furthermore, this type of modelling of the tensile failure doesn't seem to be appropriate for thick targets or reinforced targets where the penetrator is stopped, and the models also seems more sensitive to the element size that is used. Different sets of material parameters should be used for other types of loading, e.g. for simulation of structural response (Magnusson and Hansson, 2005).

Table 5.4. Recommended parameters for the P-α equation of state for penetration simulations for a normal strength concrete with approximately 48 MPa compressive strength.

Parameter	**Value**	**Parameter**	**Value**
ρ	2.314 g/cm^3	A_1	35.27 GPa
ρ_{porous}	2.314 g/cm^3	A_2	39.58 GPa
C_{porous}	3000 m/s	A_3	9.04 GPa
p_{crush}	35.0 MPa	B_0	1.22
p_{lock}	6000 MPa	B_1	1.22
n	3	T_1	35.27 GPa
Solid EOS	Polynomial	T_2	0 GPa
ρ_{solid}	2.75 g/cm^3	T_{ref}	300 K
		C_v	654 J/kgK

Table 5.5. Recommended parameters for numerical erosion of the concrete target, interaction between target and projectile, and reinforcement modelling.

Parameter	**Value**
Erosion criteria for concrete, i.e. solid elements.	Geometric strain
Erosion strain for concrete	2
Friction coefficient between concrete and projectile	0.05
Recommended minimum no. of elements across the diameter of a projectile [a]	10
Erosion criteria for reinforcement, i.e. beam elements.	Geometric strain
Ratio of the lengths for solid elements in target and beam elements for reinforcement	1:1

Note: [a] The recommended maximum elements size in the target should be equal to the element size for the projectile.

Table 5.6. Recommended input parameters for RHT model without additional tensile failure conditions, for a normal strength concrete with 48 MPa compressive strength.

Parameter	**Recommended data set**
Type of model	RHT model without additional failure conditions.
G	16.7 GPa
f_c	48.0 MPa
f_t/f_c	0.0833 (f_t= 4.0 MPa)
f_s/f_c	0.18
A	1.60
N	0.61
Q_2	0.6805
BQ	0.0105
$\frac{G_{elastic}}{G_{elastic} - G_{plastic}}$	2
$f_{t,\,elastic}/f_t$	0.70
$f_{c,\,elastic}/f_c$	0.53
Cap option	Yes
B	1.6
M	0.61
α	0.032
δ	0.036
D_1	0.04
D_2	1
$\varepsilon_{fail,\,min}$	0.01
$G_{residual}/G_{elastic}$	0.13
Tensile failure model	Hydro tensile limit [a]
Crack softening	---
$\sigma_{tensile\ failure}$	Not used
$\tau_{maximum}$	Not used
Gf	Not used
Bulking option	--
Comment	Limited ability to consider tensile failure, e.g. due to radial cracking.

Note: [a] The use of "Hydro tensile limit" results in the use of the original damage evolution desciption for the RHT material model.

This page intentionally blank.

6. Future research and development

It is recommended that a methodology for prediction of weapon effects on hardened structures, including field fortifications and civilian structures, should be established. This requires that several of the research topics mentioned below needs to be investigated, and the results should then be used to develop a methodology that can predict the overall behaviour of protective structures. When a methodology is established it is recommended to be used to estimate the weapon effects for penetration cases that are available from the literature to increase the number of studied projectiles and targets types. This is needed to show the limitations for the used methodology, and also verify for which cases the used approach will produce acceptable results. This type of methodology is not limited to the type of penetrators studied here, rather when established it should be easily adapted to a large number of different types of weapons and protective constructions.

Simulations were only performed with projectiles with a CRH value of 8. Since tests were performed using projectiles with CRH values of both 3 and 12 (Hansson, 2005), further simulations with these projectile designs are likely to enhance the understanding of the interaction between target and penetrator. It is only the targets with the fine meshes that are suitable for this type of study, even if the coarse mesh may be used to get a quick estimate in some cases. Further, material tests to establish parameters, including failure conditions, for the used projectile material are necessary to further study the interaction between projectile and target. Furthermore, a study of the friction forces between target and projectile is also recommended to enhance the understanding of projectile and target interactions. Research of different projectile designs, e.g. nose geometries, are of interest in the future to predict the penetration performance and behaviour of different types of warheads in targets.

Simulations of the penetration tests performed in high performance concrete (Hansson, 2003b and 2005) are also recommended. Material parameters for the P-α equation of state and the RHT material model were determined at EMI by Wicklein and Riedel (2002), and Riedel and Machens (2004). This makes it possible to combine material data determined for a specific high performance concrete, together with penetration results obtained for the same type of material. Thereby, a direct comparison of the experimental results and numerical simulations are possible to perform. It is likely that the used material models needs to be modified to better describe the mechanical behaviour of the HPC. Further, the properties for different types of HPC, also for HPC with equal uni-axial compressive strength, varies more than for normal strength concrete.

Since many structures uses geological material for backfilling and/or protective layers it is of interest to determine the influence from these layers on the penetration performance of warheads, especially for warheads with shaped charges, including dual-charge warheads. High performance concrete and geological materials seems to have a high penetration resistance against shaped charge penetration in relation to the density of the materials,. Additional work within this area is performed at FOI (Elfving and Karlsson, 2003, Elfving, 2003, and Elfving et al., 2005).

Research regarding close in detonations, and also contact detonations, are needed to describe the residual performance of a defeated penetrating warhead. Further, this area of work should be combined with studies of structural response from detonations close to a protective structure, e.g. verification of structural behaviour simulations. The results from this type of studies is needed to determine weapon effects from attacks with multiple warheads, and can also be used to estimate effects from terrorist attacks, both against civilian structures and protective structures used for out of area operations.

There is a possibility that the use of a combination of high strength construction materials, e.g. armour steels and high performance concrete, for burster slabs and other hardened structures may give a substantial decrease of the penetration depths compared with a normal strength concrete. A preliminary study of this is reported earlier (Hansson, 2004). However, the protection of hardened structures against attacks with shaped charges, and dual charge warheads that include a shaped charge, need to be further discussed and investigated. The use of a shaped charge as pre-cursor charge is likely to enhance the penetration performance of penetrating warheads, and especially for non-normal impact conditions were the bending forces on the projectile is likely to be considerably reduced. To protect hardened structures from these types of warheads it is probably necessary to use additional protection constructions and systems. A suitable research area for the use of meshless formulations or Euler formulations combined with advanced material models in the near future are studies of the effects from penetrating dual charge warheads.

Research regarding the damage evolution in concrete is necessary to further enhance the possibility to estimate penetration performance of projectiles by the use of simulations. At EMI (Ernst-Mach-Institut) another improved damage model for concrete ha been developed (Schuler, 2004). This improved failure model considers the influence of strain rate on the tensile strength of concrete, and also the influence of the crack opening velocity on the fracture energy for concrete. The use of improved failure models is likely to enhance simulations of concrete penetration in the future. The most interesting areas where this new type of failure models can be used are to determine required thickness of protective concrete structures, damage due to contact detonations, estimations of shaped charge performance and studies of dual charge warheads.

An initial study of a dual charge warheads performance against concrete walls using the original implementation of the RHT material model and Autodyn 2D is reported by Helte et al. (2005), see figures 6.1 and 6.2. This wall breaching tandem warhead with a diameter of 114 mm is developed at FOI, and the warhead uses a single copper liner to form both a shaped charge jet and a ring shaped explosively formed penetrator. This EFP with a velocity of approximately 2000 m/s is intended to cut a relatively large hole through walls, e.g. reinforced concrete or brick walls. Different types of dual charge warheads are in use, or under development, in several sizes from man portable rocket propelled versions to cruise missiles. When used during urban combat this type of bunker busters will be much more effective than an ordinary shaped charge rocket propelled grenade. Further, this type of dual charge warheads may also be equipped with thermobaric warheads instead of a high explosive charge in the future.

Figure 6.1. Shape of a tandem warhead with jet and ring shaped EFP calculated 80 µs after detonation (Helte et al., 2005).

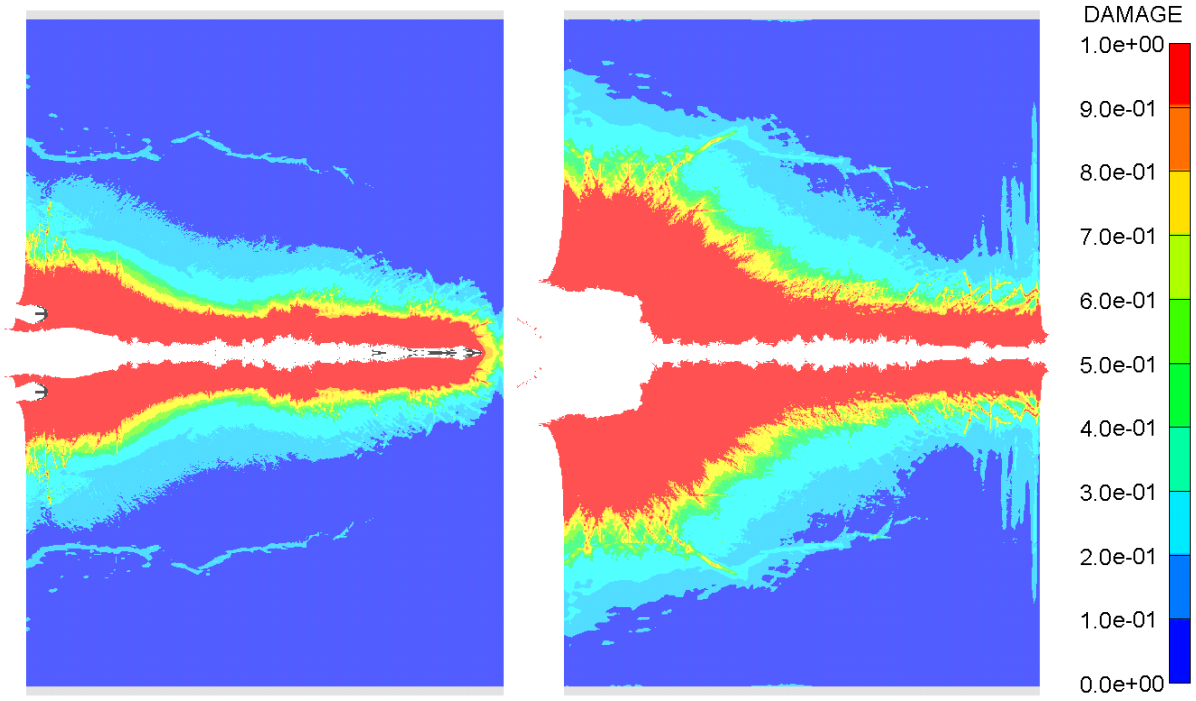

Figure 6.2. Cross section plots showing calculated damage levels in a 700 mm diameter concrete target for the warhead with jet and EFP at times 275 µs (left) and 450 µs (right) (Helte et al., 2005). Times are given relative to the time of detonation of the charge.

This page intentionally blank.

References

CEB-FIB model code 1990, published by Thomas Telford services for the Comité Euro-International du Béton, ISBN 0 7277 1696 4, London, 1993.

Elfving, C. and Karlsson, S.: Penetration of shaped charge warheads in buried fortifications, 11th Int. Sym. on Interaction of the Effects of Munitions with Structures, Mannheim, May 2003.

Elfving, C.: Verksamhet avseende RSV 2003, FOI Memo dnr 02-2394:4, FOI, Tumba, 2003.

Elfving, C., Karlsson, S. and Hansson, H.: Model for penetration of shaped charges in protective coverings, FOI-R--1680--SE, ISSN 1650-1942, Tumba, 2005.

Forrestal, M. J., Hightower, M. M., Luk, V. K. and Christensen, B. K.: Penetration and perforation of reinforced concrete targets, SAND--88-1467C, Sandia national laboratories, 1988.

Hansson, H.: 2D and 3D simulations of concrete penetration using the RHT material model, FOI-R--0922--SE, ISSN 1650-1942, Tumba, October 2003a.

Hansson, H.: Experimental study of concrete penetration for L/D=9 projectiles, FOI-RH--0226--SE, Tumba, October 2003b. Classification: HEMLIG/RESTRICTED.

Hansson, H.: Penetration in Armox 500 and concrete for a projectile with L/D=9, FOI-RH--0354--SE, Tumba, December 2004. Classification: HEMLIG/RESTRICTED.

Hansson, H.: Penetration in concrete for projectiles with L/D≈9, FOI-R--1659--SE, ISSN 1650-1942, Tumba, June 2005.

Helte, A., Calsson, T., Hansson, H., Karlsson, S., Lundgren, J., Westerling, L. and Örnhed, H.: Wall breaching tandem warhead, 22nd Int. Sym. on Ballistics, Vancouver, 2005.

Herrmann, W.: Constitutive equation for the dynamic compaction of ductile porous materials, Journal of Applied Physics, Vol 40, No 6, 1969. pp. 2490-2499.

Johnson, G. R. and Cook, W.H.: A constitutive model and data for metals subjected to large strains, high strain rates, and high temperatures. 7th International Symposium on Ballistics. Holland, 1983. pp. 541-547.

Johnson, G. R. and Cook, W.H.: Fracture characteristics of three metals subjected to various strains, strain rates, temperatures and pressures, Engineering Fracture Mechanics, Vol 21, No. 1, pp 31-48, 1985.

Leppänen, J.: Concrete structures subjected to fragment impacts - Dynamic behaviour and material modelling, Chalmers University of Technology, ISBN 91-7291-511-0, Gothenburg, 2004.

Li, Q. M. and Meng, H.: About the dynamic strength enhancement of concrete-like materials in a split Hopkinson pressure bar test, Int. J. of Solids and Structures, Vol. 40, Issue 2, pp 343-360, January 2003.

Malvar, L.J. and Crawford, J.E.: Dynamic increase factors for steel reinforcing bars, 28th Department of Defence Explosives Safety Seminar (DDESB), 1998.

Malvar, L.J. and Ross, C.A.: Review of static and dynamic properties of concrete in tension, ACI Materials Journal, vol. 95, no. 6, November-December 1998.

Magnusson, J. and Hansson, H.: Simulations of structural reinforced concrete elements, FOI-R--1764--SE, Tumba, December 2005.

Magnusson, J., Unosson, M. and Carlberg, A.: High performance concrete ”HPC” - Field experiments and production, FOI-R--0256--SE, Tumba, November 2001.

Meyer, M. A.: Dynamic behavior of materials, John Wiley & Sons inc., ISBN 0-471-58262-X, 1994.

Riedel, W.: Beton unter dynamishen lasten, Meso- und makromechanische modelle und ihre parameter. EMI-Bericht 6/00, Freiburg, July 2000.

Riedel, W. and Machens, M.: Mechanical properties of concrete and limestone, EMI Report E 07/04, Freiburg, 2004.

Schuler, H., Mayrhofer, C. and Thoma, K.: Experimental determination of damage parameters and implementation into a new damage law, 11th Int. Sym. on the Effects of Munitions with Structures, Mannheim, May 2003.

Schuler, H.: Experimentelle und numerische untersuchungen zur schädigung von stossbeanspruchten beton, Fraunhofer, Institut Kurzzeitdynamik Ernst-Mach-Institut, ISBN 3-8167-6463-0, Freiburg, 2004.

Wicklein, M. and Riedel, W.: Mesomechanical characterization of a high strength concrete - Experimental investigation and material modelling, EMI Report E 14/02, Freiburg 2002.

William, K.J. and Warnke, E.P.: Constitutive model for the triaxial behaviour of concrete, Int. Association of Bridge and Structural Engineers, Seminar on concrete structure subjected to triaxial Stresses, IABSE Proceedings 19, Italy, 1975.

Weerheijm, J.: Concrete under impact loading and lateral compression, Delft University of Technology, The Netherlands, 1992.

Appendix 1: General definitions of parameters

Some frequently used definitions and their relationships are shown in table A1.1 below.

Table A1.1. General parameters and their relationships.

Parameter	Definition / Relationship
Sound velocity	c
Mass	m
Volume	v
Stress	σ
Density	$\rho = m/v$
Initial density	$\rho_0 = m/v_0$
Strain rate	$\dot{\varepsilon} = \varepsilon/t$
Bulk modulus	$K = \rho \cdot c^2 = \frac{E}{3(1-2\nu)}$
Poison's ratio	$\nu = \frac{E}{2G} - 1$
Young's modulus	$E = \sigma/\varepsilon = 3K(1-2\nu) = 2G(1+\nu)$ $E = \frac{9K}{1+3K/G}$
Shear modulus	$G = \frac{E}{2(1+\nu)}$
Compression	$\mu = \frac{\rho}{\rho_0} - 1$
Linear EOS	$P = \mu \cdot K$
Polynomial EOS (general expression)	$P = A_1\mu + A_2\mu^2 + A_3\mu^3$

This page is intentionally blank

Appendix 2: Material models and parameters

The material models for steel, reinforcement and concrete are described in this appendix. The used values for the material parameters are also compiled in this appendix.

Appendix 2.1: Material model for the steel

The standard steel materials S-7 and 1006 are used for the description of steel for projectile and confinement of concrete targets, with the use of the Johnson and Cook (1983) material model combined with a shock (Mie-Grüneisen) equation of state. However to avoid local deformation of the elements in the nose of the projectile it was necessary to increase the yield strength for these elements. A more thorough description of the material model is given by for example Meyer (1994).

The equation of state for the steel projectile is given by a shock equation of state, where pressure as a function of density and specific internal energy e is described by a Mie-Grüneisen form of EOS based on the shock Hugoniot.

$$P = P_H + \Gamma\rho(e - e_H) \qquad \text{(eq A-1)}$$

where it is assumed that $\Gamma\rho = \Gamma_0\rho_0 =$ constant and

$$P_H = \frac{\rho_0 c_0{}^2 \mu(1+\mu)}{\left[1-(s-1)\mu\right]^2} \qquad \text{(eq A-2)}$$

$$e_H = \frac{1}{2}\frac{P_H}{\rho_0}\left(\frac{\mu}{1+\mu}\right) \qquad \text{(eq A-3)}$$

The Grüneisen gamma is defined as $\Gamma = \frac{1}{\rho}\left(\frac{dp}{de}\right)_v$.

Thus, the pressure and internal energy of the material are related to the pressure and internal energy for a point on the Hugoniot with the same volume. Further, as seen in the Mie-Grüneisen form the pressure varies linearly with internal energy at constant volume. The input data for the Mie-Grüneisen EOS is usually given as a linear relationship between the shock velocity (U_s) and the particle velocity (u_p), which can be related to other necessary parameters, see for example Meyer (1994). The equation for the "shock" equation of state used for the projectile is found below, with the notation used in Autodyn.

$$U_s = c_0 + s\,u_p \qquad \text{(eq A-4)}$$

With c_0 being the sound velocity at zero pressure and s is the slope in a plot of shock velocity versus particle velocity. Tables A2.1 and A2.2 presents the necessary material data for the shock equation of state for the steels.

The Johnson and Cook (1983) material model describes the relation between the flow stress σ of a metal and the plastic strain ε, plastic strain rate $\dot{\varepsilon}$ and temperature T. The J&C equation has successfully been used to describe the constitutive behaviour of a number of metals and is very often used for penetration simulation. Even if the projectile behaves more or less as a rigid body, it is suitable to use a deformable projectile for the simulations. The reason is to get

feedback on the projectile behaviour and limit the stresses in the projectile. The J&C model is described by the equation below.

$$\sigma = \left(A + B\varepsilon^{n} \right)\left(1 + C \ln \frac{\dot{\varepsilon}}{\dot{\varepsilon}_0} \right)\left(1 - \left(\frac{T - T_r}{T_m - T_r} \right)^{m} \right) \qquad \text{(eq A-5)}$$

In this equation, T_r and $\dot{\varepsilon}_0$ are reference temperature (room temperature) and reference strain rate (1 s^{-1}) at which the material parameters A, B and n are determined. The constant C in the second term takes the strain rate dependency into account. Finally, in the third term, T_m is the melting temperature and m is a parameter that includes the effect of temperature on the flow stress. It is emphasised that the model is semi-empirical and that influence of strain hardening, strain rate and temperature are decoupled from each other. Material parameters for the steels are shown in tables A2.1 and A2.2.

Table A2.1. Material model for the projectile (Steel S-7).

Shock equation of state		Johnson & Cook strength model	
Reference density	7.83 g/cm^3	Shear modulus	81.8 GPa
Grüneisen gamma, Γ	2.17	Yield stress, A	1539 MPa [a]
Parameter c_0	4569 m/s	Hardening constant, B	477 MPa
Parameter s	1.49	Hardening exponent, n	0.18
Reference temperature	300 K	Strain rate constant, C	0.012
Specific heat	477 J/kgK	Thermal softening exponent, m	1.0
		Melting temperature, T_m	1763 K

Note: [a] A value of 2500 MPa was used for the yield strength of the first elements in the nose of the projectile to avoid large local deformations.

Table A2.2. Material model for the steel confinement (1006 steel).

Shock equation of state		Johnson & Cook strength model	
Reference density	7.83 g/cm^3	Shear modulus	81.8 GPa
Grüneisen gamma, Γ	2.17	Yield stress, A	350 MPa
Parameter c_0	4569 m/s	Hardening constant, B	275 MPa
Parameter s	1.49	Hardening exponent, n	0.36
Reference temperature	300 K	Strain rate constant, C	0.022
Specific heat	452 J/kgK	Thermal softening exponent, m	1.0
		Melting temperature, T_m	1811 K

Appendix 2.2: Material model for steel bars

A piece-wise linear strain hardening model with thermal softening and strain rate dependence together with a linear equation of state are used for the steel rebars. The parameters for the B500BT type 1 rebar steel are based on quasi-static testing at a strain rate of approximately 0.0003 s^{-1}. The nominal yield stress for this steel is 500 MPa. The stress-strain relationship for a representative steel bar and the used approximation for the numerical model are shown in figure A2.1, and data from standard tests of rebars are shown in table A2.3. Post failure conditions of a rebar is shown in figure A2.2. The dependence on the measurement length on the elongation of a bar at failure is shown in figure A2.3. This data can be used to estimate the failure strain for beam elements in simulations.

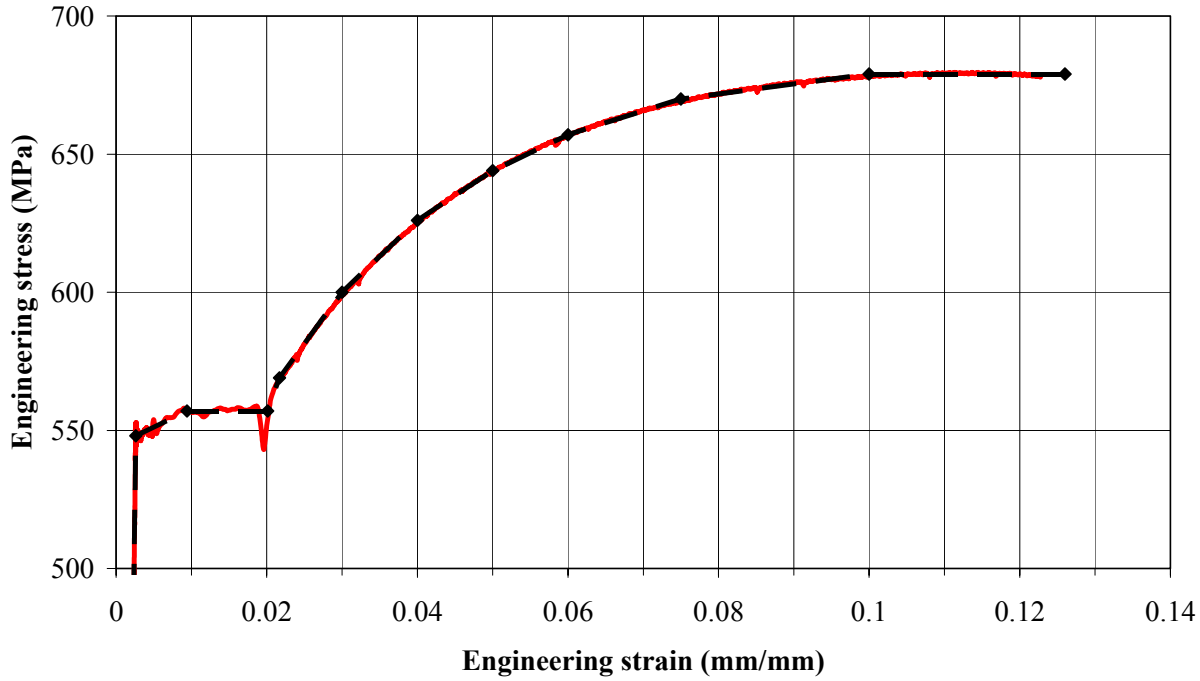

Figure A2.1. Stress strain relationship for B500BT type 1 bars compared with tensile test of a representative bar (no. 16-4). Note that the strain refers to elongation of the bar and not true strain, and the stress is also calculated with respect to the original cross section of the bar.

Table A2.3. Test results from standard tensile testing of B500BT type 1 rebars.

Bar no.	Nominal diameter	Upper yield stress (R_{eH})	Ultimate stress (R_m)	Elongation A_{10}	Ultimate strain [a]
12-1	12 mm	601 MPa	694 MPa	16.5%	10%
12-2	12 mm	604 MPa	701 MPa	18%	10%
12-3	12 mm	540 MPa	647 MPa	20%	13%
12-4	12 mm	576 MPa	672 MPa	19%	10%
16-1	16 mm	562 MPa	685 MPa	-----	13%
16-2	16 mm	539 MPa	633 MPa	19%	11%
16-3	16 mm	565 MPa	684 MPa	22%	14%
16-4	16 mm	553 MPa	680 MPa	19%	13.5%

Note: [a] Ultimate strain refers to the strain at ultimate stress before necking occurs.

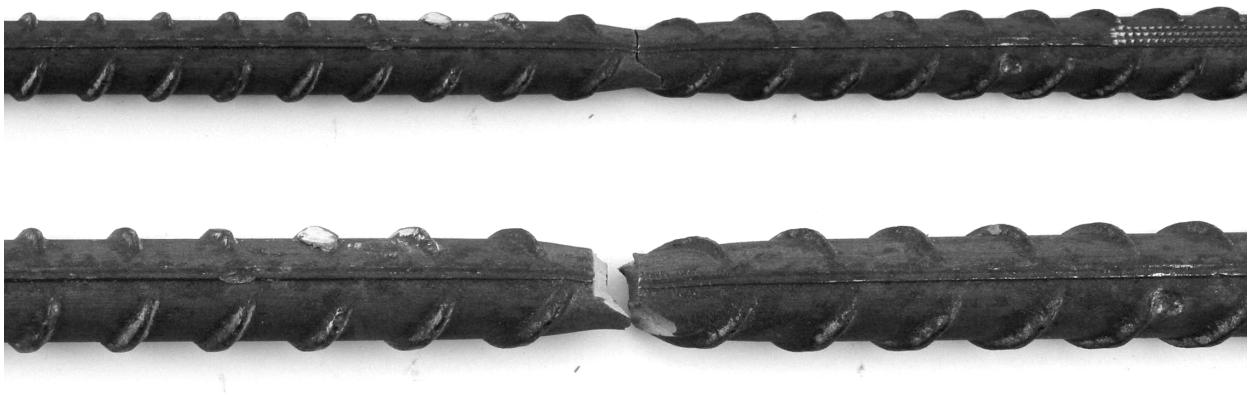

Figure A2.2. Example of post failure condition for a tested 16 mm rebar (bar no. 16-4).

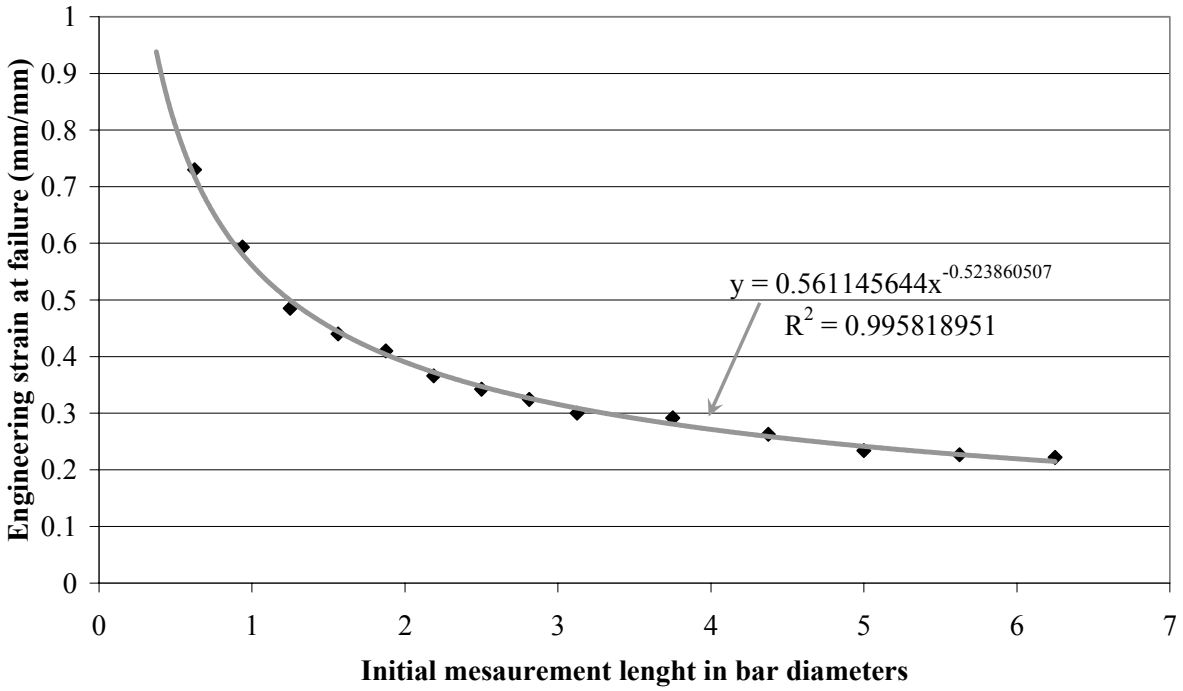

Figure A2.3. Example of failure strain vs. initial measurement length for a 16 mm B500BT rebar (bar no. 16-4).

The material model uses the same strain rate dependence and thermal softening for the strength as J&C model described earlier. The ultimate strain at the ultimate stress before necking for the reinforcement is used as failure strain for the material model. The model uses a value of 12.6% elongation of the bar/truss elements for the failure of the bar in longitudinal direction. To obtain a better material description it is necessary to determine the relationship between stress and strain also for strain greater than the ultimate strain during the necking phase of the deformation. However, the chosen gauge length will effect the value of the strain during the necking part of the deformation. The elongation measured over a distance equal to 10 diameters (A_{10}) is approximately 18 to 22 % for the B500BT type 1 rebar steel, see table A2.3. The strain rate dependence and thermal softening parameters for 4340 steel may be used for this type of rebars, see table A2.4. This is assumed to be a reasonable approximation to obtain a relevant material model for this steel, specially since both strain rate and temperature in the rebars are relatively low for these types of simulations. Dynamic increase factors for ASTM rebar steels are reported by Malvar and Crawford (1998) and more suitable material parameters for the strain rate dependence may be determined from this data. The ASTM A615 grade 75 have roughly the same strength (see table A2.5.), and strain rate parameters determined for this steel might be acceptable for the B500BT type 1 steel. An even better material description is possible to obtain from material tests of the used type of rebar steel at different strain rates and temperatures.

Table A2.4. Elastic behaviour, strain rate and thermal softening parameters used for rebars.

Parameter	**Value**
Bulk modulus	159 GPa
Shear modulus	81.8 GPa
Strain rate constant, C	0.014
Thermal softening exponent m	1.03
Melting temperature [1], T_m	1793 K

Table A2.5. Best estimate properties of ASTM A615 bars (Malvar and Crawford, 1998).

ASTM A615 grade	**Nominal strength**	**Yield stress**	**Ultimate stress**	**Ultimate strain [b]**
40 [a]	276 MPa	331 MPa	559 MPa	15.5%
60 [a]	414 MPa	476 MPa	752 MPa	12%
75 [a]	518 MPa	600 MPa	821 MPa	7%

Note: [a] The grade refers to nominal strength in ksi.
[b] Ultimate strain refers to the strain at ultimate stress before necking occurs.

Appendix 2.3: Material model for the concrete

Concrete is a very complex composite material with aggregates, varying in size, embedded in a matrix of porous grout. Thus, due to the inherent inhomogenity it is difficult to describe the mechanical behaviour of the concrete. However, Herrman (1969) developed a general equation of state that takes porosity into account and this has been incorporated as an important part of the concrete material model discussed below. The RHT strength model includes residual strength of the failed material under compression. The main components of the material model are given here, while further details of the material model are given by Herrman (1969) and Riedel (2000). Material parameters for a standard concrete with a uni-axial compressive strength (f_c) of 35 MPa are given by Riedel (2000). A thorough description of the model can be found in this Ph.D. thesis. The yield surfaces of the concrete for the material model are scaled with reference to the f_c for the concrete. Therefore, the measured uni-axial strength for the concrete is used for the parameter f_c in the simulations.

Concrete has a non-linear compression behaviour due to the inhomogenity and the porosity of the material. Herrman has proposed a porous equation of state that takes this into account. The equations below describe the most essential parts of the P-α model, and the entire parameter list used for the concrete EOS can be seen in table A2.5. The behaviour of the fully compacted material is, in this case, described with a polynomial according to equation A-6 for the compaction and tension states, while the porous material is scaled using the parameter α with respect to the fully compacted material as the reference. Thus, for the fully compacted material the pressure P equals P_{lock} and α is 1, and the pressure is calculated using equation A-6. For pressures between the initial compaction (P_{crush}) and P_{lock} the pressure is scaled with equation A-7. The compaction, $\alpha(P,e)$, gives the behaviour of the porous material in the pressure range of pore collapse (P_{crush}) and full compaction (P_{lock}). The recommended value for the initial compaction pressure in the equation of state is $2f_c/3$ (Riedel, 2000). In the case of deep penetration into concrete with large confining pressures, this value might be increased. Suitable values for this initial compaction pressure can be obtained by hydrostatic pressure testing of the used concrete type.

$$P = A_1\mu + A_2\mu^2 + A_3\mu^3 + (B_0 + B_1\mu)\rho_0 e \qquad for \quad \mu > 0 \quad with \quad \mu = \frac{\rho}{\rho_0} - 1 \qquad \text{(eq A-6a)}$$

$$P = T_1\mu + T_2\mu^2 + B_0\rho_0 e \qquad for \quad \mu < 0 \quad with \quad \mu = \frac{\rho}{\rho_0} - 1 \qquad \text{(eq A-6b)}$$

$$P = f(\rho, e) \quad \overset{porous}{\rightarrow} \quad P = f(\rho\alpha, e) \quad with \quad \alpha = 1 + (\alpha_{init} - 1)\left[\frac{P_{lock} - P}{P_{lock} - P_{crush}}\right]^n \qquad \text{(eq A-7)}$$

Considering the equation of state the pressure vs. density data is based on meso-mechanical simulations (Riedel, 2000). This relationship between pressure and density is determined under static loading. However, it is known that the relationship between pressure and density is influenced by the loading rate for the material. It has been shown that a high strain rate results in greater pressure for the same compaction of the concrete. According to this it is difficult to determine a correct EOS to be used for the concrete subjected to high strain rate loading from static tests. However, no dynamic data are available and the static values are used. Parameters for the P-α EOS as it is implemented in Autodyn are tabulated in table A2.6. Compared to equations A-6 and A-7 the additional parameters (T_1 and T_2) in table A2.6 corresponds to the polynomial equation of state in tension, while the $A_{1\text{-}3}$ are the compression EOS data for the

solid material. The heat capacity C_v is used for temperature (energy) calculations and the porous sound speed C_{porous} is related to the shock wave velocity in a similar manner as in equation A-4, see also Meyer (1994).

Table A2.6. P-α equation of state parameters for the concrete target (Riedel, 2000).

Parameter	Explanation	Value
ρ	Initial density	2.330 g/cm^3 [a]
ρ_{porous}	Porous density	2.314 g/cm^3
C_{porous}	Porous sound speed	3000 m/s
p_{crush}	Initial compaction pressure	23.3 to 64.0 MPa [b]
p_{lock}	Solid compaction pressure	6000 MPa
n	Compaction exponent n	3
Solid EOS	Type of solid EOS	Polynomial
ρ_{solid}	Reference density for solid EOS	2.75 g/cm^3
A_1	Parameter A_1 for polynomial EOS (compression)	35.27 GPa
A_2	Parameter A_2 for polynomial EOS (compression)	39.58 GPa
A_3	Parameter A_3 for polynomial EOS (compression)	9.04 GPa
B_0	Parameter B_1 for polynomial EOS	1.22
B_1	Parameter B_2 for polynomial EOS	1.22
T_1	Parameter T_1 for polynomial EOS (expansion)	35.27 GPa
T_2	Parameter T_2 for polynomial EOS (expansion)	0 GPa
T_{ref}	Reference temperature	300 K
C_v	Specific heat	654 J/kgK

Note: [a] Different values are used for this parameter, i.e. 2.330 and 2.314 g/cm^3, respectively.
[b] Different values are used for this parameter. The recommended value according to Riedel (2000) is $2f_c/3$.

Concrete, like many other hard and brittle materials, is sensitive to tensile loading and fractures at small deformations. On the other hand, with increasing pressure the strength of the concrete also increases. Further, in case of confinement the flow resistance of the crushed concrete under compression can be significant. The different tensile and compressive behaviour of the concrete under deformation together with the residual strength of the material under compression indicates that a complex strength model is needed. One material model for hydrocodes which include all these phenomena is the RHT concrete model (Riedel, 2000). The RHT model is described briefly in the following.

The descriptions of the stress state in the material model is based on the three invariants of the stress tensor for the definition of the elastic limit surface, failure surface and remaining residual strength surface for the crushed material, see figure A2.3. These three surfaces are all pressure dependent and described below. The failure surface can be seen as a function of the strength along the compression meridian $Y_{TXC}(P)$ multiplied by the factors $F_{Rate}(\dot{\varepsilon})$ and $R_3(\theta)$ as in equation A-8.

$$Y_{failure}(P,\theta,\varepsilon) = Y_{TXC}(P)F_{Rate}(\varepsilon)R_3(\theta) \qquad \text{(eq A-8)}$$

The strength along the meridian is given by equation A-9, where $Y^*_{TXC}(P)$ defines the pressure dependent curved meridian of three axial compression normalised to the unconfined compression strength f_c. Further, P^* and P^*_{spall} are normalised values of pressure and spall strength, while A and N are material constants characteristic for the specific concrete investigated.

$$Y^*_{TXC}(P) = \frac{Y_{TXC}(P)}{f_c} = A \cdot \left[P^* - \left(P^*_{spall} F_{Rate}\right)\right]^N \qquad \text{(eq A-9)}$$

The factor $F_{RATE}(\dot{\varepsilon})$ takes the strain rate enhancement into account and follows from equation A-10 below. As seen different strain rate enhancements are used in different pressure regions, with α and δ being material constants. Testing of concrete at increased strain rates using a split Hopkinson pressure bar (SHPB) have resulted in an increased dynamic compressive strength, e.g. is the CEB-FIB model code 1990 (1993) suggesting a bilinear approximation of the strain rate enhancement factor both in tension and compression. This results in a rapid increase of the dynamic compressive strength according to the CEB-FIB model code at a strain rate above of 30 s^{-1}. However, it seems that the major part of the dynamic increase of the compressive strain rate is related to the pressure dependent yield strength of concrete. Simulations of SHPB tests has shown that a pressure dependent constitutive model is likely to account for the major part of so called dynamic increase of the compressive strength for concrete subjected to strain rates higher than 30 s^{-1} (Li and Meng, 2003).

$$F_{RATE}(\dot{\varepsilon}) = \begin{cases} \left(\dfrac{\dot{\varepsilon}}{\dot{\varepsilon}_0}\right)^{\alpha} & for\ P > f_c/3\ ,\ with\ \dot{\varepsilon}_0 = 30\times10^{-6}\ s^{-1} \\ \left(\dfrac{\dot{\varepsilon}}{\dot{\varepsilon}_0}\right)^{\delta} & for\ P < f_c/3\ ,\ with\ \dot{\varepsilon}_0 = 3\times10^{-6}\ s^{-1} \end{cases} \qquad \text{(eq A-10)}$$

Reduced failure strength for states off the compression meridian on the failure surface is introduced and given by a factor $R_3(\theta)$. The factor, which scales the strength from the highest value at the compression meridian, is given by equation A-11. Thus, with θ rotating around the hydrostatic axis the entire failure surface can be calculated, see also figure A2.4.

$$R_3(\theta) = \frac{2\left(1-Q_2^2\right)\cos\theta + \left(2Q_2-1\right)\left[4\left(1-Q_2^2\right)\cos^2\theta + 5Q_2^2 - 4Q_2\right]^{\frac{1}{2}}}{4\left(1-Q_2^2\right)\cos^2\theta + \left(1-2Q_2\right)^2} \qquad \text{(eq A-11)}$$

The strength reduction as described by $R_3(\theta)$ depends also of Q_2. This parameter is the distance from the hydrostatic axis to the tensile meridian divided with the distance between the hydrostatic axis to the compressive meridian. The extreme case of Q_2 = 0.5 is found at low tensile pressures giving a triangular failure surface in the deviatoric plane. At the other extreme, Q_2 = 1, gives a circular cross section of yield surface. Thus at large confining pressures the surface approaches the circular form. The pressure dependence of Q_2 follows from equation A-12. This method to account for reduced concrete strength off the compression meridian was first used by William and Warnke (1975).

$$Q_2 = Q_{2,o} + BQ \cdot P^* \; with \; 0.51 \le Q_2 \le 1 \; and \; BQ = 0.0105 \qquad \text{(eq A-12)}$$

The elastic limiting surface is scaled around P=0 and σ_{eq}=0 from the failure surface and the scaling factors varies linearly, depending on the pressure, according to TENSRAT and COMPRAT. Where COMPRAT defines the ratio between the elastic compressive limit and the compressive strength and TENSRAT the corresponding ratio in tension. The slope of the elastic-plastic part is given by PREFACT, which defines the ratio between the original shear modulus and the corresponding value after the elastic limit has been passed. The elastic part of the deformation decreases at high pressures and the option to use a "cap" on the elastic surface ensures that the elastic surface closes at high pressures. Thus, by multiplying the right part of equation A-8 above with a dimensionless factor $F_{CAP}(P)$, which goes smoothly from unity to zero, the elastic surface can be forced to close at high pressures. The cap function is unity up to the pressure P_u where the uniaxial compression path intercepts with the elastic surface. At higher pressures $F_{CAP}(P)$ decreases and reaches zero at the pressure P_0, which is obtained from the pore crush pressure (p_{crush}) in the EOS input data. In equation A-13 below the mathematical expression for $F_{cap}(P)$ is given.

$$F_{CAP}(P) = \begin{cases} 1 \quad for \; P \le P_u \\ \sqrt{1 - \left(\dfrac{P - P_u}{P_o - P_u} \right)^2} \; for \; P_u < P < P_0 \\ 0 \; for \; P_0 \le P \end{cases} \qquad \text{(eq A-13)}$$

The damage in the material grows after the stress point passes the failure surface according to equations A-14 and A-15. Where the accumulated plastic strain $\Delta\varepsilon_p$ is compared to the failure strain $\varepsilon_p^{failure}$ which is pressure dependent and given by equation A-15 with the material parameters D_1 and D_2. At low pressures, a lower limit of the failure strain is set by introducing a minimum failure strain, $E_{f,min}$. The strain measures include here both volumetric and deviatoric contributions. Other improved damage models are under development, see Schuler et al. (2003).

$$D = \sum \frac{\Delta\varepsilon_p}{\varepsilon_p^{failure}} \qquad \text{(eq A-14)}$$

$$\varepsilon_p^{failure} = D_1 \left(P* - P*_{spall} \right)^{D_2} \qquad \text{(eq A-15)}$$

The residual strength $Y^*_{residual}$ (normalised to the unconfined compression strength) of the fully damaged concrete is calculated from equation A-16). The strength is then interpolated from the strength values for the undamaged material (D=0) at the failure surface and the completely damaged material (D=1) according to equation A-17.

$$Y^*_{residual} = B \cdot \left(P^* \right)^M \qquad \text{(eq A-16)}$$

$$Y^*_{fractured} = (1 - D) Y^*_{failure} + D \cdot Y^*_{residual} \qquad \text{(eq A-17)}$$

In figure A2.4 some of the characteristics of the RHT model are schematically shown. An important difference compared to the J&C strength model for the steel projectile is the pressure dependency of the strength. It is also important to note that concrete, under compression, has an additional strength surface for the failed material. The parameters for the model are compiled in table A2.7.

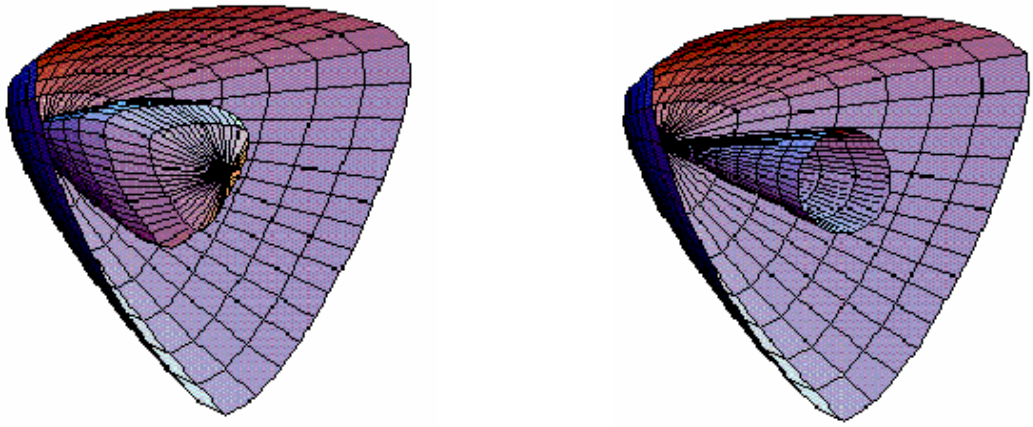

Figure A2.4. The left figure shows the failure surface (outer) and the elastic limit surface (inner), while the right show the failure surface (outer) and the residual strength surface (inner) as 3D-projections. After Riedel (2000).

The unconfined compressive strength f_c is 48 MPa based on uni-axial cylinder compression experiments. All other RHT constants are taken from results on similar concrete and can be found in the literature, Riedel (2000). The values used for the concrete RHT strength model are summarised in table A2.7. As seen, a large number of parameters are needed to give a complete characterisation of the concrete. Simulations with Lagrange or ALE formulations for the target also requires the use of numerical erosion to remove distorted elements, and the default value 2 for the erosion strain in the RHT model is used for these simulations.

Table A2.7. RHT strength model parameters for normal strength concrete (Riedel, 2000).

Parameter	Explanation	Value
G	Shear modulus	16.7 GPa
f_c	Compressive strength	48.0 MPa [a]
f_t/f_c	Tensile compressive strength ratio	0.0833, 0.10 [b, d]
f_s/f_c	Shear compressive strength ratio	0.18 [d]
A	Failure surface parameter A, initial slope of failure surface	1.60
N	Failure surface exponent N, pressure dependence for failure surface	0.61
Q_2	Tensile compression meridian ratio	0.6805
BQ	Brittle to ductile transition	0.0105
$\frac{G_{elastic}}{G_{elastic} - G_{plastic}}$	Ratio between elastic shear modulus and elastic-plastic shear modulus. (PREFACT)	2
$f_{t,\,elastic}/f_t$	Ratio between elastic surface and failure surface for tension (TENSRAT)	0.70
$f_{c,\,elastic}/f_c$	Ratio between elastic surface and failure surface for compression (COMPRAT)	0.53
Cap option	Use cap on elastic surface	Yes
B	Residual strength constant, initial slope of residual surface	1.6
M	Residual strength exponent, pressure dependence for residual surface	0.61
α	Compressive strain rate exponent	0.032
δ	Tensile strain rate exponent,	0.036
D_1	Damage constant	0.04
D_2	Damage exponent	1
$\varepsilon_{fail,\,min}$	Minimum strain to failure	0.01
$G_{residual}/G_{elastic}$	Residual shear modulus fraction (SHRATD)	0.13
Tensile failure model	Use of "Hydro tensile limit" or "Principal stress" for tensile failure description	Hydro tensile limit [c, d]
$\sigma_{tensile\ failure}$	Tensile failure stress for "Principal stress" failure condition	Not used [d]
$\tau_{maximum}$	Shear failure stress for "Principal stress" failure condition	Not used
Gf	Crack softening for "Principal stress" failure condition	Not used [d]

Note: [a] Value modified according to uni-axial cylinder test of the used concrete. The data set is originally developed for a concrete with 35 MPa compressive strength.
[b] Value modified to obtain different tensile strength, 0.10 is the recommended value for a concrete with 35 MPa compressive strength and an estimated value for a 45 MPa concrete is 0.0833.
[c] The use of “Hydro tensile limit” results in the use of the original damage evolution description for the RHT material model.
[d] Modified for use with tensile failure conditions.

This page intentionally blank.

Appendix 3: Penetration tests in a normal strength concrete

Appendix 3.1. Introduction

An experimental test of penetration in a normal strength concrete reported was performed during 2002, and was part of a larger test series that considered penetration in concrete with ogive nosed model projectiles. Three different concrete types were used for the performed tests, these were a normal strength concrete (NSC) with an uniaxial compressive strength of 40-45 MPa and HPC of two grades, with approximately 90 and 135 MPa unconfined compressive strength. A projectile design developed at FOI with a length to diameter (L/D) ratio of nine was used for the tests. These tests were earlier described by Hansson (2003b), and this appendix contains data from a reference test performed in normal strength concrete target.

Additional tests with a strengthened projectile were performed in 2004 (Hansson, 2005) in targets of NSC and the HPC with an uni-axial strength of 135 MPa. Eight of these tests are also given for references in this appendix.

Appendix 3.2. Experimental set up

Penetrators

A penetrator design developed at FOI was used for the tests. The diameter of the used model penetrator was 50 mm. The properties for the used projectile are given in table A3.1 below. The FOI designed projectile is shown in figure A3.1. The projectiles are fabricated from 34CrNiMo6 steel (Swedish standard SS 14 2541) with HV ≈500-600. Measured stress vs. strain for the used steel type at a nominal strain rate of approximately 400/s is shown in figure 2.3. Stress-strain relationship for the SS 14 2541 steel with HV 300 and 450 are also shown for comparison.

Ballast consisting of cement based mortar was used to obtain the desired mass of the projectiles for the earlier tests performed in 2002. An empty space of approximately 90 mm length was left between the mortar and the 10 mm base plate, i.e. the mortar was poured in the projectile to a distance of 350 mm measured from the projectile nose.

A dentist mould plaster, i.e. dental stone casting material, with a lower density than the mortar was used as ballast for the projectiles used for the tests performed in 2004. This, together with the increase of the casing thickness, results in a penetrator with increased performance compared with the earlier test series, see table A3.1.

Table A3.1. Properties of the used projectiles.

	Test series in 2002	**Test series in 2004**
Body diameter	50 mm	
Length	450 mm	
Total mass	≈ 3.65 kg	4.50 ±0.02 kg
Solid nose length	≈ 83 mm	≈ 85 mm
Case thickness for cylindrical section	5.0 mm	10.0 mm
Ogive radius	400 mm	
Casing material	34CrNiMo6 (SS 14 2541)	
Hardness of casing material	HRC 50.2-50.6 [a] HV 560-620 [a]	HV ≈500 [b]
Filling material	Cement based mortar with $\rho \approx 2.4 \times 10^3$ kg/m^3	Dental stone with $\rho \approx 1.8 \times 10^3$ kg/m^3

Note: [a] HRC and HV values were measured on a cross section of a projectile after the test series.
[b] HV values were measured on a cross section of an unused projectile.

Figure A3.1. The 50 mm diameter model scale projectile shown with guidance ring and aluminium pusher plate. The masses of the guidance ring and pusher plate are approximate 130 g and 350 g, respectively.

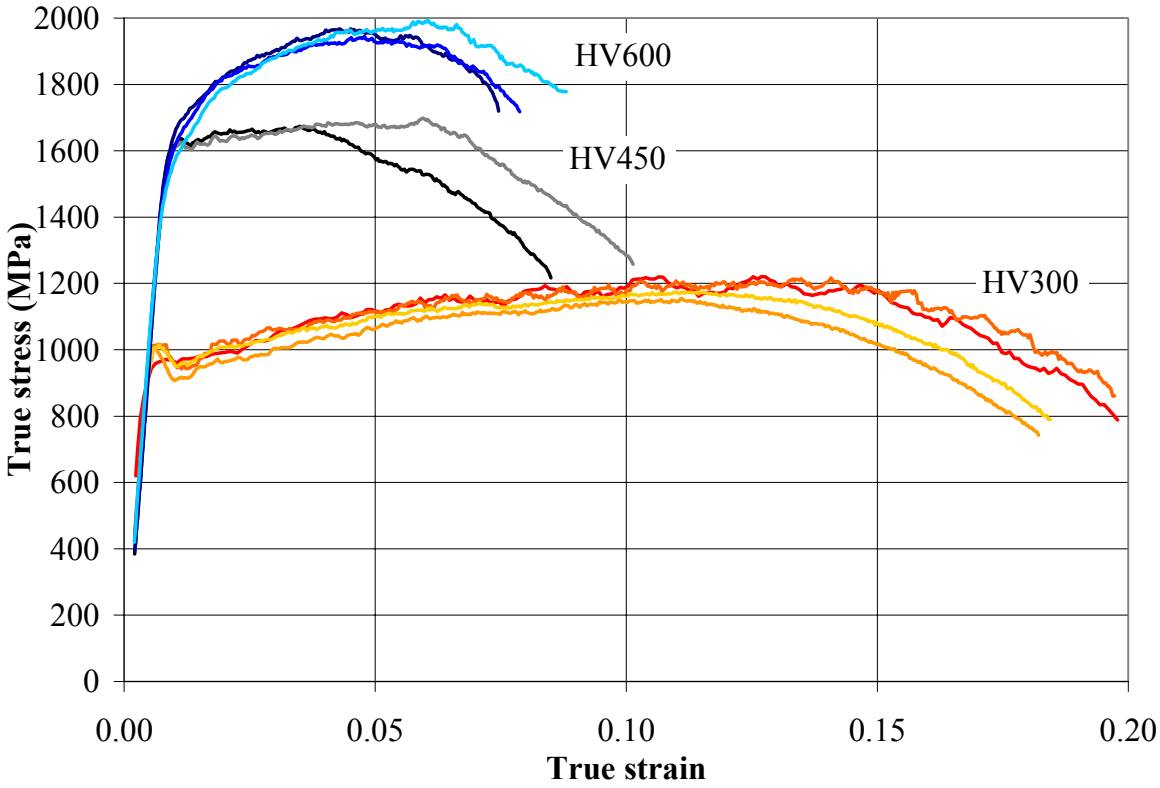

Figure A3.2. Measured stress-strain relationship at a nominal strain rate of approximately 400/s for SS 14 2541 steel with HV300, HV450 and HV600. The data in the figure are not valid for strains referring to necking of the samples.

Concrete types and targets

The experiment was performed with a normal strength concrete (NSC), see table A3.2. Mix proportions for the NSC is given in table A3.3 below. The concrete grade is designated by the approximate uniaxial cube ("Kub") strength in MPa, i.e. K45. The NSC target used in 2002 was cast in a steel pipe with 1.25 m diameter and 8 mm thickness of the material. The concrete was approximately eight months old when the test was performed. A few steel rebars were welded inside the steel cylinders to obtain an axial connection between concrete and steel pipe for all targets. The locations of the rebars were chosen to minimize the influence on the projectile penetration path. The NSC target used in 2004 was cast in a steel pipes with 1.20 m diameter, and the steel thickness for these pipes were also 8 mm. This concrete was approximately five months old when the test was performed. Standard strength tests were performed on the used concrete batches, these tests are compiled in tables A3.4 and A3.5.

Table A3.2. Approximate values for material properties of the used concrete type, based on earlier material test and literature data.

Parameter	**NSC K45**
Density	≈2350 kg/m^3
Compressive cube strength at 28 days for 150 mm cubes	45-50 MPa
Compressive cylinder strength after several months [a]	45-50 MPa
Splitting strength [b]	3-4 MPa
E_0 and E_c modulus	≈30-35 GPa

Note: [a] Determined on ∅100×200 mm cylinders.
[b] The tensile strength is approximately 80 to 90 % of the tensile splitting strength.

Table A3.3. Mix proportions of the normal strength concrete.

Materials	**Amount**
Cement, *c*	330 kg/m^3
Aggregate 0 – 4 mm	990 kg/m^3
Aggregate 4 – 8 mm	825 kg/m^3
Water, *w*	215 kg/m^3
w/c = 0.65	
Total:	2360 kg/m^3

Table A3.4. Tested compressive strength for the used concrete target in 2002, NSC K45.

Sample geometry	**Age**	**Compressive strength (MPa)**		
		Average	**Standard deviation**	**No. of samples**
150 mm cubes [a]	28 days	49.2	±1.9	4
∅100×200 mm cylinders [a]		45.5	±0.9	4
150 mm cubes [b]	42 days	41.8	------	2
150 mm cubes [b]	91 days	47.0	±3.0	3
∅100×200 mm cylinders [b]		48.2	±1.7	5
∅100×200 mm cylinders [c]	131 days	42.5	±0.3	4
		Density (kg/m^3)		
		Average	**Standard deviation**	**No. of samples**
150 mm cubes [a]	28 days	2.31×10^3	$\pm0.03\times10^3$	4
∅100×200 mm cylinders [a]		2.33×10^3	$\pm0.01\times10^3$	4
150 mm cubes [b]	42 days	2.24×10^3	------	2
150 mm cubes [b]	91 days	2.28×10^3	$\pm0.02\times10^3$	3
∅100×200 mm cylinders [b]		2.33×10^3	$\pm0.01\times10^3$	5
∅100×200 mm cylinders [c]	131 days	2.28×10^3	$\pm0.01\times10^3$	4

Note: [a] Cured in water the first four days and then stored dry at 20°C.
[b] Cured with the targets at approximately 20°C.
[c] Cored cylinders.

Table A3.5. Tested compressive strength for the used concrete target in 2004, NSC K45.

Sample geometry	**Age Date**	**Compressive strength (MPa)**				
		Sample 1	**Sample 2**	**Sample 3**	**Sample 4**	**Average**
150 mm cubes [a]	291 days 2004-09-20	59.7	60.0	61.4	---	60.4
∅100×200 mm cylinders [a]	291 days 2004-09-20	53.7	56.5	54.2	54.9	54.8
		Density (kg/m^3)				
		Sample 1	**Sample 2**	**Sample 3**	**Sample 4**	**Average**
150 mm cubes [a]	291 days 2004-09-20	2303	2305	2296	---	2.30×10^3
∅100×200 mm cylinders [a]	291 days 2004-09-20	2311	2304	2310	2324	2.31×10^3
		Young's modulus (GPa)				
		Sample 1	**Sample 2**	**Sample 3**	**Sample 4**	**Average**
∅100×200 mm cylinders [a]	291 days 2004-09-20	30.5	30.5	32.5	31.5	31.5

Note: [a] Cured in water the first four days and then stored with the targets.

Shooting technique

A 61 mm smooth bore gun was used for the tests, and is shown in figure A3.3. Both horizontal and vertical view of the projectile before impact and at exit were filmed with two 70 mm high speed cameras at approximately 900 to 950 frames/s, to estimate the yaw and pitch of the projectile. Both cameras covered front and back face of the target for redundancy if a camera failed to record the event. The firing of the gun was synchronized with the high-speed camera to allow the film transport mechanism to accelerate the film before the firing of the projectile. The impact velocities for the projectiles were determined both from the high-speed photos and with short circuit screens mounted in front of and on the target, see figure A3.4. The velocity error for the velocity determined from the high-speed film is estimated to be within ±10 m/s. Therefore, the velocity determined in this way is only used for a verification of the short circuit screen velocity measurement.

Figure A3.3. 61 mm smooth bore gun.

Figure A3.4. Target placement for the test series conducted in 2002. The positions of the short circuit screens for velocity measurement are also shown.

Appendix 3.3. Penetration experiment performed in 2002

Three pre-tests were performed before the actual penetration tests to test the measurements, high speed cameras and shooting technique. Then one test was performed in a normal strength concrete (NSC) target with an impact angle close to 90°.

An overview of the NSC test is presented in table A3.6. The results obtained during the tests and post conditions of the targets are given in this chapter. The definitions of the used crater measurements are given in figure A3.5, and the post-test condition of the target is shown in figure A3.6. The high-speed film from the test is shown in figure A3.7.

Table A3.6. Impact velocity, angle of attack and penetration depth for the test in the NSC target.

Test no.		**2002-10**
Target	No.	40-1
	Diameter	1.25 m
	Length	1.50 m
	Age	8 months
Projectile	Mass	3.64-3.66 kg
	Impact velocity (screens)	420 m/s
	Impact velocity (photos)	420 m/s
	Pitch	≈0.8°
	Yaw	≈1.0° [a]
Penetration depth		49 cm
Crater	Diameter at impact surface	53 cm
	Total crater depth	12 cm
	Inner crater diameter: At crater depth:	21 cm 7 cm
Frame rate for high speed film		923 frames / s

Note: [a] Measurement of yaw is uncertain, see figure A3.7.

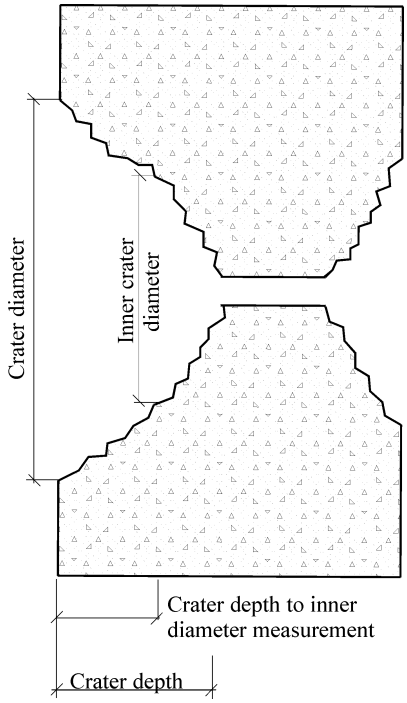

Figure A3.5. Figure of a concrete target, with definitions of crater measurements.

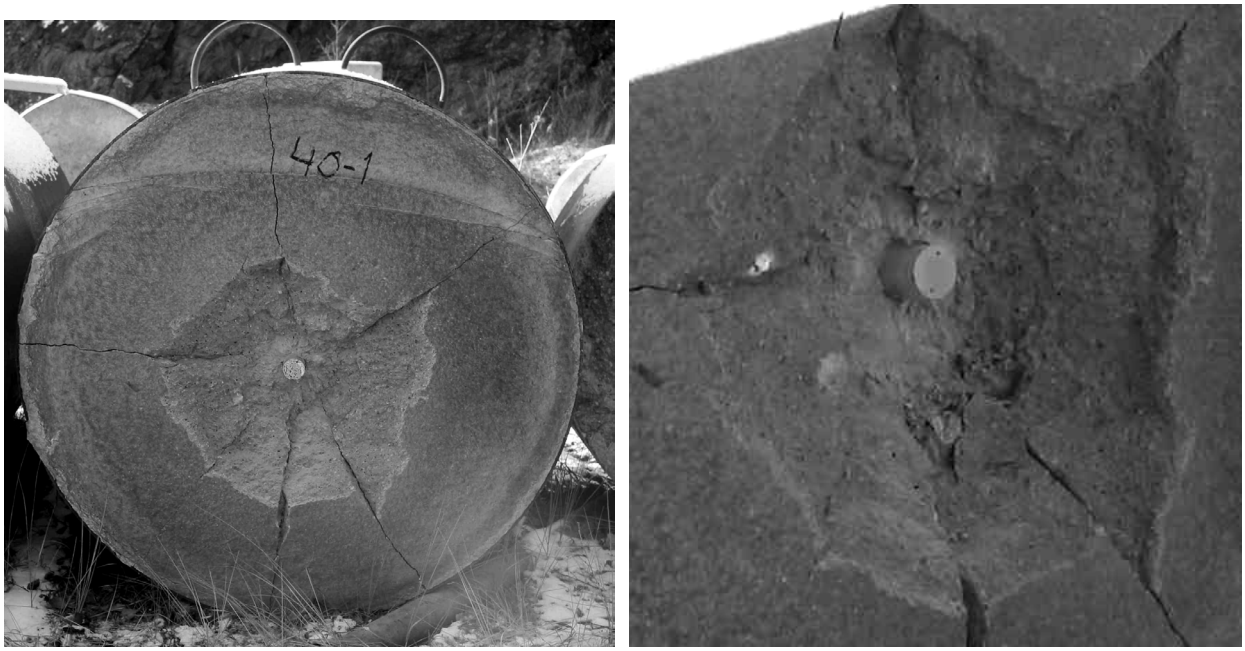

Figure A3.6. Normal strength concrete target after test number 2002-10, with a close up of the projectile shown to the right.

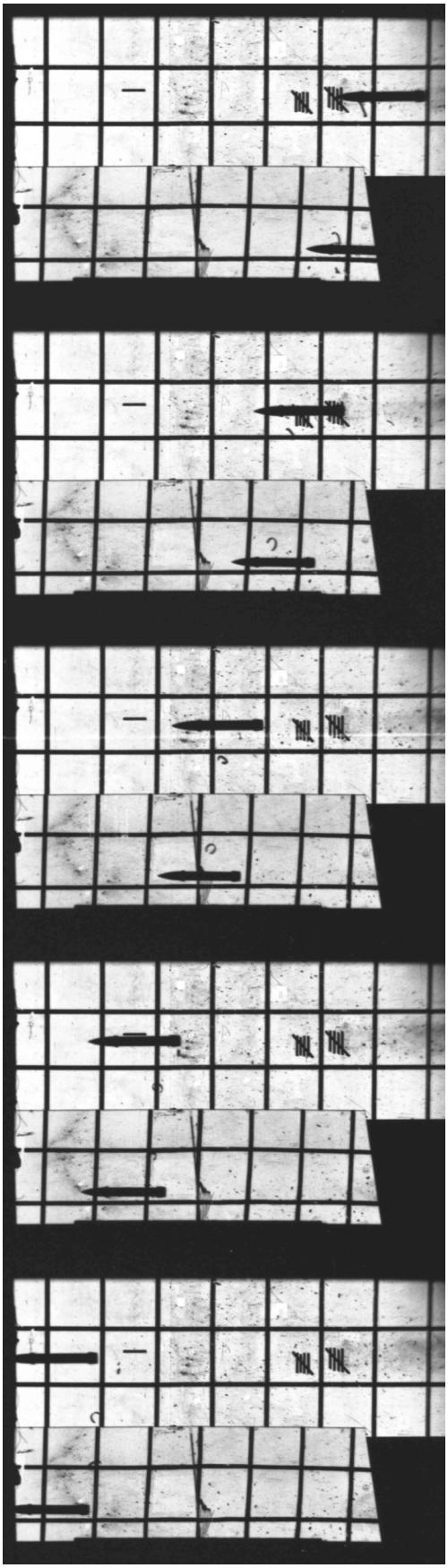

Figure A3.7. High-speed film frames from test number 2002-10.

Appendix 3.4. Penetration experiments performed in 2004

During 2004 reference tests of penetration in normal strength concrete, and also in HPC with approximately 135 MPa unconfined compressive strength, were performed. These concrete types were the same as for the tests performed earlier in 2002. Further, tests with heavy reinforced normal strength concrete targets were also performed. Two nominal impact velocities were also used, these were 420 m/s and 460 m/s. The projectile velocities were determined by three short circuit screens, and then checked against the high speed film. The yaw and pitch angles, and exit velocities, were also determined from the high speed films. The test results for the normal strength concrete targets and projectiles with CRH values of 8 are compiled in tables A3.7 to A3.9. Post test photos of the three unreinforced normal strength concrete targets with 90° impact angle are shown in figures A3.8 to A3.10, and the high speed films from these tests are shown in figures A3.11 and A3.12.

Table A3.7. Impact velocity and test results for tests performed in 2004 (Hansson, 2005).

Test no.		**2004-3**	**2004-4**	**2004-6**
Date	(yyyy-mm-dd)	2004-04-28	2004-05-04	2004-05-06
Target	Concrete type	NSC	NSC	NSC
	Diameter	1.20 m	1.20 m	1.20 m
	Length	0.90 m	1.20 m	0.60 m
	Age in months	4.8	5.0	5.1
Projectile	CRH	8	8	8
	Mass	≈4.53 kg	≈4.53 kg	≈4.53 kg
	Impact velocity [a]	409 m/s	463 m/s	425 m/s
	Impact velocity [b]	404 m/s	455 m/s	425 m/s
	Impact angle	90°	90°	90°
	Pitch [c]	1.25°	0.21°	1.10°
	Yaw [c]	0.49°	0.42°	0.21°
Exit velocity		---	---	139 m/s
Penetration depth [d]		62.0 cm	69.0 cm	---
Front crater	Diameter	≈60 cm	≈80 cm	60-65 cm
	Depth [d]	≈12.5 cm	≈15.0 cm	≈11.0 cm
Back crater	Diameter	---	---	50-90 cm
	Depth [d]	---	---	≈ 15.5 cm
Frame rates	1st camera	913/s	911/s	929/s
	2nd camera	Not used	Not used	916/s

Note: [a] Measured by short circuit screens.
[b] Measured from high speed film.
[c] Estimated measurement error: ≤0.20°
[d] Estimated within ±2.5 mm

Table A3.8. Impact velocity and test results for tests performed in 2004 (Hansson, 2005).

Test no.		**2004-20**	**2004-24-1**	**2004-24-2**
Date	(yyyy-mm-dd)	2004-06-09	2004-06-16	2004-06-16
Target	Concrete type	Reinforced NSC	Reinforced Normal Strenght Concrete	Reinforced Normal Strenght Concrete
	Width	1.20 m	1.20 m	1.20 m
	Height	1.20 m	1.50 m	1.50 m
	Length	0.60 m	0.54 m	0.54 m
	Age in months	6.2	6.4	6.4
Projectile	CRH	8	8	8
	Impact velocity [a]	424 m/s	421 m/s	420 m/s
	Impact velocity [b]	416 m/s	420 m/s	417 m/s
	Impact angle	90°	59.5° ±¼°	59.5°±¼°
	Pitch [c]	0.55°	1.59°	1.06°
	Yaw [c]	0.69°	0.38°	0.14°
Exit velocity		---	---	---
Penetration depth [d]		53.0 cm	39.0 cm	34.5 cm
Estimated penetration path		---	56.5 cm	71.0 cm
Angle between projectile and front face of target		---	≈45.5°	≈29°
Front crater	Diameter	50-60 cm	≈60 cm	85-100 cm
	Depth [d]	≈4.5 cm	8.0 cm	8.5 cm
Back crater	Diameter	70-80 cm	---	Minor spalling
	Depth [d]	≈5.0 cm	---	---
Frame rates	1st camera	926/s	910/s	923/s
	2nd camera	Not used	Not used	Not used
Note		Spalling recovered directly behind target	Fractures on target back face	

Note: [a] Measured by short circuit screens.
[b] Measured from high speed film.
[c] Estimated measurement error: ≤0.20°
[d] Estimated within ±2.5 mm

Table A3.9. Impact velocity and test results for tests performed in 2004 (Hansson, 2005).

Test no.		**2004-25**	**2004-26**
Date	(yyyy-mm-dd)	2004-08-08	2004-08-09
Target	Concrete type	NSC	NSC
	Diameter	1.50 m	1.50 m
	Length	0.54 m	0.54 m
	Age in months	8.1	8.2
Projectile	CRH	8	8
	Impact velocity [a]	424 m/s	422 m/s
	Impact velocity [b]	419 m/s	422 m/s
	Impact angle	59.5° ±¼°	59.5° ±¼°
	Pitch [c]	1.07°	1.19°
	Yaw [c]	0.00°	0.23°
Exit velocity		16 m/s	---
Penetration depth [d]		---	≈50 cm
Estimated penetration path		---	---
Angle between projectile and front face of target		---	≈40°
Front crater	Diameter	80-90 cm	≈65 cm
	Depth	≈24 cm	≈23 cm
Back crater	Diameter	90-105 cm	75-105 cm
	Depth	≈22 cm	≈18 cm
Frame rates	1st camera	916/s	921/s
	2nd camera	913/s	Not used
Note			Angle between projectile and front face of target: 40°

Note: [a] Measured by short circuit screens.
[b] Measured from high speed film.
[c] Estimated measurement error: ≤0.20°
[d] Penetration depth measured perpendicular to front face of target.

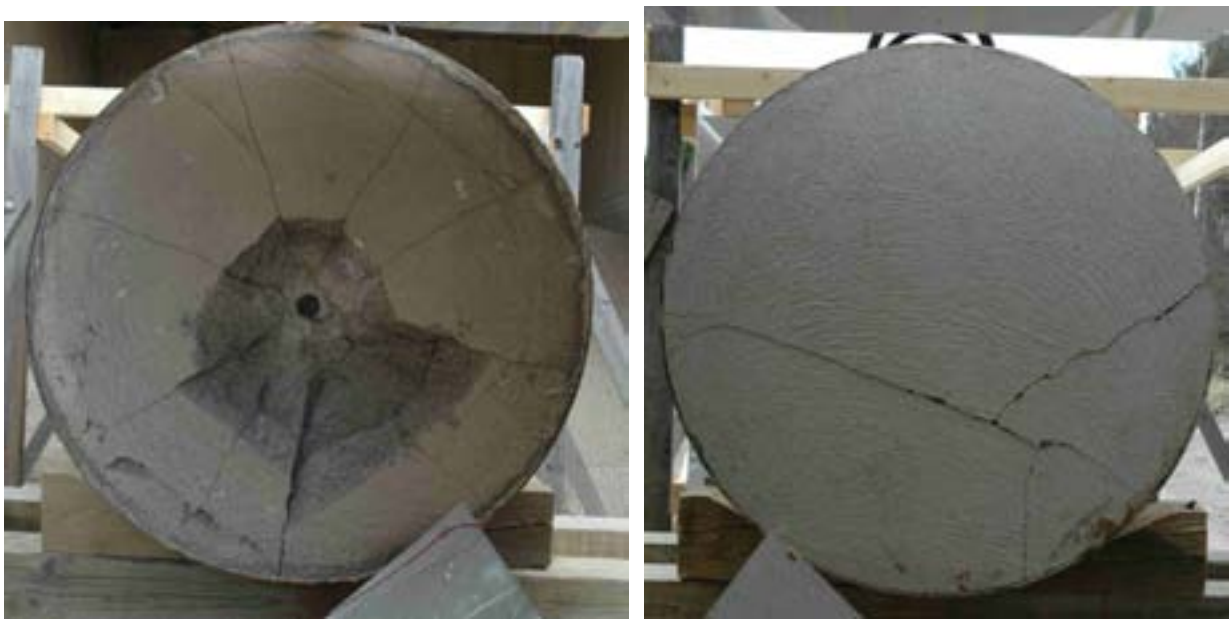

Figure A3.8. Normal strength concrete target after test number 2004-3.

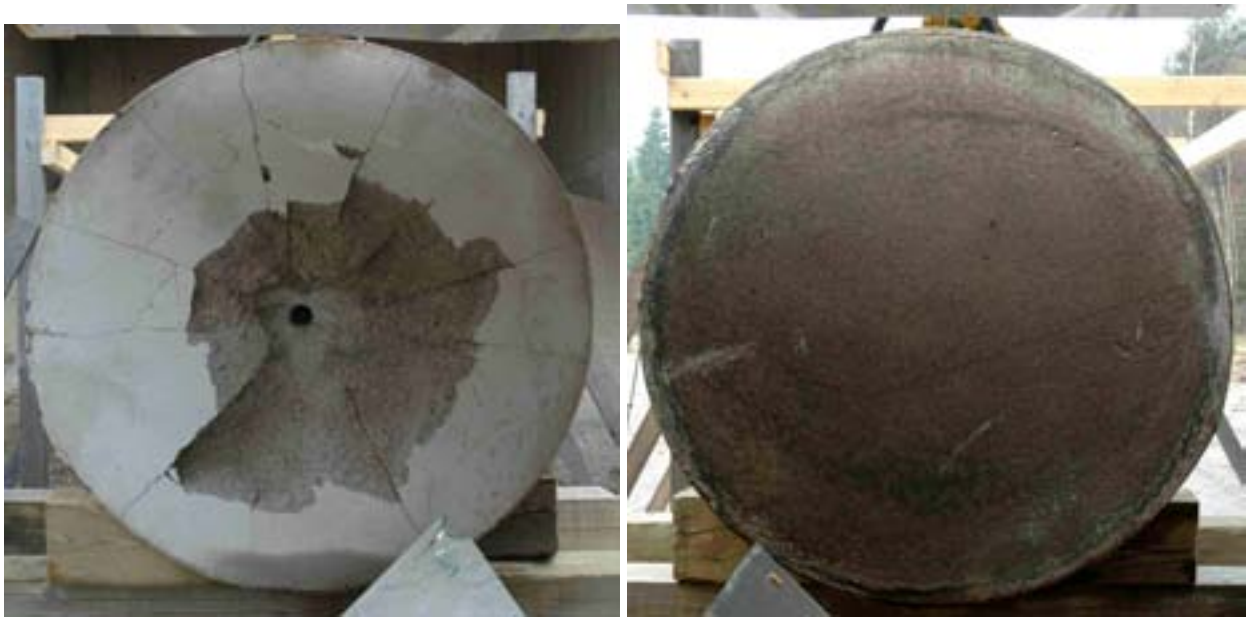

Figure A3.9. Normal strength concrete target after test number 2004-4.

Figure A3.10. Normal strength concrete target after test number 2004-6.

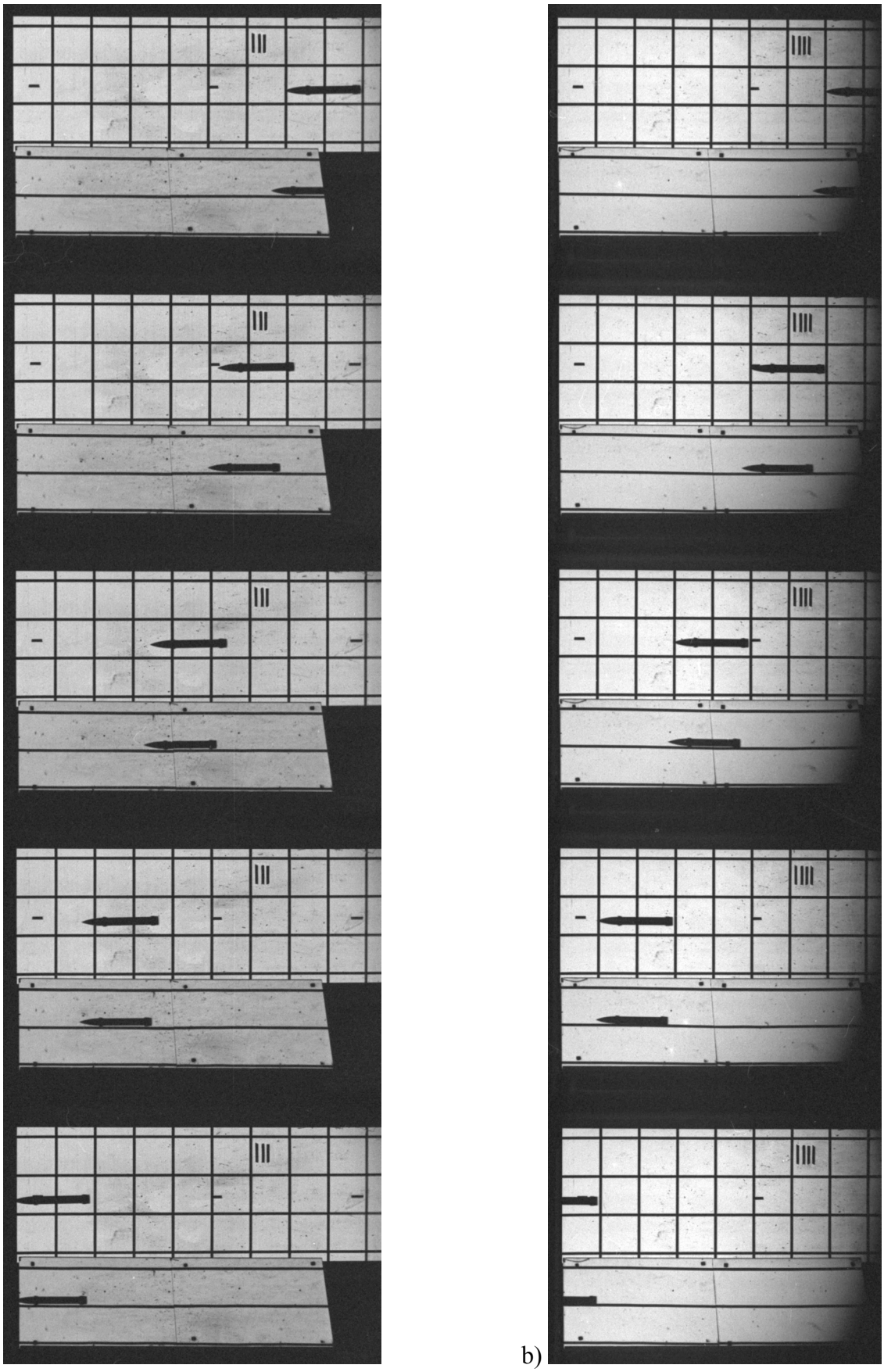

a) b)

Figure A3.11. High-speed film frames from test numbers 2004-3 (a) and 2004-4 (b).

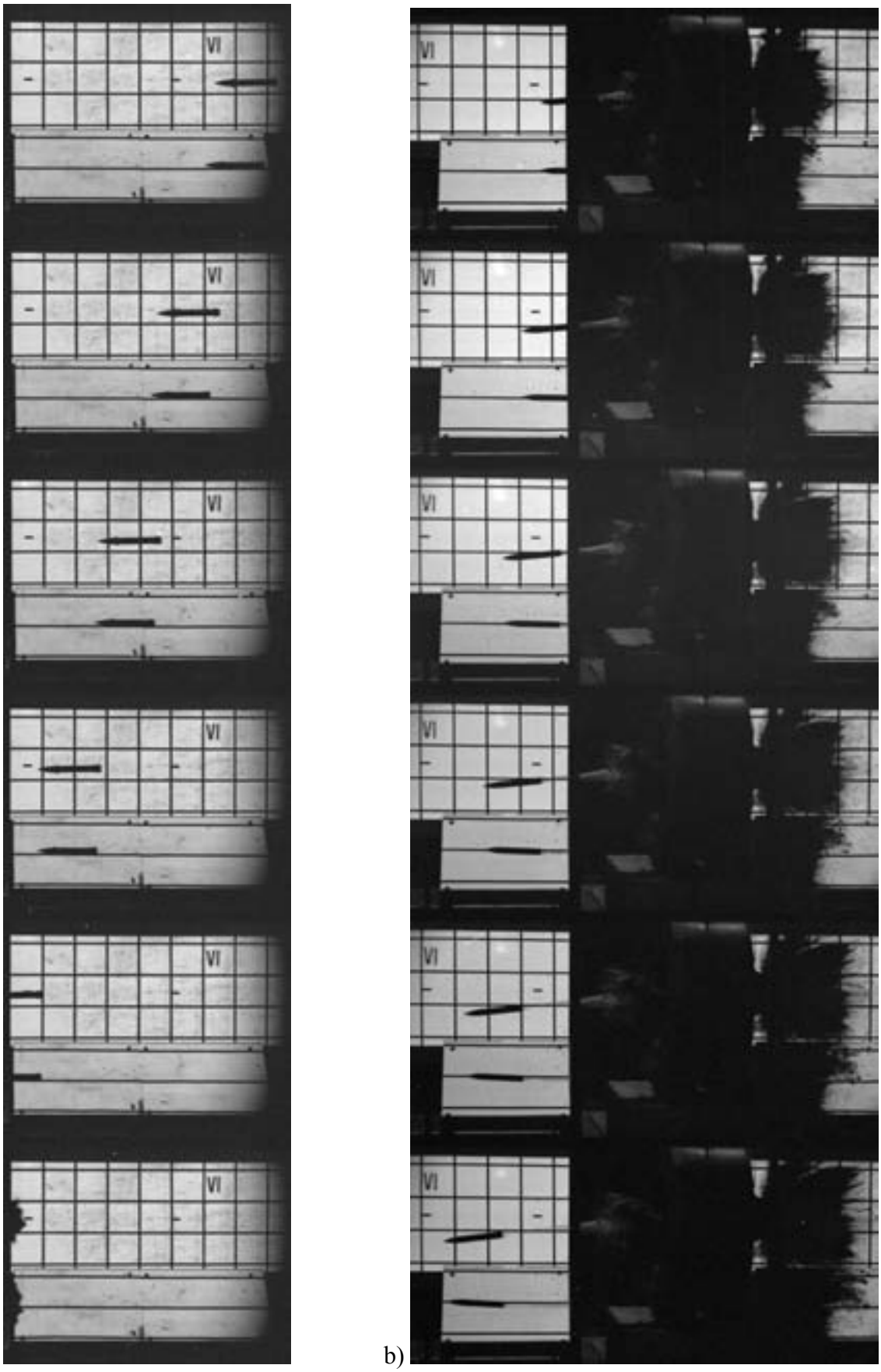

Figure A3.12. High-speed film frames from test number 2004-6, front (a) and back face (b) cameras.

Test number 2004-20 was performed in reinforced concrete with approximately normal impact of the projectiles. The target was 1.20 m by 1.20 m, with a thickness of 0.60 m. The projectile with CRH value of 8 impacted the target at a velocity of 424 m/s and penetrated to a depth of approximately 53.0 cm. Back face spalling occurred for the test. However, the visual damage at the back face was limited to the concrete cover behind the reinforcement. Post test photos of the reinforced target are shown in figure A3.13.

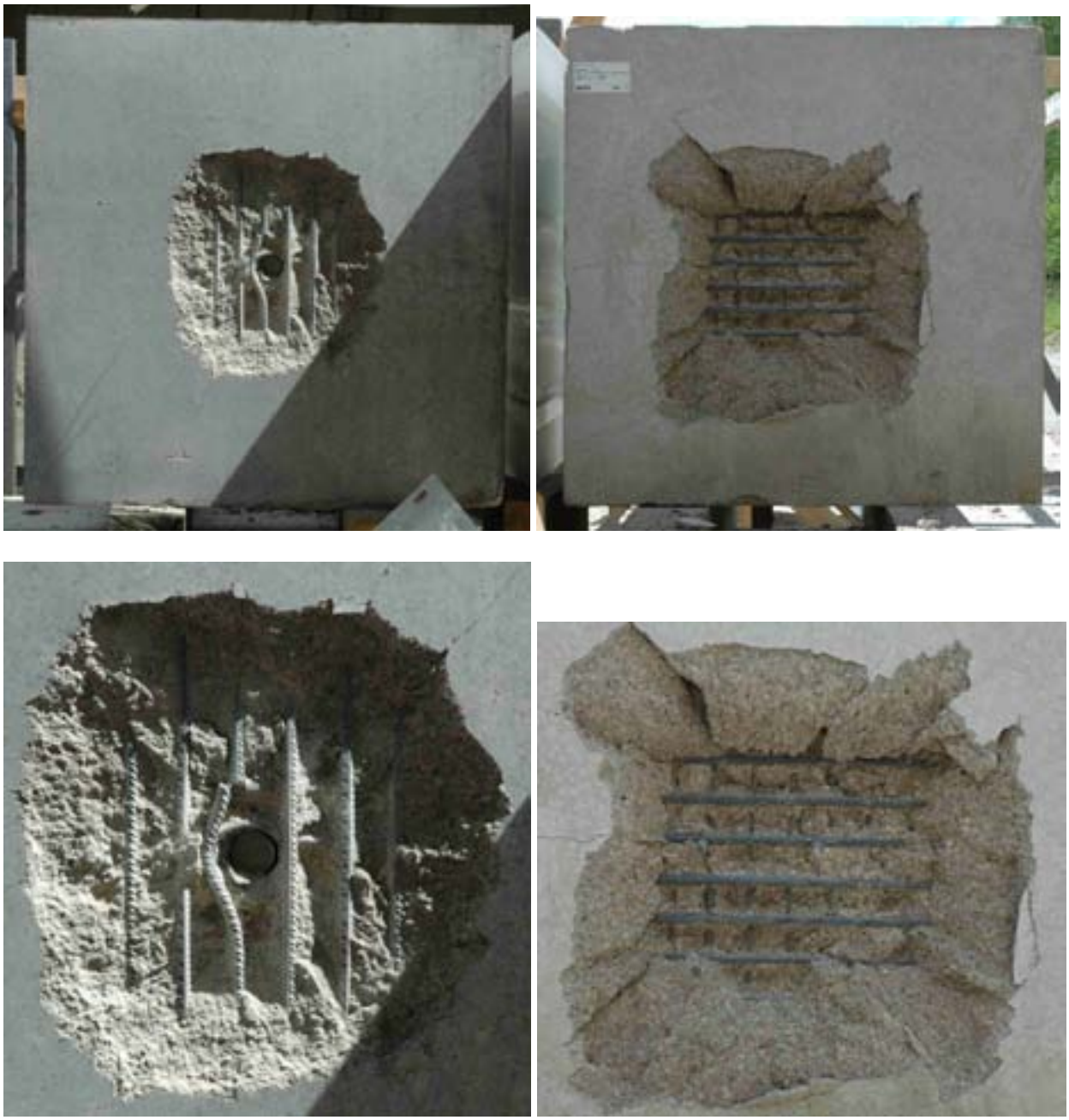

Figure A3.13. Reinforced normal strength concrete target after test number 2004-20, incl. details of craters. Front views to the left, and back face shown to the right.

Test with an impact angle of the projectile close to 59.5° were performed with confined unreinforced concrete targets and also reinforced NSC targets. The targets were placed in a rig to obtain the same angle for each test, and the line of sight through the gun barrel was determined by a laser and adjusted approximately through the centre of the target. The height of the projectile impact is marked with a white tape strip in figure A3.14 below. The targets for these tests have a diameter of 1.50 m. The thickness for the targets are 0.54 m.

Figure A3.14. Target location for test no. 2004-25 and 2004-26.

The targets for test numbers 2004-25 and 2004-26 were 54 cm unreinforced NSC. These tests used the projectile design with a CRH value of 8. The impact velocity for test no. 2004-25 was 424 m/s, resulting in a perforation of the target and an exit velocity for the projectile of 16 m/s. For test no. 2004-26 the impact velocity was 422 m/s, and the projectile was stopped close to the back face of the target. These targets are shown in figures A3.15 and A3.16, with the recovered projectile from test no. 2004-25 shown in figure A3.17. Figure A3.18 show the the high-speed video of test no. 2004-26.

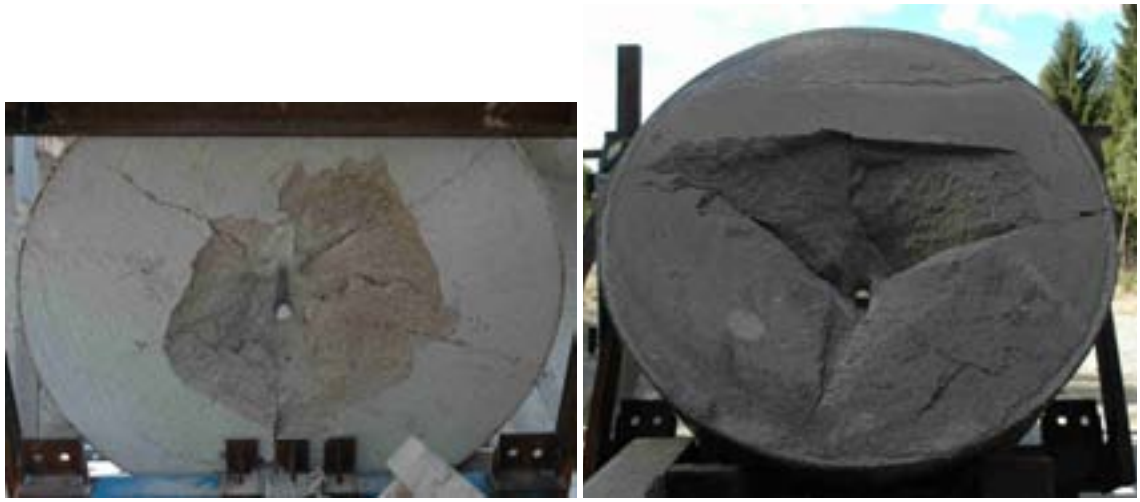

Figure A3.15. Normal strength concrete targets after test number 2004-25.

Figure A3.16. Normal strength concrete targets after test number 2004-26.

Figure A3.17. Recovered projectile from test number 2004-25.

Figure A3.18. Frames from high-speed video of test no. 2004-26.

Reinforced NSC targets were also used to study the effect of non-normal impacts. The heights of these targets are 1.50 m, with a width of 1.20 m. The thicknesses of the reinforced targets are the same as for the unreinforced NSC, i.e. 0.54 m. Two tests were performed in each of the two targets, to study the influence of multiple impacts of a target. The placement of the targets in the test rig is shown in figure A3.19. The targets were then moved sideways before the second test in the target.

Figure A3.19. Target location for first test in target no. 2004-24. The target was then moved to the right before the second test in this target was performed.

Target 2004-24 was used for tests with two projectiles with CRH value of 8. The impact velocity for the first test was 421 m/s, resulting in a penetration depth of approximately 39.0 cm measured perpendicular to the front face. The impact velocity for the second test in the target was 420 m/s, resulting in a penetration depth of approximately 34.5 cm measured perpendicular to the front face of the target.

Both projectiles that penetrated target 2004-24 were broken into two pieces. Post test photos of the target are shown in figures A3.20 to A3.22, with the recovered projectiles shown in figure A3.23. High-speed video frames from test no. 2004-24-1 are shown in figure A3.24 and A3.25.

Figure A3.20. Reinforced normal strength concrete target after test number 2004-24-1.

Figure A3.21. Reinforced normal strength concrete target after test number 2004-24-2.

Figure A3.22. Reinforced normal strength concrete target 2004-24 shown during removal of the projectiles. The projectile from test no. 2004-24-1 is shown to the right.

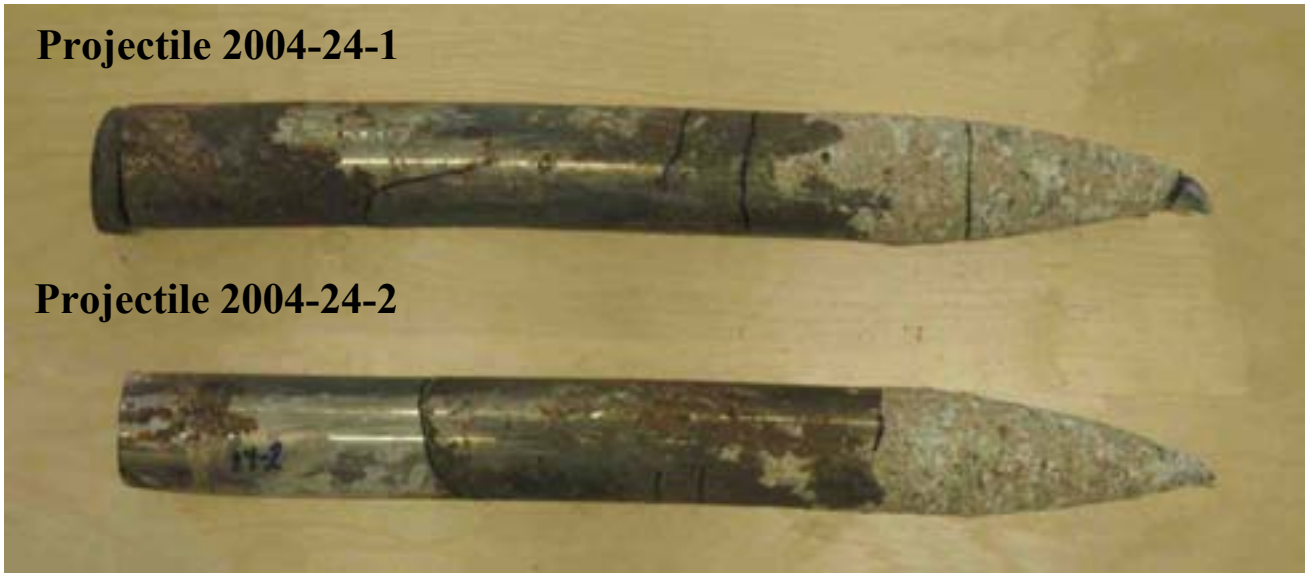

Figure A3.23. Recovered projectiles from target number 3004-24. Both of the projectiles were broken into two pieces, with the projectile from test 2004-24-2 fractured approximately 10 cm from the nose and the projectile from test 2004-24-2 fractured approximately 13 cm from the back face.

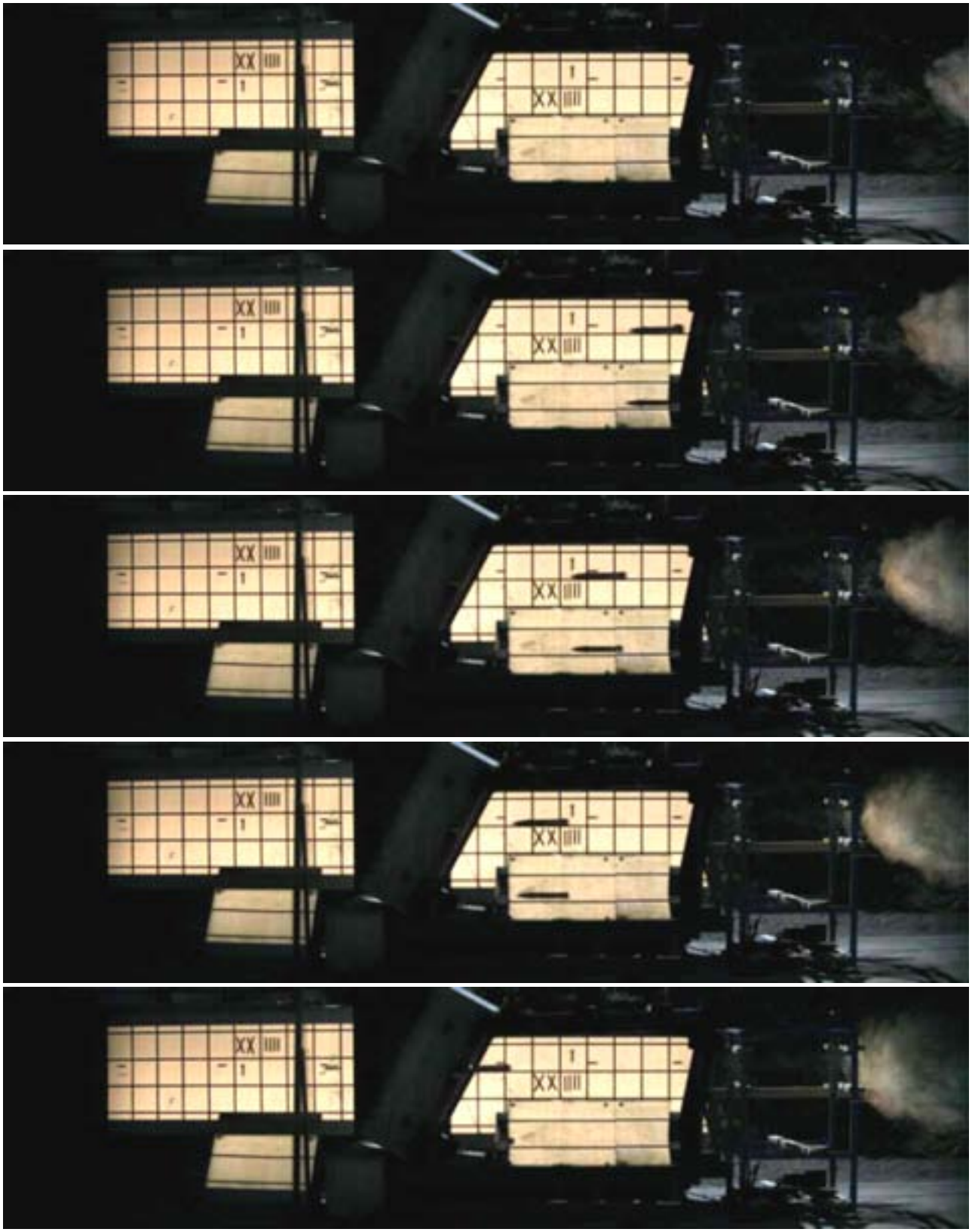

Figure A3.24. Frames from high-speed video of test no. 2004-24-1, before impact.

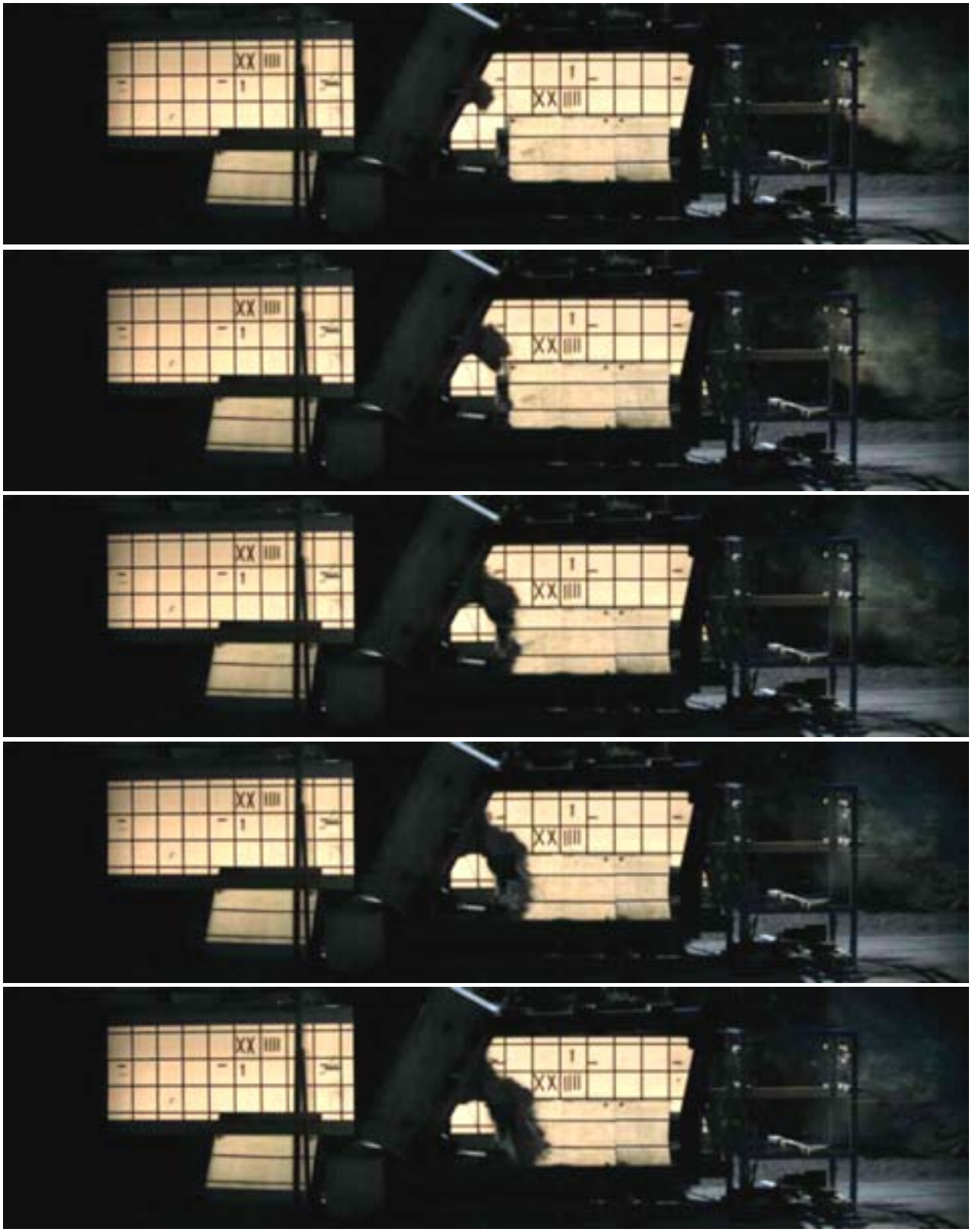

Figure A3.25. Frames from high-speed video of test no. 2004-24-1, after impact.

Appendix 3.5. Summary of penetration test

A penetration test with a sharp ogive nosed 50 mm projectile with a mass of 3.65 kg into a normal strength concrete with approximate 48 MPa uni-axial compressive strength was performed in 2002. The calibre to ogive head radius (CRH) of the projectile was 8.0 and the diameter to length ratio was 9.0. The penetration depth for the used projectile was 49 cm at an impact velocity of 420 m/s.

Two penetration tests with an increased mass of the projectile to 4.53 kg, and with different impact velocities, were performed in the same type of concrete in 2004. The penetration depths with this projectile design were 62 cm at a velocity of 409 m/s, and 69 cm at a velocity of 463 m/s.

The increase of the projectile mass with 24% resulted in an increase of the penetration depth with approximate 27%. However, the concrete batches were not identical and the impact velocities were not identical for the tests, but it seems like the tests indicate that the penetration depth roughly is proportional to the mass of the penetrator for deep penetration into concrete. This is not the case for relative small penetration depths were the cratering of the target is of major concern.

Further, the 13% increase of impact velocity only increased the penetration depth by 11%. In this case the kinetic energy is increased by almost 30%. The likely reason for this is that with increased impact velocity the energy losses, i.e. due to cratering effects, is increased. The crater diameter and depth are increasing when the impact velocity increases.

Tests with reduced thicknesses of the concrete targets to 0.60 m, and using the projectile with increased mass to approximately 4.53 kg, resulted in perforation of the target. The impact and exit velocities for the penetrator were 425 m/s and 139 m/s, respectively. For the inclined targets with 0.54 m thickness and a 60° impact angle it seems that a velocity of 420 m/s is close to the required velocity for perforation of the target with the used projectile type.

The heavy reinforced concrete targets increased the penetration resistance compared with the unreinforced targets, for both tests with 90° and 60° impact angle.